ACOUSTIC PRESSURE OSCILLATIONS INDUCED BY CONFINED TURBULENT PREMIXED NATURAL GAS FLAMES

Jaap van Kampen

De promotiecommissie is als volgt samengesteld:

Voorzitter en secretaris:	
Prof.ir. J.W.L.H. Croonen	Universiteit Twente
Promotor:	
Prof.dr.ir. Th.H. van der Meer	Universiteit Twente
Assistent promotor:	
Dr.ir. J.B.W. Kok	Universiteit Twente
Leden:	
Prof.dr.ir. A. de Boer	Universiteit Twente
Prof.dr. L.P.H. de Goey	Technische Universiteit Eindhoven
Prof.dr. A. Hirschberg	Universiteit Twente
Dr. W. Krebs	Siemens Power Generation
Prof.dr. W. Polifke	Technische Universität München

This research project is performed within the framework of the EU project DESIRE.

Acoustic pressure oscillations induced by confined turbulent premixed natural gas flames
Kampen, Jacobus Franciscus van
PhD thesis, University of Twente, Enschede, The Netherlands
March 2006

ISBN 90-365-2277-3

Printed by Febodruk BV, Enschede, The Netherlands

Cover: Photograph of a turbulent premixed flame (20 kW), taken by R. Loendersloot.

ACOUSTIC PRESSURE OSCILLATIONS INDUCED BY CONFINED TURBULENT PREMIXED NATURAL GAS FLAMES

PROEFSCHRIFT

ter verkrijging van
de graad van doctor aan de Universiteit Twente,
op gezag van de rector magnificus,
prof.dr. W.H.M. Zijm,
volgens besluit van het College voor Promoties
in het openbaar te verdedigen
op donderdag 9 maart 2006 om 15.00 uur

door

Jacobus Franciscus van Kampen

geboren op 18 januari 1978

te Villanueva y Geltrú

Dit proefschrift is goedgekeurd door de promotor

Prof.dr.ir. Th.H. van der Meer

en door de assistent promotor

Dr.ir. J.B.W. Kok

Summary

In modern industrial gas turbine designs, low NO_x emissions are achieved by introducing lean premixed techniques. However, this provokes a higher risk for so-called thermo-acoustic instabilities, which arise from the interaction of heat and sound.

In gas turbine combustors, the heat source is the turbulent flame. The turbulent fluctuations in the flame act as a sound source, producing a sound field in the combustor and in the burner, upstream of the flame. In the burner, the fluctuating nature of sound causes inlet properties of the flame to fluctuate, resulting in an acoustic response of the flame. This leads to a correlated sound field in the burner. Under the 'right' circumstances a feedback loop arises in which the acoustic pressure amplitude reaches intolerable levels. Amplitudes up to 0.7 bar have been measured in industrial gas turbines. These high acoustic amplitudes lead to engine damage. Since lean premixed flames are more sensitive to perturbations at their inlet, the problem described above limits the reduction of NO_x emissions.

The present study is concerned with the development and validation of efficient numerical algorithms to check combustion systems for their sensitivity to thermo-acoustic instabilities. For this purpose, a good acoustic model is needed. Since the acoustics in combustion systems are essentially one-dimensional, an efficient one-dimensional acoustic network model has been used to model this acoustic system. The most important effects that play a role in the acoustic modelling of combustion systems have been included in this network model. These effects comprise acoustic damping due to turbulence, acoustic reflection at contractions and expansions with a mean flow, modification of the acoustic speed of sound due to a mean flow and the effect of a temperature gradient. Consequently, the network model can handle most combustion system layouts.

Supplementary to the acoustic model, a so-called flame transfer function is needed for the analysis of the thermo-acoustic stability. The flame transfer function represents the dynamic relationship between a fluctuation in the inlet conditions of a flame and its acoustic response. A numerical experiment involving spectral analysis in transient CFD is usually conducted to predict the flame transfer function. An important disadvantage of this method is its computational effort. Since the applied spectral analysis requires the system to behave linearly, a much more efficient way to determine the transfer function can be derived by constructing a linear representation of the system from the steady-state solution. The dynamic transfer function can be calculated directly from this linear description. As a consequence of the large order of the linear representation of a CFD problem (i.e. usually $> \mathcal{O}(10^6)$), the transfer

function calculation also involves an order reduction step. This alternative approach is called the *linear coefficient method*. With the method the transfer function can be calculated several orders of magnitude faster and more accurate than with the conventional transient methods. This makes the method suitable as a thermo-acoustic design tool.

The experimental validation of the developed models is done in a combustion test rig with a maximum thermal power of 500 kW at 5 bars absolute pressure. The setup distinguishes itself from other experimental combustion setups by the fact that it is designed for thermo-acoustic measurements at elevated pressures, at which full visual access to the flame zone is provided. Moreover, the combustor wall vibrations as a response to the acoustic field generated by the flame can be measured.

Flame transfer functions have been determined experimentally by exciting the fuel mass flow with an amplitude of 5% of the mean flow, and reconstructing the acoustic response of the flame from acoustic pressure measurements in the combustor. A good agreement between the flame transfer function measurements and the numerical calculations is found, which proves that the Unsteady RaNS approach combined with a relatively simple combustion model correctly predicts the flame location and the flame length, as these are the most important factors for the flame transfer function. Measurements at elevated pressures show an effect of the mean pressure on the flame transfer function. This effect is attributed to the pressure dependence of the reaction rate.

At a specific operating point of the experimental setup, a thermo-acoustic instability is encountered. The frequency of this instability could be matched by the acoustic network model coupled to a flame transfer function. This coupled model also correctly predicts stability behaviour at another operating point, where the increased acoustic damping and the smaller time delay in the feedback loop increase the stability.

The numerical simulations in this thesis have been conducted with a relatively simple combustion model. To reveal possible shortcomings of this model, a more advanced combustion model has been considered as well. This model is called the CFI model and is based on reducing the chemical reaction mechanism by projecting it onto a limited number of reaction progress variables. The results with the CFI model show a slightly different flame than the flame calculated by the relatively simple model. Nonetheless, the effect on the flame transfer function is small.

Samenvatting

In de huidige industriële gasturbines worden lage emissies van NO_x bereikt door arme, voorgemengde verbranding toe te passen. Dit type verbranding leidt echter tot een groter gevaar voor het optreden van zogenaamde thermo-akoestische instabiliteiten, die het gevolg zijn van de interactie van warmte en geluid.

In de verbrandingskamer van een gasturbine is de warmtebron de turbulente vlam. Door de turbulente fluctuaties in de vlam gedraagt deze zich als een geluidsbron en veroorzaakt een geluidsveld, zowel in de verbrandingskamer als in de brander. In de brander zorgt het akoestische veld ervoor dat de toevoer van de vlam fluctueert. Deze fluctuaties zorgen voor een akoestische reactie van de vlam, en dientengevolge voor een nieuw gecorreleerd geluidsveld. Onder de 'juiste' omstandigheden bouwt zich een thermo-akoestische instabiliteit op, waarin de akoestische druk amplitude een onacceptabel hoog niveau bereikt. In industriële gasturbines zijn amplitudes tot 0.7 bar gemeten. Deze hoge amplitudes leiden tot schade aan de machine. Omdat de arme, voorgemengde vlammen gevoeliger zijn voor fluctuaties, beperkt het hierboven beschreven probleem de verlaging van NO_x emissies.

Deze studie behandelt de ontwikkeling en validatie van efficiënte numerieke algoritmen om verbrandingssystemen te controleren op hun gevoeligheid voor thermo-akoestische instabiliteiten. Op de eerste plaats is hiervoor is een goed akoestisch model nodig. Aangezien de akoestiek in verbrandingssystemen hoofdzakelijk één-dimensionaal is, is hiervoor een efficiënt één-dimensionaal akoestisch netwerkmodel gebruikt. De belangrijkste processen die invloed hebben op de akoestiek in verbrandingssystemen zijn opgenomen in dit netwerkmodel. Deze processen zijn: akoestische demping door turbulentie, akoestische reflectie bij oppervlakte contracties en expansies, verandering van de geluidssnelheid door stroming en het effect van een temperatuurgradiënt. Derhalve is het netwerkmodel geschikt voor het beschrijven van de akoestiek in de meeste verbrandingssystemen.

Naast het akoestische model is er een zogenaamde vlamoverdracht nodig. De vlamoverdracht vertegenwoordigt het dynamische verband tussen een fluctuatie in de toevoer van een vlam en zijn akoestische reactie daarop. Tot dusver was het gebruikelijk om deze vlamoverdracht te bepalen door het toepassen van spectrale analyse op grootheden uit een tijdsafhankelijke, zeer tijdrovende, CFD simulatie. Aangezien de spectrale analyse vereist dat het systeem zich lineair gedraagt, is het veel efficiënter om de overdrachtsfunctie te bepalen uit de lineaire beschrijving van het systeem. Deze lineaire beschrijving kan afgeleid worden uit de stationaire CFD oplossing. De overdrachtsfunctie kan vervolgens direct uit deze lineaire beschrijving

worden berekend. Als gevolg van de grote omvang van de lineaire beschrijving (ongeveer $\mathcal{O}(10^6)$), is er een reductie methode toegepast in de berekening van de overdrachtsfunctie uit de lineaire beschrijving. Deze alternatieve benadering wordt de *lineaire coëfficiënten methode* genoemd. Met de methode kan de overdrachtsfunctie een aantal ordegroottes sneller én nauwkeuriger worden berekend dan met de conventionele methodes. Dit maakt de methode geschikt als thermo-akoestisch ontwerphulpmiddel.

De ontwikkelde modellen zijn experimenteel gevalideerd in een verbrandingsinstallatie met een thermische vermogen van maximaal 500 kW bij een absolute druk van 5 bar. De opstelling onderscheidt zich van andere experimentele verbrandingsinstallaties door de mogelijkheid om thermo-akoestische metingen uit te voeren op hoge druk. Daarbij verschaffen glazen vensters de mogelijkheid om de vlam te bestuderen met laser apparatuur. Voorts kunnen de trillingen van de wand van de verbrandingskamer ten gevolge van het, door de vlam geproduceerde, geluidsveld worden gemeten.

De overdrachtsfuncties van de vlam zijn experimenteel bepaald door de brandstofstroom met 5% te fluctueren. Vervolgens is de akoestische reactie van de vlam gereconstrueerd uit akoestische drukmetingen in de verbrandingskamer. De gemeten en de numeriek berekende overdrachten vertonen een goede overeenkomst. Dit betekent dat de belangrijkste factoren van de overdrachtsfunctie, namelijk de locatie en de lengte van de vlam, goed voorspeld worden door de Unsteady RaNS CFD berekeningen en het gebruikte verbrandingsmodel. In de experimenten is tevens het effect van de gemiddelde druk op de vlamoverdracht onderzocht. De gemiddelde druk blijkt invloed te hebben op de gemeten overdracht, wat toegeschreven kan worden aan de drukafhankelijke reactiesnelheid.

Op een bepaald werkpunt van de experimentele opstelling is een thermo-akoestische instabiliteit aangetroffen. Door het koppelen van het akoestisch netwerkmodel met de vlamoverdracht kan de frequentie van deze instabiliteit correct worden voorspeld. Het gekoppelde model voorspelt tevens een correct stabiliteitsgedrag op een ander werkpunt, waar de stabiliteit verhoogd wordt door de hogere akoestische demping en de kleinere tijdsvertraging in de vlamoverdracht.

De numerieke simulaties in dit proefschrift zijn uitgevoerd met een relatief eenvoudig verbrandingsmodel. Om mogelijke tekortkomingen van dit model te identificiëren is ook het geavanceerdere CFI-verbrandingsmodel gebruikt. In dit model wordt het gedetailleerde chemische reactiemechanisme geprojecteerd op een beperkt aantal reactievoortgangs-variabelen. Het CFI-model berekent een vlam die verschillen vertoont met de vlam die verkregen was met het eenvoudige verbrandingsmodel. Desalniettemin is het effect op de vlamoverdracht minimaal.

Contents

Chapter 1

Introduction

1.1 Background

> "I happened to be one of a party of eight persons assembled after tea for the purpose of enjoying a private musical entertainment. Three instruments were employed in the performance of several of the grand trios of Beethoven, namely, the piano, violin and violoncello. Two '*fish-tail*' gas-burners projected from the brick wall near the piano. (...) Soon after the music commenced, I observed that the flame of the last-mentioned burner exhibited pulsations in height, which were *exactly synchronous* with the audible beats. This phenomenon was very striking to every one in the room, and especially so when the strong notes of the violoncello came in. (...) *A deaf man might have seen the harmony.*"

The preceding quotation is from John LeConte (1818-1891) and was written down in 1858 [105]. He describes the effect of acoustic waves on the behaviour of flames, and his work helped in the development of means to visualise sound wave effects. The effect described by LeConte can easily be mimicked by placing a candle in front of a loudspeaker. The acoustic pressure waves influence the combustion process and therewith the flame shape, and the flame starts to 'dance' on the rhythm of the music.

Two decennia later, in 1878, Lord Rayleigh recognised that unsteady flames or, more general, fluctuating heat sources have an effect on acoustics as well [143], and the research field of 'thermo-acoustics' was founded. In the successive period, many authors have studied the interaction of heat and sound, resulting in a basic knowledge of this interaction for simple systems [25, 106]. The interest of most authors is related to the problem known as *thermo-acoustic instabilities*.

A thermo-acoustic instability can be described as a feedback loop caused by the interaction between heat and sound, which results in a build up of acoustic pressures with time. In the same way as a loudspeaker connected to a microphone can produce a screeching sound due to feedback (in audio terms this is called *howlback* or *howlround*), a flame can produce a loud tonal noise because the sound produced by the flame affects the flame itself (see figure 1.1). Generally speaking, combus-

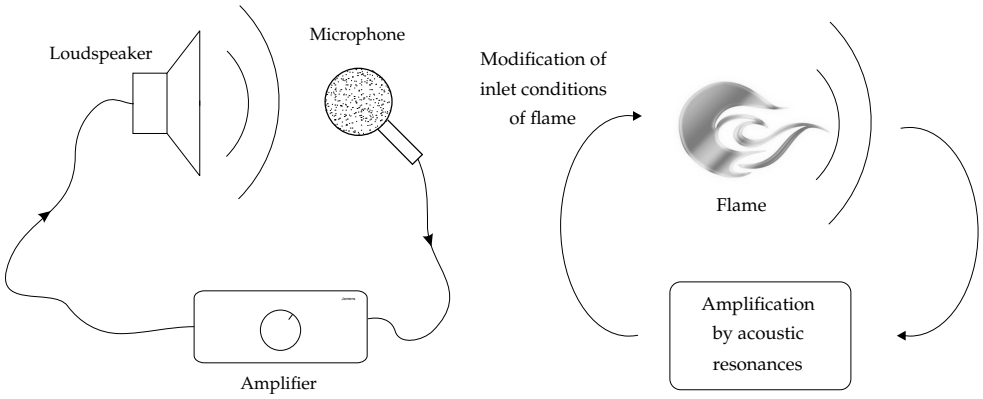

(a) Electronic feedback (b) Thermo-acoustic feedback

Figure 1.1: Feedback loops that can lead to an unstable build up of sound.

tion instabilities are the result of a resonant interaction between at least two oscillatory mechanisms in the system: an excitation mechanism and a feedback effect. The sound pressure level resulting from a thermo-acoustic instability is only limited by changes in the thermo-acoustic feedback system, or by non-linear effects.

The ever ongoing search for more efficient and clean combustion systems and the ever increasing power density have increased the interest in the subject of thermo-acoustic instabilities. This interest is mainly driven by the desire to decrease the levels of nitrogen oxides (NO_x).

Recently, the Institute of Environmental Physics of the University of Heidelberg published a world map coloured by the mean tropospheric NO_2 as measured by the SCIAMACHY satellite (see figure 1.2). It can be seen that above the industrialised countries, the measured levels are relatively high. Nitrogen dioxide is one of the family of chemicals collectively known as NO_x (oxides of nitrogen). These substances are produced when fuel is burnt in power stations and cars. NO_2 is an irritant gas which can have serious effects on health when inhaled at high concentrations.

Despite these increased NO_x levels, future forecast for electricity generation by power stations indicates an annual increase of 2 to 3%. A large share of this electricity is produced by driving a generator with a gas turbine, in which natural gas is combusted. Natural gas, being the cleanest of all well-available fossil fuels, has become a very popular fuel for the generation of electricity. Composed primarily of methane, the main products of the combustion of natural gas are carbon dioxide (CO_2) and water vapour (H_2O). However, when the temperature at which combustion takes place is relatively high, NO_x is produced as well, polluting the atmosphere.

The combustion temperature can be lowered by burning a leaner mixture, i.e. a mixture with an excess of air compared to fuel. This mixture must be well premixed to prevent local variations of the fuel-to-air ratio and therefore locally higher temperatures. This concept is applied in the latest generation of combustion systems for gas turbines, which are indicated as lean premixed combustion systems.

The downside of these combustion systems is that they are prone to thermo-

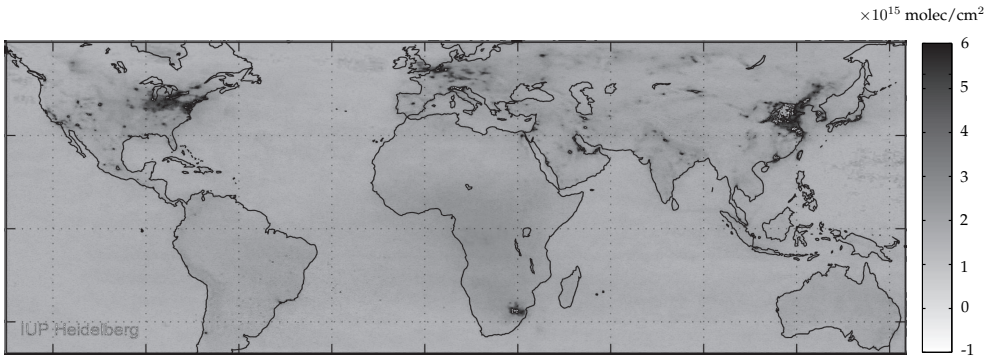

Figure 1.2: Mean tropospheric NO_2 vertical column density (VCD) from SCIAMACHY (January 2003-July 2004).

acoustically induced combustion instabilities. The high levelled acoustic pressure oscillations occurring with a thermo-acoustic instability impose an extra mechanical load on the wall of the combustor, which is usually called the liner. Additionally, heat transfer to the liner is augmented by the unsteady flow and local overheating may be induced. Finally, electronic systems controlling combustion may fail due to high vibration or temperature levels, leading to loss of control of the system. In short, thermo-acoustic oscillations cause increased wear and tear and hence have a dramatic impact on reliability and availability of the power station*.

The effect of the acoustic pressure oscillations on the structure and the consequences on the liner design play a crucial role with respect to the reliability of the engine. To investigate this effect, the EU supported the project DESIRE (Design and demonstration of highly reliable low NO_x combustion systems for gas turbines), which was started in 2002 and ends in 2006. The investigation presented in this thesis is done within the scope of this project.

The partners in the DESIRE project are Siemens Power Generation (initiator and coordinator), DLR, KEMA, E.ON, CERFACS, CIMNE and the University of Twente. The primary objective of DESIRE is to provide models for predicting the interaction between the sound produced by the flame and the resulting vibrations of the liner. The development and the experimental validation of these models is done at the University of Twente, where a combustion test rig is built. This test rig has a nominal thermal power of 100 kW/bar and can operate up to 5 bars absolute pressure.

To understand strategies applied by gas turbine manufacturers to reduce pollutants, the next section is devoted to the general working principle and design issues of a gas turbine. After this, the thermo-acoustic problem in the combustion chamber of this turbine will be discussed.

*Oscillating combustion can also produce positive results, such as increased rates of thermal energy transfer (Nusselt number increases of a factor 2.5 can be achieved [40]) and enhanced mass transport processes. The exploitation of these attributes is by the development of pulsating combustors [141].

1.2 The gas turbine

There are two basic types of gas turbines: aeroengines and industrial gas turbines. As their name suggests, aeroengines are aircraft jet engines. Currently, these units have a maximum output of about 40 MW. Industrial gas turbines range in electrical power output from 500 kW to more than 260 MW and are used for base-load electricity generation. Because efficiency and pollutant issues play a much greater role than in aeroengines (in which reliability is the most important design parameter), the focus of this thesis is on the industrial gas turbines.

The Siemens SGT5-4000F gas turbine (see figure 1.3) is currently one of the most powerful industrial gas turbines. It has a maximal electrical power output of 278 MW in a simple cycle arrangement. In a combined cycle arrangement (i.e. a gas turbine combined with a heat recovery steam generator, after which the steam is expanded in a steam turbine), the power output increases to 407 MW. In a combined cycle plant, efficiencies of more than 55% (57.7% for the Siemens SGT5-4000F turbine) and a reliability above 95% can be achieved. Using natural gas, NO_x values below 25 ppm are guaranteed.

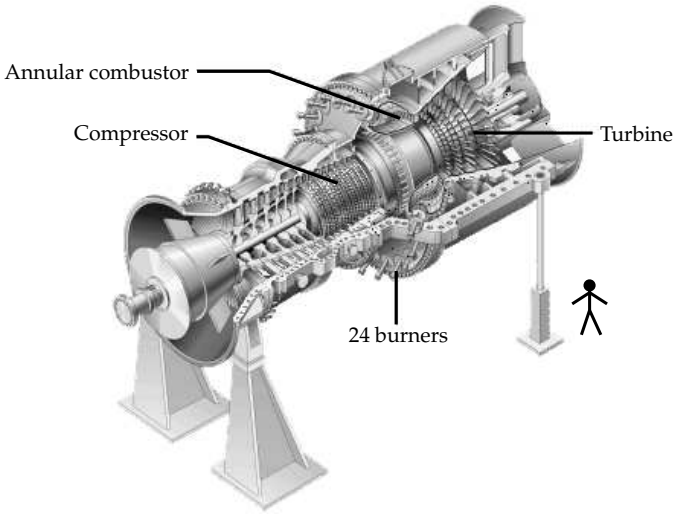

Figure 1.3: Siemens SGT5-4000F gas turbine.

The gas turbine engine working principle is as follows. The compressor section of the gas turbine compresses air. Subsequently, natural gas is premixed with the air. The mixture is combusted in the annular combustion chamber at constant pressure, and the hot gasses expand in the turbine to atmospheric pressure. The turbine drives the generator, as well as the compressor. The extreme conditions in which the gas turbine operates and the different interests involved makes the design process very complex. Numerous research fields in engineering apply their state-of-the-art knowledge in the gas turbine. An overview of the involved design issues can be found in the book by Lefebvre [106].

The focus in this thesis is on thermo-acoustic instabilities, which occur in the combustion chamber of the turbine. In figure 1.4 a schematic cross-section of a typical annular combustion chamber is shown (currently many variations to this layout are used). It can be seen that the air coming from the compressor is partly used for combustion, and partly for cooling the liner. The cooling air is rejoined with the flue gasses in the combustion chamber through the liner. The cooling air flowing through the dilution holes is used to bring down and improve the temperature profile of the exhaust gasses to acceptable turbine inlet values before they flow to the turbine section. The cooling air that flows through the cooling slots is used for film cooling and provides a protective thermal barrier inside the combustion chamber.

Apart from the cooling air, a part of the air is used to prevent the clearances between the liner segments from hot gas ingestion. Since the liner consists of segments to allow for thermal expansion, gaps exist between the liner segments. The air flowing through these gaps is called leakage air.

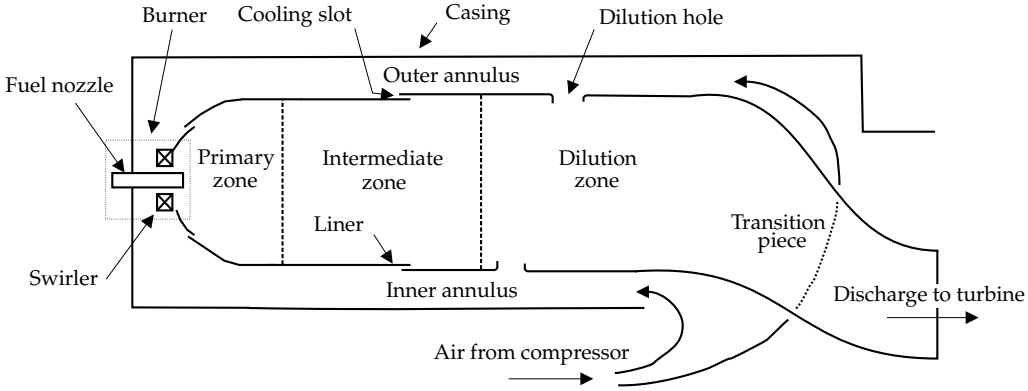

Figure 1.4: Schematic cross-section of a typical annular combustor [106].

The combustion exit temperature is limited by the maximum turbine inlet temperature. Since the maximum turbine inlet temperature is determined by the strength and heat resistance of the turbine blades, the combustion exit temperature is considered a fixed quantity. Because all air is eventually mixed with the hot flue gasses, the combustion exit temperature is determined by the total air mass flow and the heat added by combustion. To decrease the NO_x levels, the design goal is to use as much air as possible for combustion, and consequently as little air as possible for cooling and leakage. This lowers the flame temperature in the primary zone, and therewith the NO_x levels, as combustion occurs at leaner conditions.

Decreasing the amount of cooling air requires a more efficient use of the available cooling air. This issue has especially gained attention as engine pressure ratios have increased by more than 800% in the last 60 years [106]. Difficulties arise from the increase in inlet air temperature that accompanies the higher pressure ratio. A higher inlet temperature has a twofold adverse effect: it raises the flame temperature and it reduces the effectiveness of air as a coolant.

Decreasing the relative amount of leakage air results in a very compact combus-

tor design to reduce the gaps between the liner segments. Additionally, sealing techniques have reduced the leakage air between the segments. In the early nineties, gas turbines have been supplied with silo type combustors featuring a power density of about 20 MW/m^3 whereas the recent designs are supplied with annular combustors or CAN type combustors. These compact designs are characterised by power densities between 150 and 200 MW/m^3. This dramatic change in design of the combustion system, driven by the requirements of NO_x reduction, is visualised in figure 1.5.

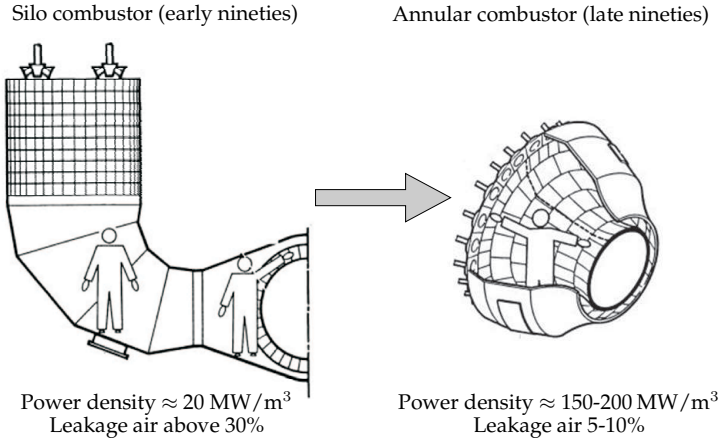

Figure 1.5: Combustor development from silo to annular combustor.

Due to the compact design the area of the combustor to be cooled can be reduced significantly. The reduced surface has also helped to reduce the leakage air needed for purging the gaps between the segments from values above 30% to values around 5%. Nonetheless, a further reduction of leakage air is needed to meet future requirements for low NO_x emissions. The strategy of reducing the NO_x emissions is schematically displayed in figure 1.6 [94].

It can be seen that improving the air management, i.e. the amount of leakage air, decreases the combustion temperature, and therewith the NO_x emissions. However, big improvements in the NO_x emissions can still be reached while keeping the mean combustion temperature at a constant level. By decreasing or eliminating the pilot diffusion flame, intended to stabilise the premixed flame, significant reductions in the NO_x emissions can be reached. Since the pilot flame is usually of the diffusion type, high temperatures occur in this flame, producing much NO_x. Finally, improving the mixture quality of the reactants brings down NO_x levels, since hot pockets of gas during combustion are prevented.

Nevertheless, the NO_x reduction potential of the lean premix operation mode is often limited by thermo-acoustically induced pressure oscillations. Operating very lean, i.e. close to the extinction limit of the flame, increases the acoustic response of the flame to small perturbations. Moreover, the increased premixing removes fuel concentration gradients in the flow field, which would otherwise provide flame stabilisation [156].

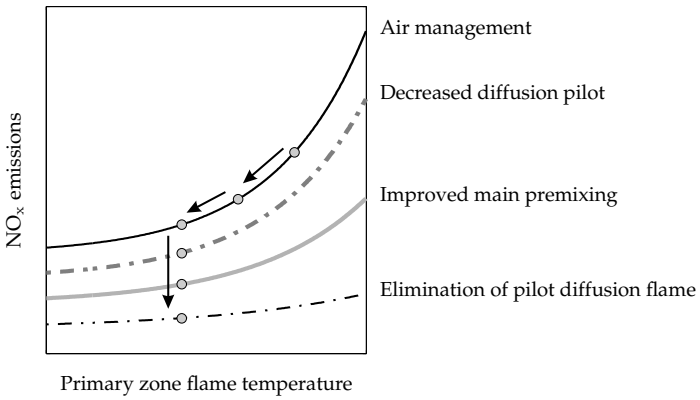

Figure 1.6: Reduction strategy [94].

1.3 Thermo-acoustic instabilities

A classic example explaining thermo-acoustic phenomena is the Rijke tube. The Rijke tube was first built by Rijke [149] in the 19^{th} century and consists of a straight duct with a heat source in it (see figure 1.7). The heat source (in this case a heated gauze) induces natural convection through the duct when it is placed vertically. When the heat source is placed in the upstream half of the duct, a loud tonal noise is generated. The heat source should be hot enough so that its energy transfer to the acoustic system overcomes the damping in the system.

The first step in understanding why a tonal noise builds up is that there are always acoustic perturbations in the Rijke tube (for instance produced by turbulent natural convection). An acoustic velocity fluctuation near the heated gauze in the direction of the mean flow causes an increase in the heat released to the flow (more heat is extracted from the heat source). Conversely, a velocity fluctuation in the reverse direction causes a decrease in the released heat. Note that due to a memory effect of the thermal boundary layer, the heat release fluctuation lags the velocity fluctuation [147]. The behaviour of the Rijke tube can now be explained by applying the statement of Lord Rayleigh, known as the Rayleigh criterion: the amplitude of a sound wave will increase when heat is added less than 90 degrees out of phase with its pressure*. Note that the Rayleigh criterion is only a necessary condition for instabilities to occur, since in its original form it does not account for acoustic losses at the boundaries of the acoustic domain. The criterion can be further extended to account for entropy fluctuations and acoustic losses at the boundaries [127].

*The original statement of Lord Rayleigh in his paper of 1878 reads [143]: "If heat is periodically communicated to, and abstracted from, a mass of air vibrating (for example) in a cylinder bounded by a piston, the effect produced will depend on the phase of the vibration at which the transfer of heat takes place. If heat be given to the air at the moment of greatest condensation, or taken from it at the moment of greatest rarefaction, the vibration is encouraged. On the other hand, if heat is given at the moment of greatest rarefaction, or abstracted at the moment of greatest condensation, the vibration is discouraged."

The mode shapes for the acoustic pressure p' and velocity u' at the natural acoustic eigenfrequency of the Rijke tube are shown in figure 1.7. The pressure fluctuations in the lower half of the tube are 90 degrees out of phase with the velocity fluctuations. The heat release rate fluctuations are however delayed by a memory time. When this corresponds to a quarter of an oscillation period the heat release rate fluctuations are exactly in phase with the acoustic pressure. Therefore, according to the Rayleigh criterion, energy is transported from the source to the acoustic field and the amplitude of the acoustic waves grows until it is limited by non-linear effects.

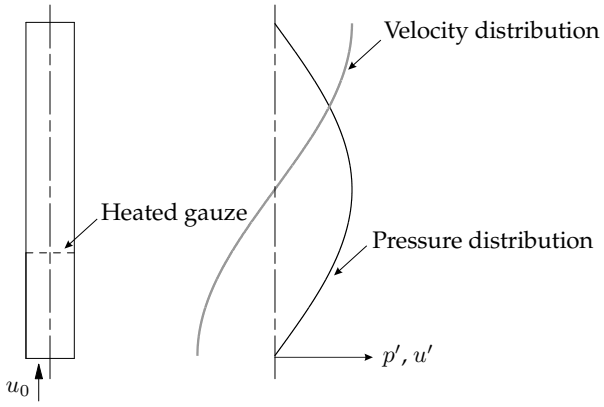

Figure 1.7: Acoustic fields in the Rijke tube.

When focussing on combustion systems, a distinction can be made between static and dynamic instabilities. The static instabilities are controlled by the static conditions of the flame, i.e. the mean inlet temperature of the mixture, the ratio between fuel and air of the mixture, the liner temperature etc. Blow-off of the flame by a static instability can happen when the amount of air in the inlet mixture is increased above a critical concentration. At a certain moment a condition is reached where the flame cannot exist anymore (extinction limit) and blows off. Usually the approach of this extinction limit is characterised by increased noise production of the flame. This increased noise production can be acted upon to keep the flame away from its extinction limit [138].

A thermo-acoustic instability can be categorised as a dynamic instability. Dynamic instabilities include acoustic effects and can result in shifts of the extinction limit. Strong oscillations can result in flame blow-off far away from the extinction limit determined by the static system. Moreover, the increased mechanical and thermal loads on the combustor structure lead to problems during a dynamic instability.

1.3.1 Active versus autonomous flame noise

In gas turbine combustors, the heat source is the turbulent flame. The turbulent fluctuations in the flame act as a sound source, causing a sound field in the combustor

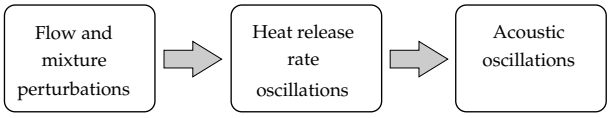

Figure 1.8: Schematic representation of autonomous combustion noise [109].

(see figure 1.8). This broadband flame noise is called the autonomous flame noise or 'roar'. The frequency range of this type of noise is typically below 1 kHz [106, 140]. For continuous burning systems it is convenient to express combustion noise in terms of the thermo-acoustic efficiency [62], which is given by:

$$\eta = \frac{W}{Q} \tag{1.1}$$

where Q is the heat release rate and W is the total energy contained within a sound pulse. Typical values for the thermo-acoustic efficiency are $\mathcal{O}(10^{-6})$ to $\mathcal{O}(10^{-5})$ [120,170] for open, spherically expanding, hydrocarbon flames. For a confined flame, the thermo-acoustic efficiency generally increases [120]. The confinement modifies the steady flow through the flame and therefore the turbulence levels increase. Moreover, thermo-acoustic feedback can increase the noise radiated by the flame.

For spherically expanding flames, all parts contribute equally to the sound intensity in the far field. However, for turbulent flames in which the monopole sound sources are randomly distributed it is reasonable to expect some cancellations of various compressions and rarefactions to occur. Hence, $\mathcal{O}(10^{-6})$ represents the likely upper limit of the thermo-acoustic efficiency for hydrocarbon open flames. Besides the estimated thermo-acoustic efficiency, frequency dependent estimations of the autonomous flame noise can be found in the literature [18, 165, 166].

Applying this estimated thermo-acoustic efficiency to a gas turbine with a thermal power of 200 MW gives a produced acoustic energy of 200 W, or 143 dB ref 10^{-12} W. Nevertheless, for the structure of the system, this sound energy level is usually no problem, as long as structural eigenfrequencies are sufficiently damped.

The autonomous noise produced by the flame also propagates into the supply system of the flame, i.e. the burner. In the burner, the fluctuating nature of sound causes inlet properties of the flame to fluctuate. As a result, the heat released by the flame fluctuates correlated to the perturbation in the inlet properties. This correlated part of the combustion noise is called the active combustion noise (see figure 1.9). The active flame noise needs to be considered when studying thermo-acoustic instabilities, since this type of flame noise includes a correlated feedback loop in which the sound amplitude can reach undesirable levels, much higher than the autonomous noise produced by the flame. This can induce intolerable structural vibrations causing engine damage. In large gas turbines, pressure fluctuations up to 0.7 bars have been measured. While autonomous noise can trigger an instability by providing disturbances to the flow field, it can never maintain or build up an instability since this noise is not correlated over a long period.

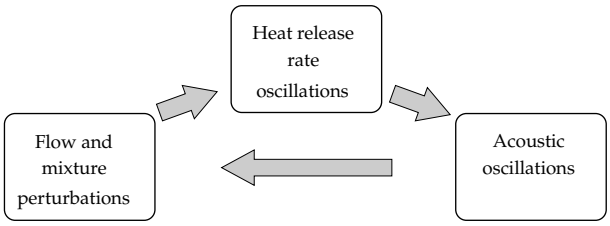

Figure 1.9: Schematic representation of a thermo-acoustic feedback loop [109].

1.3.2 Premixed versus diffusion flames

When we restrict ourselves to turbulent flames, two combustion categories can be identified based on whether fuel and oxidiser (e.g. air) are mixed first and burned later (*premixed combustion*) or combustion and mixing occur simultaneously (*non-premixed combustion*). In nonpremixed combustion, fuel and air are mixed in the flame itself by (turbulent) diffusion. Therefore, nonpremixed flames are also called *diffusion flames*. Diffusion flames include a more complex chemistry than premixed flames, because the fuel-to-air ratio covers the whole range from zero (in the air) to infinity (in the fuel) [183]. The flame front of a diffusion flame is fixed to regions near the location of the stoichiometric composition. Therefore, diffusion flames are fixed in place by the mixing front.

This is in contrast with premixed flames. The premixed flame front burns and propagates into the incoming turbulent fluid flow with reactants. This makes the premixed flame inherently dangerous, as the flame front can propagate into the burner system (flash-back). Moreover, there can be an accidental collection of large volumes of premixed reactants, which could burn in an explosion.

A perfectly premixed flame is difficult to accomplish, because reaching a high degree of premixing requires a large residence time and volume. This is often not desired since it decreases the safety of the system. The lack of volume and the safety issues drive the designers to a compromise, resulting in partially premixed flames which have (small) variations in the equivalence ratio.

The premixed flame can burn in many different ways. The Borghi diagram (see figure 1.10, from [182]) classifies the type of premixed flame encountered as a function of two dimensionless parameters:

- The ratio between the characteristic turbulence velocity fluctuation u'_t and the laminar flame speed s_L

- The ratio between the characteristic turbulence length scale l_t and the laminar flame thickness δ_L

In the Borghi diagram, regimes are determined by three dimensionless numbers: the

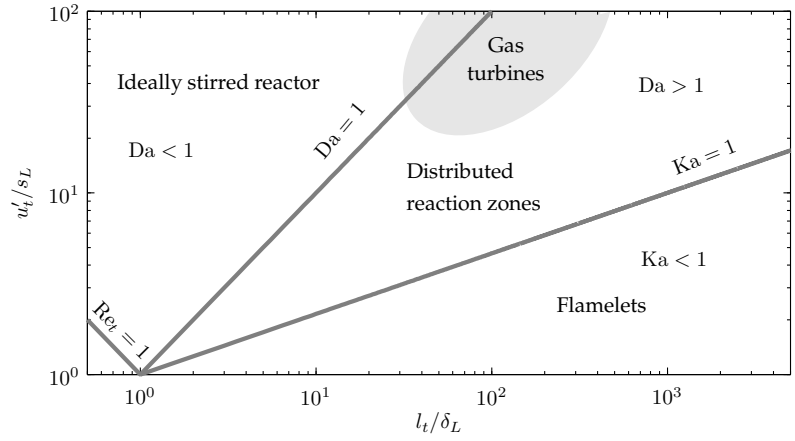

Figure 1.10: Turbulent premixed combustion diagram (Borghi diagram), from [182].

turbulent Reynolds number, the Damköhler number and the Karlovitz number:

$$\mathrm{Re}_t = \frac{\rho u'_t l_t}{\mu} \tag{1.2}$$

$$\mathrm{Da} = \frac{t_{turb}}{t_{chem}} = \frac{l_t s_L}{\delta_L u'_t} \tag{1.3}$$

$$\mathrm{Ka} = \frac{t_L}{t_{Kol}} = \frac{\delta_L^2}{\eta^2} \tag{1.4}$$

The Damköhler number denotes the ratio of the turbulent mixing time scale t_{turb} and the chemical time scale t_{chem}. The Karlovitz number is the ratio of the laminar flame time scale t_L and the Kolmogorov* time scale t_{Kol}, which can be written as the ratio between the squared flame thickness and the squared Kolmogorov length scale η.

In the turbulent regime, the lines $\mathrm{Ka} = 1$ and $\mathrm{Da} = 1$ separate three zones:

- $\mathrm{Ka} < 1$: Flamelet regime, characterised by locally laminar premixed flames embedded into a turbulent flow.
- $\mathrm{Da} < 1$: Ideally stirred reactor regime, characterised by turbulent eddies embedded in the reaction zone. The time needed for reaction is larger than the time needed for turbulent mixing. A very broad flame front is observed.
- $\mathrm{Ka} > 1$ and $\mathrm{Da} > 1$: distributed reaction zone regime, where a portion of the turbulent eddies are embedded in the flame front, which thickens it.

Finally, when $\mathrm{Re_t} < 1$ laminar combustion is observed.

*In turbulent flows kinetic energy is transferred from large scale vortices (or eddies) to smaller ones. The Kolmogorov scale η is defined as the size of the smallest eddies in the flow.

A premixed gas turbine operates mainly in the distributed reaction zone regime (see figure 1.10). However, parts of the flame may be in one of the other regimes.

From a thermo-acoustic point of view, the differences between premixed and diffusion flames lies in their excitation. In case of a premixed flame, the main type of excitation originates at the location where fuel and air are premixed (see section 2.5.2). Subsequently, the excitation is transported to the flame front with the *convection* speed. In a diffusion flame, mixing takes place in the flame itself, hence time delays between the excitation and the response of the flame can be much shorter than for premixed flames. Therefore, the time delays of the thermo-acoustic feedback loop are much larger for premixed flames, lowering the frequency at which instabilities can occur. Instabilities at higher frequencies are not so much of a problem for two reasons: more acoustic damping processes are available at higher frequencies, and the flame does not respond to the high frequency excitation anymore. This will be explained in further detail in chapter 4.

Another effect is that diffusion flames are usually much more stable than premixed flames. Higher flame temperatures (stoichiometric combustion) and the absence of a propagating flame front makes the flame less sensitive to excitation of its inlet properties. The obvious disadvantage of this mode of combustion is the high NO_x emission resulting from the high flame temperatures.

1.3.3 Acousto-elastic interaction

The rising acoustic pressures in the combustor during a thermo-acoustic instability excite the relatively thin liner surrounding the combustion chamber. The liner is the structural interface between the hot combustion gasses and the cooling air. The large temperature differences between these gasses force the choice of a thin liner to avoid high thermal stresses.

The coupling between the acoustic field and the vibration of the liner is called acousto-elastic interaction, which is a dynamic form of fluid-structure interaction (FSI). The study of the acousto-elastic interaction in combustion systems is one of the main activities in the DESIRE project. Studies have been performed by Huls [75–79] to show the ability of numerical Finite Element models (FEM) to satisfactory model the acousto-elastic interaction in combustion setups. It has been shown that it is possible to include the vibration of the liner directly in a stability analysis of a combustion system. By coupling linear transfer functions between the flame, the acoustics and the liner vibration (see figure 1.11), frequencies of high acoustic response u' and structural response u'_s can be identified [76]. Especially when these frequencies coincide there is a risk for structural damage.

1.4 Control and modelling of instabilities

Thermo-acoustic instabilities should preferably be avoided in the design stage of a combustion system. In many practical situations, a detailed understanding of the instability mechanisms is not an engineering objective. Simple and complete suppression of all instabilities is the rule in most combustor development programs. This

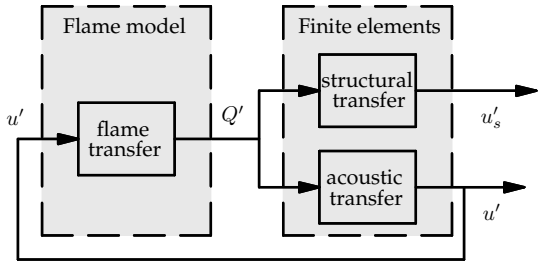

Figure 1.11: Coupling of flame and acousto-elastic system using transfer functions [76].

is commonly achieved by a process of trial and error which does not include any detailed description of oscillatory phenomena. By common sense, one can already decrease the risk for an instability to occur, e.g. designers introduce asymmetry in the combustion systems to prevent a harmonic coupling of sources with the acoustic system. However, preventing thermo-acoustic instabilities is an important, but not the only design issue in gas turbines. Therefore one is limited in the changes that can be made to a system.

Apart from common sense, good models are required to predict whether the system will be free of instabilities. Moreover, these models can help to understand the basic physics of instabilities. Many models have been used in the past, with various levels of success. Still, a universal model for predicting combustion instabilities does not exist yet, and instability modelling has generally been conducted on a case by case basis.

In the next sections, a brief overview of the solutions that have been applied to combustion systems to prevent instabilities is given. A division into passive and active solutions is made. Subsequently, the most common models used to predict instabilities are presented.

1.4.1 Passive solutions

Passive solutions use modifications of geometry, flow conditions and acoustic conditions. Resonators can, for example, be attached to the combustor to suppress observed peaks in the acoustic power spectrum [9,74]. The disadvantage of these methods is that they usually work in a very narrow frequency range, so that information of the acoustic spectrum must be known prior to dimensioning the resonators. Because of the narrow frequency band, and the uncertainty of the exact frequencies of the peaks in a complex combustion system, this usually requires an experimental investigation. Especially when applied to full scale gas turbines these experiments are very costly. Also it is difficult to have the resonator work in the range of idle to base load operation.

1.4.2 Active solutions

In active control methods, the thermo-acoustic instability is suppressed by a closed feedback loop which returns a compensating signal to the system. For an overview of the applied active methods, see [47, 123]. Several researchers have studied the subject of active control applied to thermo-acoustic systems. One of the first was Heckl [66], who applied an active control system to a Rijke tube to successfully suppress the instability.

Some active control methods require a knowledge of the thermo-acoustic model, either measured or modelled. However, there are also adaptive methods, in which controllers have internal algorithms allowing time-varying transfer functions through parameter optimalisation. Still, gas turbine manufacturers have been reluctant in applying active control systems for the suppression of the highly destructive thermo-acoustic instabilities. The large range of operating conditions requires complex controllers, which increases the chance for controller errors.

1.4.3 Low order modelling

The term 'low order modelling' is used for thermo-acoustic models that have the following properties [46]:

1. capture essential physics

2. give results quickly

3. predict frequencies and mode shapes of instabilities, as well as the susceptibility to oscillations at different operating conditions

The most widely used method for the modelling of thermo-acoustic systems is based on linear acoustics and a representation of the system as a network of elements, or acoustic multiports [44, 51, 96, 130, 136]. Based on such a network, a linear system of equations is constructed that serves as the basis for investigating system dynamics and stability [156].

The acoustic multiports can be measured directly [130], derived from theoretical principles or a combination of both. Because the network models combine different methods for different aspects of the problem to yield a description of the full thermo-acoustic system, they may also be called hybrid models [128]. In these models, the flame transfer function, reflecting the flame behaviour, is usually provided by a separate model.

The flame transfer function is the most difficult element to model. It represents the dynamic transfer between an excitation in the inlet conditions of a flame and its acoustic response. The flame transfer function can be approximated by an analytical model, which in its most basic form can be a combination of a time delay τ and an interaction index n (the $n - \tau$ models [36, 37]). Analytical models can also use a kinetic model of flame oscillations [45, 117, 153, 154].

1.4.4 High order modelling

More advanced models to calculate the flame transfer function involve the application of numerical methods which directly solve the Navier-Stokes equations together with a combustion model. Transient simulations combined with a spectral analysis are performed to construct the transfer function. As a result of the required computational effort, this method cannot be categorised as a low order model anymore. Hence it is categorised as high order modelling.

In high order models the physics of the system are described as accurately as possible, at the expense of a considerable increase in the required computational time. The numerical simulations to obtain a flame transfer function were already mentioned in the previous section. One can extend this concept by not only including the flame dynamics, but also the acoustic wave propagation. This again requires a considerable increase in computational time. After this step, the step towards a fully coupled thermo-acousto-elastic simulations is not large anymore.

One can question the usability of these high order models. Due to the large computational time and the complexity of the models, a sensitivity analysis is difficult to conduct and post processing of the results becomes a major challenge. Moreover, one has so many parameters that it might be difficult to identify the cause of certain phenomena. Nevertheless, these large models have been used successfully for specific cases in a sense that they showed similar modes and instability behaviour as observed in measurements [151].

1.5 Research objective

The investigation presented in this thesis has been initiated by the EU-DESIRE project. The *primary objective* of DESIRE is to provide models for predicting the interaction between the sound produced by the flame and the resulting vibrations of the liner. The developed models have been validated in an experimental setup built at the University of Twente.

The acousto-elastic interaction and the consequences for the liner design are discussed by Huls in his PhD thesis [75]. The main excitation of the liner is the sound produced by the flame. This sound depends strongly on the flame structure and the thermo-acoustic feedback. Therefore, the present thesis focuses on the flame component and the prediction of instabilities in a combustion system. The objective of this thesis is the development and validation of efficient measurement techniques and numerical algorithms to check combustion systems for their sensitivity to combustion instabilities. The following topics are considered to meet this objective:

- Development of a stability analysis method by coupling a flame transfer function with a one-dimensional acoustic model that can accurately represent the acoustic behaviour of combustion systems.
- Development of efficient and accurate tools for predicting the flame transfer function for a premixed swirling turbulent natural gas flame. For this purpose, the accuracy of a high order model is combined with the low computational load of a low order model.

- Validation of the calculated flame transfer functions and the predicted frequencies of instability in a test rig which is representative for gas turbine applications.

1.6 Outline

The present chapter introduced the general thermo-acoustic problem in modern gas turbine combustors. Moreover, it introduced solution methods to check combustion systems for instabilities in the very early design stage of the combustor.

The thermo-acoustic problem involves theory from many research fields. This gives the research field a multi-disciplinary character. A schematic overview of the aspects discussed in this thesis is shown in figure 1.12.

In chapter 2 the acoustic theory is explained. This is supplemented by an efficient linear stability analysis, which results in frequencies at which unstable growth of acoustic pressures can occur in a combustion system.

The key feature in this stability analysis is the flame transfer function, which represents the relationship between an acoustic perturbation, which in general occurs upstream of the flame, and the response of the flame. In figure 1.12, these quantities are indicated as f' and Q', respectively. Models to obtain this transfer function are discussed in chapter 4 and 5. The difference between these chapters lies in the

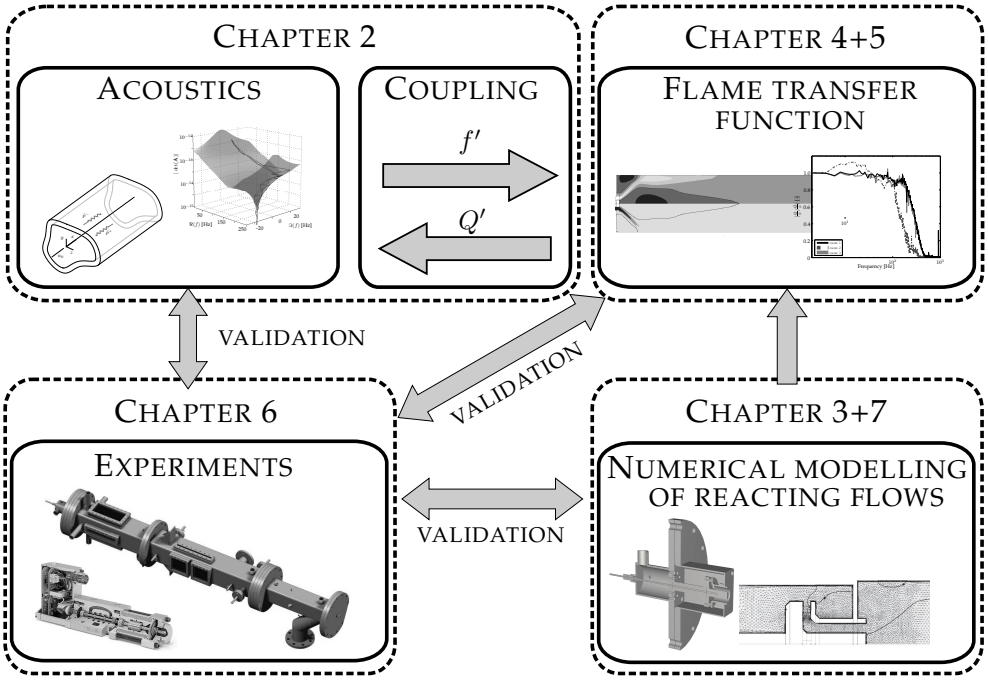

Figure 1.12: Schematic overview of the aspects discussed in this thesis.

method with which the flame transfer function is calculated. Chapter 4 deals with conventional methods, although it also gives new insight in several aspects of the transfer function in relationship to the flame shape. Chapter 5 is completely devoted to a new, more efficient method to accurately predict the flame transfer function. This new model is called the linear coefficient method, and is based on the linearisation of the equations in a steady-state CFD simulation. The speed and accuracy of this method makes it extremely suitable as a thermo-acoustic design tool.

The dynamic numerical simulations presented in chapter 4 and 5 require an accurate solution of the mean flow field. For this reason, the general numerical modelling of reacting flows will be discussed in chapter 3. This chapter also describes modelling issues for the unsteady modelling of these flows.

Following the successful development and numerical validation of the acoustic and flame transfer function models, the models are experimentally validated. To do so, a well-defined experimental setup is designed for the validation of the modelled flame transfer functions, acoustics and acousto-elastic interaction (discussed in the PhD thesis of Huls [75]). In chapter 6 this experimental setup is described together with its peripheral equipment. Additionally, the experimental results are compared with the models.

Finally, a more advanced combustion model based on a progress variable approach [41] is used in chapter 7. This is done to reveal possible shortcomings of the relatively simple combustion model that is used in other parts of the thesis.

The thesis is concluded by chapter 8, which summarises the main results and draws conclusions. Moreover, directions for further research are indicated. Note that a list of all abbreviations and symbols used in this thesis can be found in the Nomenclature on page 181.

Chapter 2

Thermo-acoustics and instabilities

2.1 Introduction

Sound generation by turbulent flames originates from the fluctuating heat release rate in the flame. The description of this fluctuating heat release rate is complicated due to the interaction of turbulence, combustion and acoustics. Additionally, the steep temperature gradients and flow noise complicate the modelling of the acoustic field inside a combustion system. To predict unstable operating ranges of a combustion system, all aspects need to be considered.

In this chapter, a description of a turbulent premixed flame as a thermo-acoustic source term will be given. Because the sound field in a gas turbine combustor is to good approximation one-dimensional, the basic one-dimensional acoustic theory will be discussed next. This is followed by a description of an acoustic network model to calculate acoustic fields in a network of coupled one-dimensional elements. Finally, a method to predict unstable operating ranges by coupling the acoustic model with a flame source model is presented.

2.2 The thermo-acoustic source term

In a gas turbine combustion chamber, the thermo-acoustic source is the flame. The dimensions of this flame are small compared to the acoustic wavelengths in the combustor. This is especially true for the swirl-stabilised flames discussed in this thesis. The compactness of the source compared to the acoustic wavelengths is seen to promote instabilities [53], for it is easier for the source to couple with the sound field. Consequently combustion installations with short flames are more sensitive to combustion driven oscillations than similar installations with long flames [140].

The acoustic wavelength λ is related to the speed of sound c_0 and the frequency f according to:

$$\lambda = c_0/f \tag{2.1}$$

Furthermore, the combustion gas can be taken to be a perfect gas and hence c_0 depends on the temperature T as:

$$c_0 = \sqrt{\gamma RT} \tag{2.2}$$

in which γ is the ratio between the specific heat capacities and R is the specific gas constant. With equation 2.1 and 2.2 the wavelength can be evaluated as a function of the temperature and the frequency (figure 2.1). Figure 2.1 clarifies that combustion noise has typical wavelengths of the order of several metres, while the size of the flame is of the order of centimetres. This condition, i.e. $L_{flame} \ll \lambda$, implies that all acoustic sources in the flame can be volume integrated to obtain one acoustic point source exciting the acoustic field.

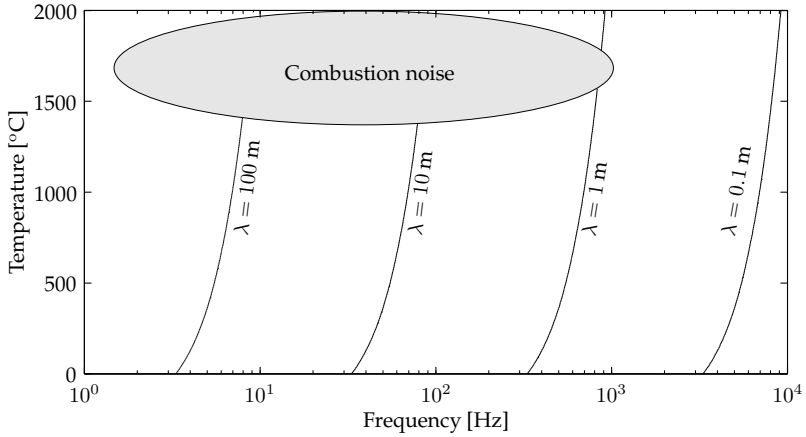

Figure 2.1: Acoustic wavelength λ in air as a function of the temperature and frequency. Typical wavelengths for unsteady combustion lie in the order of metres.

The radiated sound power by combustion covers a frequency range $f < 1$ kHz [106, 140], reaching a blunt peak between 300 to 500 Hz. This general shape of the spectrum appears to be surprisingly independent of burner size, engine power and flame temperature, although these factors strongly affect the radiated sound power *level* [120]. The engine power has the largest influence on the radiated sound power level. Both the mass flow and the combustor temperature level increase with the engine power level. Since there is a tendency for the thermo-acoustic efficiency to increase with the mass flow rate, the radiated acoustic power level is more than proportional to the engine power level [120].

An expression for the acoustic source of a flame can be derived using the analogy of Lighthill as a starting point. The analogy of Lighthill is often used in aeroacoustics (see [4, 147]), for it also gives a mathematical description of the noise produced by a turbulent flow.

2.2.1 Lighthill's analogy

The objective of Lighthill's analogy [112–114] is to get a wave equation derived from the flow equations. Lighthill based his theory on the exact Navier-Stokes equations and showed, by their rearrangement, how the acoustic source terms could be obtained from exact time-accurate calculations or experiments. To achieve this, Lighthill uses the emission or propagation theory where an observer in a uniform medium at rest receives acoustic radiation from a distribution of sources of sound. It is inherently assumed that the source lies in a limited region which is surrounded by a uniform fluid to which the acoustic wave equation applies. The term 'analogy' refers to the idea of representing a complex fluid mechanical or thermo-acoustic process by an acoustically equivalent source term. For example, internal processes in the flame are replaced by a representative acoustic source term which excites the quiescent acoustic medium surrounding this source term.

The derivation of Lighthill's analogy starts with the equations of conservation of mass and momentum, written below in coordinate-free notation:

$$\frac{\partial \rho}{\partial t} + \nabla \cdot (\rho \mathbf{u}) = 0 \tag{2.3}$$

$$\frac{\partial (\rho \mathbf{u})}{\partial t} + \nabla \cdot \left(\rho \mathbf{u} \otimes \mathbf{u}^T\right) = -\nabla p + \nabla \cdot \sigma + \mathbf{f} \tag{2.4}$$

In these equations, ρ represents the density of the fluid, $\mathbf{u}$ is the velocity vector, σ is the viscous stress tensor and $\mathbf{f}$ represents the momentum generation due to a force exerted on the fluid (for example the gravitational force). The operator $\otimes$ represents the direct product between two vectors (resulting in a matrix).

Taking the time derivative of equation 2.3 and the divergence of 2.4, and subtracting the resulting equations leads to the following expression:

$$-\nabla^2 p = \nabla \cdot \left(\nabla \cdot \left(\rho \mathbf{u} \otimes \mathbf{u}^T - \sigma\right)\right) - \frac{\partial^2 \rho}{\partial t^2} - \nabla \cdot \mathbf{f} \tag{2.5}$$

To obtain a wave equation, the pressure is decomposed in terms of a mean (independent on time and space) and fluctuating pressure according to $p = p_0 + p'$. A similar substitution is introduced for the density*, i.e. $\rho = \rho_0 + \rho'$. Moreover, the term $\frac{1}{c_0^2}\frac{\partial^2 p'}{\partial t^2}$ is added to both sides of equation 2.5, in which c_0 is the speed of sound at the listeners location. The resulting equation is an inhomogeneous wave equation and is called the equation of Lighthill, written in terms of pressure fluctuations:

$$\frac{1}{c_0^2}\frac{\partial^2 p'}{\partial t^2} - \nabla^2 p' = \nabla \cdot \left(\nabla \cdot \left(\rho \mathbf{u} \otimes \mathbf{u}^T - \sigma\right)\right) - \nabla \cdot \mathbf{f} + \frac{\partial^2}{\partial t^2}\left(\frac{p'}{c_0^2} - \rho'\right) \tag{2.6}$$

Equation 2.6 is exact, on the condition that a space and time-independent pressure and density can be defined. This is possible when the medium is quiescent, which is one of the original applications of Lighthill's analogy.

*In this thesis, fluctuating quantities are always expressed in standard characters *with* an apostrophe. A mean quantity is indicated with a subscript 0 or an over-bar. Total quantities do not have an addition.

2.2.2 Acoustic source types

The RHS of equation 2.6 can be categorised into three different sound source types: a monopole, a dipole and a quadrupole. A monopole is a sound source that radiates sound equally well in all directions (see the directivity pattern in figure 2.2). The simplest example of a monopole source is a sphere whose radius expands and contracts oscillatory. The monopole sound source in Lighthill's equation is the term $\frac{\partial^2}{\partial t^2}\left(\frac{p'}{c_0^2} - \rho'\right)$. As will be explained in the next section, the thermo-acoustic source term can be derived directly from this term and is therefore a monopole sound source. Intuitively this is not difficult to grasp, since the thermo-acoustic source is basically caused by hot gasses expanding in all directions.

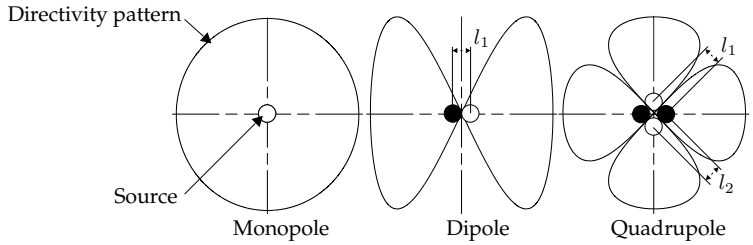

Figure 2.2: Acoustic source types and their directivity patterns.

A dipole source consists of two monopole sources of equal strength but opposite phase and separated by a distance l_1, which is small compared to the acoustic wavelength. While one source expands, the other source contracts. The directivity pattern in figure 2.2 shows that a dipole source does not radiate sound equally in all directions. There are two regions where sound is radiated well, and two regions where sound is diminished. The dipole sound source of equation 2.6 is the term $\nabla \cdot \mathbf{f}$ (i.e. a gradient in the force field produces a dipole).

Finally, the term $\nabla \cdot \left(\nabla \cdot \left(\rho \mathbf{u} \otimes \mathbf{u}^T\right)\right)$ in Lighthill's equation acts as a quadrupole sound source. If two opposite phase monopoles make up a dipole, then two opposite dipoles make up a quadrupole source. Sound from a quadrupole is radiated well in front of each monopole source, but sound is diminished at points equidistant from adjacent opposite monopoles. To generate a quadrupole, one must have a second order gradient. A turbulent velocity field satisfies this condition and can therefore produce a quadrupole sound field.

In combustion systems, the contribution of the dipole source $\nabla \cdot \mathbf{f}$ to the RHS of equation 2.6 can be neglected, since no significant fluctuating force is exerted on the fluid. Furthermore, at the high Reynolds numbers that combustion systems are operating, the contribution of the viscous forces is small, i.e. the viscous stress tensor in equation 2.6 can be neglected. The remaining sound sources that are present in a combustion chamber are represented by the terms $\nabla \cdot \left(\nabla \cdot \left(\rho \mathbf{u} \otimes \mathbf{u}^T\right)\right)$ (quadrupole) and $\frac{\partial^2}{\partial t^2}\left(\frac{p'}{c_0^2} - \rho'\right)$ (monopole) in Lighthill's equation. A dimensional analysis performed on the sound power produced by these sources in *combustion systems* shows that the acoustic power from the combustion process (the monopole sound source)

is of the order $1/\mathrm{Ma}^4$ larger than the acoustic power generated by turbulence (the quadrupole source) [35, 88]. Hence, for low Mach-number flows, the quadrupole source term in Lighthill's equation can be neglected as well. To decrease pressure losses induced by high speed flows, most combustion systems indeed operate at low Mach numbers. Additionally, the high temperatures occurring in the flame zone decrease the Mach number via the increased speed of sound.

The monopole sound source is therewith identified as the sound source responsible for the sound generated by combustion. Therefore, this monopole will be expressed in terms of heat release rate perturbations in the next section.

2.2.3 The flame source term

The wave equation for the density, which is the homogeneous form of equation 2.6, is valid for an observer in a medium in rest, i.e. *without* a mean flow. All flow effects are incorporated in the RHS of equation 2.6 (the equation was derived from the NS equations, and therefore flow effects are still contained in the equation). The sources at the RHS of the equation may therefore move through the uniform stationary fluid. An alternative procedure to derive Lighthill's equation is to regard the sources of sound at rest in a uniform medium moving at a constant speed [115, 188], and can be extended to consider any arbitrary mean fluid motion. This procedure is more appropriate for thermo-acoustic sources, for the movement of these sources (for instance flames) is relatively small compared to the acoustic wavelengths occurring in combustion systems. However, extra source terms arise in Lighthill's equation, as a result of flow-acoustic interaction.

Due to the high temperatures the Mach number in a flame is relatively small. It is therefore assumed that flow-acoustic interaction is negligible. However, in other parts of a combustion system (especially in the low temperature regions), the influence of flow on acoustic wave propagation can be significant. Therefore, the equivalent acoustic sources derived with Lighthill's analogy are left unmodified, but the homogeneous form of the conventional wave equation is replaced by its *convective* variant, defined as [147]:

$$\frac{1}{c_0^2}\frac{\mathrm{D}^2 p'}{\mathrm{D}t^2} - \nabla^2 p' = 0 \tag{2.7}$$

in which $\frac{\mathrm{D}}{\mathrm{D}t}$ is the material derivative, denoting a time-derivative moving with the mean flow $\mathbf{u}_0 \neq 0$.

For an inviscid and homentropic (entropy $s = s_0 =$ constant everywhere at all times) fluid, the relationship between a pressure and density fluctuation is given by [147]:

$$\frac{p'}{\rho'} = c_0^2 \tag{2.8}$$

For isentropic flows, in which equation 2.8 is valid, the monopole source term $\frac{\partial^2}{\partial t^2}\left(\frac{p'}{c_0^2} - \rho'\right)$ in Lighthill's equation (equation 2.6) equals zero. However, the source term is evaluated in the flame zone, where the assumption of isentropic behaviour

of the flow is no longer valid. This can be shown using the thermo-dynamic relationship for the change in total enthalpy h_{tot}, expressed as (see appendix A):

$$\mathrm{d}h_{tot} = T\mathrm{d}s + \frac{1}{\rho}\mathrm{d}p - \sum_{i=1}^{n} h_0^i \mathrm{d}y_i \tag{2.9}$$

in which h_0^i is the enthalpy of formation of species i with mass fraction y_i. In an adiabatic reaction process, the total enthalpy in the flame zone is constant, i.e. $\mathrm{d}h_{tot} = 0$. Moreover, combustion processes in gas turbine combustors usually proceed at constant pressure, i.e. $\mathrm{d}p = 0$. Hence, since the term $\sum_{i=1}^{n} h_0^i \mathrm{d}y_i \neq 0$ in the reaction zone, equation 2.9 requires that the entropy changes in a chemical reaction.

Accounting for this non-isentropic behaviour, the inhomogeneous convective wave equation in terms of pressure perturbations, having a thermo-acoustic source as source term, reads (see appendix A):

$$\frac{1}{c_0^2}\frac{\mathrm{D}^2 p'}{\mathrm{D}t^2} - \nabla^2 p' = \frac{\partial}{\partial t}\left[\frac{\gamma - 1}{c_0^2} q_f'\right] \tag{2.10}$$

in which q_f' is the heat release rate in $\mathrm{W\,m^{-3}}$. It can be shown [134] that the source term q_f' is proportional to an acoustic mass flow source m_s' $[\mathrm{kg\,s^{-1}\,m^{-3}}]$:

$$m_s' = \frac{\gamma - 1}{c_0^2} q_f' \tag{2.11}$$

In the flame, a large range of temperatures is present. The question rises whether the factor $\frac{\gamma-1}{c_0^2}$ can be taken out of the time-derivative in the RHS of equation 2.10 and if so, at which temperature this factor should be evaluated. Both these questions will be answered in chapter 6, dealing with the experiments. In these experiments, the acoustic mass flow source of the flame is measured. This mass flow source is compared with the heat release rate source from numerical simulations. It is therefore important that the factor $\frac{\gamma-1}{c_0^2}$ is handled correctly. It appears that only a small error is made when evaluating the factor at the adiabatic flame temperature and assuming it to be constant.

An effect of the flame temperature is that it can amplify the acoustic strength of the heat release rate perturbation. In the factor $\frac{\gamma-1}{c_0^2}$ in equation 2.11 both γ and c_0 are functions of the temperature at the source, or the flame temperature. For perfectly premixed flames, the flame temperature is a function of the temperature of the inlet mixture and its fuel-to-air ratio. This fuel-to-air ratio can be expressed in terms of the mean equivalence ratio ϕ_0, which is the fuel-to-air ratio referenced to the stoichiometric* fuel-to-air ratio:

$$\phi_0 = \frac{y_{f,0}/y_{a,0}}{[y_{f,0}/y_{a,0}]_{st}} \tag{2.12}$$

*In a stoichiometric mixture the amount of air (in terms of mass) in the mixture exactly matches the air needed to combust all the available fuel. The stoichiometric ratio for natural gas is 0.077106 [56].

where $y_{i,0}$ is the mean mass fraction of fuel ($i = f$) or air ($i = a$) and the subscript st indicates the stoichiometric situation. Another way to express the fuel-to-air ratio is by means of the air factor λ, which equals the reciprocal of the equivalence ratio.

When the factor $\frac{\gamma-1}{c_0^2}$ is expressed as a function of the air factor and the preheating temperature, the factor increases with almost 70% when the mean air factor is increased from 1 (stoichiometric flame) to 2 (lean flame). This implies that for an equal heat release rate perturbation input, a lean flame causes a relatively large acoustic perturbation compared to a richer flame.

2.2.4 Sound producing mechanisms in a flame

In appendix A it is shown that the fluctuating heat release rate can be written in terms of independent quantities as:

$$q'_f = -\nabla \cdot \mathbf{D_q}' - \sigma : \nabla \mathbf{u}' + \rho \sum_{i=1}^{n} h_0^i \frac{\mathrm{D}y'_i}{\mathrm{D}t} \tag{2.13}$$

in which $\nabla \cdot \mathbf{D_q}$ represents the heat flow by conduction. Moreover, h_0^i is the enthalpy of formation of species i. The operator : represents the double inner product of two tensors, which are second-rank in case of a three-dimensional problem.

The material derivative of y'_i is given by the transport equation for species i:

$$\rho \frac{\mathrm{D}y'_i}{\mathrm{D}t} = -\nabla \cdot D'_i + \omega'_i \tag{2.14}$$

where $-\nabla \cdot D'_i$ is the laminar diffusion of species i, and ω_i is the chemical source term. In the flame zone, the chemical source term is in general much larger than $-\nabla \cdot D_i$. Neglecting this diffusion term, equation 2.13 can be written as:

$$q'_f = -\nabla \cdot \mathbf{D_q}' - \sigma : \nabla \mathbf{u}' + \sum_{i=1}^{n} h_0^i \omega_i \tag{2.15}$$

Equation 2.15 shows that in a flame, where multiple species are mixed and chemically reacting, noise can be generated by fluctuations in heat conduction, viscous dissipation and chemical reaction. At combustion interfaces the difference between the enthalpies of formation of the reactants and the products is large, hence in a flame the third RHS term in equation 2.15 is the main source term driving pressure fluctuations. Generally, at high Reynolds numbers, the other terms can be neglected.

Neglecting the contribution due to heat conduction, viscous heating and laminar diffusion, the source term can be written as:

$$q'_f = \sum_{i=1}^{n} h_0^i \omega'_i \tag{2.16}$$

For an ideal gas, the total enthalpy h_{tot} of the mixture can be written as:

$$h_{tot} = \sum_{i=1}^{n} h_0^i y_i + \int_{T_0}^{T} c_p \mathrm{d}T \tag{2.17}$$

in which c_p is the specific heat capacity of the total mixture. Taking the material derivative of this equation, and using equation 2.14 (again neglecting the contribution due to laminar diffusion), q'_f can also be written as:

$$q'_f = -\rho c_p \frac{\mathrm{D}T'}{\mathrm{D}t} \tag{2.18}$$

in which it is assumed that changes in the mixture do not influence the specific heat capacity of the mixture. Equation 2.18 shows that heat release rate perturbations are directly related to temperature fluctuations. Note that a positive q'_f implies that heat is *absorbed* by the flame. For convenience, in the remainder of this thesis the variable $q' = -q'_f$ will be used, i.e. a positive q' always corresponds to heat *released* by the flame.

2.2.5 Validity of linearity in combustion applications

The convective wave equation (equation 2.7) was derived from the linearised conservation laws, which implies that the relative fluctuations need to be small in order for the wave equation to be valid (i.e. $\rho'/\rho_0 \ll 1$). Using the relationships $u' \sim p'/(\rho_0 c_0)$ and $p' = c_0^2 \rho'$ it follows that:

$$\frac{\rho'}{\rho_0} \sim \frac{p'}{\rho_0 c_0^2} \sim \frac{u'}{c_0} \tag{2.19}$$

At standard air conditions, the limit of the validity of the linear acoustic theory lies at a pressure fluctuation p' of about 200 Pa (140 dB ref 20μPa) according to [12]. At standard air conditions $\rho_0 c_0^2 \propto p_0 \approx 10^5$ Pa, so the relative pressure fluctuations are $\mathcal{O}(10^{-3})$. Using equation 2.19 the absolute velocity and density fluctuation at the limit of the linear acoustic theory can be determined.

In thermo-acoustics, high temperatures are common in the acoustic system. For an ideal gas, the density is negatively proportional to the temperature, while c_0^2 is proportional to the temperature. So the net effect on the term $\rho_0 c_0^2$ is zero. This means that linear theory is valid until sound pressures of 200 Pa, independent of the temperature of the system.

2.3 One-dimensional acoustic wave propagation

The sound field in a gas turbine combustor can be considered as one-dimensional because of the typically large wavelength compared to the characteristic diameter of the combustor. For this reason one-dimensional acoustic models [44, 51, 96, 104, 136] have been used to describe the acoustics of a combustion system.

2.3.1 Basic equations

As discussed in section 2.2.1 acoustic wave propagation in gases is described by the homogenous version of the convective wave equation (equation 2.7). In this wave equation, viscous and thermal effects are neglected.

When a mean flow with velocity u_0 is present in a tube, the one-dimensional, harmonic solution to the convective wave equation reads [134]:

$$p'(x) = \hat{p}^- e^{\mathrm{i}k^- x} + \hat{p}^+ e^{-\mathrm{i}k^+ x} \tag{2.20}$$

The coefficient $k^\pm$ is the wave number defined as $\frac{\omega}{c_0 \pm u_0}$ where ω is the angular frequency. The mean velocity u_0 is seen to act as a kind of Doppler effect and modifies the effective speed of sound $c_{eff} = c_0 \pm u_0$, as included in the wave number.

In equation 2.20 a plane wave (i.e. no variations of p' in the y or z-direction) with a complex amplitude $\hat{p}^+$ is travelling in the positive x-direction ('forward') with speed $c_0 + u_0$ and a plane wave with a complex amplitude $\hat{p}^-$ is travelling in the negative x-direction ('backward') with speed $c_0 - u_0$ (see figure 2.3). These amplitudes can be obtained by considering the boundary conditions at both ends of the tube. The assumption that the waves are plane is valid for frequencies lower than the cut-off frequency. Above this frequency, transverse modes can occur in the tube. For a circular cross-section, the cut-off frequency is determined by $f \approx c_0/(1.7D)$ [177], with D the diameter of the tube.

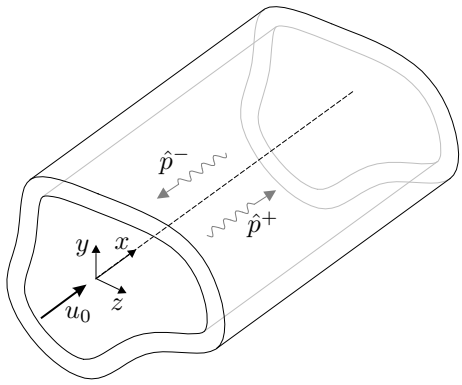

Figure 2.3: Sound waves travelling in a prismatic tube with a mean flow.

From the one-dimensional solution of the acoustic pressure perturbations, the expression for the acoustic velocity perturbation u' in the tube can be obtained from momentum conservation:

$$u'(x) = \frac{-1}{\rho_0 c_0}(\hat{p}^- e^{\mathrm{i}k^- x} - \hat{p}^+ e^{-\mathrm{i}k^+ x}) \tag{2.21}$$

Note that the undisturbed speed of sound c_0 appears in the factor $\frac{-1}{\rho_0 c_0}$ in equation 2.21 and that the mean flow only affects the propagation speeds of the forward and backward travelling waves.

2.3.2 Damping

When gas is trapped in narrow tubes or layers, boundary layer effects can have a significant effect on acoustic wave propagation. Effects of viscosity and thermal con-

ductivity can dissipate a significant amount of acoustic energy. In combustion systems, these viscothermal effects can be neglected though. The viscothermal effects are generally small due to the large characteristic lengths in these systems.

With a mean flow or at large acoustic amplitudes, acoustic losses can also occur as a result of the generation of turbulence. A turbulent air flow at low Mach numbers does not disturb the acoustic field other than providing an additional convective and damping effect [176]. The convective effect was already accounted for by using the convective wave equation as a starting point for the derivation of the one-dimensional acoustic model.

Different models for describing the acoustic damping in hard-walled pipes carrying a mean flow are available in literature. The influence of a *laminar* flow on acoustic wave propagation is discussed in [80]. For *turbulent* flows, a description is given in [81].

In this thesis the relatively simple quasi-steady description of Ingard [81] is used to account for acoustic damping due to a turbulent mean flow. A quasi-steady modulation of the pressure drop in the pipe can be expressed as an equivalent turbulent friction acting on the oscillatory flow. The approach does not deal explicitly with the detailed mechanism of the interaction of the sound wave with the turbulent flow. In a more detailed analysis not only the mean flow, but also the turbulent spectrum should be considered, as well as the mean flow profile in the duct. Still, measurements show that reasonable results are obtained until a Mach number of 0.45 [81]. The theory of Ingard will be briefly discussed in the remainder of this section. An overview of more accurate approaches to account for the effect of turbulence on acoustic wave propagation can be found in [19, 71].

With an additional damping effect due to a turbulent mean flow, the wave number is modified to:

$$k^{\pm} = \frac{\omega/c_0 \pm \mathrm{i}\beta_t}{1 \pm \mathrm{Ma}} \tag{2.22}$$

where β_t is the turbulent damping coefficient. From the denominator in equation 2.22 it follows that the turbulent damping is larger in the upstream than in the downstream direction. At sufficiently high Reynolds numbers β_t can be expressed as:

$$\beta_t = \frac{\psi \mathrm{Ma}}{2a} \tag{2.23}$$

where a is the ratio between the area of the duct cross-section and its perimeter ($2a = R$ for a circular tube with radius R). Moreover ψ is the empirically determined friction factor which depends on the Reynolds number and the wall roughness. Relationships between these factors can be found in most text books on fluid flow. For smooth pipes, the formula of Blasius can be used to calculate the friction factor:

$$\psi = 0.3164 \mathrm{Re}^{-1/4} \tag{2.24}$$

which is valid for $\mathrm{Re} < 10^5$. Using this relationship the attenuation in decibels per metre can be plotted as a function of the Mach number. This is done in figure 2.4 for a circular pipe of diameter $D = 50$ mm. Especially at high Mach numbers the upstream and downstream attenuation start to differ.

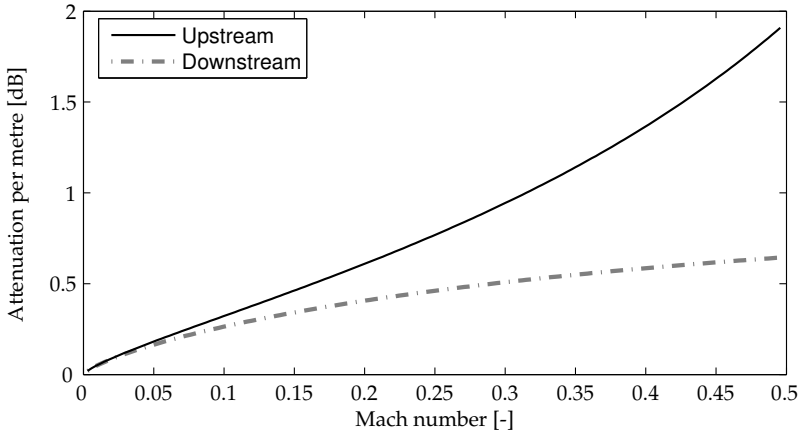

Figure 2.4: Attenuation per metre in decibel in a pipe with diameter $D = 50$ mm carrying a turbulent flow.

In equation 2.22 only the damping effect due to the turbulent flow field is included. In turbulent flows this damping effect is usually much larger than the viscothermal damping effect. For air at standard conditions (see Nomenclature on page 187), the turbulent damping coefficient exceeds the viscothermal damping coefficient if [81]:

$$\mathrm{Ma} > C\sqrt{f} \tag{2.25}$$

where $C = 2.86 \cdot 10^{-3}$ $\sqrt{\mathrm{s}}$. When $f = 100$ Hz this condition is already satisfied if $\mathrm{Ma} \approx 0.03$.

2.3.3 Impedance

Impedance (i.e. 'something impeding motion') is used in acoustics as a measure for the resistance of a fluid against pressure waves. In the one-dimensional case, the impedance at a certain location gives information about the acoustic behaviour of the system *behind* that location. The impedance is defined in the frequency domain. Assuming harmonic perturbations and a one-dimensional sound field, the specific acoustic impedance Z_s for a certain frequency ω is only a function of the position x and is defined as the ratio between the pressure perturbation and the velocity perturbation according to:

$$Z_s(x,\omega) = \frac{p'(x,\omega)}{u'(x,\omega)} \tag{2.26}$$

For a freely propagating one-dimensional sound wave (i.e. no reflection: $\hat{p}^- = 0$), equation 2.20 and 2.21 can be inserted in equation 2.26 giving the characteristic impedance Z_c of a fluid in a tube:

$$Z_c = \rho_0 c_0 \tag{2.27}$$

A useful quantity arises when dividing both impedances:

$$\zeta(x,\omega) = \frac{Z_s(x,\omega)}{Z_c} = \frac{1}{\rho_0 c_0}\frac{p'(x,\omega)}{u'(x,\omega)} \tag{2.28}$$

which is called the scaled (dimensionless) impedance ζ. This quantity will be used throughout this thesis. When $\zeta = 1$, i.e. the specific acoustic impedance equals the characteristic impedance, the sound wave can propagate freely and no sound is reflected. When $\zeta \to \infty$, almost all sound is reflected (i.e. at an acoustically hard wall, where the velocity perturbation must be zero). A sudden drop or jump in the impedance also reflects sound waves, for example at a water-air surface, where sound is reflected because of the difference in characteristic impedance of the fluids. A good example of this are the echoes near a swimming pool.

The reflection coefficient R is defined here as the ratio between the pressures of the backward and forward travelling sound wave in a duct:

$$R(x,\omega) = \frac{\hat{p}^-}{\hat{p}^+} e^{\mathrm{i}(k^+ + k^-)x} \tag{2.29}$$

With the help of equations 2.28 and 2.29, the impedance and the reflection coefficient can be related according to:

$$R(x,\omega) = \frac{\zeta(x,\omega) - 1}{\zeta(x,\omega) + 1} \tag{2.30}$$

The reflection coefficient can take values from -1 to 1. When $R = -1$ (i.e. $\zeta = 0$) the sound waves are reflected with a 180 degrees phase shift. When $R = 1$ the waves are reflected without a phase shift. Finally, when $R = 0$, no incident waves are reflected. The latter case corresponds to the situation where $\zeta = 1$.

2.4 Acoustic network model

In this section a one-dimensional acoustic network model is derived. With this model, the acoustic field in a network of coupled, one-dimensional acoustic elements can be predicted. The individual acoustic elements in the network are represented by a transfer matrix which describes the relationship between acoustic quantities at both ends of the acoustic element.

It is assumed that the acoustic elements are prismatic tubes in which one-dimensional acoustic wave propagation occurs. As long as the transfer matrix of a certain acoustic element can be derived or measured it can be included in the network model. In this section, the acoustic transfer matrix of a single prismatic tube will be derived. Subsequently, the boundary conditions necessary for coupling several of these elements in the acoustic network model will be posed. Finally, the difference between the boundary conditions valid for situations without flow and with flow will be pointed out.

2.4.1 Transfer matrices

For each one-dimensional acoustic element, such as a tube, the mass flow perturbation M' and the pressure perturbation p' at the inlet and outlet of the element can be related by a certain transfer function. When the acoustic elements are coupled, these relations can be combined in one system matrix $\mathbf{A}$ that relates the acoustic pressures to the acoustic mass flows at each coupling point (node):

$$\mathbf{A}\mathbf{p}' = \mathbf{M}' \tag{2.31}$$

When sufficient boundary conditions are present, the unknown pressure perturbations p' at each node can be solved by $\mathbf{p}' = \mathbf{A}^{-1}\mathbf{M}'$.

Advantages of the network model are that the computational load is very low and that, as long as the analytical solution of a transfer function can be calculated, it allows for including effects like temperature gradients, mean flow and turbulent or viscous damping.

Prismatic tube

For a prismatic tube J the symbolic conventions are shown in figure 2.5. The length and cross-sectional area of the tube are denoted as L_J and S_J, respectively. The quantities at $x_J = -L_J/2$ have the subscript 1, while the quantities at $x_J = L_J/2$ have the subscript 2.

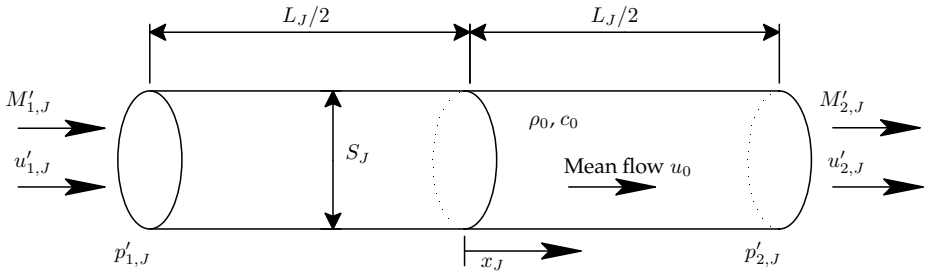

Figure 2.5: Symbolic conventions for one single prismatic tube.

With the one-dimensional analytical expression for the sound pressure perturbation (equation 2.20), the (complex) pressure amplitudes $\hat{p}^-$ and $\hat{p}^+$ can be written as a function of $p'_{1,J}$ and $p'_{2,J}$ and inserted into the expression for the velocity perturbation (equation 2.21). From this velocity perturbation, the mass flow perturbation M' can be calculated according to:

$$M' = S\rho_0 u' \tag{2.32}$$

Because $u'_{1,J}$ and $u'_{2,J}$ were written in terms of $p'_{1,J}$ and $p'_{2,J}$, the element matrix for a prismatic tube can be derived:

$$\frac{S_J}{c_0 \sinh(C_J)} \begin{bmatrix} \cosh(C_J) & -e^{\mathrm{i}L_J(k^+-k^-)/2} \\ e^{-\mathrm{i}L_J(k^+-k^-)/2} & -\cosh(C_J) \end{bmatrix} \begin{Bmatrix} p'_{1,J} \\ p'_{2,J} \end{Bmatrix} = \begin{Bmatrix} M'_{1,J} \\ M'_{2,J} \end{Bmatrix} \tag{2.33}$$

in which $C_J = \mathrm{i}L_J(k^+ + k^-)/2$. In [178] another element matrix is derived, valid for a one-dimensional acoustic field in a duct with a linear axial temperature profile. This specific element is useful in combustion applications and will also be used when constructing a network model of the experimental setup that is considered in this thesis (see chapter 6).

For convenience the coefficients of the derived element matrix are written as A_{ij}^J:

$$\begin{bmatrix} A_{11}^J & A_{12}^J \\ A_{21}^J & A_{22}^J \end{bmatrix} \begin{Bmatrix} p'_{1,J} \\ p'_{2,J} \end{Bmatrix} = \begin{Bmatrix} M'_{1,J} \\ M'_{2,J} \end{Bmatrix} \tag{2.34}$$

When several tubes are coupled, a system matrix can be filled with the element matrices of these tubes. This system matrix is a square matrix with dimension n, where n is the number of nodes. The boundary conditions necessary for coupling the elements in the system matrix will be discussed in the next section.

2.4.2 Coupling and boundary conditions

When a mean flow is present in a system of coupled tubes, having different cross-sectional areas, the mean flow can induce additional acoustic reflection and absorption at these area changes. At an area expansion the incident sound field may synchronise the unsteady shedding of vorticity at the edge of the expansion to produce an organised train of vortices, thereby converting acoustic into vortical energy, or vice versa. Obviously, these three-dimensional effects cannot be directly accounted for in a one-dimensional approach and hence an analogy must be applied. It is therefore assumed that the Kutta condition compensates the singularity in the energy equation and stands for the sound that is converted into vorticity energy [124]. The Kutta condition states that the velocity should remain finite at the edge of the exit, implying that a thin shear layer is shed at the edge. Obviously, vorticity generation and flow separation are not possible without viscosity, but the magnitude of the viscosity does not enter as an explicit parameter here.

Bechert [7] used a quasi-steady approximation to model the sound absorption due to unsteady vortex shedding. He showed that a properly designed contraction placed at the end of a pipe is an anechoic termination at a specific Mach number. A quasi-steady theory assumes that the acoustic response of the system can be described as a succession of steady flow states. In a quasi-steady system, the Strouhal number $\mathrm{St} = \frac{\omega L}{u_0} \ll 1$, and therefore the local change in acoustic pressure or velocity as a result of wave propagation is much smaller than changes due to a change in geometry. While more elaborate theories are available [16, 17, 48], the quasi-steady theory remains a useful design tool. This theory is restricted to low frequencies. Moreover, an isentropic flow is assumed, implying that $\mathrm{Ma}^2 \ll 1$. In the next section it will be shown how this theory can be used to provide the boundary conditions necessary for coupling two acoustic network elements. A more thorough description of the theory can be found in [49]. Subsequently, general boundary conditions like an acoustic mass flow source and an impedance are discussed.

Coupling

The coupling point of two tubes J and $J+1$ having different cross-sectional areas is depicted in figure 2.6.

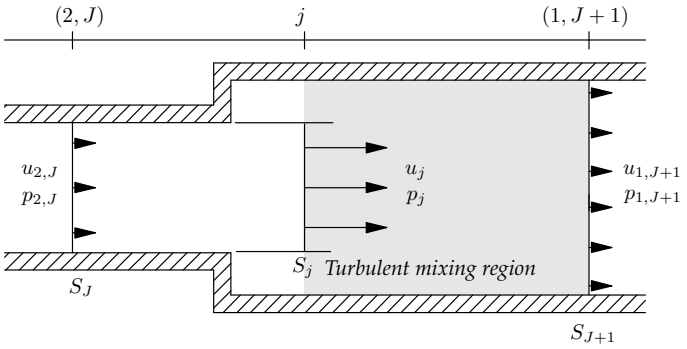

Figure 2.6: Coupling point of two tubes including a mean flow.

Three axial locations are indicated in figure 2.6. Location $(2, J)$ and $(1, J+1)$ are considered to be the end of tube J and the beginning of tube $J+1$, respectively. At the end of tube J, a free jet of cross-section S_j is formed by separation of the flow. Further downstream the end of tube J the jet becomes unstable and breaks up in a turbulent mixing region. Finally, at location $(1, J+1)$ a fully developed pipe flow is recovered. The turbulent mixing region can be quite long, but it is assumed here that all the three-dimensional acoustic phenomena occur upstream of location $(1, J+1)$. This typically occurs at distances of the order of a few times the pipe diameters from the discontinuity [148] (the junction is acoustically compact).

The acoustic velocity field is considered to be irrotational and viscous effects are neglected. Moreover, from tube J until location j the free jet is homentropic and frictionless. Also, the turbulent mixing region is adiabatic, without any wall friction. Using these assumptions, mass conservation can be formulated as:

$$\rho_0 S_J u_{2,J} = \rho_0 S_{J+1} u_{1,J+1} = \rho_0 S_j u_j \tag{2.35}$$

The variables in this equation are still total quantities. It can be seen that the flow is considered incompressible, which is only valid for low frequencies and moderate Mach numbers. Because the flow is adiabatic, the total enthalpy is conserved. With an incompressible gas the conservation of enthalpy, valid along a streamline, can be written as:

$$\frac{1}{2}u_{2,J}^2 + \frac{p_{2,J}}{\rho_0} = \frac{1}{2}u_j^2 + \frac{p_j}{\rho_0} \tag{2.36}$$

Because the jet separates from the trailing edge, the kinetic energy of the jet is not converted back into potential energy (pressure). Therefore, a part of the energy of the flow is converted into heat during downstream development of the jet flow. Nevertheless, the free jet still transfers momentum to the stagnant flow downstream of

the area change. The momentum conservation applied to the mixing region yields:

$$S_{J+1}p_j + S_j\rho_0 u_j^2 = S_{J+1}p_{1,J+1} + S_{J+1}\rho_0 u_{1,J+1}^2 \tag{2.37}$$

The pressure and velocity in the jet, p_j and u_j, can be eliminated from equations 2.35-2.37. The following equations remain:

$$p_{2,J} = p_{1,J+1} + \frac{\rho_0 u_{1,J+1}^2}{2}\left[\left(\frac{S_{J+1}}{S_j} - 1\right)^2 - \left(\frac{S_{J+1}^2}{S_J^2} - 1\right)\right] \tag{2.38}$$

$$\rho_0 S_J u_{2,J} = \rho_0 S_{J+1} u_{1,J+1} \tag{2.39}$$

Blevins [14] defines a loss coefficient K to account for the effect of the separation of the flow at the various area transition geometries. This loss coefficient is defined as:

$$\frac{p_1 - p_2}{\frac{1}{2}\rho_0 u_2^2} = 1 - \frac{S_{J+1}^2}{S_J^2} + K \tag{2.40}$$

where the indices 1 and 2 indicate the states far upstream and downstream the transition, respectively. When equation 2.40 is compared with equation 2.38, it is seen that the loss coefficient of Blevins can be substituted in the expression for the pressure:

$$p_{2,J} = p_{1,J+1} + \frac{\rho_0 u_{1,J+1}^2}{2}\left[K - \left(\frac{S_{J+1}^2}{S_J^2} - 1\right)\right] \tag{2.41}$$

This equation offers the possibility to use loss coefficients applicable to the geometry under consideration. Blevins [14] showed that especially the radius of the edge of the transition can have a large influence on the loss coefficient.

The results of equation 2.38 and 2.39 are now linearised in order to be used for acoustic purposes. This gives the following coupling conditions:

$$p'_{2,J} = p'_{1,J+1} + \rho_0\overline{u_{1,J+1}}u'_{1,J+1}\left[\left(\frac{S_{J+1}}{S_j} - 1\right)^2 - \left(\frac{S_{J+1}^2}{S_J^2} - 1\right)\right] \tag{2.42}$$

$$M'_{2,J} = M'_{1,J+1} \tag{2.43}$$

It is noticed that the mean flow only affects the first balance equation. *Without* flow, this equation would reduce to $p'_{2,J} = p'_{1,J+1}$. The extra term seen in the case with flow accounts for the energy transfer from the acoustic field to the flow. It is observed that this energy transfer does not depend on the frequency. This is true unless the effects of friction and heat transfer start to play a role. Nonetheless, at low frequencies these are very inefficient mechanisms.

To include equation 2.42 in the system matrix, $u'_{1,J+1}$ is written as $u'_{1,J+1} = \frac{M'_{1,J+1}}{S_{J+1}\rho_0}$. By doing so, the following boundary condition evolves:

$$p'_{2,J} = p'_{1,J+1} + \overline{u_{1,J+1}}\frac{M'_{1,J+1}}{S_{J+1}}\left[\left(\frac{S_{J+1}}{S_j} - 1\right)^2 - \left(\frac{S_{J+1}^2}{S_J^2} - 1\right)\right] \tag{2.44}$$

Together with the mass balance equation, this coupling equation can be incorporated in the system matrix. An extra 2×2 transfer matrix has to be inserted to account for the transfer of pressures at the coupling point. This implies that the size of the matrix is not equal to the number of coupling points anymore. The system matrix of a system with two tubes J and $J+1$, including a mean flow, can be written as:

$$\begin{bmatrix} A_{11}^{J} & A_{12}^{J} & 0 & 0 \\ A_{21}^{J} & A_{22}^{J} - R & R & 0 \\ 0 & R & -A_{11}^{J+1} - R & -A_{12}^{J+1} \\ 0 & 0 & -A_{21}^{J+1} & -A_{22}^{J+1} \end{bmatrix} \begin{Bmatrix} p'_{1,J} \\ p'_{2,J} \\ p'_{1,J+1} \\ p'_{2,J+1} \end{Bmatrix} = \begin{Bmatrix} M'_{1,J} \\ 0 \\ 0 \\ -M'_{2,J+1} \end{Bmatrix} \tag{2.45}$$

in which $R = S_{J+1}\overline{u_{1,J+1}}^{-1} \left[\left(\frac{S_{J+1}}{S_j} - 1 \right)^2 - \left(\frac{S_{J+1}^2}{S_J^2} - 1 \right) \right]^{-1}$.

Note that for large R, i.e. when $\overline{u_{1,J+1}} \downarrow 0$ or $\frac{S_{J+1}}{S_J} \approx 1$, the boundary condition $p'_{2,J} = p'_{1,J+1}$ appears again. When $S_J < S_{J+1}$ a similar procedure can be conducted, resulting in the same correction as when $S_J > S_{J+1}$.

With the approach described in this section, good results are obtained until a Mach number of 0.3 [19]. For higher Mach numbers the reader is referred to [48, 49].

By imposing additional boundary conditions at the entrance and exit of this system, it can be solved for the acoustic pressures.

Boundary conditions

In section 2.2.3 it was shown that the thermo-acoustic source behaves as an acoustic mass flow source. $\mathcal{M}'_s = \int_V m'_s \mathrm{d}V$ is the mass flow perturbation, volume integrated over the source with volume V. The acoustic mass flow source $\mathcal{M}'_s$ is proportional to the volume integrated heat release rate $Q' = \int_V q' \mathrm{d}V$ (refer to equation 2.11). The volume integration can be applied to the flame-zone only, as heat release rate sources do not occur outside this flame zone. Because of the compactness of this source, it can be lumped into one node in the acoustic network model. This boundary condition can be applied by replacing the mass conservation equation at a certain node by:

$$M'_{2,J} = M'_{1,J+1} + \mathcal{M}'_s \tag{2.46}$$

At the ends of the network model, an impedance boundary condition should be applied to account for the influence of the surroundings on the acoustic system. An impedance boundary condition at node j of element J can be derived from the dimensionless impedance $\zeta = \frac{1}{\rho_0 c_0} \frac{p'}{u'}$:

$$M'_{j,J} = \frac{S_J}{c_0 \zeta} p'_{j,J} \tag{2.47}$$

which can be applied by subtracting the coefficient $\frac{S_J}{c_0 \zeta}$ from the coefficient in the system matrix corresponding to $p'_{j,J}$ and $M'_{j,J}$.

2.4.3 Acoustic reflection at contractions

In the experimental setup, described in chapter 6, contractions are used to isolate the acoustic system of interest. The effect of a contraction on the acoustics can be accounted for by using a similar derivation as done in the previous section for the area transition including a mean flow. The only difference is that a contraction is present at the connection between the two elements in figure 2.6. This only affects the area of the jet S_j, which is now equal to the area of the contraction, corrected by the so-called vena contracta effect. Due to the vena contracta effect, the final cross-section area S_j of the jet from the contraction is a factor Γ_0 smaller than the physical area of the contraction. An overview of dependence of the vena contracta factor Γ_0 on the Mach number, the ratio S_J/S_{J+1}, the Reynolds number and the geometry is given in [49, 72]. For a sharp-edged discontinuity and moderate Mach numbers (incompressible flow) the theoretical value valid for a flow through a slit-shaped orifice in an infinite baffle of $\Gamma_0 \approx 0.7$ is a good estimate, and will be used in this thesis.

The derivation for the effect of a contraction on the acoustics is again only valid for low Mach and Strouhal numbers. When multiple contractions are present in the same cross-section (perforated disc) it turns out to be easier to obtain a low Strouhal number for a given contraction ratio. The resulting correction to the system matrix of the network model is also the same as derived in section 2.4.2.

2.5 Prediction of the onset of instability

In the previous sections an acoustic network model was derived and an expression was found for the thermo-acoustic source term. This thermo-acoustic source term (heat release rate) was proportional to an acoustic mass flow source (refer to equation 2.11). It turned out to be relatively simple to include this source term in the acoustic network model. To achieve this, the heat release rate was volume integrated and applied as an acoustic mass flow source at a specific node of the network model. From now on, the term 'heat release rate perturbation' will refer to the volume integrated heat release rate perturbation.

With technical applications in mind, a conservative approach can be made with respect to the stability analysis. It can be expected that the equilibrium of a self-excited instability, which is limited by non-linear effects, usually exhibits unacceptably high pulsations and that the amplification of pulsations in the linear regime must be avoided at all times. Therefore, assessing the linear stability of combustion processes is an important issue. This type of analysis delivers information about whether the combustor is stable or unstable, including the growth rate of the amplitude.

Thermo-acoustic instabilities are caused by the fact that the acoustic source in the system is a function of perturbations occurring in the system itself. The heat release rate perturbation is, in general, a function of a perturbation f' in a flame burning rate parameter at some earlier time $t - \tau$, in which τ is the time that the perturbation needs to travel to arrive in the flame zone. Having arrived there, the perturbation induces a heat release rate response Q'. The level of this response depends on the *local*

transfer function Q'/f'. The total transfer function from the location of the acoustic perturbation to the heat release rate response can be written as:

$$H_f = \left|\frac{Q'}{f'}\right|_{flame} e^{-\mathrm{i}\omega\tau} \tag{2.48}$$

in which the subscript *flame* means that the indicated transfer function is evaluated at the flame front. The total transfer function H_f is the so-called *flame transfer function*. Usually this transfer function is presented as a dimensionless value by scaling it with the mean transfer function $\frac{Q_0}{f_0}$ [45,74,163].

The dependence of Q' on acoustic properties requires the rewriting of equation 2.48 in terms of acoustic mass flow perturbations and acoustic pressures at the nodes of the network model. This allows for including it as a boundary condition in the system matrix $\mathbf{A}$ of the network model. It is assumed that the acoustic perturbation f' and the thermo-acoustic response Q' occur at node 1 and 2 of a regular one-dimensional acoustic element (see figure 2.5).

Moreover, for simplicity, it is assumed that the acoustic perturbation is a velocity perturbation at node 1, i.e. $f' = u'_{1,J}$. Using equation 2.11 and 2.48, the boundary condition for the acoustic mass flow perturbation $M'_{2,J}$ at node 2 of the thermo-acoustic element can be written as:

$$M'_{2,J} = H_f \frac{\gamma - 1}{c_0^2} u'_{1,J} \tag{2.49}$$

To include this boundary condition in the system matrix, $u'_{1,J}$ is written as a function of $p'_{1,J}$ and $p'_{2,J}$. This can be done using equation 2.33, which results in:

$$M'_{2,J} = H_f \frac{\gamma - 1}{c_0^2} \frac{1}{\rho_0 c_0} \left[\frac{1}{\tanh\left(C_J\right)} p'_{1,J} - \frac{e^{\mathrm{i}L_J(k^+ - k^-)/2}}{\sinh\left(C_J\right)} p'_{2,J} \right] \tag{2.50}$$

When this expression is introduced in the system matrix $\mathbf{A}$, it results in a system matrix having singularities for complex frequencies. In the next section it will be shown how these singularities are related to instabilities of the acoustic system.

2.5.1 Solution method

With a heat release rate perturbation depending on an earlier acoustic perturbation the system is not harmonic anymore, but depends on its time-history. Consequently, instabilities can build up in the system. When this is the case, the smallest disturbance of the system results in large pressure perturbations. Mathematically, this occurs when the determinant of the system matrix is zero. The acoustic system represented by the system matrix then has a non-trivial solution.

The system matrix $\mathbf{A}$ is a function of the frequency ω. When no time delays are present in the system, $\det\left(\mathbf{A}\right) = 0$ for the real eigenfrequencies of the system. However, when time delays are present, $\det\left(\mathbf{A}\right)$ becomes zero for complex eigenfrequencies $\omega_r + \mathrm{i}\omega_i$. A time dependence of $e^{\mathrm{i}\omega t}$ is assumed, so inserting a complex frequency for ω, this time-dependence can be written as:

$$e^{\mathrm{i}\omega t} = e^{\mathrm{i}(\omega_r + \mathrm{i}\omega_i)t} = e^{-\omega_i t} e^{\mathrm{i}\omega_r t} \tag{2.51}$$

Thus when $\omega_i < 0$ the oscillation grows exponentially in time. The opposite is true when $\omega_i > 0$. So ω_r is the frequency of the thermo-acoustic oscillation and ω_i is an indication of the growth rate of the oscillation in time. Some authors [136,156] define a growth rate GR as the ratio of the pulsation amplitude of two successive pulsation cycles:

$$\mathrm{GR} = e^{-2\pi \frac{\omega_i}{\omega_r}} - 1 \tag{2.52}$$

When GR> 0 fluctuations will be amplified in time. Fluctuations will vanish when GR< 0.

To find the complex eigenfrequencies for which $\det(\mathbf{A}(\omega_r, \omega_i)) = 0$, the problem is relaxed by searching for the eigenfrequencies for which $|\det(\mathbf{A}(\omega_r, \omega_i))| \downarrow 0$. This is a non-linear problem which is solved here in MATLAB. The Nelder-Mead simplex search method [99] is used, which is a direct search method that does not use numerical or analytic gradients, and therefore only requires function evaluations. With the two variables ω_r and ω_i the simplex is a triangle in the (ω_r, ω_i) plane. The vertices of this triangle are defined by the values of $\det(\mathbf{A}(\omega_r, \omega_i))$, i.e. the simplex lies on the surface defined by $\det(\mathbf{A}(\omega_r, \omega_i))$. At each step of the search, a new point in or near the current simplex is generated. The function value at this new point is compared with the function values at the vertices of the simplex and, when smaller, replaces one of these points (see figure 2.7).

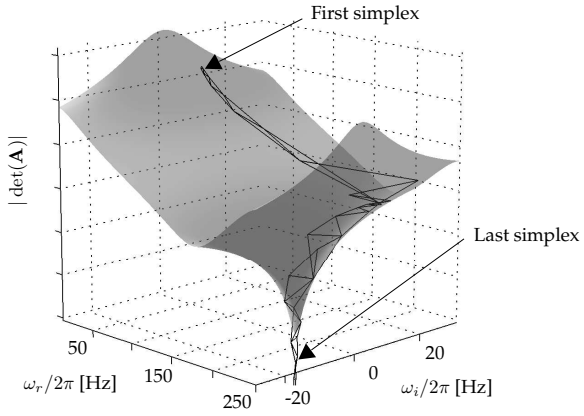

Figure 2.7: Example of a simplex travelling over the surface defined by $|\det(\mathbf{A})|$.

The overall effect of the algorithm is for the simplex to crawl around the parameter space, creeping down valleys and shrinking to get to the very bottom of narrow valleys. When the procedure is started with different start values for ω_r and ω_i, it converges to different eigenfrequencies. Consequently, there is a chance that eigenfrequencies are missed by the algorithm. To speed up the search procedure while keeping the probability of missing an eigenfrequency low, a relatively coarse grid of starting values $(\omega_r, \omega_i)_{start}$ is chosen, covering the interesting frequency range. The grid is refined once to check whether all eigenfrequencies are found.

Example

To gain insight in the unstable feedback loop, a simple system is considered as an example. The system consists of two tubes, having equal radii R and lengths L. The network model representation of this simple system is depicted in figure 2.8.

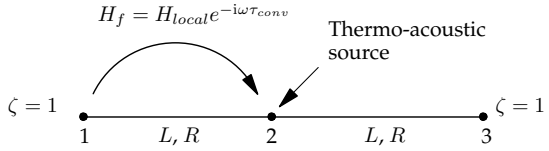

Figure 2.8: Acoustic network model with thermo-acoustic source.

At node 2 in this model, the thermo-acoustic boundary condition is applied (equation 2.50). Acoustic velocity perturbations at node 1 influence this boundary condition. It is assumed that these perturbations are convected to node 2. They arrive there after a time delay τ_{conv} and cause a mass flow perturbation via a local flame transfer function H_{local}. Both ends of the system are assumed to be anechoic.

The complex eigenfrequencies of this system are determined for two different values of H_{local}. The remaining parameters are listed in table 2.1. The real and imaginary part of the eigenfrequencies, indicated by $\Re(f)$ and $\Im(f)$, respectively, are shown in figure 2.9.

Parameter	Value
c_0	343 [m s^{-1}]
τ_{conv}	10 [ms]
γ	1.4 [-]
R	0.025 [m]
L	0.125 [m]
ρ_0	1.29 [kg m^{-3}]

Table 2.1: Parameters used for the calculations.

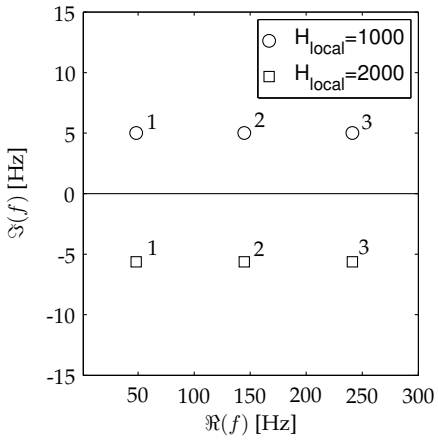

Figure 2.9: Found eigenfrequencies for two different amplification factors H_{local}. The numbers are the mode-numbers, following equation 2.53.

The first thing that is noticed from this figure is that $\Im(f)$ depends on H_{local}, while the real parts do not. For low amplifications, the gain in the feedback loop is too small to build up a self-excited oscillation ($\Im(f) > 0$). When the amplification is increased, $\Im(f)$ decreases and when $\Im(f) < 0$, the gain in the feedback loop adds energy to the loop and a self-excited oscillation builds up.

The observed real frequencies can be explained by considering the time it takes for one feedback loop to complete. When a velocity perturbation departs from the source location (node 2) it arrives $\tau_{sound} = L_1/c_0$ s later at node 1. This velocity perturbation is negative (remember that the acoustic source at node 2 is a monopole sound source) and arrives, via convection, τ_{conv} s later at the flame front. When the total time of the feedback loop equals the time of half an acoustic period T, the induced heat release rate perturbation couples with the fluctuating heat release rate at the source location, and depending on the amplification a self-excited oscillation can occur. This can be summarised as:

$$\tau_{sound} + \tau_{conv} = nT - T/2 \quad (n = 1, 2, 3...) \tag{2.53}$$

In figure 2.9, the values of n are indicated next to each eigenfrequency.

As soon as the boundary conditions are not anechoic anymore, or when area changes occur in the system, standing waves may occur and the eigenfrequencies cannot be easily described by an equation like equation 2.53. Simple examples of systems with non-anechoic boundaries can be found in [109].

2.5.2 Feedback mechanisms in combustion systems

A heat release rate perturbation of a turbulent premixed flame can be the result of many different processes. It was already mentioned that the flame is *acoustically* compact, which allowed the volume integration of the acoustic source term over the flame. With respect to the excitation, the flame does not necessary have to be compact though. Some types of excitation are transported through the flame with the convection speed, which is usually much smaller than the speed of sound (see figure 2.10).

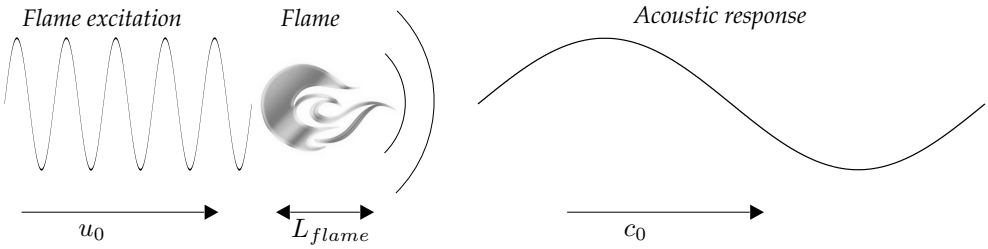

Figure 2.10: Overview of different wavelengths occurring when exciting the flame at a specific frequency.

An example of an excitation that is transported with the convection speed, is the equivalence ratio perturbation. The fluctuations in equivalence ratio originate at the position in the burner where fuel is mixed with air. Acoustic fluctuations at this position cause a fluctuation in the amount of fuel and/or air that is supplied for mixing. As a result, the equivalence ratio also fluctuates. Subsequently, this fluctuation is transported to the flame front where it causes a heat release rate perturbation.

In chapter 4 the effect of the non-compactness of the flame with respect to its excitation will be discussed in more detail. For now, it is assumed that the excitation

arrives at the flame front at the same instant, so that the heat release rate perturbation has the same phase over the whole flame. This implies that $L_{flame} \ll u_0/\omega$ [44]. Moreover, it is assumed that combustion is infinitely fast, so that a perturbation instantaneously causes a heat release rate perturbation. The total instantaneous, volume integrated heat release rate can then be written as [95]:

$$Q = \Delta H \cdot \rho \cdot S_f \cdot u \cdot y_f \tag{2.54}$$

where S_f is the total area of the flame front, y_f the fuel mass fraction, u is the velocity at the flame front and ΔH is the net calorific heat of combustion (40.80 MJ/kg for natural gas [56]).

Linearising equation 2.54 yields:

$$Q' = \Delta H \left\{ \rho_0 S_{f,0} y_{f,0} u' + S_{f,0} u_0 y_{f,0} \rho' + \rho_0 u_0 y_{f,0} S'_f + \rho_0 S_{f,0} u_0 y'_f \right\} \tag{2.55}$$

All perturbations in equation 2.55 can be induced by an acoustic field. The first term between the accolades in equation 2.55 shows that heat release rate perturbations can be a result of a fluctuating velocity at the flame front. This fluctuating velocity changes the total chemical enthalpy that is fed to the flame. In [95] it is assumed that the velocity fluctuations at the flame front can, besides being a result of the local acoustic field, be a function of a lagged acoustic velocity perturbation originating at the burner exit, at some time τ_u earlier. τ_u then denotes the time lag characterised by the convection time a fluid element needs to flow from the burner exit to the flame front. This counter-intuitive behaviour (why would a velocity perturbation travel with the convection speed, and not with the speed of sound) was also observed in experiments [70, 93, 98, 163]. The behaviour can be explained by realising that it is not the velocity perturbation itself that has to be convected to the flame; A new flame shape is induced by the velocity perturbation. This flame adjustment convects through the flame with the convection speed (i.e. also when the speed of sound would be infinity, still it is possible to have a time delay, since the flame has to re-adjust). A mathematical derivation on this behaviour can be found in a paper by Boyer and Quinard [22].

The second term between the accolades in equation 2.55 shows that density fluctuations can cause the heat release rate to fluctuate. A larger density with an unchanged volume flow results in a larger mixture mass flow and therefore a larger input of enthalpy.

The third term shows the influence of a fluctuating flame front area on the heat release rate. These area fluctuations are caused by fluctuations in the mass flow of fuel and/or air, possibly in combination with flow instabilities or vortex shedding. Vortex shedding from the burner mouth (diameter D) happens especially at frequencies where the Strouhal number $\mathrm{St} = fD/u \approx 1$ [159]. Dowling [45] uses a kinematic ducted flame model with which she shows that flow perturbations influence the heat release rate via area and position variations of the flame front.

Finally, the last term contains the effect of fuel mass fraction fluctuations. The fuel mass fraction fluctuations originate at the location where fuel and air are mixing and are induced by acoustic fluctuations at that position. Subsequently, they are convected to the flame front, and arrive there τ_ϕ s later.

The difficulty of the preceding description is that fluctuations in a certain parameter can induce fluctuations in other parameters (as is the case with flame front area fluctuations, which can be induced by for instance velocity fluctuations). Therefore, a lumped approach is usually taken, where all effects of a certain excitation is included in a flame transfer function. It was shown in different papers that for premixed flames, equivalence ratio perturbations are the most likely cause for feedback to the flame [31,70,74,108]. Raman measurements have also been used in an unstable lean premixed methane swirl flame to show that indeed equivalence ratio perturbations are causing the instability [185]. The flame transfer function H_f between heat release rate perturbations and equivalence ratio perturbations is then defined as:

$$H_f = \frac{Q'}{\phi'} \tag{2.56}$$

This transfer function includes all effects induced by the equivalence ratio perturbation. Moreover, when ϕ' is defined at the location where fuel and air are mixed, it also includes the phase shift between Q' and ϕ' due to the convective time delay and possibly the time delay due to a finite combustion rate. Consequently, it is no surprise that H_f is a complex number.

2.5.3 Example of a combustion system analysis

To give some insight in the performance of the network model and the instability search method, a simple combustion system is considered in this section (see also [179]). In appendix B an additional example of the method applied to a Rijke tube can be found.

In the model of the combustion system (figure 2.11) an air supply tube and a fuel supply tube come together at node 3, where both streams are mixed. Subsequently, the mixture is transported to the flame front (node 4), where the thermo-acoustic source (flame) is located. A duct downstream of the source represents the remainder of the combustion chamber. Each element has a length of 0.25 m. Moreover, the area of all elements, except the fuel supply element, is $2 \cdot 10^{-3}$ m^2. The area of the fuel supply element is 10 times smaller. Those dimensions are chosen so that the resulting eigenfrequencies can easily be explained and give insight in the thermo-acoustic feedback loop.

The example calculations are performed at atmospheric pressure with a fuel (natural gas) and air mass flow corresponding to a thermal power of 100 kW and an air factor of 1.5.

The temperature in the tubes influences the speed of sound and the mean density. For this example problem, it is assumed that two zones exist in the model, i.e. a hot zone downstream of the thermo-acoustic source (gray line), and a cold zone upstream of the source (black lines). The cold zone has a constant temperature of 300 K. The temperature in the hot zone is determined by the adiabatic flame temperature, which depends on the ratio between the supplied air and fuel. There is no heat loss included in this system, so the temperature remains constant.

When there is a system surrounding the combustion system, its acoustic influence can be represented by imposing frequency-dependent impedances ζ on the bound-

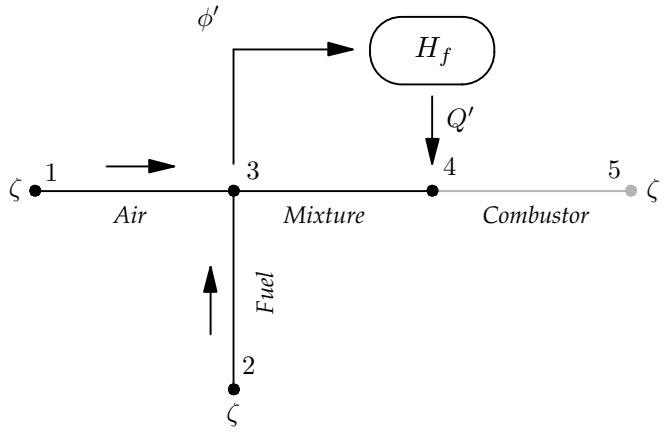

Figure 2.11: Acoustic model coupled with the flame dynamics model.

aries. In gas turbine applications, usually a near-sonic condition applies to the end of the combustion chamber. This is equivalent to an echoic (full reflection) acoustic boundary condition.

Only the effect of fuel mass fraction perturbations is considered in this example problem, so equation 2.55 reduces to:

$$Q' = \Delta H \rho_0 S_{f,0} u_0 y'_f \tag{2.57}$$

The fuel mass fraction perturbation originates at the mixing location and travels to the flame front with the convection speed. It arrives there delayed with a time τ_ϕ, so that the fuel mass fraction fluctuation at the flame front can be written as a function of the fuel mass fraction fluctuation at the mixing position, using the factor $e^{\mathrm{i}\omega\tau_\phi}$.

The fuel mass fraction fluctuation at the mixing position is determined by the velocity perturbations at the downstream ends of the fuel and air supply. The fuel mass fraction can be written as:

$$y_f = \frac{M_f}{M_f + M_a} \tag{2.58}$$

in which M_f and M_a are the fuel and air mass flow, respectively. Moreover, the equivalence ratio ϕ can be written as:

$$\phi = \frac{M_f/M_a}{[y_f/y_a]_{st}} \tag{2.59}$$

When this equation is linearised around a mean equivalence ratio ϕ_0, the following expression can be derived:

$$\frac{\phi'}{\phi_0} \approx \frac{M'_f}{M_{f,0}} - \frac{M'_a}{M_{a,0}} \tag{2.60}$$

The fluctuations of the fuel and air mass flow are directly related to the acoustic velocity perturbation u' at the ends of the fuel and air element, i.e. $M' = \rho_0 S u'$.

To promote the mixing with air, the fuel is usually supplied at high speeds through small nozzles. When the velocity in the fuel supply nozzle would reach the speed of sound (*choked flow*), no acoustic fluctuations can exist in the fuel supply and the first RHS term of equation 2.60 is zero. However, to be able to control the power at constant pressure, fuel nozzles are not choked in practice [145].

With equation 2.59, equation 2.58 can be written as:

$$y_f = \phi[y_f/y_a]_{st} \frac{M_a}{M_f + M_a} \approx \phi[y_f/y_a]_{st} \tag{2.61}$$

because $M_{a,0} \gg M_{f,0}$ [52] for lean combustion of natural gas. So with equation 2.61 and 2.60 the fuel mass fraction perturbation y'_f can now be written as a function of velocity perturbations in the fuel and air supply and included as a boundary condition in the acoustic network model.

The model described above has been implemented in the network model, in which for simplicity effects of flow and turbulent damping are excluded. The effect of the boundary conditions on the found eigenfrequencies is shown in figure 2.12. Two types of boundary conditions are considered here: anechoic and echoic boundary conditions.

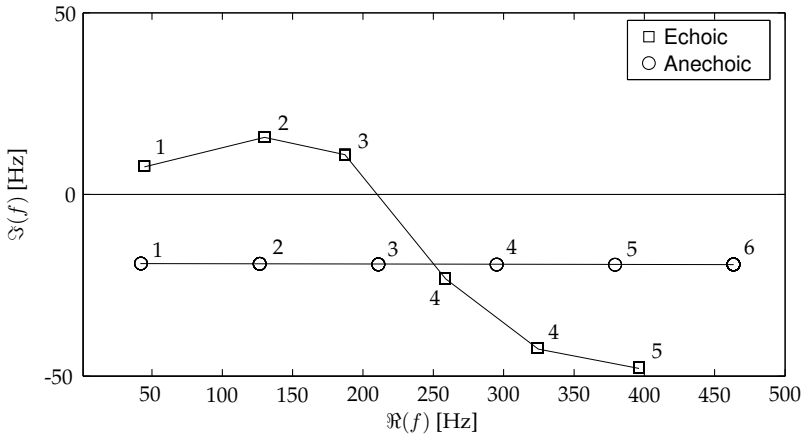

Figure 2.12: Complex frequencies for which $|\mathbf{A}| = 0$ for the anechoic system (circles) and the echoic system (squares).

In this example, the fluctuations in the fuel mass flow supply have the largest influence on the equivalence ratio. Therefore, a positive velocity fluctuation causes a positive equivalence ratio perturbation, and the real frequencies can again be determined with:

$$\tau_{sound} + \tau_\phi = nT - T/2 \quad (n = 1, 2, 3...) \tag{2.62}$$

In figure 2.12 the value of n is shown besides the appropriate eigenfrequency.

With echoic boundaries, standing waves occur in the system, which change the value of τ_{sound} to an equivalent time delay derived from the phase between the

acoustic wave at the flame location and at the mixing location (i.e. $\tau_{sound} = \frac{\angle(\phi'/Q')}{2\pi f}$). Note that the mode number 4 occurs twice for the echoic system. Because τ_{sound} is a function of the frequency, similar mode numbers can occur at different frequencies. When the boundary conditions are fully echoic and when there is no further damping in the acoustic system $\angle(\phi'/Q')$ can only be equal to 0 or π, i.e. the fluctuations are in or out of phase.

The imaginary parts of the eigenfrequencies show that some points are more unstable ($\Im(f) < 0$) with echoic boundaries. Obviously, the sound levels are much higher in the echoic system, and therefore the acoustic feedback to the mixing location can be much more efficient. The sinus-like sequence of the eigenfrequencies in the echoic case comes from changing mode shape and its amplitude with the frequency.

It was already mentioned that in an anechoic system the real frequencies are solely determined by the delay time of the thermo-acoustic feedback loop. This time delay consists of an acoustic and a convective time delay. At constant flow conditions, the convective time delay can be changed by changing the cross-sectional area. When the area of the combustor is increased by 20%, the real frequencies are seen to decrease, as expected (see figure 2.13). Another effect of changing the convective time delay is that the imaginary frequencies decrease. This implies that the amplification of the feedback loop *per* second is smaller when the convective time delay is larger, which is the result of the instability occurring at a lower frequency. This convective time delay is independent of the frequency and much larger than the acoustic time delay. When the convective time delay goes to zero, all eigenfrequencies collapse into a single point for which $\Im(f) = 0$ and $\Re(f)$ can still be determined using equation 2.62. Without convective time delay, the system is harmonic again, which explains why $\Im(f) = 0$ (harmonic time-dependency).

The build up of the acoustic pressure in time is shown in figure 2.14. The time

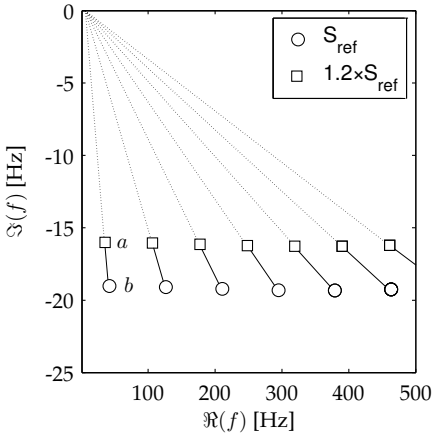

Figure 2.13: Effect of an increase of the system area on the system eigenfrequencies.

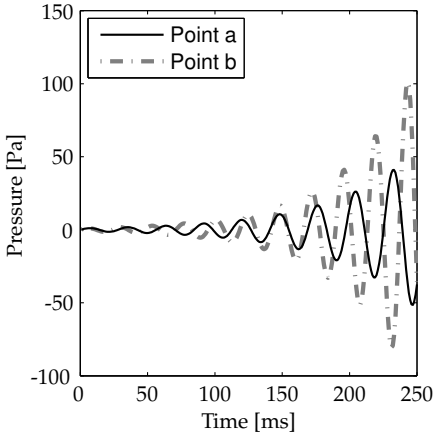

Figure 2.14: Time history of the points a and b of figure 2.13.

history of the points a and b of figure 2.13 is shown here. It is seen that a small variation in the imaginary part of the frequency can have a large effect on the build up of the acoustic pressure amplitude in time. Obviously, both of the cases are unwanted.

It should be mentioned that the location of the thermo-acoustic source in the acoustic system is very important for the coupling of the source with the acoustic system. The flame is usually present at the beginning of the combustion chamber. Due to the area transition from the burner to the combustion chamber, a velocity node and a pressure anti-node are usually present here as well. Since acoustically, the flame can be considered as an acoustic volume source, it can couple very well with the acoustic system when it is located in a velocity node or a pressure anti-node, i.e. at the beginning of the combustion chamber. Solutions in which the location of the flame is moved to a more favourable location in the acoustic system might be interesting to consider.

In this example, the amplification factor or flame transfer function was independent on the frequency. In section 2.5.2 it was already pointed out that the non-compactness of the flame with respect to its excitation causes the flame transfer function to be frequency dependent. Additionally, feedback mechanisms in the flow (like recirculation zones and vortices) can influence the flame transfer function. These effects will be discussed in more detail in chapter 4, where more sophisticated methods to obtain or describe the flame transfer function are presented.

2.6 Concluding remarks

In the preceding chapter the tools necessary to model the acoustics in combustion applications were discussed. Moreover, the mechanisms responsible for turning the flame into an acoustic source were explained. Finally, it was shown how combustion and acoustics can turn a system into an unstable one.

For the premixed flame, the heat release rate perturbations were taken to be related to fluctuations in the equivalence ratio. The mechanisms responsible for creating a heat release rate perturbation from an equivalence ratio perturbation were lumped into a flame transfer function H_f. A method to numerically predict this transfer function is by means of Computational Fluid Dynamics (CFD). The setup of a CFD model of a turbulent premixed flame and the issues of performing an unsteady transient simulation are discussed in the next chapter.

Chapter 3

Numerical simulation of reacting flows applied to the DESIRE combustor

3.1 Introduction

In this thesis, the flame transfer function, discussed in the previous chapter, will be obtained from both measurements and numerical simulations. For this purpose, a *generic* premixed natural gas burner has been designed. The term 'generic' indicates that the geometry is chosen such that convenient numerical modelling is possible, without losing characteristics relevant for gas turbine applications.

Computational Fluid Dynamics (CFD) simulations are used in the design process of the generic burner. The flow field through this burner is highly turbulent. Since turbulence is described by the Navier-Stokes (NS) equations, a turbulent flow can be computed from first principles by solving the NS equations in a direct way. This is called *Direct Numerical Simulation* (DNS). Nevertheless, for engineering computations, this method requires far too much computational effort to be solved on any foreseeable computer. The ratio between the Kolmogorov scale η_{Kol} and the length scale of the largest turbulent eddy L is related to the Reynolds number according to (see for example [137]):

$$\eta_{Kol}/L = \mathcal{O}(\mathrm{Re}^{-3/4}) \tag{3.1}$$

To resolve the Kolmogorov scale, the mesh size Δx of the computational grid must at least satisfy $\Delta x < \eta_{Kol}$. This implies that the number of grid cells N is given by:

$$N > L/\Delta x = \mathcal{O}(\mathrm{Re}^{3/4}) \tag{3.2}$$

So the total number of cells in a three-dimensional simulation is $\mathcal{O}(\mathrm{Re}^{9/4})$. Obviously, with typical Reynolds numbers in the order of 10^5 and (much) higher, DNS is inappropriate for engineering applications. Nonetheless, at moderate Reynolds

numbers and in simple geometries, DNS is a valuable tool for studying the fundamental properties of turbulence.

Generally two other methods can be distinguished which try to decrease the computational effort by incorporating some additional turbulence model: *Large Eddy Simulation* (LES) and a solution based on the *Reynolds averaged Navier-Stokes* (RaNS) equations. The effect of both methods on a quantity in a turbulent flow is shown in figure 3.1 [135].

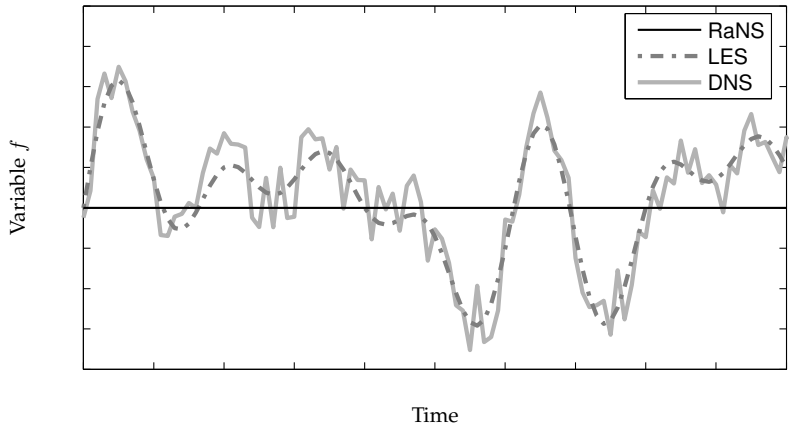

Figure 3.1: Value of a quantity f in a turbulent flow as a function of time in a RaNS, LES and DNS simulation.

It can be seen that with DNS, all turbulent fluctuations are resolved. In LES the high frequency components are filtered out, whereas with RaNS all turbulent fluctuations are averaged.

Both LES and RaNS methods require far less computational effort than DNS, as they both incorporate a model for dealing with turbulent fluctuations. In LES, the larger eddies are resolved numerically, but the effect of the small eddies is modelled. The assumption is that the structure of the small eddies is to a large extent independent of the particular geometry at hand, and largely universal.

In the RaNS equations, all chaotic turbulent motions are captured by averaging the equations. Models are provided to account for the influence of the averaged turbulent fluctuations on the mean flow field. The RaNS equations are relatively efficient to solve, since the (small) time scale of turbulent fluctuations do not need to be resolved. As a result, solving the RaNS equations requires much less computational effort than the LES approach. The price that has to be paid for this speed up is that the mean flow field solutions are generally not as accurate as the solutions obtained with LES.

Modelling in RaNS is conducted in this thesis since the method is still the backbone for industry. Moreover, since RaNS models have received an enormous amount of attention, their strengths and limitations are well-known. But since RaNS has its counterpart in LES, a comparison will be made for selected simulations. Within the

DESIRE project, LES simulations on similar geometries and under similar conditions are performed by CERFACS and are calculated with their AVBP [27] code.

The application of RaNS to *unsteady* flows (in which the unsteadiness occurs at another time scale than the turbulent fluctuations) is called a Very Large Eddy Simulation (VLES) and is based on the Unsteady RaNS (URaNS) equations. Some conditions must be satisfied to allow the application of these equations. The URaNS equations will be solved in the unsteady simulations performed in chapter 4 to obtain the flame transfer function.

This chapter starts with a brief description of the RaNS and URaNS equations that are solved in the numerical fluid flow problem. This includes a discussion on combustion modelling, necessary for the reacting flow simulations.

In the remainder of the chapter, the designed generic burner will be presented, accompanied with isothermal and hot flow results, both validated by measurements.

3.2 Basic RaNS equations

The RaNS equations are obtained from the Navier-Stokes (NS) equations by averaging them over time. To avoid products of density fluctuations and fluctuations of other quantities (which cannot be averaged out of the equations) a density-weighted average or so-called 'Favre average' is taken instead of the regular, non-density weighted Reynolds average. The Favre average of a quantity $A(\mathbf{x},t)$ is defined as [186]:

$$\tilde{A} = \overline{\rho A}/\bar{\rho} \tag{3.3}$$

where $\bar{\rho}$ is the Reynolds average of ρ, defined as:

$$\bar{\rho}(\mathbf{x},t) = \frac{1}{T}\int_{-T/2}^{T/2} \rho(\mathbf{x},t+\tau)\mathrm{d}\tau \tag{3.4}$$

in which T is much larger than the characteristic turbulence time scale. The fluctuation corresponding with the Favre average is:

$$A'' = A - \tilde{A} \tag{3.5}$$

Note that $\overline{\rho A''} = 0$.

The three-dimensional, unsteady, adiabatic, compressible RaNS equations, used to describe gas-phase reactive flows can be written as:

$$\frac{\partial \bar{\rho}}{\partial t} + \nabla\cdot(\bar{\rho}\tilde{\mathbf{u}}) = 0 \tag{3.6}$$

$$\frac{\partial \bar{\rho}\tilde{\mathbf{u}}}{\partial t} + \nabla\cdot(\bar{\rho}\tilde{\mathbf{u}}\otimes\tilde{\mathbf{u}}^T) = \nabla\cdot\left(\sigma - \bar{\rho}\overline{\mathbf{u}''\mathbf{u}''}\right) \tag{3.7}$$

$$\frac{\partial \bar{\rho}\tilde{h}_{tot}}{\partial t} + \nabla\cdot(\bar{\rho}\tilde{\mathbf{u}}\tilde{h}_{tot}) = \nabla\cdot\left(\kappa\nabla\tilde{h}_{tot} - \bar{\rho}\overline{h''_{tot}\mathbf{u}''}\right) + (\sigma - \bar{\rho}\overline{\mathbf{u}''\mathbf{u}''}) : \nabla\tilde{\mathbf{u}} \tag{3.8}$$

In these equations, the conserved variables are $\bar{\rho}$, $\bar{\rho}\tilde{\mathbf{u}}$ and $\bar{\rho}\tilde{h}_{tot}$ as opposed to the primitive (independent) variables $\bar{\rho}$, $\tilde{\mathbf{u}}$ and $\tilde{h}_{tot}$. The effect of radiation is neglected

in the equation for the total enthalpy $\tilde{h}_{tot}$. Using Stokes' law, the viscous stress tensor σ can be written as:

$$\sigma = 2\mu\dot{\mathbf{D}} - \frac{2}{3}\mu(\nabla \cdot \tilde{\mathbf{u}})\mathbf{I} - \tilde{p}\mathbf{I} \tag{3.9}$$

where $\dot{\mathbf{D}} = \frac{1}{2}\left[(\nabla\tilde{\mathbf{u}})^T + \nabla\tilde{\mathbf{u}}\right]$ is the rate of strain tensor.

In equation 3.8 the thermal diffusivity κ can be written as the ratio between the thermal conductivity λ and the mixture's mass fraction weighted specific heat capacity at constant pressure c_p according to $\kappa = \lambda/c_p$.

In the set of equations 3.6-3.8 the Favre averaging procedure introduces products between fluctuating quantities. The term $-\bar{\rho}\widetilde{\mathbf{u}''\mathbf{u}''}$ is the turbulent momentum flux (usually called the *Reynolds stress*), and causes additional momentum transfer due to turbulent fluctuations*. At high Reynolds numbers and remote from walls, this term is often much larger than the viscous stress tensor [135]. Additionally, the turbulent convective heat flux $-\bar{\rho}\widetilde{h''_{tot}\mathbf{u}''}$ shows up in the Favre averaged version of the enthalpy equation.

With the additional turbulent fluxes, more unknowns than equations are encountered. This problem is often referred to as the *closure problem* and can be overcome by incorporating a turbulence model which provides expressions for the products of the fluctuations in terms of mean quantities. Turbulence models often contain empirical constants which are determined from experimental and DNS data.

The most popular turbulence models are the eddy-viscosity models, which give an analogy between the turbulent and viscous diffusion (*eddy-viscosity hypothesis*, introduced by Boussinesq in 1877) and model the effects of turbulence by introducing the turbulence viscosity and diffusivity coefficients μ_t and κ_t, respectively:

$$-\bar{\rho}\widetilde{\mathbf{u}''\mathbf{u}''} = 2\mu_t\dot{\mathbf{D}} - \frac{2}{3}\left(\mu_t(\nabla \cdot \tilde{\mathbf{u}})\mathbf{I} + \rho\tilde{k}\mathbf{I}\right) \tag{3.10}$$

$$-\bar{\rho}\widetilde{h''_{tot}\mathbf{u}''} = \kappa_t\nabla\tilde{h}_{tot} \tag{3.11}$$

where k stands for the turbulence kinetic energy.

Multiple models exists for obtaining the turbulence coefficients μ_t and κ_t. The most widely used two-equation eddy-viscosity model is the k-ϵ turbulence model. In this model, two additional transport equations are solved for the turbulence kinetic energy k and the turbulence eddy dissipation ϵ in the numerical simulation. Subsequently, the diffusivities can be obtained from:

$$\mu_t = C_\mu\bar{\rho}\frac{\tilde{k}^2}{\tilde{\epsilon}} \tag{3.12}$$

$$\kappa_t = \frac{\mu_t}{\mathrm{Pr}_t} \tag{3.13}$$

where C_μ is an empirical constant, listed in table 3.1. Moreover, Pr_t stands for the turbulent Prandtl number. The turbulent Prandtl number represents the ratio between the turbulence momentum and turbulence thermal diffusivity. In turbulent

*The viscous stress ultimately stems from momentum transfer (diffusion) due to fluctuations at a molecular level. So also the Reynolds stress stems from momentum transfer by a fluctuating velocity field.

flows, this ratio tends to a constant value close to unity, i.e. velocity and thermal boundary layers have about the same thicknesses. The departures from unity are not great, even for large variations in the Reynolds number, different types of flows and variations in the surface roughness [84]. A value of 0.9 is used here for the turbulent Prandtl number. Table 3.1 also includes coefficients that show up in the transport equations for k and ϵ, which are not shown here. The purpose of showing the coefficients is that several modifications to the standard k-ϵ turbulence model (due to Launder and Sharma [102]) exist, each having different coefficients. The coefficients shown in the table are used in the simulations discussed in this thesis.

$C_{\epsilon 1}$	$C_{\epsilon 2}$	C_μ	σ_k	σ_ϵ	Pr_t	Sc_t
1.44	1.92	0.09	1.0	1.3	0.9	0.9

Table 3.1: Constants of the standard k-ϵ turbulence model [102].

The set of equations is closed by the equation of state and a constitutive equation, both valid for ideal gases:

$$\tilde{p} = \bar{\rho} R \tilde{T} \tag{3.14}$$

$$\tilde{h}_{tot} = \int_{T_{ref}}^{\tilde{T}} c_p(T) \mathrm{d}T + \frac{1}{2}\tilde{\mathbf{u}}^2 + \tilde{k} + \sum_{i=1}^{n} \tilde{y}_i h_i^0 \tag{3.15}$$

where h_i^0 is the enthalpy of formation of species i at temperature T_{ref}.

The total set of equations discussed in this section is solved using the commercial code CFX. Version 5.6 was used for all the simulations presented in this thesis. CFX is a general purpose CFD code, which can handle unstructured staggered grids and solves the compressible equations using a Finite Volume approach with co-located variables [160]. The term 'co-located' means that the variable values are stored at the nodes.

It is well-known that integrating the k-ϵ model through the near-wall region and applying the no-slip condition yields unsatisfactory results [86]. To correct this, a wall-function approach (sometimes referred to as the 'law-of-the-wall' approach) is used in which the near-wall region is explicitly modelled using the standard scalable wall functions of CFX. The scalable wall functions are less sensitive to the grid-spacing at the wall than standard wall functions.

3.3 Combustion modelling

Combustion problems typically involve additional transport equations for scalar variables such as species mass fractions. As a result of the additional computational costs of incorporating the effects of combustion in CFD simulations, most models of turbulent combustion for industrial applications are averaged in a manner similar to the Favre averaging [23]. Overviews of combustion models that are currently used can be found in [135, 182].

In this thesis, chemical reaction is modelled with a single-step overall reaction mechanism, valid for lean to stoichiometric combustion of methane-air mixtures. For

laminar combustion, it has been shown that the single-step mechanism is well suited to model the response of lean methane/air flames at low frequency distortions [158].

The single-step mechanism uses the local mean quantities to calculate a reaction rate from an effective Arrhenius law. This Arrhenius model is combined with an eddy dissipation model, which assumes that the reaction rate is limited by mixing. With the eddy dissipation model, the reaction rate is directly related to the turbulence quantities. Depending on the local Damköhler number the eddy dissipation model ($\mathrm{Da} > 1$) or the Arrhenius model ($\mathrm{Da} < 1$) is used. Later in this chapter a combustion simulation with the described combustion model will be characterised in the Borghi diagram.

The relatively simple combustion model was chosen on purpose since the focus of this thesis is on smart methods to obtain flame transfer functions from CFD simulations. Replacing the combustion model by a more advanced one (e.g. [41]) can influence the results, but does not influence the method. In chapter 7 it will be shown how large this effect actually is. Moreover, a validation of the results obtained with the combustion model will be done in the current chapter, therewith revealing possible shortcomings of the model.

The one-step combustion model requires additional transport equations to be solved for each particular species in the one-step reaction. The Favre averaged transport equation for the mass fraction of species y_i can be written as:

$$\frac{\partial \bar{\rho}\tilde{y}_i}{\partial t} + \nabla \cdot \left(\bar{\rho}\tilde{\mathbf{u}}\tilde{y}_i - (\bar{\rho}D_i + \frac{\mu_t}{\mathrm{Sc}_t})\nabla \tilde{y}_i \right) = \bar{\omega}_i \tag{3.16}$$

The diffusion coefficient D_i is based on Fick's diffusion law, which describes the diffusion of the species i into another species j. This law is valid if the mixture is binary, thermal diffusion is negligible, body forces are identical for species i and j and if the molecular masses of both species are the same, or the pressure is constant [187]. A simplification is made to Fick's law by assuming an effective diffusion coefficient D_i of species i into the bulk species. The effect of making this assumption is small as a major part of the mixture consists of nitrogen.

From equation 3.16, it can be seen that the influence of the turbulent fluctuations is already accounted for by the term $\frac{\mu_t}{\mathrm{Sc}_t}$. In this term, Sc_t is the turbulent Schmidt number, which represents the ratio of momentum to species diffusivity. Note that the Schmidt number is expected to be identical to the Prandtl number (i.e. $\mathrm{Sc}_t = 0.9$, see table 3.1). When different turbulent Prandtl and Schmidt numbers would be used, the transport of bulk enthalpy would become inconsistent to the transport of enthalpy inherent with the components. This would contradict the assumption that the total enthalpy of the mixture is the average of the components enthalpies weighed by mass fractions (see equation 3.15). As a consequence, this may lead to an unphysical temperature distribution in the solution.

3.4 Unsteady RaNS

In the transient simulations the turbulent flow is modelled by the Unsteady Reynolds averaged Navier-Stokes (URaNS) equations. These equations can be derived by de-

composing the variables into a Favre mean value $\tilde{A}$, a *turbulent* fluctuation A'' and a *periodic* fluctuation A^p as:

$$A = \tilde{A} + A'' + A^p \tag{3.17}$$

In the URaNS approach, it is assumed that the turbulent fluctuations occur at a much smaller time scale than the periodic fluctuations (see figure 3.2), i.e. the characteristic frequency at which the turbulent fluctuations occur is much higher than the frequency of the periodic fluctuation (see for example [174]). Thus, the large-scale organised unsteady motions are resolved by the numerical scheme, and the chaotic turbulent motions are captured by the RaNS equations.

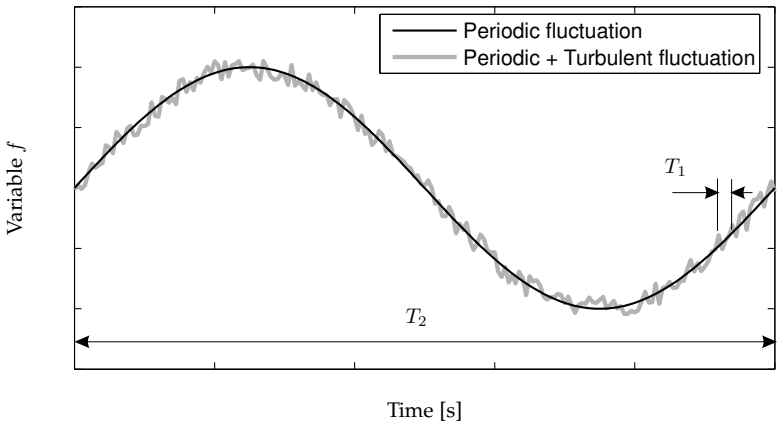

Figure 3.2: Time scales in URaNS simulation.

When this requirement is met, the turbulence structure is unaffected by the unsteadiness, and equation 3.17 can be rewritten as:

$$A = \tilde{A} + A'' \tag{3.18}$$

in which the Favre mean $\tilde{A}$ is defined as:

$$\tilde{A}(t, \mathbf{x}) = \frac{1}{\bar{\rho} T} \int_{-T/2}^{T/2} \rho A(t + \tau, \mathbf{x}) \mathrm{d}\tau \tag{3.19}$$

where T is a time scale which is much larger than the characteristic time scale of the turbulent fluctuations T_1, but much shorter than the time scale of the periodic fluctuations T_2, so that the periodic fluctuations do not influence the turbulent fluctuations, i.e.:

$$T_1 \ll T \ll T_2 \tag{3.20}$$

Such a choice for T is often possible, because in a very turbulent flow (Re large) the time scale of the turbulent fluctuations is often very small compared to the time scale of the other periodic features of the flow.

When an appropriate time scale T can be chosen, equation 3.18 can be used to derive the RaNS equations, keeping in mind that the time averages are determined at time scale T. This way, the original RaNS equations can still be used in the URaNS simulations.

3.4.1 Error analysis

In the transient simulations, an implicit second order time discretisation is used to march through time (see appendix C). Errors due to the discrete approximation are produced by truncation errors in the time discretisation. The often used second order time discretisation scheme has a *truncation error* of the discrete approximation that decreases quadratically with the time step Δt. In practice, an approximate solution by direct-time integration produces an amplitude and phase error, as illustrated in figure 3.3.

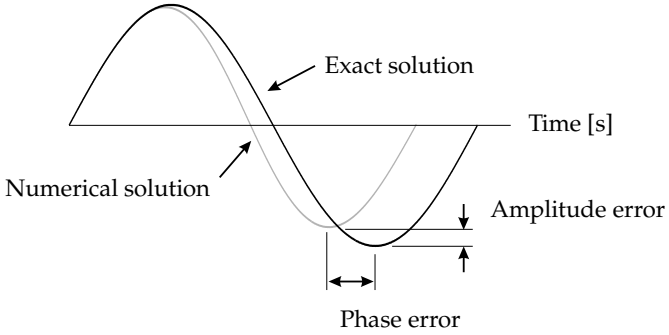

Figure 3.3: Possible amplitude and period errors in the numerical simulation.

The truncation error will be derived as a function of the number of time steps per period. This can be used to determine the time step size in unsteady transient simulations. The derived expression will be validated in the next section, where acoustic wave propagation in a duct will be evaluated at different time step sizes.

The truncation error of the implicit second Euler discretisation (see equation C.10) can be calculated using the Taylor series expansion of the discrete approximation. The Taylor series of a variable ψ reveals the largest truncation error, which is $\mathcal{O}(\Delta t^2)$ and can be written as:

$$\varepsilon_1 = \frac{\Delta t^2}{3}\frac{\partial^3 \psi}{\partial t^3} + \mathcal{O}(\Delta t^3) \tag{3.21}$$

Neglecting the third and higher order terms, and using a sinusoidal fluctuation, the maximum absolute truncation error can be written as:

$$\varepsilon_1 = \frac{8\pi^3 f}{3N^2} \tag{3.22}$$

where f and N are the frequency and the number of time steps per period, respectively. Equation 3.22 describes the error in the time derivative of the variable ψ.

Referencing the error by the exact derivative of ψ yields:

$$\varepsilon_{1,rel} = \frac{\varepsilon_1}{2\pi f} = \frac{4\pi^2}{3N^2} \tag{3.23}$$

The absolute relative error in the instantaneous value of ψ can be obtained by multiplying the second-order term with Δt to convert the error in the derivative by an error estimate in the instantaneous value. Subsequently, the error is referenced to the amplitude of the sinus, yielding a relative error of:

$$\varepsilon_{2,rel} = \frac{8\pi^3}{3N^3} \tag{3.24}$$

The derived expressions for the relative errors are plotted as a function of the number of time steps per period (see figure 3.4). Taking 1% as a measure for an accurate simulation, this simulation would require over 40 time steps per period. In the next section, this value will be applied to a simple test case.

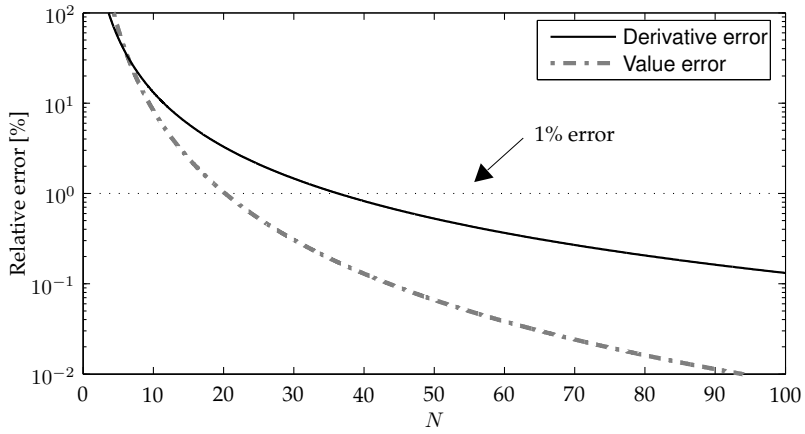

Figure 3.4: Truncation errors as a function of N, the number of time steps per period.

3.4.2 Acoustics

RaNS codes are designed to solve the total quantities, which implies that the small perturbations are subjected to a relatively high numerical damping. Nevertheless, several authors show that small perturbations can be solved in RaNS, however many time steps per period must be used to decrease the effect of numerical damping to an acceptable level [34,68]. Polifke *et al.* [136] use a time-dependent one-dimensional RaNS simulation to show that it is possible to obtain information on the acoustic behaviour of a heat source with a time delay placed in a low Mach number flow. The minimum number of time steps per period in that study is 50. With this number

of time steps, the thermo-acoustic properties of the test system could be satisfactory reconstructed.

In a recent study, Chatterjee *et al.* [28] successfully predict instability growth and the limit-cycle oscillation in a Rijke tube. The measured instability frequencies and its harmonics are captured well by the RaNS simulations they performed. A minimum of 40 time steps per period are used.

In this section, the acoustic wave propagation in a tube is studied with unsteady RaNS simulations. By comparing results obtained with different time step sizes, an idea of the accuracy of the unsteady numerical simulation is obtained. In unsteady simulations there are two options to determine the time step size. First, the Courant-Freidricks-Levy (CFL) number can be used, defined as:

$$\mathrm{CFL} = (u_0 + c_0)\frac{\Delta t}{\Delta x} \tag{3.25}$$

The CFL number is a measure, in characteristic grid spacings Δx, of how far a disturbance can travel through the flow in a single time step. It is mainly a measure for the expected numerical stability of the problem, since many computational fluid dynamics methods do not perform well when the CFL number increases to and above 1; however, implicit time discretisations do allow CFL values well above 1, although the accuracy of the discrete schemes diminishes. Equation 3.25 shows that for low Mach number flows, disturbances which are transported with the convection speed u_0 instead of with the speed of sound c_0 need less time steps to yield the same CFL number. A second method to estimate the time step size is by considering the error as a function of the number of time steps per wavelength or period (obviously, both yield the same result).

To show the ability of the URaNS method to correctly solve sound propagation, a one-dimensional acoustic field in a flow duct has been considered. The flow duct is a cylindrical duct with a diameter of $D = 5$ cm and a length of $L = 25$ cm. Air at standard conditions (see Nomenclature on page 187) is flowing through the duct. At one side of the duct, the velocity is imposed. The outflow of the duct is marked by a pressure boundary condition $p' = 0^*$. Figure 3.5 depicts the cylindrical tube and the applied boundary conditions.

Two cases are considered: without and with a (highly turbulent, $\mathrm{Re} \approx 2.4 \cdot 10^5$) flow. For the case with flow, an inlet velocity of $\mathrm{Ma} = 0.2$ ($u_1 \approx 68.6\ \mathrm{m\,s^{-1}}$) is imposed. A turbulent damping effect and an additional Doppler frequency-shift can be expected due to the imposed mean flow.

At the inlet (location 1 in figure 3.5), an impulse fluctuation in the pressure is imposed (more detailed information on impulse excitation can be found in chapter 4). By applying this excitation here, all modes are excited (the modes never have a pressure node at the location where the velocity is imposed). The response is monitored at $2/3^{\mathrm{rd}}$ of the length (location m).

The numerical model contains 9,801 (unstructured) elements (5,033 nodes), with a characteristic length scale of 5 mm, corresponding to 3% of the smallest considered wavelength (i.e. at 2000 Hz). The numerical simulations are performed using two

*By applying an acoustic impedance matrix to the boundary of the CFD simulation, any desired acoustic boundary condition can be realised [162].

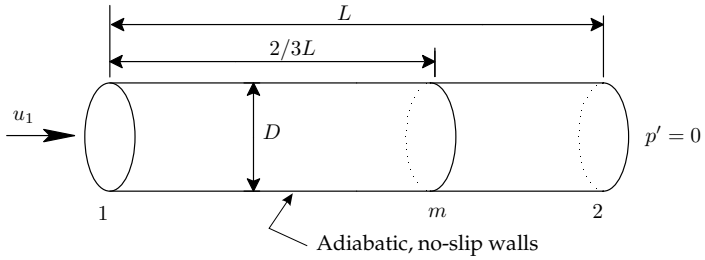

Figure 3.5: Geometry and boundary conditions for testing the ability of CFX to describe acoustic wave propagation.

different values for the time step Δt: $5 \cdot 10^{-5}$ s and $2 \cdot 10^{-5}$ s, corresponding to a minimum of 10 and 25 time steps per period, respectively. Using the definition of the CFL number (equation 3.25) and the characteristic length scale of the mesh, the time steps yield a maximum CFL number of 4.1 (for the flow case and with the largest time step). Even in the non-flow case and with the smallest time step, the CFL number is still larger than one. However, as mentioned earlier, the implicit time discretisation scheme allows this.

The transfer function $H = \frac{p_m}{p_1}$ obtained from CFX is compared with the transfer function obtained from the one-dimensional network model discussed in chapter 2 (including turbulent damping and flow effects). The frequency range below 2000 Hz is considered. The transfer functions are displayed in figure 3.6 (no flow) and 3.7 (flow) for two different time steps. The noise that is seen in the CFX results is caused by the low damping in the system in combination with the available computational resources. After applying an impulse to the system, oscillations remain present in

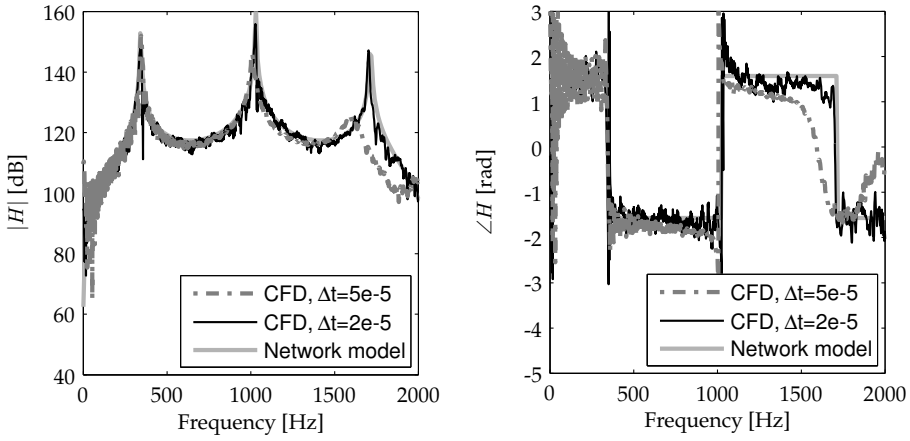

(a) Amplitude (b) Phase

Figure 3.6: Transfer function $H = \frac{p_m}{p_1}$ in system *without* flow.

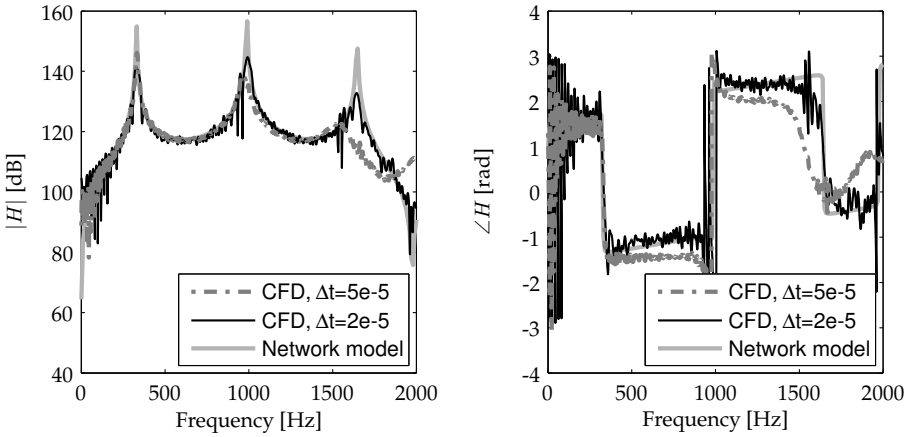

(a) Amplitude (b) Phase

Figure 3.7: Transfer function $H = \frac{p_m}{p_1}$ in system *with* flow.

the system. Especially in the non-flow case, where there is very little damping, the simulation has to run for a very long time to let all the oscillations damp out. Due to the large computational effort it would require to let the system damp out completely, this was not done: when a system is not fully damped out this shows up as noise in the spectrum of the transfer function.

From figure 3.6 and 3.7 it is clear that the numerical simulation with the smaller time step approaches the network model also at higher frequencies. Both flow and non-flow cases give good results when the number of time steps per period is larger than 40. Note that in the flow case, additional damping and a frequency-shift in the eigenfrequencies is seen (compare the eigenfrequencies in figure 3.6 and 3.7).

In the previous section, the truncation error was used to make an estimate for the minimum number of time steps per period. Using a maximum error of 1%, 40 time steps per period should be used. This value compares well with the empirically determined value and can be used as a guideline for the transient numerical simulations to be performed in this thesis.

3.5 Burner design

In the previous sections the models used in the numerical approach have been presented. These models are now applied to obtain flow field solutions for the geometry corresponding to a 100 kW/bar experimental setup that has been built in the framework of the DESIRE project. A description of this experimental setup is included in chapter 6.

The numerical simulations presented in the current chapter require the knowledge of the generic burner used in the experimental setup, as well as the operating points at which the setup is operated. Therefore, this section is dedicated to a de-

scription of the design considerations of the generic burner, as well as the presentation of the final design. Moreover, a list of the operating points is included. These operating points determine the boundary conditions of the numerical simulations, which are presented later in this chapter.

3.5.1 Burner

In figure 3.8 a cross-sectional view of the burner and the supply system of fuel and air is depicted. The burner is designed to operate under lean conditions at a nominal power of 100 kW/bar, burning Dutch natural gas.

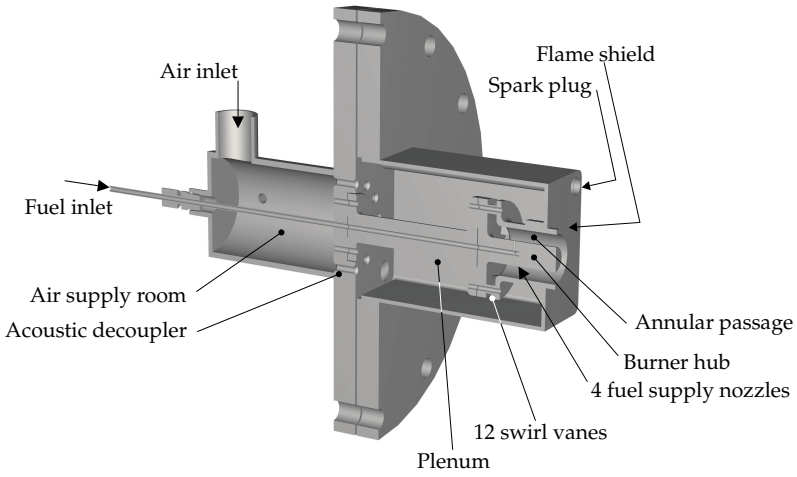

Figure 3.8: Cross-sectional view of the generic burner and the fuel and air supply system.

The burner is supplied with air from a plenum. The plenum is separated from the hot gasses in the combustion chamber by a flame shield. The 'cold' air in the plenum cools the flame shield. The burner ends 10 mm from the flame shield inside the combustion chamber. This distance is chosen to allow the laser measurements to start at the burner exit, not hindered by the flame shield. The combustible mixture is ignited with a spark plug, located in the corner of the combustion chamber.

The burner is connected to the burner flange by a tube, which is part of the fuel supply tube. In the burner flange, holes are drilled through which the air enters the plenum. The air velocity in these holes is preferably high, since this provides a more or less axisymmetrical air distribution due to the pressure drop and also acts as an acoustic decoupler (due to the high velocities and large area contraction).

The 12 holes in the burner flange connect the plenum to the air supply room. Air is supplied sideways by a 50 mm diameter pipe. Placing the air supply tube concentrically with the fuel tube was no option, due to additional difficulties to extract the fuel tube from the air tube. CFD simulations and water tunnel measurements showed that due to the large pressure drop over the acoustic decoupler, supplying the air sideways does not affect the axisymmetry at the burner exit.

The burner is of the radial swirler type. This type of swirler appears to be over two times more efficient* than an axial swirler (when the swirl number $S_n \approx 1$, see [8]). The radial swirler consists of a radial inlet with radial swirlers that swirl the air into an annular passage. Assuming a plug flow through the annular passage, the mean velocity at nominal conditions is 64 m/s ($\mathrm{Ma} = 0.13$ and $\mathrm{Re} \approx 6.3 \cdot 10^4$). This velocity is low enough not to cause large pressure drops, and high enough for intense turbulence (and therefore good mixing).

By using a burner hub the axisymmetry of the flow is preserved. Hubless swirlers have been used in an attempt to improve outlet conditions, but separation and blade stall give complex, non-axisymmetric flow patterns [62]. The edges inside the burner are chamfered to prevent vortex sound production.

Swirl considerably increases the stability limits of most flames [168]. A representation of the flow field arising from a swirling inlet flow is shown in figure 3.9. When the reactants are ignited once, they return to the burner exit via the recirculation zones. Here, they ignite the fresh incoming reactants. The central recirculation zone is of most interest to the combustion process, as the outer recirculation zone is less efficient for flame stabilisation because of high rates of heat transfer to the walls.

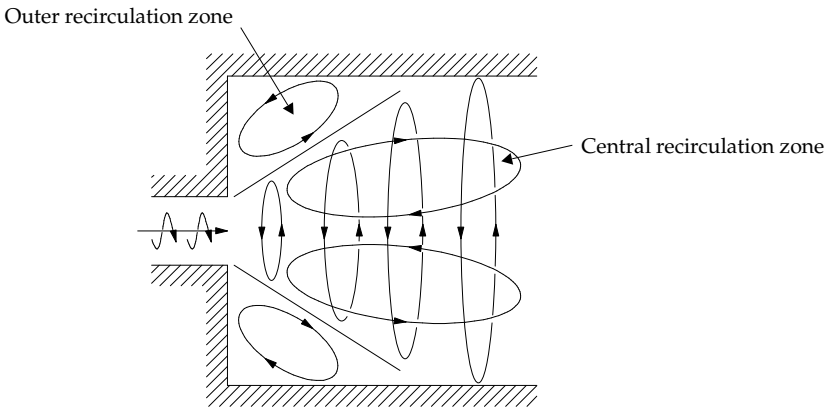

Figure 3.9: Flow field induced by a strongly swirling inlet flow (swirl number $S_n > 0.6$ [62]), resulting in significant lateral and longitudinal pressure gradients, a much wider, slower jet than its non-swirling counterpart and a central toroidal recirculation zone.

The ratio between the diameters of the burner hub ($D_h = 25$ mm) and the annular passage ($D_e = 50$ mm) is $D_e/D_h = 2$ (see dimensions in figure 3.10). By choosing an appropriate D_e/D_h ratio an extension of the central recirculation zone to the burner itself can be prevented: a too large annular passage results in low axial velocities and flow separation at the burner hub, providing little resistance against the incoming recirculating hot flue gasses. Burner hub overheating or flash-back can be the consequence of this. The Strscheletzky criterion is a commonly used criteria for flow

*The efficiency of swirl generation is defined as the ratio of the flux of kinetic energy of the swirling flow to the drop of total pressure over the burner.

separation on the hub in passages with swirling flow [50] and has been used here to determine an appropriate D_e/D_h ratio.

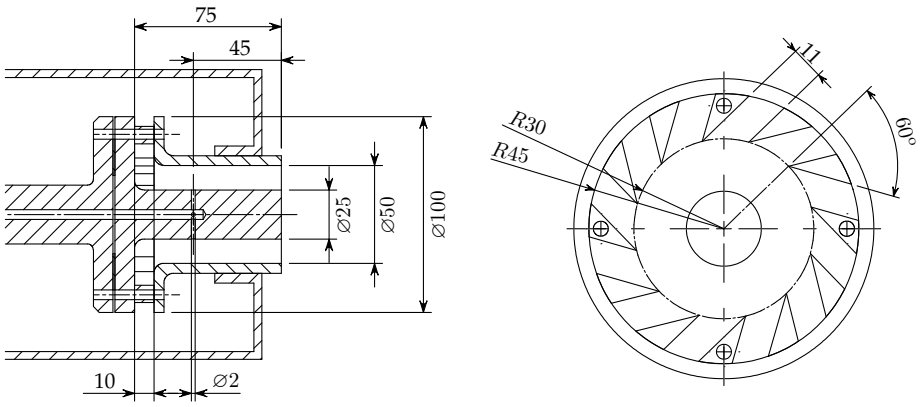

Figure 3.10: Dimensions of the burner and the radial swirler (in mm).

The 12 vanes have a swirl angle of 60 degrees (see figure 3.10). The swirl angle is determined such that a strong swirling flow is induced (i.e. $S_n > 0.6$). To have a constant, non-accelerating flow through the swirler vanes, the distance between two vanes is kept constant. Furthermore, the swirler vanes are flat (non-curved) to ease their manufacturing and the numerical modelling of the burner. Moreover, for the swirl number (see appendix D) produced by this burner the efficiency of swirl generation is still acceptable when using straight vanes [62]. For higher swirl numbers, curved vanes should be used to prevent the dramatic decrease of the efficiency of straight vanes in this region.

Based on CFD calculations, 4 fuel inlets, equally distributed along the circumference of the burner core, have been used to inject fuel. The maximum penetration Y_{max} of a round jet (diameter d_j) perpendicular to a flow through a circular tube can be approximated with [106]:

$$Y_{max} = 1.15 d_j \sqrt{J} \tag{3.26}$$

in which J is the ratio of the momentum of the jet and the main flow. With 4 fuel jets and taking a penetration depth of half the height of the annular channel, each fuel inlet should have a diameter of 2 mm (fuel exit velocity ≈ 250 m/s which corresponds to $\mathrm{Ma} = 0.58$, based on the speed of sound in natural gas). In section 3.7.2 it will be shown that this diameter results in sufficient mixing of the fuel and air flow at the burner exit. The fuel inlet holes are located at 45 mm from the burner exit, as a compromise between sufficient mixing and convenient modelling.

The burner presented in this section is the result of an extensive CFD design study. In this study, variations in the geometry and swirl angle have been analysed. Apart from these geometrical variations, various dimensional variations have been considered as well.

A disadvantage of using a burner hub is that the central recirculation zone can attach to the hub. This might cause problems of overheating the hub, since the central

recirculation zone carries hot combustion products. Usually, a pilot burner or some additional air flow is provided through the central hub to prevent attachment of the central recirculation zone. However, in order to have a burner that is convenient to model it was decided to omit such a solution here. It is expected that the high speed flow around the hub (air that flows through the annular passage) provides enough cooling to prevent the hub from overheating. Moreover, it appeared to be very difficult to find a geometry for which the central recirculation zone is detached from the hub. In figure 3.11 a geometry is depicted for which no back flow onto the hub occurs. However, a detached recirculation zone only appears under very specific flow conditions. Moreover, the flow field induced by the burner is far less stable than the chosen burner.

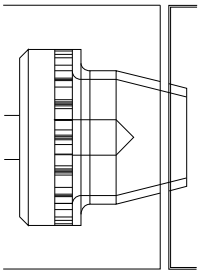

Figure 3.11: Burner geometry that showed no attached central recirculation zone.

With the current burner geometry, the central recirculation zone is firmly attached to the hub. This would be better than when it would only be loosely attached to it, since transient behaviour can show up due to arbitrary attachment and detachment of the recirculation zone to the burner hub.

3.5.2 Operating points

In table 3.2 a list of operating points of the experimental setup is presented. At the operating points, numerical simulations and measurements are performed. An operating point is fully defined with the air factor, power, preheating temperature and combustor pressure.

At some operating points only *adiabatic* numerical simulations (and consequently no experiments) are possible. These points are used to gain insight from the numerical simulations. The adiabatic flame temperatures listed in this table are determined with the 'equil' software of CHEMKIN. Each operating point has been given a reference-code to make it convenient to reference it in the text. The prefix 'cold' in the reference-code means that this it is an isothermal situation, i.e. without combustion. The power and the air factor given in this cold case fixes the air mass flow. Because the cold case is isothermal, no fuel is injected here.

Reference code	Power [kW]	Abs. pres. [bar]	Air factor [-]	Air preh. temp. [°C]	Ad. flame temp. [°C]
10.5	100	1.1	1.6	300	1638
15.1	150	1.5	2.1	300	1387
15.2	150	1.5	1.8	100	1388
15.4	150	1.5	1.8	300	1513
15.7	125	1.5	1.8	300	1513
20.4	200	2.0	1.8	300	1514
30.7	250	3.0	1.8	300	1514
cold 10.1	100	1.0	1.8	20	-

Table 3.2: Operating points at which numerical and/or experiments are performed.

3.6 Simplified geometries for CFD

The performed CFD simulations consist of isothermal flow simulations and reacting flow simulations. The latter can be further categorised in perfectly premixed (PP) simulations, in which fuel and air are perfectly premixed at the inlet of the combustion chamber, and imperfectly premixed (IP) simulations, where the fuel supply nozzles are included and the local fuel and air mixture is determined by turbulent mixing. To reduce the computational effort of the simulations, only the part of the geometry that is relevant for the simulation under consideration is included in the analysis. The boundary conditions of this part of the geometry are transferred from CFD simulations performed on a larger part of the geometry. Using this approach, three simplified geometries can be distinguished, indicated as Model 1 to 3. In this section, the geometry and the equations solved for each model are discussed.

Figure 3.12 shows the geometry of the Model 1, as well as the main dimensions of the combustion chamber. It is based on the geometry of the experimental setup presented in chapter 6 and is used to obtain an isothermal flow solution. Moreover, the boundary conditions for Models 2 and 3 are extracted from Model 1. Since the isothermal flow solution is required, only the 4 hydrodynamical equations and the 2 turbulence equations need to be solved in this model. In figure 3.12 it is noticed that the air supply room is omitted in Model 1. Hence the inlet of the simulated geometry is located just downstream of the acoustic decoupler. At this inlet, an uniformly distributed velocity field is imposed, together with high intensity turbulent fluctu-

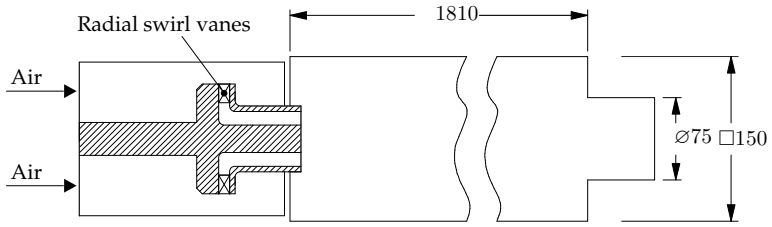

Figure 3.12: Geometry used in Model 1. Dimensions are in mm.

ations (10% of the mean values). With the length scale at the inlet this turbulence intensity is used to calculate k and ϵ. Simulations have shown that using this boundary condition instead of including the air supply room and the acoustic decoupler hardly influences the flow field downstream the burner. This lack of influence can be explained by the large pressure drop induced by the acoustic decoupler.

Model 1 includes the full plenum room, the burner and the combustion chamber with a contraction at the end of the chamber. This contraction functions as acoustic decoupler. Like the acoustic decoupler upstream of the plenum, it provides a static pressure drop at which acoustic waves are reflected (echoic end condition). Moreover, it gives a well defined boundary condition for the CFD simulations, and it separates the combustion chamber from the water cooler, downstream of the contraction. Model 1 does not include the fuel injection nozzles, as it only serves for isothermal flow simulations. To reduce the calculation time of the CFD simulations, only a quarter of the cross-sectional area is modelled. The effect of the remainder is accounted for by imposing periodic boundaries at the radial planes. This assumption is not only made for Model 1, but also for Model 2 and 3.

In the slightly reduced Model 2 (see figure 3.13) the plenum and the swirlers are omitted. This model is used for simulating the mixing between fuel and air, and for reacting flow simulations of the imperfectly premixed simulations. For this purpose, the fuel injectors are included in Model 2, which requires a high resolution mesh nearby the injectors. Model 2 starts just upstream of these injectors, 55 mm upstream of the burner exit. The boundary conditions (turbulence quantities, velocities etc.) at this inlet are obtained from simulations with Model 1. Since additional transport equations for the species mass fractions and the enthalpy need to be solved, a total of 11 equations is solved in Model 2.

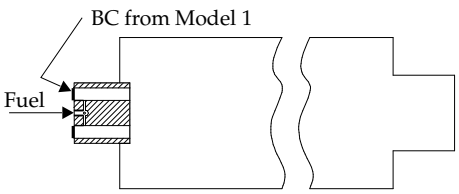

Figure 3.13: Geometry used in Model 2.

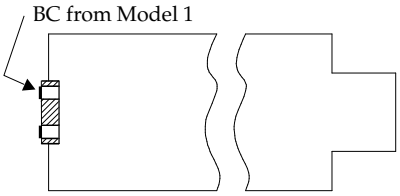

Figure 3.14: Geometry used in Model 3.

Finally, Model 3 represents the most reduced model (see figure 3.14). It starts downstream the fuel injectors, 15 mm upstream of the burner exit. Hence, the high resolution mesh near the fuel injection holes is excluded. The inlet boundary conditions for Model 3 come again from Model 1. Since the fuel injectors are not included in Model 1, Model 3 can only be used for reacting flow simulations of the perfectly premixed mixture.

A summary of the relationship between the three models is shown in table 3.3. In this table, the number of elements and nodes is listed as well. It can be seen that Model 3, in which both the swirlers and the fuel injectors are excluded, has the least number of elements, and therefore requires the least computational effort to solve.

The amounts of elements listed in table 3.3 are chosen from a grid-size depen-

Model	Nodes	Elements	No. of eqns	BC from...	Purpose
1	583,135	2,291,423	6	Op. point sheet	Isothermal sims
2	566,247	3,046,958	11	Model 1	Mixing and imperfectly premixed sims.
3	111,559	527,018	11	Model 1	Perfectly premixed sims

Table 3.3: Number of nodes and elements used in the three models.

dence study performed on the models (see appendix E). The elements are mostly concentrated in the flame zone, at the end of the recirculation zone and (if applicable) around the fuel injectors. Furthermore, inflated boundaries are used to provide an accurate wall boundary condition. Model 2 shows to have more elements (however, less nodes) than Model 1, which is a consequence of the inclusion of the fuel injection nozzles in Model 2.

The main parameter that is monitored in the grid-size dependence study is the stagnation point of the recirculation zone. This parameter is very sensitive to the chosen grid-size and therefore a good indicator of the grid dependency of the solution. Especially for Model 1 and 2, the size of the model limits the level of grid-independency of this stagnation point that could be reached. However, for Model 1, still satisfactory grid-independent solution are obtained at the locations where boundary conditions are transferred to Model 2 and 3.

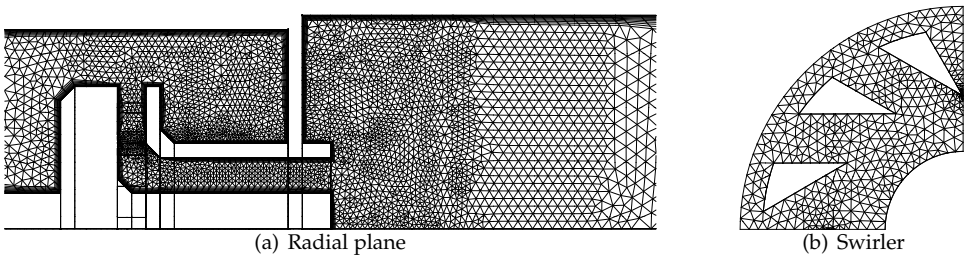

(a) Radial plane (b) Swirler

Figure 3.15: Mesh resolution of Model 1.

An example of the mesh of Model 1 in a radial plane and in the swirler is shown in figure 3.15. The figure demonstrates the advantage of using an unstructured grid: nodes can be concentrated relatively easy in regions with large gradients, while away from these regions the grid becomes quickly coarse again.

3.7 CFD simulations

In this section CFD simulations performed at the nominal operating condition of the burner are presented. Isothermal, mixing and reacting flow simulations are discussed. The isothermal flow simulations are validated with a water tunnel experiment. The reacting flow simulations are compared with the OH field measured in the experimental setup.

3.7.1 Isothermal flow simulations and water tunnel experiments

When modelling the combustion process using CFD, the first step is to accurately predict the isothermal flow properties, before adding the complexities of combustion. The geometry of Model 1 is used for the isothermal simulations. The operating condition corresponding to operating point 'cold 10.1' is used. The flow is steady-state, isothermal, three-dimensional, and turbulent. In agreement with Model 1, the inlet lies directly downstream the acoustic decoupler. At the outlet of the model, an outflow condition with a relative pressure of 0 Pa is imposed.

The numerically obtained velocity profiles are compared with measured profiles from a water tunnel experiment. The water tunnel layout and the basic idea behind the water tunnel measurements will be briefly discussed in the next section. A more extensive discussion of the measurements can be found in appendix F.

Water tunnel experiments

The water tunnel is a geometrically exact copy of the DESIRE test rig. By equating the Reynolds numbers in the water tunnel and the cold flow simulations, both flows behave similarly (the dimensionless equations describing the flow are the same for equal Reynolds numbers, see for example Pope [137]) and are comparable. Since the water tunnel is designed to be actual size, the diameters do not affect the Reynolds number. The kinematic viscosity of water is about $1/13^{\text{th}}$ that of air at room temperature, therefore the ratio of the velocity of water to air also has to be about $1/13^{\text{th}}$.

Since the water tunnel is made of perspex, Laser Doppler Velocimetry (LDV) measurements can be done to obtain the velocity profiles downstream of the burner exit. The measurement data from the LDV system is further processed with a DIFA spectral analyser installed on a PC, resulting in the mean velocities and the Reynolds stresses. More information on the LDV measurement can be found in appendix F.

Measurements are conducted in 9 planes downstream of the burner exit. In each plane, the mean velocities and Reynolds stresses are determined at 174 different locations (see figure 3.16). One half-quadrant is fully measured. Furthermore, the velocity profiles along the x and y axis are determined. These profiles are used for comparison with the isothermal flow simulations. Because one of LDV laser beams enters the water tunnel under a slight angle, there is a small 'dead' zone in which no measurements can be taken due to diffraction of the main beam.

Validation results

Since the measurement volume has the shape of a cylinder aligned with the optical axis (in the y-direction), the measurements are more accurate when the velocity gradients in y-direction are low. For the swirling flow field that is considered here, the profile for the axial velocities is more accurate when measured along the x-axis since the velocity gradients in the y-direction are relatively small.

To be able to compare the simulation results (using air as a medium) with the water tunnel results the mean velocities and the Reynolds stresses are scaled by the mean area velocity u_z^0 and by $k_{zz}^0 = (u_z^0)^2$, respectively [150]. In appendix F it is

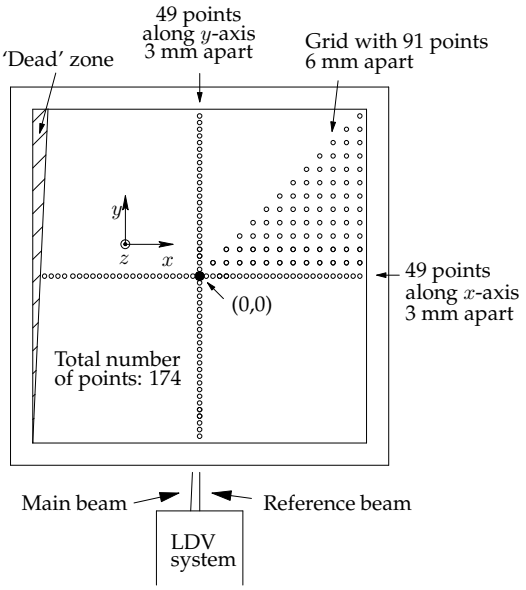

Figure 3.16: Grid layout of data points in a plane.

shown that the Reynolds number is high enough for the flow field to be Reynolds-independent, i.e. the flow profiles are self-similar. Therefore, for reasons of measurement accuracy, the water tunnel measurements are performed at a threefold lower Reynolds number than the CFD simulation. Still a comparison is possible when scaling the obtained mean velocities and Reynolds stresses by u_z^0 and by k_{zz}^0, respectively.

Figure 3.17 shows the mean dimensionless axial velocity (z-velocity) along the x-axis of 9 planes. As a result of the swirling flow, a central recirculation zone, necessary for flame stabilisation, is present. This circulation zone can be identified by the negative axial velocities at the axis. Both the measurements and the numerical results are shown the figure. Near the burner exit, the location of the maximum axial velocity and the radial size of the recirculation zone are predicted satisfactory. Further downstream, deviations between the model and the measurements become larger. It is seen that the spreading of the jet coming from the burner is over-predicted by the CFD model. The deviation between the measurements and the numerical results can be partially attributed to the isentropic nature of the used turbulence model. The k-ϵ model is often inadequate for strongly swirling flows [85] and detached flows.

The measured profiles show to be very symmetrical, although the water is supplied asymmetrically to the air supply room. The acoustic decoupler strongly decreases the asymmetry of the flow by providing a large pressure drop. The small asymmetry that can still be seen in figure 3.17 is partially caused by the experimental difficulty of producing a perfectly symmetric flow and partially by the limited resolution of the measurement points to correctly resolve the peaks in the velocity, especially in the plane closest to the burner, where the velocity gradients are high.

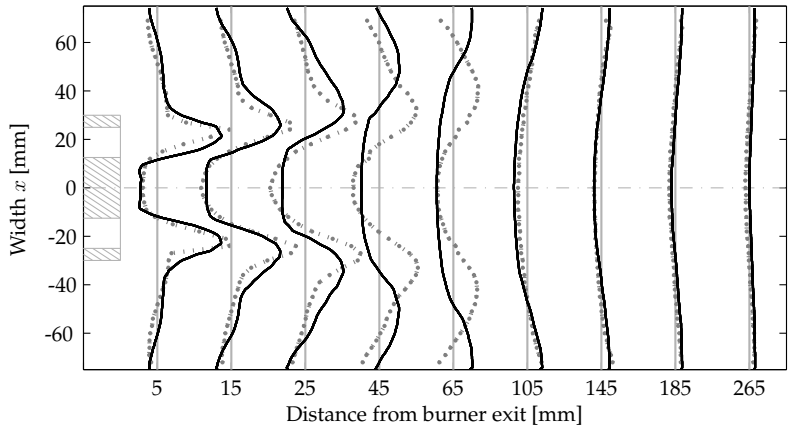

Figure 3.17: Isothermal mean dimensionless axial velocity profiles, simulation results (——) and water tunnel measurements (●—●—●).

Figure 3.18 shows the mean dimensionless tangential velocity along the y-axis. The swirling nature of the flow can be seen. The peak values decrease when moving farther from the burner exit. The numerical model shows the same over-prediction of the spreading of the jet as was seen in the profile of the axial velocity.

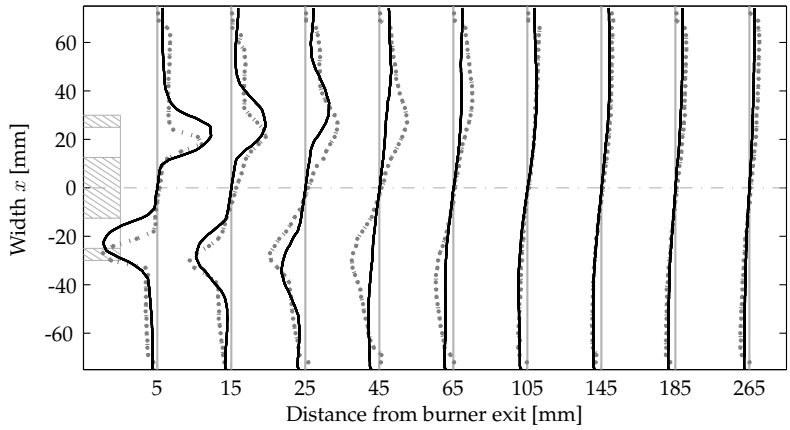

Figure 3.18: Isothermal mean dimensionless tangential velocity profiles, water tunnel measurements (●—●—●) and simulation results (——).

In figure 3.19 the axial Reynolds stress component k_{zz} is plotted against the x coordinate. Obviously, higher Reynolds stresses are observed in the planes that are closer to the burner exit. These stresses are caused by the shear layer at the edge of the central recirculation zone. The stresses decrease rapidly when moving further downstream.

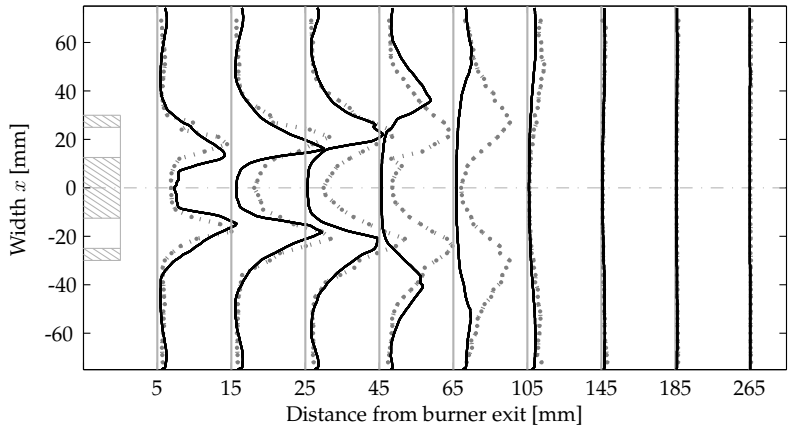

Figure 3.19: Isothermal mean dimensionless Reynolds stress in the axial direction k_{zz}, simulation results (——) and water tunnel measurements (●—●—●).

The comparison of the Reynolds stresses is good near the burner, but becomes worse further downstream. The k-ϵ model assumes that the Reynolds stresses (which can be determined from equation 3.10) are directly related to the velocity gradients, with corrections in the principal directions depending on the velocity and the turbulence kinetic energy. Assuming anisentropic Reynolds stresses that depend on the mean velocity gradients is only allowed when the mean gradients vary slowly [137]; it gives bad results for contractions or expansions.

In figure 3.20 the mean dimensionless axial velocity at the centreline is displayed,

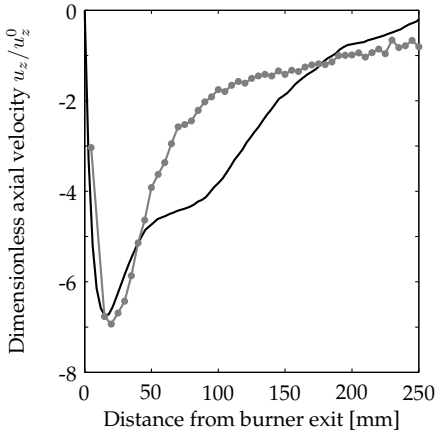

Figure 3.20: Isothermal mean dimensionless axial velocity profiles along centreline of the combustion chamber, simulation results (——) and water tunnel measurements (●—●—●).

plotted as a function of the z coordinate. A strong recirculation zone can be seen, with some back flow onto the burner hub. Furthermore, the recirculation zone seems to extend itself beyond 250 mm above the burner. The crossing point with the zero velocity axis cannot be obtained due to limitations of the traverse system of the LDV system.

Again, farther from the burner exit the simulation results and the measurements deviate strongly. For the axial velocity at the centreline, this is especially true for the region between 50 and 150 mm.

Finally, a few results of the grid-measurements are presented. These results give insight in the influence of the square combustion chamber on the flow and recirculation zone. In figures 3.21(a) and 3.21(b), the mean dimensionless axial velocities in a quadrant in the plane 5 mm downstream the burner exit and 45 mm downstream the burner exit are shown, respectively. For visualisation purposes, the velocities in the whole quadrant are obtained from the grid data (covering only $1/8^{\text{th}}$ of the cross-sectional area) by assuming periodicity (this is not entirely correct, since the smallest periodic part of the cross-section would be $1/4^{\text{th}}$ of the cross-section).

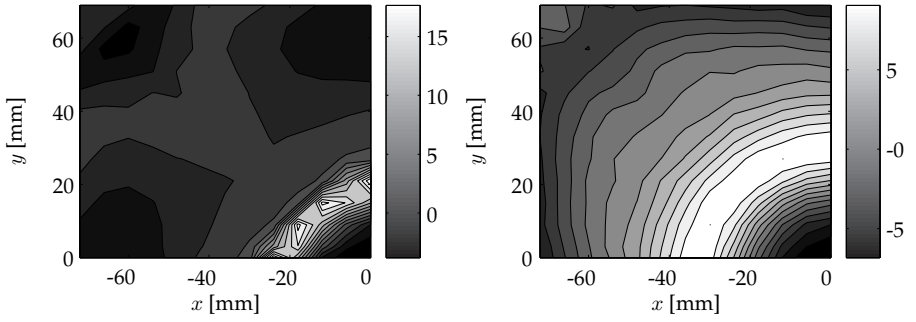

(a) 5 mm above burner exit (b) 45 mm above burner exit

Figure 3.21: Contour plot of the dimensionless mean axial velocity in a quadrant of the square combustion chamber.

From the figures it can be seen that the outer recirculation zone is not present along the whole circumference of the combustion chamber. The square chamber breaks the outer recirculation zone in different parts, mainly present in the corner and halfway the sides of the combustion chamber. It is also seen that the effect of the combustion chamber being square becomes stronger when moving closer to the walls; the flow field in the centre of the chamber is hardly affected by the square cross-section.

The burner showed to perform well. A strong, symmetrical recirculation zone was observed, without any signs of harmonic flow behaviour. In the flame zone (i.e. $z < 50$ mm), the numerical model is able to describe the profiles satisfactorily, despite the known limitations of the k-ϵ model in predicting recirculating flows. Downstream the flame zone, the numerical prediction becomes worse. A better prediction can be obtained at the expense of higher computational costs by using LES. A

comparison between LES simulations performed by CERFACS and the water tunnel measurements is presented in appendix G [164].

3.7.2 Mixing simulations

As already mentioned, 4 fuel nozzles with a diameter of 2 mm are used to inject the fuel in the main air flow. In this section, the effectiveness of mixing with this configuration is shown with the help of CFD simulations. Instead of the complete geometry, as used in the previous section, Model 2 is used for the mixing calculations. Following Kok [91], the turbulent Schmidt number is set manually to 0.2. This value is a good choice for the turbulent mixing in T-junctions.

The simulations are performed at operating point 15.1. To have a reference, the results with the 2 mm nozzles are compared to results with 5 mm nozzles.

In different cross-sections of the combustor, the maximum and minimum mass fraction of methane, the main component in the fuel, is determined. These values are displayed in figure 3.22 for 2 mm and 5 mm diameter nozzles. In figure 3.23 the standard deviation, defined as $s = \sqrt{\frac{1}{n}\sum_{i=1}^{n}(y^i_{CH4} - \overline{y_{CH4}})^2}$, is depicted for both cases. In both figures 3.22 and (b), the values are plotted as a function of the distance from the burner exit.

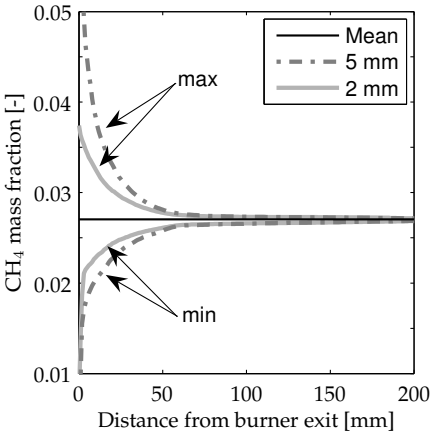

Figure 3.22: Minimum and maximum CH_4 mass fraction for nozzles with a diameter of 2 and 5 mm, plotted as a function of the distance from the burner exit.

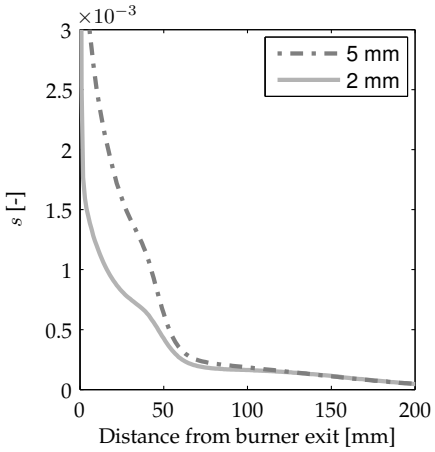

Figure 3.23: Standard deviation of CH_4 mass fraction for nozzles with a diameter of 2 and 5 mm, plotted as a function of the distance from the burner exit.

When the mixing would be perfect, the minimum and maximum lines would both collapse to one value: the mean mass fraction of methane. The 2 mm nozzles are seen to perform much better than the 5 mm nozzle. Still, the reactants remain partially premixed. This can also be seen from the standard deviation; the main effect of using 2 mm nozzles lies in the first 50 mm from the burner exit. In this range, the 2 mm nozzles are seen to perform much better than the 5 mm nozzles. This is

important since the flame is located mainly in this range, as will be shown in the next section. Decreasing the nozzle diameter, and adding more nozzles to prevent the nozzles from choking, can further enhance the mixing. However, it would also complicate the numerical modelling on the burner. Therefore, the 2 mm nozzles are chosen as a compromise.

3.7.3 Combustion simulations

Two steady-state combustion simulations are discerned: the perfectly premixed (PP) and imperfectly premixed (IP) case. The difference between the cases lies in the location of the inlet boundary. For the PP case, Model 3 is used. The domain of the IP case starts 55 mm upstream of the burner exit, just upstream of the fuel nozzles. Therefore, Model 2 is used for this purpose.

First, the PP case is considered. Figure 3.24 shows contour plots of the velocity and temperature fields at one of the periodic boundaries, using the conditions of case 15.1. Strong recirculation zones are observed, together with a flame enveloping the central recirculation zone. This recirculation zone is longer than in the isothermal simulation, which confirms that the swirl number decreases in a combustion situation as compared with an isothermal situation [62, 184] (see appendix D).

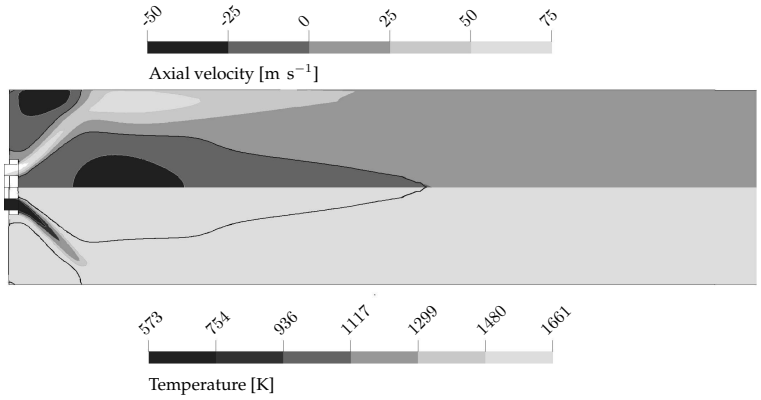

Figure 3.24: Velocity and temperature fields of case 15.1 (PP).

For the IP case, the velocity and temperature fields are displayed in figure 3.25. The central recirculation zone is significantly shorter. Also the flame is somewhat shorter and thicker. Moreover, the flame temperature rises above the adiabatic flame temperature for the mixture. Due to the IP mixture, the air factor can locally be lower than for the PP case, increasing the flame temperature.

The assumption of a PP fuel/air mixture leads to different results than those obtained with mixing included. However, due to the size of the model necessary for the IP case, it is far more computationally expensive to perform a transient simulation to obtain a flame transfer function (see chapter 4). Therefore, the flame transfer function study presented in the next chapter will be done with the PP boundary condition.

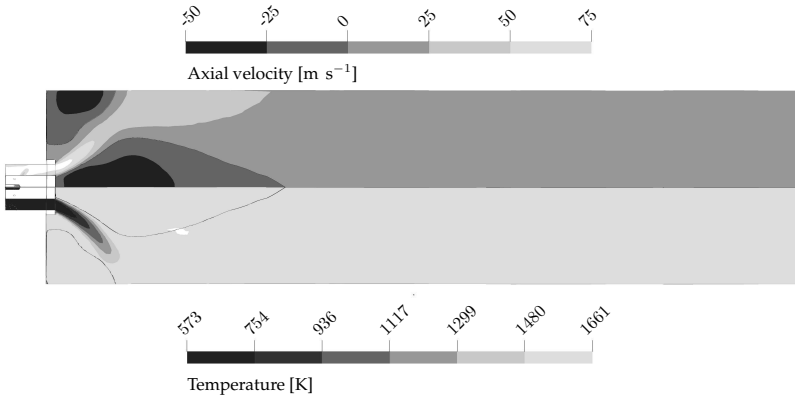

Figure 3.25: Velocity and temperature fields of case 15.1 (IP).

Nevertheless, the flame transfer functions that are compared to the measurements are all calculated with the IP model.

Heat loss

When operating the test rig it is not possible to reach the air factor specified in operating point 15.1 (see table 3.2). At an air factor of 2.0, the flame is seen to become unstable. The CFD simulations performed so far at this operating point are all using adiabatic walls. However, in reality, heat is lost through the wall, lowering the flame temperature. This decreases the air factor at which extinction occurs. To have an indication of the temperature field in the non-adiabatic situation (which is useful for acoustic models), a non-adiabatic CFD simulation is set up. This simulation consists of a few steps:

1. A simulation is performed at operating point 15.4 (see table 3.2). In this simulation, a liner temperature of 600°C was imposed. Convection and radiation to the liner wall is accounted for.

2. Subsequently, the wall heat flux distribution from step 1 is multiplied with a factor, such that the combustor outlet temperature is equal to the measured combustor outlet temperature.

With this procedure, a few assumptions are made. Firstly, the wall heat flux distribution calculated in step 1 is based on a constant liner temperature. A non-constant temperature leads to a different heat flux distribution. A one-dimensional heat transfer model (see chapter 6) shows that the liner temperature is indeed relatively constant, which justifies this assumption. A second assumption is related to the fact that the heat flux is fitted by scaling it with a factor. This linear scaling of the heat flux does not account for the 4^{th} order dependence of the radiative heat flux on the temperatures. This is also not accounted for when the heat transfer coefficients would be used as a boundary condition together with an imposed cooling air temperature.

Using the procedure described above, a temperature distribution is calculated for operating point 15.4. A plot of the average cross-sectional temperature and the maximum temperature as a function of the axial coordinate is depicted in figure 3.26. At operating point 15.4, the adiabatic flame temperature is 1786 K. It can be seen that the maximum non-adiabatic temperature is only 1687 K. Also, a considerable and almost linear negative temperature gradient is seen in the post flame zone downstream the combustor.

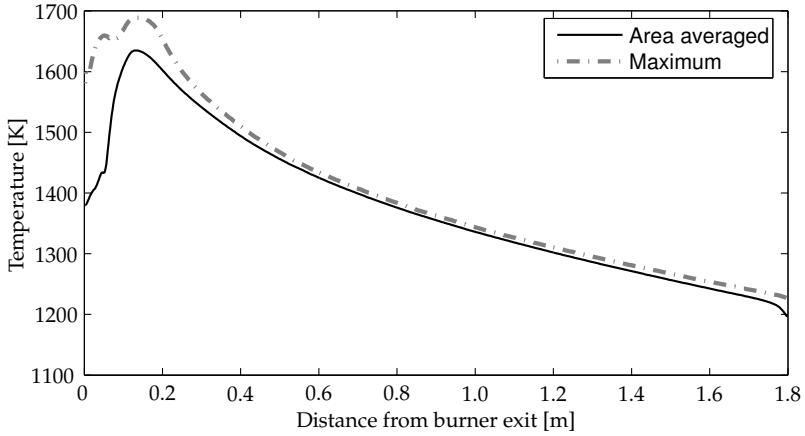

Figure 3.26: Cross-sectional area averaged temperature and maximum temperature as a function of distance from the burner exit.

Especially in the flame zone much heat is lost, which explains the large difference between the adiabatic flame temperature and the flame temperature observed in the model that accounts for heat loss. In the outer recirculation zones, the high rates of heat transfer to the walls cool down the recirculating gasses, decreasing the available enthalpy for heating up the fresh reactants [168]. Also radiative heat loss can significantly decrease the flame temperature [33]. In total 23% of the mean heat released by combustion is lost through the liner walls for this operating point. At higher pressures and powers, this relative amount decreases (see chapter 6).

Combustion regimes

With the obtained reacting flow simulation results at operating point 15.1 (PP and IP) the location in the Borghi diagram is checked.

The Borghi diagram is characterised by the turbulence velocity fluctuation u'_t, the laminar flame speed s_L, the characteristic turbulence length scale l_t and the laminar flame thickness δ_L. These values need to be expressed as a function of the available

variables in the simulation results [133, 183]:

$$u'_t = \sqrt{\frac{2}{3}k} \tag{3.27}$$

$$l_t = \frac{{u'_t}^3}{\epsilon} \tag{3.28}$$

$$\delta_L = D/s_L \tag{3.29}$$

where D is the molecular diffusivity of the mixture. The laminar flame speed s_L is determined with the code PREMIX. For operating point 15.1, the laminar flame speed is 34 cm/s. In the IP case, this laminar flame speed varies throughout the field depending on the local air factor. Nevertheless, a value of 34 cm/s is used for the IP case as well.

The Borghi diagram for the PP and IP operating point 15.1 is presented in figure 3.27. The symbols are points taken from the simulation results. Since quantities as flame speed and flame thickness are only relevant in the flame zone, the points are taken from the flame zone only (defined here as the locations where the reaction rate is larger than 1% of its mean value).

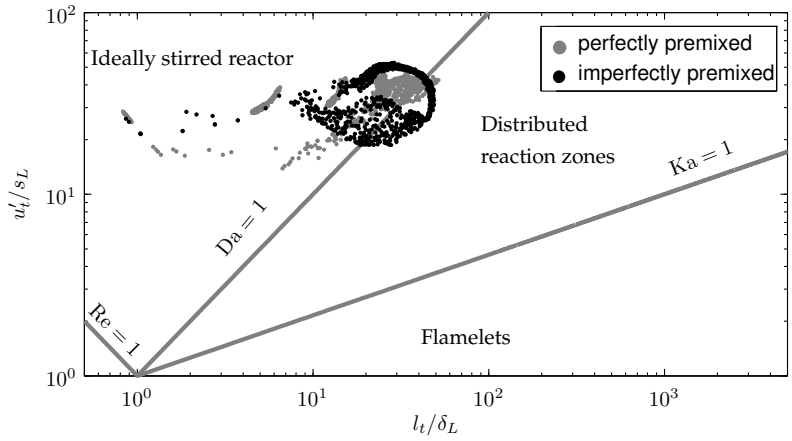

Figure 3.27: Turbulent premixed combustion diagram (Borghi diagram), from [182] including reacting flow simulation results at operating point 15.1.

Figure 3.27 shows that most of the point fall into the perfectly stirred reactor regime. However, combustion takes also place in the distributed reaction zones regimes, in which the used combustion model switches from the Arrhenius model to the eddy dissipation model. The points of the IP case are more scattered than the PP case. This is due to the large variation of air factors in the flame, and the fact that the laminar flame speed is taken constant.

3.7.4 Validation of combusting flow simulations

OH PLIF

For validating the reactive flow simulations, a qualitative OH field is measured in a cross-section of the flame. Since OH has a steep increase in the reaction zone [125] its gradient is an indication for the heat released at the flame front. Because OH is formed due to splitting of water it extends its zone with high concentration to the exhaust gas side of the flame zone. The OH field is measured using Planar Laser Induced Fluorescence (PLIF). The PLIF measurement technique is explained in appendix J.

A comparison between simulation results and the measured OH field is made at operating point 15.4. Unfortunately the simple combustion model does not predict OH. Useful comparisons can be made with the predicted temperature field and rate of heat release. Figure 3.28(a) show the averaged OH field overlayed with the heat release rate field, obtained from the numerical simulations (imperfectly premixed). At the locations where OH starts to appear, an increased heat release rate is predicted by the numerical simulations. Also a good agreement of the opening angle of the jet is seen. In the outer recirculation zone of the flame, less OH is noticed. This is most likely the result of considerable heat loss in this zone, as was shown in section 3.7.3. This heat significantly slows down the local reaction rate.

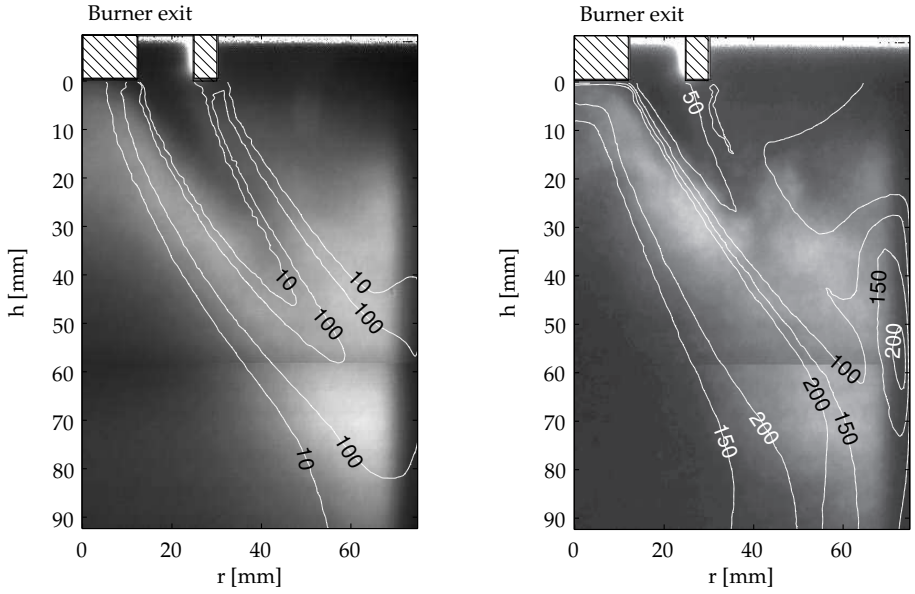

(a) Mean OH intensity, overlayed by heat release rate contours [MW m^{-3}] from a numerical simulation.

(b) RMS OH intensity, overlayed by contours of the turbulence kinetic energy k [m^2 s^{-2}] from a numerical simulation.

Figure 3.28: Mean and RMS OH intensity, overlayed by contours from a numerical simulation.

To compare the measured RMS OH field, it is assumed that fluctuations in the combustion rate are directly related to the turbulence kinetic energy k, i.e. reaction rate fluctuations are induced by velocity fluctuations. For that reason, a comparison between the k field from the numerical simulation and the measured RMS OH field is depicted in figure 3.28(b). Despite the crude assumption that k represents fluctuations in the heat release rate, its maximum values are found at the locations with high RMS values of the OH field, indicating a strong correlation between both quantities.

CH* Chemiluminescence

Another technique that has been used for validation of the reacting flow simulations is chemiluminescence of CH* (electronically excited molecules are indicated with a '*'). The radical CH* is a good marker for the flame front since it is linearly related to the heat release rate. Since chemiluminescence is a line of sight technique, special techniques have to be applied to obtain a planar picture. When the flame has an axisymmetrical shape, an Abel transformation [1] ('onion peeling') can be applied. Although the flow field under consideration is not entirely axisymmetrical, the flame is to good approximation axisymmetrical near the centreline axis.

When the Abel transformation is applied to the CH* field measured by chemiluminescence, the picture shown in figure 3.29 is obtained (again at operating point 15.4). Also shown in the figure is the temperature field obtained from a CFD simulation. A good correspondence of the opening angle and the reaction zones is again observed. The increased CH* intensity at the centreline is due to inaccuracies in the Abel transformation.

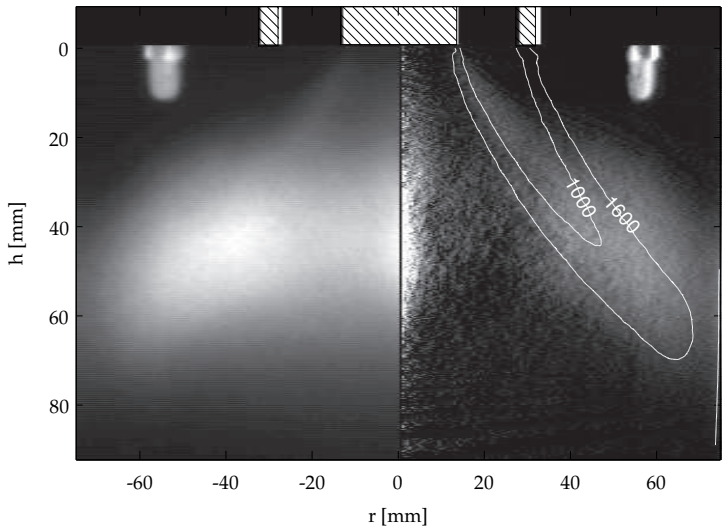

Figure 3.29: Line of sight CH* intensity (left) and Abel transformed CH* intensity (right), overlayed by contours of temperature from a numerical simulation.

When comparing the Abel transformed CH* field with the PLIF OH field (see figure 3.30), it is observed that the narrow region with CH* overlaps perfectly with the start of the OH formation and confirms that the dark V-shape in the OH-field is unburned fuel which ignites at the inner recirculation zone. At the outer side of the injected fuel, little CH* is seen and apparently less combustion takes place. This agrees with the weak OH signal. In the central part of the image, where turbulent flame movements create a diffuse OH field, the transformed CH* distribution is also spread over a larger area.

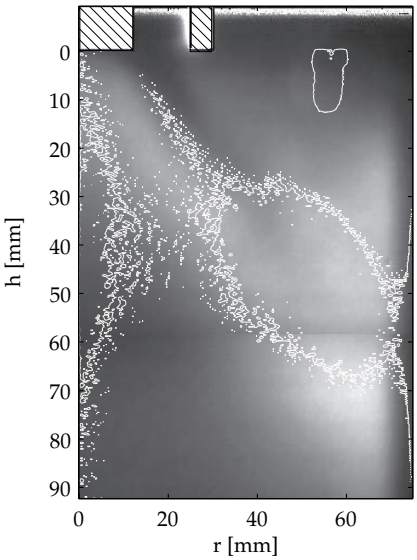

Figure 3.30: OH profile measured by PLIF overlayed by contours of Abel transformed CH* intensity.

3.7.5 Validity of the URaNS approach

To judge to which extent (or frequency) the considered reacting flow is suitable for applying an URaNS approach, the time scales need to be determined. In the considered problem, the k-ϵ model is used to describe the turbulence (for the performance of other turbulence models with URaNS, see [21]). To dissipate an amount of energy k at a constant dissipation rate ϵ, one needs $\tau_{turb} = k/\epsilon$ seconds. Taking this quantity as a crude approximation of the turbulence time scale, the characteristic turbulence frequency can be defined as $f_{turb} = \epsilon/k$. A contour plot of this quantity at a periodic boundary of case 15.1 is shown in figure 3.31.

It can be seen that the highest frequencies occur in the flame zone. This gives confidence in the URaNS approach, in which periodic oscillations of $<$500 Hz are considered. However, moving farther from the flame zone, the characteristic tur-

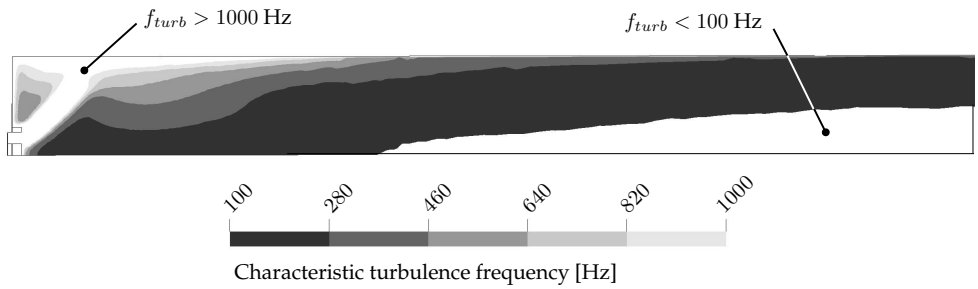

Figure 3.31: Characteristic turbulence frequency.

bulent frequency decreases. So here, the URaNS approach might give inaccurate results.

Taking $\tau_{turb} = k/\epsilon$ for the turbulence time scale is probably an overestimation of the typical time scale of the turbulent fluctuations. $\tau_{turb} = k/\epsilon$ is the time it takes to dissipate *all* the turbulence energy. However, the results of the flame transfer function calculation at higher frequencies have to be interpreted with care.

3.8 Concluding remarks

This chapter introduced the burner that will be used in the following chapters. Moreover the numerical tools that are used to model the steady flow field of this burner have been discussed. Finally, some important considerations regarding the use of Unsteady RaNS simulations are treated.

One important conclusion of this chapter is that while deviations between the isothermal measurements and simulations have been observed (i.e. see figure 3.17 and 3.19), the reacting flow field could be satisfactorily predicted (i.e. see figure 3.28(a)). A reason for this is the well-defined, relatively simple geometry of the burner. Obviously, a correct prediction of the reacting flow field is very important for the numerical thermo-acoustic characterisation of the combustion system.

The simulations performed in this chapter form the starting point of the transient simulations that will be conducted in the next chapter. The purpose of these transient simulations is to characterise the flame as an acoustic element, i.e. to obtain the relationship between an acoustic perturbation upstream of the flame and its acoustic response.

Chapter 4

The flame transfer function

4.1 Introduction

A key parameter in predicting the acoustically unstable operating conditions of the combustor is the flame transfer function (FTF), which represents the dynamic relationship between a fluctuation in the inlet conditions of a flame and its acoustic response. When the FTF is linked to the acoustic network model, the unstable frequencies and the growth rate of the instability can be calculated [9, 66, 156, 157, 179].

For similar flame shapes, the FTF is seen to depend mainly on the air factor. In general, leaner flames induce more stability problems in combustors. Since a lean flame operates closer to its extinction limit, it is more sensitive to perturbations at its inlet, hence the amplitude of its FTF is larger [31, 32]. Additionally, lean flames are longer than their richer counterparts. This larger flame length favours the distributed flame effects, which manifest itself in the amplitude of the FTF by a more oscillatory behaviour.

A FTF can be obtained in several ways. Firstly, the transfer function can be obtained from measurements [11, 97, 98, 130, 163]. In chapter 6 the measurements of the FTF in the DESIRE test rig are discussed. In the current chapter, analytical and numerical methods to obtain the FTF will be presented. As discussed in chapter 2 (section 2.5.2), the most likely cause for inducing heat release rate perturbations in turbulent premixed flames are equivalence ratio perturbations [29, 31, 32, 74]. Therefore the equivalence ratio is chosen as the excitation in all methods for obtaining the transfer function. Note that the setup of the models is such that choosing another excitation variable is relatively straightforward. The FTFs obtained with the different methods applied to similar combustion systems and operating conditions will be compared in terms of accuracy and computational effort. Moreover, the effect of an imperfectly and perfectly premixed inlet mixture on the FTF will be discussed.

The chapter starts with a general discussion on the FTF. Simple analytical models from literature [29, 109, 129] will be presented here. Moreover, the effect of the finite length of the flame on the transfer function is discussed. Subsequently, one of the simplest combustion models, i.e. an effectively zero-dimensional well-stirred reactor (WSR) model is used for FTF calculations. Although the model is simple, some

general aspects of the transfer function can be derived from it.

In the WSR model only the physics of the combustion model itself are included. To add the influence of the flow field on the FTF, a certain flow field (e.g. plug flow) can be assumed, and a relatively simple simulation suffices to obtain the transfer function. This concept can be extended by using the flow and temperature field as calculated by CFD simulations. After the discussion of the WSR, a numerical experiment involving spectral analysis is performed in CFD [15, 180]. In URaNS simulations, the numerical flame is perturbed by an excitation signal in the inlet quantities. Simultaneously, the response of the flame in terms of the volume integrated heat release rate Q is monitored. In this chapter, two types of excitation will be used and compared: white noise and impulse excitation. After applying these types of excitation to the perfectly premixed flames, the differences of the transfer function of the imperfectly premixed case will be pointed out.

4.2 Analytical model

In chapter 2, the flame transfer function H_f between the equivalence ratio perturbation ϕ' and the volume integrated heat release rate Q' was expressed as:

$$H_f = \frac{Q'}{\phi'} = n \cdot e^{-\mathrm{i}\omega\tau} \tag{4.1}$$

Equation 4.1 consists of a time delay τ between the excitation and the response, and of an amplification factor $n = |Q'/\phi'|_{flame}$, in which the subscript *flame* means that the transfer function is evaluated at the flame front. In literature this approach is called the $n - \tau$ model [36, 37].

Assuming a single constant time delay τ in expression 4.1 implies that the flame is not only acoustically compact (this justifies the volume integration of the acoustic source term over the flame), but also compact with respect to the wavelength based on the convection speed u_0, i.e. $L_{flame} \ll u_0/\omega$ (recall figure 2.10). Since an equivalence ratio perturbation is transported through the flame with the convection speed, the effect of the non-compactness of the flame with respect to its excitation influences the FTF. The magnitude of the Strouhal number, roughly given by the product of the frequency f and the flame length L_{flame}, divided by the mean flow velocity u_0 determines whether it is appropriate to treat the flame as a concentrated ($\mathrm{St} \ll 1$) or a distributed source of heat release rate ($\mathrm{St} = \mathcal{O}(1)$). Since flame Strouhal numbers appear to be generally of order unity [31, 32], accurately predicting their response requires models with capabilities to incorporate the spatial distribution of the heat release rate region.

To include the effect of non-compactness of the flame with respect to its excitation, Q' is assumed to be the result of a distributed heat release rate source. Doing so, equation 4.1 can be written as the volume integral of local FTFs at position $\mathbf{x}$, according to:

$$H_f = \frac{\int_V q'(\mathbf{x})\mathrm{d}V}{\phi'(\mathbf{x}_E)} = \int_V \frac{q'(\mathbf{x})}{\phi'(\mathbf{x}_E)}\mathrm{d}V \tag{4.2}$$

where the excitation is applied at location $\mathbf{x}_E$. When $\mathrm{d}V$ is decomposed in slices with thickness $\mathrm{d}x$ and area $\mathrm{d}S$, equation 4.2 can be written as:

$$H_f = \int_x \int_S \frac{q'(\mathbf{x})}{\phi'(\mathbf{x}_E)} \mathrm{d}S\mathrm{d}x = \int_x \frac{\int_S q'(\mathbf{x})\mathrm{d}S}{\phi'(\mathbf{x}_E)} \mathrm{d}x \tag{4.3}$$

The coordinate x can be written as a function of τ, i.e. $x = x(\tau)$. Substituting this relationship in equation 4.3 yields:

$$H_f = \int_{\tau=0}^{\infty} \frac{\int_S q'(\tau)\mathrm{d}S}{\phi'} \frac{\mathrm{d}x}{\mathrm{d}\tau} \mathrm{d}\tau \tag{4.4}$$

In this equation, the factor $\mathrm{d}x/\mathrm{d}\tau$ is a measure for the velocity of the particles through the slice over which the surface integral is determined. When the surface integral is evaluated, a new variable $q'_S(\tau)$ can be defined, representing the unsteady heat release rate in W/m as a function of τ:

$$H_f = \int_{\tau=0}^{\infty} \frac{q'_S(\tau)}{\phi'} \frac{\mathrm{d}x}{\mathrm{d}\tau} \mathrm{d}\tau \tag{4.5}$$

Finally, the complex transfer $q'_S(\tau)/\phi'$ is written in terms of an amplitude and a time delay τ, giving:

$$H_f = \int_{\tau=0}^{\infty} \left| \frac{q'_S(\tau)}{\phi'} \right| \frac{\mathrm{d}x}{\mathrm{d}\tau} \mathrm{e}^{-\mathrm{i}\omega\tau} \mathrm{d}\tau = \int_{\tau=0}^{\infty} |H_{local}| \, \mathrm{e}^{-\mathrm{i}\omega\tau} \mathrm{d}\tau \tag{4.6}$$

Equation 4.6 is actually the impulse response of the flame. In some papers, distributions of $|H_{local}|$ as a function of the time delay are represented by a probability density function (PDF) [161]. For simple flames, this PDF can be obtained analytically [109].

To derive an analytical model with the help of equation 4.6, an analytical expression for $|H_{local}|$ should be found (with impulse excitation, the expression is obtained numerically, as will be seen later). A simple approach, which however gives insight in the problem, is to assume a constant local FTF amplitude $|H_{local}|$ at the time delays where an elevated *mean* heat release rate is present. Obviously, in reality, $|H_{local}|$ might have other distributions which result in different FTFs. However, assuming a constant distribution clearly shows the effect of the finite length of the flame.

The distribution of the mean heat release rate can be determined numerically from a steady-state CFD result by calculating the convective time delay between the inlet boundary and each node in the domain. Nodes with equal time delays form (distorted) shells in the domain (see figure 4.1). The mean heat release rate integrated over the volume between two successive shells is denoted as Q_s, which represents the contribution to the total volume integrated heat release rate at a specific constant convective time delay τ (it is also possible to solve an additional transport equation for the local residence time [69]). In figure 4.2 the quantity Q_s is plotted as a function

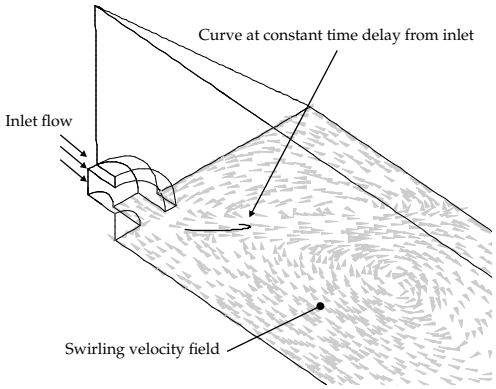

Figure 4.1: Distorted shell in the domain formed by particles that have equal time delays from the inlet boundary.

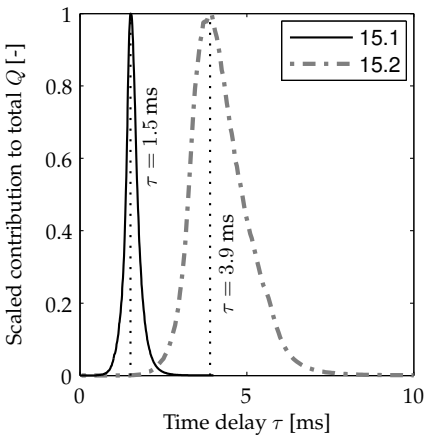

Figure 4.2: Contribution to total heat release rate at shells with the same delay time τ, normalised by their maximum values.

of τ (case 15.1 and 15.2, see table 3.2). Measurements show that this distribution of Q_s influences the observed FTF [57, 98].

Assuming a constant $|H_{local}|$ at the time delays with elevated mean heat release rate, equation 4.6 can be simplified analytically in expressions for the amplitude and phase of the resulting transfer function:

$$|H_f| = \frac{2}{\omega} |H_{local}| \sin\left(\frac{\tau_2 - \tau_1}{2}\omega\right) \tag{4.7}$$

$$\angle H_f = -\omega(\tau_1 + \tau_2)/2 \tag{4.8}$$

in which τ_1 and τ_2 are the time delays between which a constant non-zero $|H_{local}|$ is assumed. Figure 4.3(a) and 4.3(b) show the dimensionless* FTF amplitudes and phases calculated with equations 4.7 and 4.8 using the estimated time delays of case 15.1 ($\tau_1 = 0.5$ and $\tau_2 = 2.5$ ms) and 15.2 ($\tau_1 = 1.5$ and $\tau_2 = 6.5$ ms).

The characteristic aspect of the transfer functions is that they are essentially low-pass filters. This behaviour is also seen in the numerically obtained transfer function (see section 4.4) and literature.

It can be seen in equation 4.8 that the mean of τ_1 and τ_2 determines the phase. From equation 4.7 follows that half the difference between τ_1 and τ_2 determines the cut-off frequency of the low-pass filter. The spectrum cuts off purely due to the volume integration action of the local FTFs. This can be understood by realising that the wavelength λ_ϕ of the equivalence ratio excitation is based on the convective velocity rather than the speed of sound c_0, i.e. $\lambda_\phi = u_{conv}/f$. Still volume integrating the acoustic source is justified from an acoustical point of view because $u_{conv} \ll$

*All transfer functions are presented as a dimensionless value by scaling with the mean transfer function $\frac{Q_0}{\phi_0}$ [45, 74, 98, 163]. The dimensionless transfer function is denoted as $\hat{H}_f$.

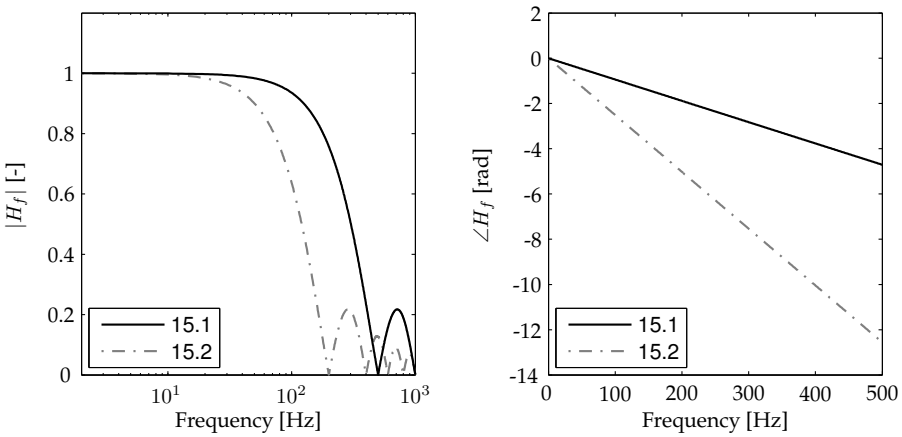

(a) Amplitude (b) Phase

Figure 4.3: FTF calculated with equations 4.7 and 4.8. A constant unit amplitude local transfer function was used.

c_0. At the frequency f where $\lambda_\phi = L_{flame}$ (i.e. $\mathrm{St} = 1$), or where the period of the fluctuating heat release rate equals the flame residence time, the *integrated* heat release rate is zero (a similar result was obtained by [57]). At the frequency at which half of a wavelength fits in the flame ($\mathrm{St} = 0.5$), the amplitude of the FTF starts to roll off. The low-pass behaviour is thus caused by the flame length being significant. Other phenomena that could cause this behaviour (not included in the model) is non-uniformity of the flow from the premix duct [155].

Based on experimental observations, a model of a FTF has been proposed [29,155] for lean premixed prevaporised combustion of methane at relatively high pressure:

$$H_f = C\frac{\mathrm{e}^{-\mathrm{i}\omega(\bar{\tau}+\Delta\tau)} - \mathrm{e}^{-\mathrm{i}\omega(\bar{\tau}-\Delta\tau)}}{\mathrm{i}\omega} = 2C\mathrm{e}^{-\mathrm{i}\omega\bar{\tau}}\frac{\sin(\omega\Delta\tau)}{\omega} \tag{4.9}$$

where $\bar{\tau}$ is the mean time delay from the excitation to the response, $2\Delta\tau$ is the (uniform) variation in time delay over the thermo-acoustic source and C is a constant. Note that equation 4.9 is also obtained from equation 4.6 by choosing $|H_{local}| = C$ for $\bar{\tau} - \Delta\tau < \tau < \bar{\tau} + \Delta\tau$. This would also result in the same expressions for the amplitude and phase as shown in equation 4.7 and 4.8, with $\tau_1 = \bar{\tau} - \Delta\tau$ and $\tau_2 = \bar{\tau} + \Delta\tau$.

With the model presented in this section it is possible to predict the cut-off frequency and time delay of the FTF from a steady-state numerical simulation. The benefit of the model lies in its simplicity, in combination with a reasonable prediction of the general shape of the transfer function. In the next section, combustion dynamics will be included in the model with the help of a Well-Stirred Reactor (WSR) model.

4.3 Well-stirred reactor model

A Well-Stirred Reactor (WSR) is a simplified combustion model [175]. Its main assumption is that the properties throughout the reactor are uniform due to intense turbulent mixing. This includes temperature, pressure and species mass fractions (see figure 4.4). Turns [175] notes that WSR models are used to guide the development of combustors for gas turbines and are used to correlate lean combustor performance, such as lean blowout.

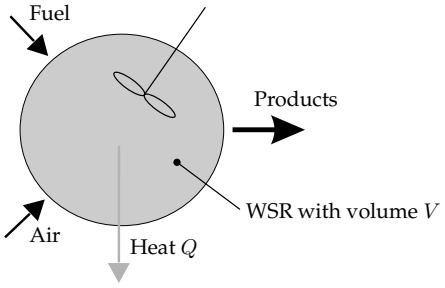

Figure 4.4: Ignition and extinction in the WSR.

The WSR takes into account the chemical reactions which can affect the species concentrations and temperature. The reactor is characterized by the reactor volume V, residence time τ_{WSR} or mass flow rate M and temperature T. The WSR is used here to approximate the dynamics of the combustion process. With the unsteady version of the model [52, 109], a dynamic transfer function between the inlet properties of the reactor and the heat release rate can be obtained.

4.3.1 Model

The WSR is described by conservation of energy and species within the reactor. A one-step reaction of fuel and air into products is assumed:

$$\underbrace{\mathrm{CH_4}}_{\text{Fuel}} + \underbrace{2\lambda(\mathrm{O_2} + 3.76\mathrm{N_2})}_{\text{Air}} \rightarrow \underbrace{\mathrm{CO_2} + 2\mathrm{H_2O} + 7.52\mathrm{N_2} + 2(\lambda - 1)(\mathrm{O_2} + 3.76\mathrm{N_2})}_{\text{Products}} \quad (4.10)$$

It can be seen that the air factor λ determines whether $\mathrm{O_2}$ is contained in the products.

Conservation of mass and species mass fraction are described by:

$$V\frac{\mathrm{d}\rho}{\mathrm{d}t} = M_{in} - M \quad (4.11)$$

$$V\frac{\mathrm{d}\rho y_i}{\mathrm{d}t} = M_{in}y_{i,in} - My_i + V\omega_i \quad (4.12)$$

where the subscript 'in' specifies user imposed boundary conditions. The other variables are quantities of the WSR itself. Combining equations 4.11 and 4.12 yields the

conservation equations for the fuel (f) and air (a) mass fractions (the mass fraction of the products follows from the constraint $\sum y_i = 1$):

$$\frac{\mathrm{d}y_f}{\mathrm{d}t} = \frac{1}{\tau_{WSR}}(y_{f,in} - y_f) + \frac{1}{\rho}\omega_f \tag{4.13}$$

$$\frac{\mathrm{d}y_a}{\mathrm{d}t} = \frac{1}{\tau_{WSR}}(y_{a,in} - y_a) + \frac{1}{\rho}\omega_a \tag{4.14}$$

in which $\tau_{WSR} = \frac{\rho V}{M_{in}}$, the residence time of the reactants in the reactor. The rate of production of species i is given by ω_i. For the fuel the rate of production is given by an effective Arrhenius equation [175]:

$$\omega_f = -24100 W_f \rho y_f^{-0.3}(0.233 y_a)^{1.3}\mathrm{e}^{-15098/T} \tag{4.15}$$

with W_f the molar weight of the fuel. The rate of production of air and products is related to ω_f through stoichiometry.

Since pressure perturbations have little direct influence on heat release rate perturbations [111] the pressure is assumed to be constant in the WSR. With this assumption, and using the continuity equation to work the time derivative of the density out of the equation, the conservation of enthalpy in an adiabatic WSR is described by:

$$\rho V \frac{\mathrm{d}h_{tot}}{\mathrm{d}t} = M_{in}(h_{tot,in} - h_{tot}) \tag{4.16}$$

Using equation 3.15, equation 4.16 can be written in terms of the time derivative of the temperature:

$$\rho V c_p \frac{\mathrm{d}T}{\mathrm{d}t} = M_{in}(h_{tot,in} - h_{tot}) - \rho V \sum_i h_i \frac{\mathrm{d}y_i}{\mathrm{d}t} \tag{4.17}$$

With the conservation equations for the mass fractions of the species and the continuity equation, this can be rewritten to:

$$\frac{\mathrm{d}T}{\mathrm{d}t} = \frac{1}{c_p}\sum_i \left(\frac{1}{\tau_{WSR}} y_{i,in}(h_{i,in} - h_i) - \frac{1}{\rho}\omega_i h_i \right) \tag{4.18}$$

With this equation, the system of equations for the WSR is closed. The independent variables are y_i and T, which can be solved with the differential equations 4.13, 4.14 and 4.18.

The equations for y_i and T are solved iteratively using a first order backward Euler time-stepping procedure. For this set of stiff equations, the time-stepping procedure is much more robust than setting the time-derivatives to zero and solve the set of non-linear equations using, for example, a Newton algorithm. With the explicit time stepping procedure, the problem always converges when the time step Δt is small enough.

4.3.2 Steady-state solution

A few examples of steady-state calculations with the WSR are discussed below. An important parameter of the WSR is the residence time τ_{WSR}. When the residence time becomes too small, blowout of the reactor occurs, since the reaction cannot be completed in the time the reactants remain in the reactor. On the other hand, when the residence time is long, all reactants can be burned completely, only it takes longer to reach a steady-state value because the refresh rate of the reactor volume is low. This concept is illustrated in figure 4.5. The initial value for the temperature is chosen at 1500 K, and the reactor temperature is monitored in time as it goes to its steady-state. When the inlet mass flow is changed, the effects described above are seen.

The volume of the reactor at each mean equivalence ratio is always chosen such that the amount of fuel that leaves the reactor unburned is small (i.e. $y_f < 10^{-5}$). Subsequently, the Strouhal number, defined as $\mathrm{St} = f\tau_{WSR}$, is used to characterise the dynamic behaviour of the WSR. By using St, the dynamic behaviour it is independent of the reactor volume and inlet mass flow.

When the volume would be kept constant for all ϕ, an extra increase of the FTF is observed when ϕ decreases. This increase is artificial though. It is a result of the lower reaction rate at lower mean equivalence ratio's, causing an increasing part of the fuel to leave the reactor unburned. Therefore relatively less heat is released at lower ϕ. As a consequence the slope of Q versus ϕ increases (see figure 4.6). This results in an increased low frequency response of the unsteady WSR.

The effect described above is the reason why Lieuwen *et al.* [111] notice an increasing heat release rate response when the mean equivalence ratio is decreased.

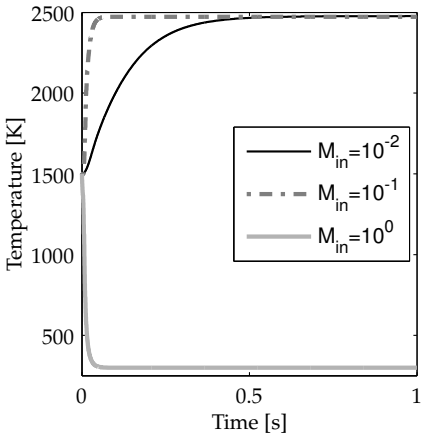

Figure 4.5: Influence of the inlet mass flow on the WSR temperature.

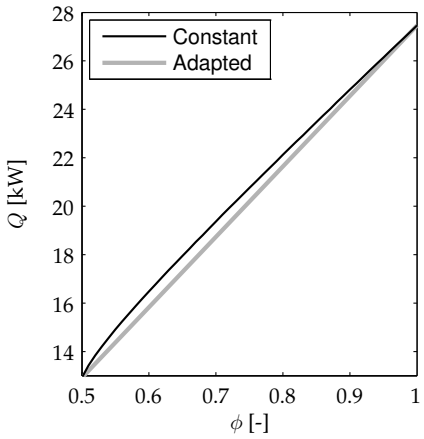

Figure 4.6: Dependence of the mean heat release rate Q on the equivalence ratio ϕ for a WSR with a constant volume and with a volume adapted such that all fuel is burned in the WSR.

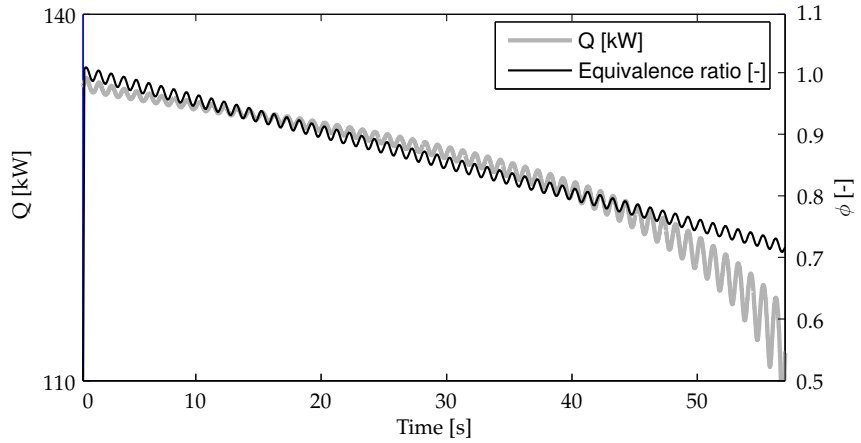

Figure 4.7: Fluctuating heat release rate as a result of a fluctuating equivalence ratio. The frequency of oscillation is 1 Hz, and the mean equivalence ratio decreases with increasing time.

In their paper, a WSR is excited by a sinusoidal signal. Simultaneously, the mean equivalence ratio is decreased, while the response of the WSR in terms of the heat release rate is monitored. A behaviour as depicted in figure 4.7 is observed.

It can be seen that the amplitude of the heat release rate response increases when the mean equivalence ratio of the reactor decreases. In Lieuwen's paper, this effect is explained by the fact that small perturbations in ϕ produce relatively large perturbations in the chemical time scale under lean conditions in comparison with stoichiometric conditions. Nevertheless, at the low frequency at which Lieuwen excites the WSR, a quasi-steady response of the heat release rate will occur, which does not depend on the mean equivalence ratio. Since Lieuwen does not adapt the volume of the WSR, it is more likely that the increased response is due to unburned fuel leaving the reactor at lower equivalence ratio's.

4.3.3 Unsteady solution

The FTF can be obtained by fluctuating an inlet quantity and performing a transient calculation with the WSR model described in the previous sections. During this transient simulation, the unsteady heat release rate is monitored. A spectral analysis subsequently reveals the FTF.

By using white noise excitation in the equivalence ratio, the FTF is obtained for the whole frequency range at once (contrary to sinusoidal excitation, used in [109], which gives the FTF at only one frequency at once). The white noise perturbation level in the unsteady simulations is 1% of the mean equivalence ratio. With these small perturbations, it is expected that the model behaves linearly. Moreover, the

system is time-invariant, stable and causal*. This justifies the use of a spectral analysis applied to the transient problem. More considerations on white noise excitation (frequency resolution, sampling rate etc.) are discussed in section 4.4.3.

The FTFs shown in this section are calculated for a stoichiometric ($\lambda = 1$) and lean ($\lambda = 1.5$) flame, both with an inlet temperature of 300 K and an atmospheric pressure. In figure 4.8 the amplitude and phase of the dimensionless FTF is plotted against a Strouhal number $\mathrm{St} = f\tau_{WSR}$.

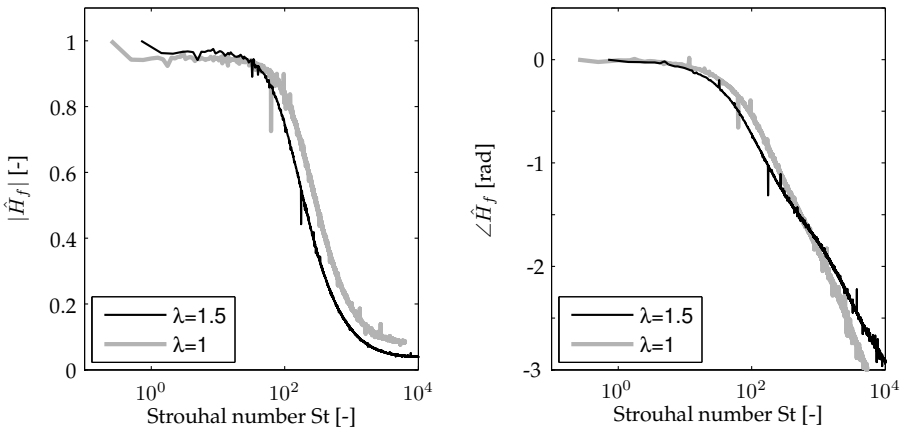

(a) Amplitude (b) Phase

Figure 4.8: Dimensionless FTF determined with white noise excitation applied to the WSR for $\lambda = 1$ and $\lambda = 1.5$.

Just as seen in the analytical model, the FTFs obtained from the WSR are essentially low-pass filters. However, this low-pass behaviour is caused by another mechanism than the finite flame length. In the WSR, the mechanism that determines the cut-off frequency is related to the reaction rate. A higher reaction rate is observed in case of the stoichiometric combustion. This shifts the cut-off frequency to a higher frequency compared to the lean case.

As long as the period of the perturbation is sufficiently longer than the chemical time, the WSR responses quasi-steady. For faster fluctuations, Q' starts to lag ϕ' and the coupling becomes weaker. The phase of the transfer calculated with the use of the WSR only includes the phase shift due to the finite combustion rate, i.e. there is no convective part included.

The added value of the WSR model is that it shows the cut-off frequency due to the finite rate of the combustion process, while the analytical model of the previous section assumed an infinitely fast combustion. However, unlike the analytical model, the WSR does not show the effects of a finite flame length caused by convection. Combining the results of both models should give a good estimate of the mechanism due to which the flame cuts-off, and the frequency associated with it.

*A causal (or physically realisable) system is a system that does not respond to an input before it is applied to the system.

When it is assumed that the residence time in the WSR is equal to the flame residence time, the Strouhal numbers of the WSR are comparable to the Strouhal numbers used in the analytical model of section 4.2. In this analytical model, it was seen that the flame cuts off at $\mathrm{St} = 0.5$. Looking at figure 4.8 it can be seen that the cut-off Strouhal number due to the finite combustion rate ($\mathrm{St} = \mathcal{O}(10^2)$) generally lies much higher than the cut-off Strouhal number due to the finite flame length (($\mathrm{St} = \mathcal{O}(10^0)$)). Consequently, it can be concluded that it is mainly the flame length that determines the low-pass filter behaviour of the flame.

4.4 CFD model

The previous sections discussed simplified models to determine the FTF. In these models, the actual flow field and flame shape were omitted from the analysis. A way to account for these aspects is by studying a CFD solution of the flame.

In chapter 3 solutions of steady reacting flows were presented. Moreover, the issue of performing unsteady simulations with a RaNS approach was assessed. When all conditions of the URaNS approach are satisfied, the numerical flame can be excited by variations in the equivalence ratio. In a transient simulation, the response of the flame in terms of the volume integrated heat release rate is subsequently monitored. A spectral analysis then reveals the FTF. This transfer function includes convective time delay, effects of the flow field (recirculation zones) and influences of the combustion process, like the chemical reaction rate.

In this section the FTF will be calculated from a CFD simulation by using three different methods of excitation: white noise, impulse and sinus excitation. After a discussion of the general aspects that are important when performing a spectral analysis in CFD, the impulse and white noise excitation methods will be treated more thoroughly (sinus excitation is considered straightforward and does not require any special post processing to obtain the transfer function). Finally, the resulting FTFs will be compared and conclusions will be drawn on the obtained FTFs and on the applied excitation techniques.

Three operating points are compared here: 15.1, 15.2 and 15.4 (see table 3.2). These operating points differ in the equivalence ratio, air preheating temperature and adiabatic flame temperature.

4.4.1 Spectral analysis in CFD

The response and excitation signals from the unsteady CFD simulations need to be transformed to the frequency domain to obtain the FTF. Moreover, the discrete time step and the length of the CFD simulation need to be chosen such that an accurate transfer function is obtained in the desired frequency range. The frequency range $[f_{min}, f_{max}]$ is determined by the sampling frequency f_s and the sample length T according to:

$$f_{min} = \Delta f = 1/T; \qquad f_{max} = f_s/2 = f_n \tag{4.19}$$

in which f_n and Δf are the Nyquist frequency* and the frequency resolution, respectively. Choosing $f_{max} = 1000$ Hz in equation 4.19 implies a sampling time of 0.5 ms, corresponding to a sampling frequency $f_s = 2000$ Hz. Moreover, a sample length of $T = 0.5$ s is chosen, which gives a frequency resolution and minimum frequency of 2 Hz.

In section 3.4.1 is was shown that about 40 time steps per period are necessary for an accurate transient simulation with a second order time discretisation scheme. This value was validated by studying acoustic wave propagation with URaNS. Since a FTF is studied here that is controlled by convection and not by the speed of sound, a lower CFL number is reached for a similar time step and mesh size. This means that the accuracy of the discrete schemes is better for the FTF simulations than for the example with acoustic wave propagation. Despite this observation, the same approach as done in section 3.4.1 is applied to obtain an indication of the error made in the transient scheme. A sampling time of 0.5 ms would yield a relative error of about 80% in the value of a quantity in the transient simulation at the maximum frequency of interest of 500 Hz. Nevertheless, this error drops rapidly for lower frequencies, i.e. at 100 Hz the error is only 1%. Still, the results in the higher frequency range should be interpreted with care. In chapter 5, a new approach is used to calculate the FTF. This approach does not suffer from time truncation errors and will therefore be used to quantify the errors made with the approach used in this section.

Because the transient data is already discrete, one cannot use an analog low-pass filter to prevent aliasing of the signal around the Nyquist frequency. Nevertheless, the time step size Δt of the CFD simulation already prevents the representation of high frequencies in the simulation itself. Therefore, no aliasing problems are expected.

The white noise and sinus perturbation level in the unsteady simulations is 1% of the mean equivalence ratio. For the impulse excitation, a level of 3% had to be used to have a sufficient signal-to-noise ratio while still avoiding the excitation of non-linearities in the system. The first step in the unsteady calculation is always to check whether there are significant transient effects present when there is no excitation. In all cases presented here this is not the case.

4.4.2 Impulse excitation

With impulse excitation the numerical flame is excited by a pulse in the equivalence ratio at the burner inlet. This pulse convects to and through the flame, and causes the volume integrated heat release rate to deviate from its mean value. This way, the heat release rate perturbation as a function of the time delay from the inlet is obtained. This perturbation does not necessarily have to be a result of a deviation in the local heat release rate at the spatial location of the pulse. Also when the pulse has already passed a certain location, heat release rate fluctuations can occur there. The FTF can subsequently be obtained from the discrete version of the impulse response

*Because a sine with a certain frequency can be represented by at least two discrete points, the Nyquist frequency represents the frequency until which the sampled transient signal theoretically gives reasonable results in the frequency domain.

(equation 4.6):

$$H_f = \sum_{k=1}^{m} \frac{Q'(\tau_k)}{\phi'} \mathrm{e}^{-\mathrm{i}\omega\tau_k} \tag{4.20}$$

in which k is the time step number of the simulation and m is the total number of time steps. Moreover, $Q'(\tau_k) = Q(\tau_k) - Q(0)$, i.e. the difference between the mean heat release rate at time step k and time step 0.

Using impulse excitation to obtain a FTF is interesting since the peaks in the FTF spectra are all wide, i.e. have a small quality factor. This indicates that there is much damping and consequently the impulse response of the system is relatively short. This is advantageous because the total number of time steps m necessary to analyse the system can be small. As a criterium, the impulse response 'measurement' is stopped when the fluctuations in the response are equal to the random fluctuations in the unexcited system (settling time).

A disadvantage of impulse excitation is that an accurate consistent linear approximation of a non-linear system cannot be obtained due to the very high crest factor (ratio of peak to RMS value) [67], which might excite non-linearities. An ideal pulse of infinitesimal small time would excite all the frequencies in the spectrum equally, but in general the pulse has a finite time length. This finite length goes at the expense of the excitation of the higher frequencies, which requires the high crest factor to excite them. The Fourier transform of a pulse with length Δt_{pulse} can be calculated as:

$$S_{pulse} = \frac{\mathrm{i}}{\omega}(\mathrm{e}^{-\mathrm{i}\omega\Delta t_{pulse}} - 1) \tag{4.21}$$

In a numerical simulation, the minimum length of a pulse is equal to the time step Δt used in the simulation. With a time step of 0.5 ms, as used in the CFD simulations, impulse excitation is able to sufficiently excite all frequencies below 1000 Hz. However, the excitation level is not equal for all frequencies, which might still give problems of exciting non-linearities in the system.

4.4.3 White noise excitation

A white noise signal is a randomly fluctuating signal that ideally excites all frequencies evenly. The white noise signal applied to the CFD simulations is generated using a MATLAB function generating uniformly distributed random numbers. An ideally flat spectrum cannot be achieved because the white noise signal is imposed to the system at the same sampling rate as the sampling of the response occurs. In spectrum analysers, the excitation is usually applied at a much higher frequency than the sampling takes place. This is not possible in CFD applications because this would cause an intolerable increase in the calculation time. Since the excitation has the same frequency as the sampling frequency, discrete jumps occur between values of the white noise at each time step, distorting the spectrum.

As a consequence of the random nature of white noise excitation (one can only tell something about the statistics of the response and the excitation), it is common to perform an averaging procedure. This is done by taking multiple (overlapping)

samples and averaging the result. The averaging procedure also reduces the influence of non-linearities in the system. In the CFD problem, a few averages are needed to get to a reasonably noise free transfer function. Therefore, 8 (75% overlapping, 1.375 s total simulation time) samples are used. The reason for using just 8 samples is to control the necessary CPU time of the simulation. Still, a single transient run takes about 6 days on 8 AMD MP 1800+ CPUs.

When the simulation has finished, and when the excitation and response signals have been Fourier transformed, a Hanning window is applied to reduce the effects of spectral leakage. This problem arises due to the assumption in the discrete Fourier transform that the time record is exactly repeated throughout all time, and that the signals contained in a time record are thus periodic at intervals corresponding to the length of the time record. So when the time record has a non-integer number of cycles, this assumption is violated. The non-integer cycle frequency does not correspond exactly with one of the spectrum frequency lines in this case. A consequence of this is that energy from a given frequency is spread over the adjacent frequencies in the Fourier transform ('leaks' to other frequencies). Leakage can completely conceal the presence of low amplitude peaks in the spectrum. Because it is not possible to satisfy the assumption of periodicity for all frequencies in the signal, windowing functions have to be used to prevent leakage. A Hanning window is used in the calculation presented here. The Hanning window has a good frequency resolution (high side lobe roll-off rate) as well as reduced spectral leakage.

When both the excitation and the response signals are windowed and Fourier transformed, the FTF can be obtained from:

$$H_f = \frac{S_{FX}}{S_{FF}} \tag{4.22}$$

in which S_{FX} and S_{FF} are cross- and auto-spectra of the excitation F and the response X, respectively. Using this version of evaluating the transfer function, only noise in the excitation can disturb the transfer function.

White noise excitation has a few advantages compared to other excitation techniques (like pseudo-random, periodic impulse, periodic random, sine and impulse excitation) [67]. Firstly, it gives the best linear fit of non-linear systems. This is because frequencies are excited at different amplitudes and phases, averaging out the non-linearities. Secondly, the energy of the excitation is equally distributed over the entire bandwidth, which result in a low crest factor, and reduces the danger for exciting non-linearities. Finally, the bandwidth can be well-controlled.

There are a few disadvantages of white noise excitation, however. Leakage can occur during the analysis due to the non-periodicity of the excitation. This is partially overcome by windows like the Hanning window. Moreover, the signal-to-noise ratio is low. However, this is not a problem in this application, because the excitation is applied directly to the numerical problem, and noise in the response signal cannot distort the transfer function in its form of equation 4.22.

4.4.4 Results

The FTF is determined at the operating points 15.1, 15.2 and 15.4. Firstly, the results of the white noise excitation will be discussed. Next, a comparison will be made with the results from the impulse excitation.

For white noise excitation, the degree of linearity between both the excitation and response was checked. This degree of linearity can be measured by the coherence-function γ^2, which is defined as:

$$\gamma^2 = \frac{S_{FX} S_{XF}}{S_{XX} S_{FF}} \tag{4.23}$$

When there are no disturbances in the excitation and response, the coherence function is equal to 1 [67]. The presence of non-linearities, noise and leakage always decreases the coherence function below one. Moreover, when a delay is present in the system, which is the case for the system studied here, the coherence is biased by a factor $(1 - \tau/T)^2$, in which τ is the time delay and T is the sample length [67]. Due to the time delays of $\mathcal{O}(10^{-3})$ s occurring in the studied cases, this value is very close to 1, though.

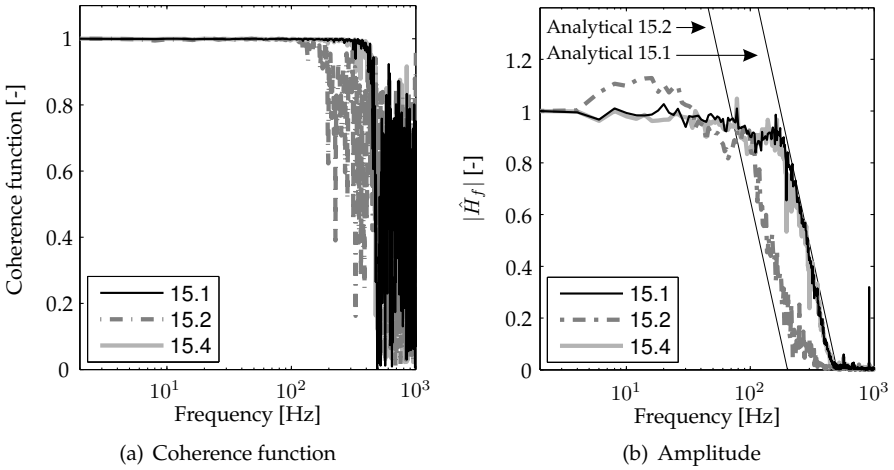

(a) Coherence function (b) Amplitude

Figure 4.9: FTFs obtained with white noise excitation.

Figure 4.9(a) shows the coherence function at each frequency for all three cases, perturbed by white noise equivalence ratio fluctuations. A good coherence is noticed below 400 Hz for operating point 15.1 and 15.4, and below 200 Hz for 15.2. The reason for the incoherence above these frequencies is that hardly any response is noticed there, which is immediately clear when the amplitude of the dimensionless FTF of the three cases is examined (figure 4.9(b)).

The characteristic aspect of the transfer functions is that they are essentially low-pass filters. In section 4.2 an analytical model was derived. The slope of the analytical results is included in figure 4.9(b). Considering the limitations of the analytical

model it can be concluded that the cut-off frequency and the slope of the spectrum are mainly determined by the flame residence time and the fact that the response is volume integrated.

Figure 4.10(a) and (b) show a comparison of the FTF amplitudes of case 15.1 and 15.2, obtained with white noise and impulse excitation. First, it should be mentioned that with white noise excitation, a transient simulation of 6 days on 8 CPUs was necessary, while the result of the impulse excitation has been obtained in only 12 hours. However, the impulse level should be a compromise between a high enough value to have a reasonable signal-to-noise ratio, but a low enough value not to excite nonlinearities, which is already the case with an excitation level of only 5 percent. Still, from figure 4.10(a) and (b) it can be concluded that considering the difference in calculation time, the agreement between both amplitudes is good. All significant peaks are present in the amplitude of the transfer function obtained by impulse excitation.

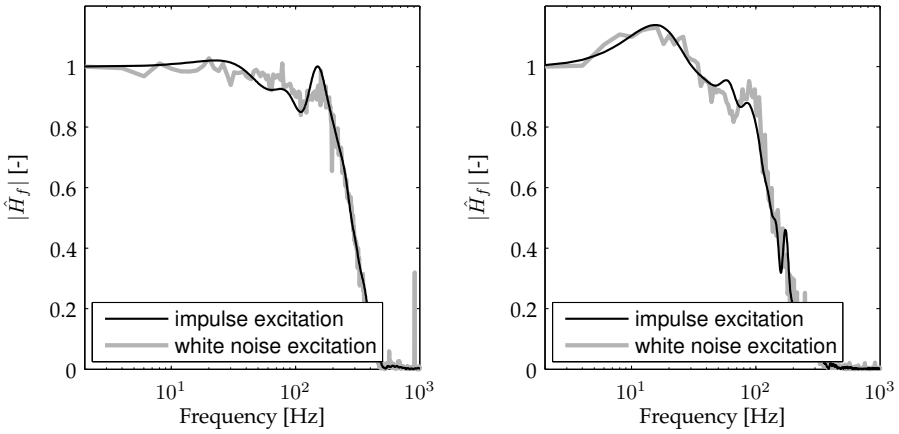

(a) Operating point 15.1

(b) Operating point 15.2

Figure 4.10: Amplitude of the FTF obtained by white noise and impulse excitation.

Finally, the phase of the calculated transfer functions is shown in figure 4.11. From the constant slope of the phase of the transfer function below 400 Hz (operating point 15.1 and 15.4) and 200 Hz (operating point 15.2), it can be concluded that constant time delays exist here. These time delays can be extracted from the figure by determining the slopes. For the operating points 15.1/15.4 and 15.2 the time delays are 1.5 and 3.9 ms, respectively. From figure 4.2, it is noticed that these values correspond to the convection time between the inlet plane and the (distorted) shell at which the relative contribution to the total heat release rate is maximal.

The impulse response technique also results in phase information of the transfer function. The phase of the transfer function of operating point 15.1 and 15.2 obtained via impulse excitation was compared to the white noise results in figure 4.12. It can be seen that especially for the phase, the agreement between the two methods

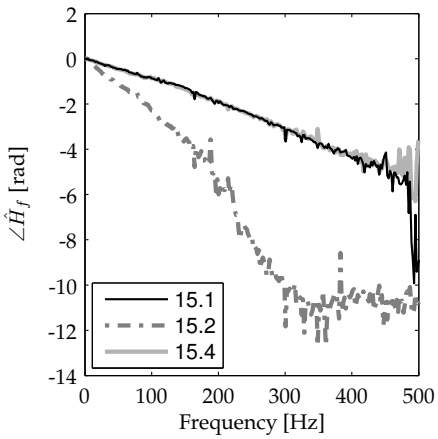

Figure 4.11: Phase of the FTF obtained by white noise excitation.

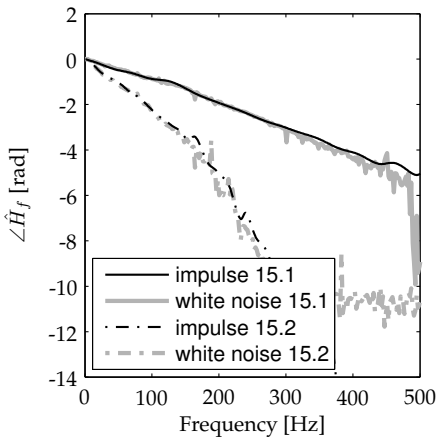

Figure 4.12: Phase of the FTF obtained by white noise and impulse excitation.

is excellent. The phase results of the impulse response method appear to be less sensitive to the chosen impulse level.

4.4.5 Discussion

The observed difference in phase between the operating points 15.1/15.4 and 15.2 is obvious. Operating point 15.2 has a relatively low inlet temperature (373 K instead of 573 K), while the differences in the inlet mass flow are relatively small. Consequently, the inlet velocities are much lower for operating point 15.2. This results in longer convective time delays, which explains the difference in phase. Another effect is that the flame residence time is longer, which decreases the flame cut-off frequency observed in the amplitude of the transfer function (figure 4.9(b)).

Apart from the low-pass behaviour of the FTFs, some distinct peaks can be observed in the amplitude of the transfer functions in figure 4.9(b). Firstly, all amplitudes show a peak at the cut-off frequency. An analysis in which particles are tracked in the central and outer recirculation zone shows that it is likely that this peak is caused by the outer recirculation zone. When the period is equal to the time that a particle needs to complete a full circulation in the outer recirculation zone, an interaction effect of the heat released in the previous period with the currently release heat occurs. This interaction shows up as a peak in the amplitude spectrum. Since approximately half of the outer recirculation zone consists of the flame, the time for a particle to complete the full outer recirculation zone is approximately twice the flame residence time. Therefore, the frequency at which a full wavelength fits in the outer recirculation zone corresponds to the frequency at which half a wavelength fits in the flame. Consequently, the peak always occurs at approximately the same frequency as the cut-off frequency.

Another peak that draws the attention is the low frequency peak at approxi-

mately 18 Hz in the amplitude of operating point 15.2. This peak is seen to be larger than one. FTFs amplitudes rising above one are also obtained from simulations and measurements by Gentemann *et al.* [57]. The fact that the amplitude rises above one indicates that periodically a larger and a smaller part of the buffer of fuel, enclosed by the flame, is burned. In other words, the volume of the flame becomes smaller and larger. The volume of the flame can be seen as the domain enclosed by the area in which relatively a large heat release rate occurs. This idea is visualised in figure 4.13, which shows the heat release rate field of the flame of operating point 15.1.

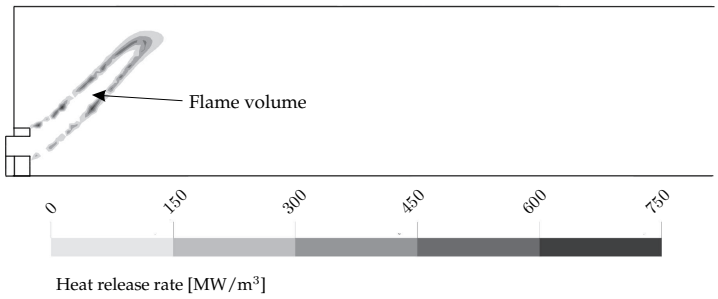

Figure 4.13: Flame volume defined by heat release rate field.

If the fuel buffer in the flame volume would remain the same, the transfer cannot rise above one, since mass conservation requires the amount of fuel that enters the domain to be equal to the amount of fuel that is being burned. In agreement with the findings of [161] it is possible that the flame front moves due to the excitation of the flame. This can induce a fluctuation in the fuel buffer and therefore an increase of the transfer function above one. A similar effect was measured in [97].

With the help of the impulse response and simulation results using sinusoidal excitation at specific frequencies, it will be proved that it is indeed a flame front movement that causes the FTF to rise above one. Moreover, the location of this movement will be identified, accompanied with suggestions about why this only happens for operating point 15.2.

The case 15.2 flame placed in the *circular geometry* is excited by a sinusoidal equivalence ratio perturbation at 13 and 29 Hz. A circular geometry is used to ease the visualisation of flame movement due to the effectively 2D periodic flow field. Figure 4.14 depicts $\left|\frac{Q/\Delta\phi}{Q/\bar{\phi}}\right|$ at both frequencies (the transfer function for this geometry is depicted in figure 4.15). It can be seen that indeed the amplitude of the heat release rate response at 13 Hz is larger than one. Also note the increased phase shift at 29 Hz compared to 13 Hz.

Another aspect that is observed in figure 4.14 is that there is no build up of the amplitude during the depicted period, i.e. the amplitude immediately rises above one. This means that there is no feedback mechanism involved and that it must be the volume oscillation of the flame (changing the buffer of fuel enclosed by the flame) that makes the amplitude overshoot above one.

The oscillation of the flame is visualised by comparing the heat release rate distri-

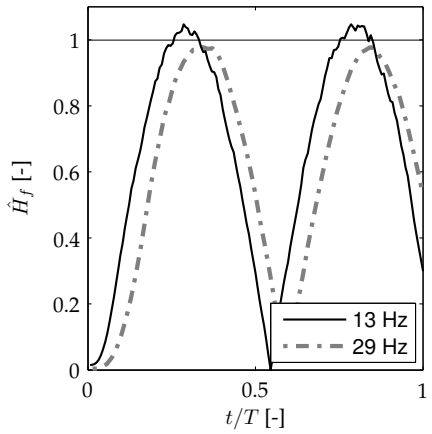

Figure 4.14: Volume integrated heat release rate response induced by a sinusoidal excitation at 13 and 29 Hz.

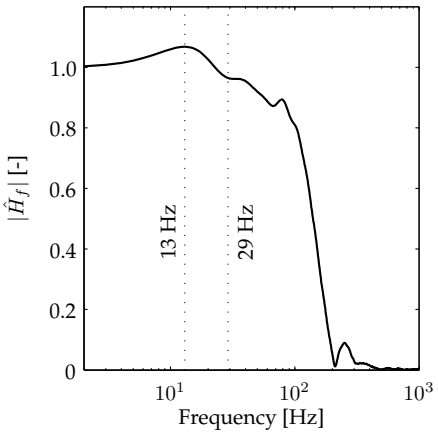

Figure 4.15: Amplitude of FTF for operating point 15.2 in the circular geometry.

bution of the 13 Hz oscillation and the 29 Hz oscillation. Because the excitation level is the same in both cases, the heat release rate field of both cases can be compared at the time steps where there is maximum and minimum heat release rate response. Figure 4.16(a) and (b) show the locations where the difference $\Delta Q = Q_{13Hz} - Q_{29Hz}$ is larger than $24\,\mathrm{MW\,m^{-3}}$ and smaller than $-24\,\mathrm{MW\,m^{-3}}$. Also the flame shape in the undisturbed situation is displayed (black line). At the time steps where maximum

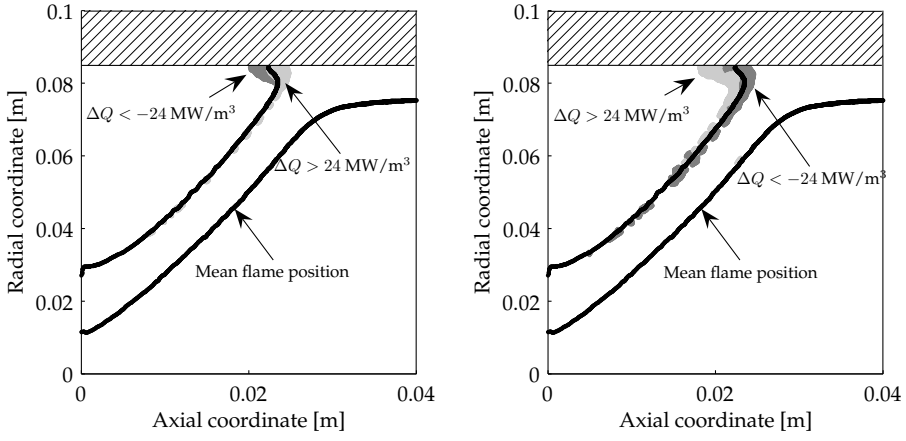

Figure 4.16: $\Delta Q = Q_{13Hz} - Q_{29Hz}$ at maximum (a) and minimum (b) of the response to sinus excitation.

heat release rate occurs for both frequencies (figure 4.16(a)), the difference between the heat release rate fields indicates that at 13 Hz, the flame is moved inwards compared to the oscillation at 29 Hz. It is seen that this movement especially occurs at the location where the flame touches the wall. At the time steps where minimum heat release rate occurs (figure 4.16(a)), exactly the opposite is true.

The difference between the heat release rate fields of the 13 Hz and 29 Hz excitation especially occurs at the position where the flame touches the wall. Here the flame front oscillates more severely at 13 Hz than it does at 29 Hz. This induces a fluctuation in the flame volume. Consequently, the buffer of fuel, enclosed by the flame, changes and therefore an increase of the transfer function above one at 13 Hz is observed. Because the flame impinges the wall almost perpendicularly at the location where the movement occurs, the flame front behaves less stiff there and an oscillation occurs at a low frequency, which can be dangerous from a thermo-acoustic point of view. Experiments also show a considerable effect of the wall on the dynamic combustion behaviour [126].

4.5 Perfectly premixed versus partially premixed

In this section, the differences in the FTF of the partially (imperfectly) premixed (IP) and perfectly premixed (PP) flame are pointed out. The boundary conditions of the compared cases correspond to operating point 15.1 (see table 3.2). Due to the large number of elements in the IP case, the transfer function is determined by impulse excitation. White noise excitation would require too much computational effort.

In the IP case, the perturbed variable is the fuel mass flow supply. This fuel mass flow fluctuation is converted to an equivalence ratio perturbation (see equation 2.60, $M'_a = 0$) to be able to compare the results with the perfectly premixed case. Figure 4.17 shows the obtained transfer functions for both cases at operating point 15.1.

The amplitude of the transfers shows that the cut-off frequency is almost similar for both cases. Nevertheless, peak locations are different for both cases. This can be explained by the fact that there is a whole range of equivalence ratios present in the flame. Accompanied by this range in equivalence ratios is a range in the burning velocity. This results in interaction effects at different frequencies. Nevertheless, the general behaviour of the FTF is the same for both cases.

The phase of the two cases shows a constant slope. From this, it can be concluded that a constant time delay exists between the excitation and the response. The time delay of the PP case can be determined at 1.5 ms. For the IP case, this time delay is 0.8 ms longer, i.e. 2.3 ms. This is not a characteristic of imperfect mixing. The longer time delay can be explained as follows. In the IP case the perturbation is imposed at the fuel injection nozzles, 45 mm upstream of the burner exit, while in the PP case, the perturbation is imposed 15 mm upstream of the burner exit. This causes an extra convective time delay.

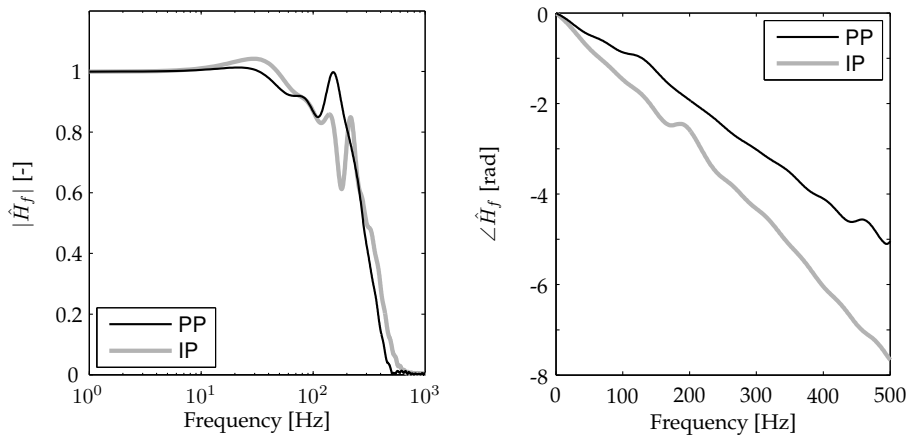

(a) Amplitude (b) Phase

Figure 4.17: Transfer function of the IP and PP flame at operating point 15.1.

4.6 Conclusions

With an analytical model, it has been shown that the typical low-pass filter behaviour of the flame transfer function can be completely attributed to the flame residence time. The finite time delay of the reaction itself also causes a cut-off of the flame transfer function spectrum. However, this cut-off frequency lies at a much higher frequency than the cut-off frequency due to the flame residence time, which was shown by a Well-Stirred Reactor (WSR) model.

To also account for flow effects, flame front movement and combustion, a method for determining a FTF from transient unsteady RaNS simulations has been presented. In these simulations, the flame is perturbed by white noise and impulse equivalence ratio perturbations. White noise excitation is a very suitable excitation method for this application. It gives a good linear fit of non-linear systems and the energy of the excitation can be equally distributed over the entire bandwidth, which results in a low crest factor, and reduces the danger for exciting non-linearities. When exciting the flame with impulse equivalence ratio perturbations, much less CPU time is required compared to white noise excitation, but the level of the excitation should be chosen with care: enough excitation must be applied to have a sufficient signal-to-noise ratio However, the excitation level must remain low enough not to excite non-linearities.

The FTF is determined for three different operating points. The amplitude and phase of the transfer functions have been presented. A low-pass behaviour is noticed, of which the cut-off frequency is mainly determined by the length of the flame, which in turn is coupled to the flame residence time. The larger this residence time, the higher the risk for low frequency peaks in the amplitude of the transfer function. This increases the risk for instabilities. Moreover, a constant time delay is ob-

served between the excitation and the response. This time delay corresponds to the convection time of a particle from the inlet boundary to the location at which the contribution to the total heat release rate is maximal.

It has been shown that a flame that is close to its extinction limit and touches the walls can inhibit low frequency oscillations. Close to extinction, the flame is less stiff to oscillations, especially at positions where it touches the walls. At those positions, oscillations of the flame front can result in low frequency peaks in the FTF.

When comparing the transfer functions of the PP and IP flame, it can be concluded that by assuming the flame as perfectly premixed, one makes an error in the amplitude of the flame transfer function. Still, the amplitude resulting from the PP case shows the similar behaviour as the IP transfer function.

A disadvantage of the transient CFD method for calculating the FTF is the required computational effort. Although impulse excitation already requires much less computational effort than white noise excitation, the amount of calculation time is still such that the method cannot be used as a design tool. To overcome this problem, a new method is developed. This method is called the *linear coefficient method*, and is the subject of the next chapter.

Chapter 5

The linear coefficient method

5.1 Introduction

An important drawback of the spectral method applied to numerical simulations is the required computational effort: lengthy transient simulations have to be performed to get an accurate result with reasonable frequency resolution. A much faster and more accurate method to calculate the transfer function can be derived by using one of the most important assumptions of spectral analysis: the fluctuations must be small enough for the system to behave linearly. This alternative method, which is called the *linear coefficient method*, uses the linear representation of the steady-state results. This linear response can be obtained *directly* from the steady-state solution and the knowledge of the equations that describe the CFD problem. Subsequently, the flame transfer function (FTF) can be calculated from this linear representation.

The maximum amplitude at which the flame still responses linearly to excitations can be questioned. Balachandran *et al.* [6] have measured that the volume integrated heat release rate of a turbulent swirling flame during a low frequency excitation in the equivalence ratio. They measure a linear response of the heat release rate up to excitation amplitudes as high as 35% (low swirl conditions) and 60% (high swirl conditions), both at a frequency of 160 Hz. At these limits, saturation of the flame response occurs and the non-dimensional heat release rate Q'/Q_0 starts to level off as a function of the excitation amplitude. The amplitude where non-linearity sets in is seen to depend strongly on the frequency. Flame kinematics has a major contribution to the saturation mechanism of the low swirl flame [73]. More experimental proof can be found for turbulent premixed flames behaving linearly at large excitation amplitudes. Finally, LES simulations performed on the DESIRE geometry showed no saturation effects (i.e. a linear response) of the heat release rate up to 80% pulsation of the fuel mass flow [164].

This chapter deals with the linear coefficient method [181], accompanied with an efficient order reduction algorithm. A significant gain in both speed and accuracy is observed when comparing the transfer function calculated from the linear representation and from spectral analysis. This makes the linear coefficient method suitable as a thermo-acoustic design tool.

5.2 The linear coefficient method

In this section, the implementation of the linear coefficient method will be discussed. Firstly, it is shown how the linearised equations can be cast in a more general form: the *state space system*. State space systems are typically used in control engineering to describe dynamical systems. The discussion on the state space system is followed by an example in which the FTF is calculated for the WSR using the linear coefficient method. The speed and accuracy of the method is compared with the conventional method in which the WSR is excited by white noise fluctuations (see chapter 4). Subsequently, the linear coefficient method is applied to a simple discretised system with convection.

5.2.1 State space system

The equations that are solved in a CFD simulation can be written as:

$$\frac{\partial \psi_i}{\partial t} = f(\psi_1, \psi_2, ..., \psi_n) \qquad i = 1, 2, .., n \tag{5.1}$$

in which ψ_i are the variables in the problem, n equals the number of variables. The index i is a unique number, indicating an *independent* variable at a node. Since each independent variable is present at each node, the variable number i is defined as:

$$i = n_{var}(i_{node} - 1) + i_{var} \tag{5.2}$$

in which i_{var} indicates the independent variable number (ranging from 1 to n_{var}, the number of independent variables at a node), and i_{node} is the node number (ranging from 1 to n_{node}, the number of nodes).

Solving equation 5.1 for $f = 0$ yields the steady-state values of the independent variables. Subsequently, small perturbations ψ_i' around these steady-state values $\bar{\psi}_i$ are considered (e.g. $\psi_i = \bar{\psi}_i + \psi_i'$). Linearisation of the resulting equations yields the following equations:

$$\frac{\mathrm{d}\psi_i'}{\mathrm{d}t} = \sum_{j=1}^{n} a_{ij}\psi_j' \qquad i = 1, 2, .., n \tag{5.3}$$

in which a_{ij} are the coefficients representing the linear relationship between a fluctuation in ψ_j and the rate of increase in time of ψ_i. Note that a higher order Taylor expansion around the steady solution would yield higher order coefficients, making it possible to describe also non-linear deviations from the steady solution.

Combining the linear coefficients in a system matrix $\mathbf{A}$, equation 5.3 can be written as:

$$\frac{\mathrm{d}\mathbf{\Psi}'}{\mathrm{d}t} = \mathbf{A}\mathbf{\Psi}' \tag{5.4}$$

The coefficient matrix $\mathbf{A}$ contains the linear coefficients a_{ij} and the vector $\mathbf{\Psi}'$ is the vector with the independent variables $\{\psi_1', \psi_2', ..., \psi_n'\}^T$. The coefficient matrix includes the coupling between the nodes. This coupling comes from the discretised

spatial derivatives in the equations (multiple nodes contribute to the gradient at a specific location, see also appendix C).

For CFD problems the matrix $\mathbf{A}$ is very sparse. For a single-step combustion simulation with a finite rate combustion model, 11 equations per node are solved ($n_{var} = 11$). These equations are solved at n_{node} nodes. If each node is coupled to maximal $c = 20$ other nodes, the sparsity (non-zero elements divided by total number of elements) of the matrix $\mathbf{A}$ (with dimensions $n_{var}n_{node} \times n_{var}n_{node}$) equals:

$$S = \frac{(c+1)n_{var}(n_{var}n_{node})}{n_{var}^2 n_{node}^2} = \frac{(c+1)}{n_{node}} \tag{5.5}$$

For $c = 20$ and $n_{node} = 25,000$, the sparsity $S = 8.4 \cdot 10^{-4}$. It is interesting to see that the sparsity decreases for increasing number of nodes, since obviously the average bandwidth of the matrix, determined by c, is approximately constant in case of a regular mesh. Consequently relatively less non-zero coefficients are encountered for larger problems.

An example of the sparsity map of the matrix $\mathbf{A}$ for a CFD problem is illustrated in figure 5.1(a). In figure 5.1(b) a preconditioned version of the matrix is shown, using the preconditioner '`au_pre`' of the LYAPACK software [131, 132]. This preconditioner consists of a transformation of the matrix $\mathbf{A}$, such that the transformed data has an improved structure from the numerical point of view, while still the original system is represented. Basically, preconditioners apply linear transformations to the state-vector $\mathbf{\Psi}'$. It can be seen that the average bandwidth of the matrix is strongly reduced by this preprocessing step.

When inlet quantities of the system are perturbed, these quantities should be included in the unsteady equations. It is assumed that only one input variable is

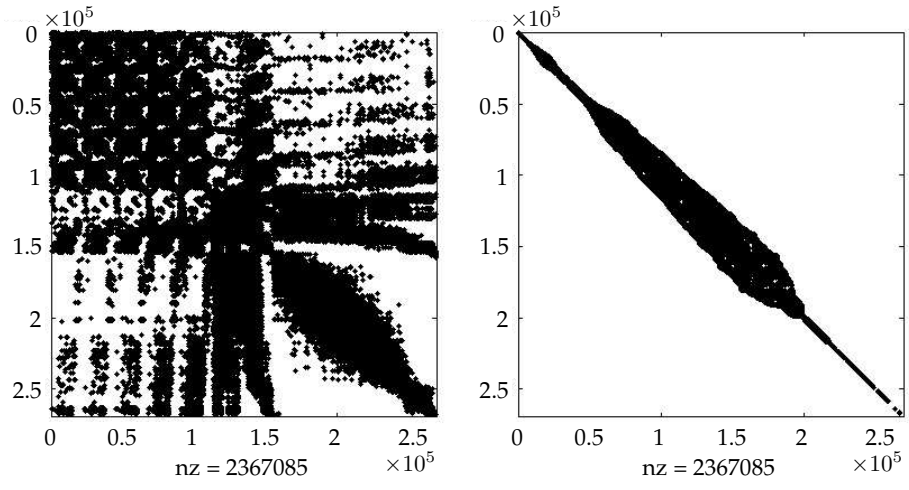

(a) Original (b) Preconditioned

Figure 5.1: Sparsity maps of the coefficient matrix $\mathbf{A}$.

fluctuated. The unsteady part due to a fluctuating inlet variable ϕ' is linearised and added to equation 5.4:

$$\frac{\mathrm{d}\mathbf{\Psi}'}{\mathrm{d}t} = \mathbf{A}\mathbf{\Psi}' + \mathbf{B}\phi' \tag{5.6}$$

in which $\mathbf{B}$ is a vector describing the linear influence of ϕ' on $\frac{\mathrm{d}\mathbf{\Psi}'}{\mathrm{d}t}$.

For FTF calculations, the single output of the system is the volume integrated unsteady heat release rate. This unsteady heat release rate Q' is a function of the unsteady variables $\mathbf{\Psi}'$ and of the fluctuating inlet variable ϕ'. This function can be linearised, resulting in the following expression:

$$Q' = \mathbf{C}\mathbf{\Psi}' + D\phi' \tag{5.7}$$

in which $\mathbf{C}$ is a vector and D is a scalar, both containing coefficients describing the linear influence on the equation for the unsteady heat release rate.

The matrix $\mathbf{A}$, vectors $\mathbf{B}$ and $\mathbf{C}$, and the scalar D in equations 5.6 and 5.7 describe the linear system in a state space formulation. The sizes of these matrices are shown schematically in figure 5.2. In this figure, the matrices for a single input, single output (SISO) system are shown, such that $m = 1$ and $p = 1$, respectively. All state space systems considered in this thesis are of this type. Moreover, the size of the system is denoted as n.

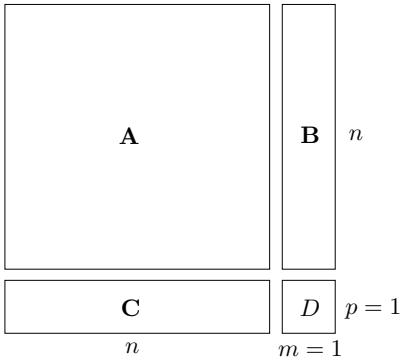

Figure 5.2: Schematic overview of the state space matrices for a SISO system.

Assuming a harmonic time-dependence of the fluctuating quantities, the transfer function H between the input ϕ' and the output Q' at a specific angular frequency ω can be calculated directly from the state space matrices [54]:

$$H(\omega) = \frac{Q'}{\phi'} = \mathbf{C}(\mathrm{i}\omega\mathbf{I} - \mathbf{A})^{-1}\mathbf{B} + D \tag{5.8}$$

where $\mathbf{I}$ is the identity matrix. Using this method, there are *no* truncation errors in time, in contrast to the transfer function obtained from a transient calculation. Moreover, no transient run has to be performed, as the state space matrices can be determined from the steady solution.

The order of the linear model is equal to the product of the number of nodes in the mesh and the number of independent variables that are solved at each node. For medium-sized systems (up to $\mathcal{O}(10^3)$), the transfer function can be explicitly calculated from the state space matrices using equation 5.8. One of the many methods available consists of the following steps:

1. Calculate $\mathbf{X} = \mathrm{i}\omega\mathbf{I} - \mathbf{A}$.
2. Calculate the term $\mathbf{Y} = \mathbf{X}^{-1}\mathbf{B}$. This can be done efficiently by first calculating the lower-upper triangularisation of the sparse matrix $\mathbf{X}$ (by Gaussian elimination, basically) to obtain $\mathbf{X} = \mathbf{LU}$. Subsequently $\mathbf{Y}$ is obtained by solving the system:

   $$\mathbf{LUY} = \mathbf{B} \tag{5.9}$$

   which can be solved efficiently by forward and backward substitution. The computational costs of this step depend on the sparsity structure of the matrix $\mathbf{A}$. The more the coefficients are located near the diagonal, and the less the bandwidth of the matrix, the faster the step is and the less memory it costs. Therefore, preconditioners are applied prior to this step. Still, the costs of step 2 is relatively high. The fact that the system that has to be solved has an imaginary part increases the required memory. This makes step 2 inappropriate for large scale problems.
3. The last operation is an addition and matrix-multiplication of the previously obtained results, i.e.:

   $$H(\omega) = \mathbf{CY} + D \tag{5.10}$$

To calculate a transfer function for large systems ($> \mathcal{O}(10^3)$), the order of the state space system is first reduced by a reduction technique, approximating the original system by a reduced order system. The technique removes insignificant information from the matrices. The reduction technique used in this thesis will be discussed in section 5.3.

5.2.2 Application to the WSR

As an example, the FTF of the WSR is determined with the linear coefficient method and compared with the FTF resulting from a transient calculation with white noise equivalence ratio perturbations. These transient calculations take about 1 day on a single CPU, while the state space calculation takes only a few seconds (three independent variables: the fuel and air mass fraction and the temperature of the reactor). A first order backward Euler time discretisation is used in the transient calculations. Two different time steps are compared: $2.5 \cdot 10^{-5}$ and $6.25 \cdot 10^{-6}$ s to show the effect of the truncation error. The resulting transfer functions are shown in figure 5.3.

It is clear that when the time step is decreased, the results of the transient calculations move closer to the result of the linear coefficient method (this is especially true for the phase at higher frequencies), indicating that the linear coefficient method does not contain truncation errors.

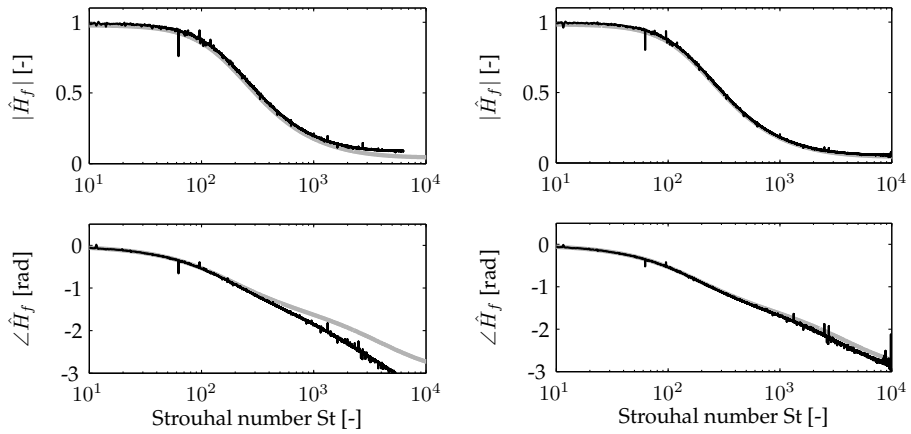

(a) $\Delta t = 2.5 \cdot 10^{-5}$ (b) $\Delta t = 6.25 \cdot 10^{-6}$

Figure 5.3: Comparison FTF obtained from a transient calculation with an excitation level of 1% (——) and from the linear coefficient method (▬).

5.2.3 Application to CFD

To obtain the state space formulation of a CFD simulation, the linear coefficients of the state space matrices need to be determined. In principle, when the equations that are solved and the spatial discretisation that is used are known, one could calculate the coefficients. In CFX 5.6, the equations are mostly solved sequentially, and iterations are applied to converge the problem to a solution. Because of this sequential approach, a full coefficient matrix in which all couplings are present is never constructed during the solving process. The largest coefficient matrix that is constructed is the matrix for the hydrodynamic equations, i.e. the momentum and mass balance equations. A modification to the solver code would be necessary to extract the coefficient matrices from CFX. Too little time was available to realise this. Therefore, to validate and test the method, the discretisation of the equations has been implemented in MATLAB. The same discretisation approach as used by CFX is applied (see appendix C).

The MATLAB program to obtain the coefficients is called CFX2FTF. The flowchart of CFX2FTF is given in appendix H. This appendix also includes a description of its main components. In CFX2FTF the mesh and the variable values from a steady-state converged CFX solution are imported. Using this information, the time derivatives of the equations can be calculated. Subsequently, the coefficients of the state space matrices can be calculated by monitoring how the transient derivatives change when independent variables are given a slightly different value. This way, the component a_{ij} of the $\mathbf{A}$ matrix can be obtained by changing variable ψ_j with a value $\Delta\psi_j$ and calculating the response of the time derivative of variable ψ_i, according to:

$$a_{ij} = \frac{\mathrm{d}\psi_i'}{\mathrm{d}t} \,/\, \Delta\psi_j \tag{5.11}$$

where $\frac{\mathrm{d}\psi_i'}{\mathrm{d}t}$ is calculated from the difference between the time derivative of the perturbed situation and the steady, unperturbed situation (which ideally would be zero).

The coefficients of the **C** matrix give the relationship between a fluctuation in the volume integrated heat release rate and the perturbed variable, i.e.:

$$c_j = \frac{Q^{new} - Q^s}{\Delta\psi_j} \tag{5.12}$$

The integrated heat release is a global variable, so the **C** matrix is one-dimensional. The superscripts s and new indicate the steady, unperturbed situation and the perturbed situation, respectively.

After the **A** and **C** matrices have been calculated, the **B** and D matrices can be constructed from them. The **B** matrix represents the difference in the time derivatives as a result of an equivalence ratio perturbation ϕ' at the inlet of the domain. In a general simulation, the fuel and air mass fractions y_f and y_a can be expressed as a function of the CH_4 and O_2 mass fractions, according to:

$$y_f = y_{CH4}/c_f \tag{5.13}$$

$$y_a = y_{O2}/c_a \tag{5.14}$$

where c_f and c_a are the mass fractions of CH_4 and O_2 present in the fuel and air, respectively. Writing everything in terms of y_{CH4} and y_{O2} gives the following expression for the equivalence ratio at the inlet:

$$\phi_{in} = \frac{c_a y^{in}_{CH4}/(c_f y^{in}_{O2})}{[y_f/y_a]_{st}} \tag{5.15}$$

Because at the inlet $y^{in}_f + y^{in}_a = y^{in}_{CH4}/c_f + y^{in}_{O2}/c_a = 1$, y^{in}_{O2} can be written as a function of y^{in}_{CH4} according to:

$$y^{in}_{O2} = c_a - c_a y^{in}_{CH4}/c_f \tag{5.16}$$

Substituting this expression in equation 5.15 and solving for y^{in}_{CH4} yields:

$$y^{in}_{CH4} = \frac{\phi_{in}[y_f/y_a]_{st} c_f}{1 + \phi_{in}[y_f/y_a]_{st}} \tag{5.17}$$

Linearising equation 5.17 around the mean value $\overline{\phi}$ results in the following expression for the perturbation ${y^{in}_{CH4}}'$ as a function of ϕ':

$${y^{in}_{CH4}}' = \left[\frac{c_f[y_f/y_a]_{st}}{(1 + [y_f/y_a]_{st}\overline{\phi})^2}\right]\phi' \tag{5.18}$$

Since ${y^{in}_{CH4}}'/c_f + {y^{in}_{O2}}'/c_a = 0$:

$${y^{in}_{O2}}' = -\left[\frac{c_a[y_f/y_a]_{st}}{(1 + [y_f/y_a]_{st}\overline{\phi})^2}\right]\phi' \tag{5.19}$$

The coefficients corresponding to a perturbation of ${y^{in}_{CH4}}'$ and ${y^{in}_{O2}}'$ are known from the **A** and **C** matrices. The coefficients of both ${y^{in}_{CH4}}'$ and ${y^{in}_{O2}}'$ at a node at the

inlet boundary together determine the coefficient corresponding to a perturbation in the equivalence ratio ϕ'. Therefore, the $\mathbf{B}$ and D matrices can be obtained from the $\mathbf{A}$ and $\mathbf{C}$ matrices, respectively, using the following procedure:

$$b_{i,1} = \left[\frac{[y_f/y_a]_{st}}{(1+[y_f/y_a]_{st}\overline{\phi})^2}\right](c_f a_{i,y^{in}_{CH4}} - c_a a_{i,y^{in}_{O2}}) \tag{5.20}$$

$$d = \left[\frac{[y_f/y_a]_{st}}{(1+[y_f/y_a]_{st}\overline{\phi})^2}\right](c_f c_{1,y^{in}_{CH4}} - c_a c_{1,y^{in}_{O2}}) \tag{5.21}$$

such that $\mathbf{B}$ becomes a $n_{var}n_{node} \times 1$ matrix, and D becomes a scalar. In the above expressions, y^{in}_{CH4} and y^{in}_{O2} in the subscript of a coefficient stand for the sum of *all* the global variable numbers which indicate the local variable y_{CH4} and y_{O2}, respectively, and are located at the inlet.

The formulation of the equations must be such that *only* the time derivative of the independent variable is explicitly output. A very straightforward way of doing so is to use the chain rule. When this rule is applied to the species transport equation it can be reformulated as:

$$\frac{\partial \tilde{y}_i}{\partial t} = \left(-\nabla\cdot(\bar{\rho}\tilde{\mathbf{u}}\tilde{y}_i - (\bar{\rho}D_i + \frac{\mu_t}{\mathrm{Sc}_t})\nabla\tilde{y}_i) + \bar{\omega}_i - \tilde{y}_{i,0}\frac{\partial\bar{\rho}}{\partial t}\right)/\bar{\rho}_0 \tag{5.22}$$

where the terms with a subscript 0 should not be perturbed when retrieving the coefficients. The term $\frac{\partial\bar{\rho}}{\partial t}$ can be obtained from the mass balance equation. However, the chain rule cannot be applied like this on the discretised system in a finite volume arrangement. The reason for this is that while the following equation is true:

$$\int_V \frac{\partial\bar{\rho}\tilde{y}_i}{\partial t}\mathrm{d}V = \int_V \bar{\rho}\frac{\partial\tilde{y}_i}{\partial t}\mathrm{d}V + \int_V \tilde{y}_i\frac{\partial\bar{\rho}}{\partial t}\mathrm{d}V \tag{5.23}$$

its discretised form is not necessarily true:

$$\left(\frac{\partial\bar{\rho}\tilde{y}_i}{\partial t}\right)_{node} V \neq \left(\bar{\rho}\frac{\partial\tilde{y}_i}{\partial t}\right)_{node} V + \left(\tilde{y}_i\frac{\partial\bar{\rho}}{\partial t}\right)_{node} V \tag{5.24}$$

A better, more conserved approach is to immediately incorporate the mass balance equation in the species transport equation:

$$\frac{\partial \tilde{y}_i}{\partial t} = \left(-\nabla\cdot(\bar{\rho}\tilde{\mathbf{u}}\tilde{y}_i - \bar{\rho}\tilde{\mathbf{u}}\tilde{y}_{i,0} - (\bar{\rho}D_i + \frac{\mu_t}{\mathrm{Sc}_t})\nabla\tilde{y}_i) + \bar{\omega}_i\right)/\bar{\rho}_0 \tag{5.25}$$

$$= \left(-\nabla\cdot(\bar{\rho}\tilde{\mathbf{u}}(\tilde{y}_i - \tilde{y}_{i,0}) - (\bar{\rho}D_i + \frac{\mu_t}{\mathrm{Sc}_t})\nabla\tilde{y}_i) + \bar{\omega}_i\right)/\bar{\rho}_0 \tag{5.26}$$

Note the subtle difference with equation 5.22: in the discretisation, $\tilde{y}_{i,0}$ is now determined at the integration points, while in equation 5.22 it would have been evaluated at the node. The latter approach is used in the implemented linear coefficient method. The procedure is also applied to the other equations. For example, the time

derivative of the enthalpy can be written as:

$$\frac{\partial \bar{\rho}\tilde{h}_{tot}}{\partial t} = \tilde{h}_{tot,0}\frac{\partial \bar{\rho}}{\partial t} + \bar{\rho}_0\frac{\partial \tilde{h}_{tot}}{\partial t} \tag{5.27}$$

$$= -\nabla\cdot(\bar{\rho}\tilde{\mathbf{u}}\tilde{h}_{tot,0}) + \bar{\rho}_0\left(\sum \tilde{h}^i_{tot,0}\frac{\partial \tilde{y}_i}{\partial t} + c_{p,0}\frac{\partial \tilde{T}}{\partial t}\right) \tag{5.28}$$

The equation for the enthalpy can now be reformulated such that only the independent variable T appears at the LHS of the equation. The time derivatives of the independent variables y_i appear at the RHS of the equations, and can be obtained from the species transport equations.

The boundary conditions do not have to be treated differently from the rest of the nodes. The equations at the boundary always have to satisfy the boundary conditions. This means than when, for example, an outlet boundary condition of $p_{out} = 0$ is imposed, a perturbation in the pressure p_i at a node that is connected to this boundary condition does not affect this boundary condition. This means that the coefficient $\frac{\partial p'_{out}}{\partial t}$ / $\Delta p_i = 0$. A similar reasoning applies to nodes at the wall.

Example

The ability of the state space method to calculate the transfer function for a discretised system with convection is shown with the help of a one-dimensional example. The example is constructed such that it has all the main features that are present in a real FTF calculation. It shows, among others, that the state space method is well able to predict convective time delays because of the fact that elements are coupled by discretised gradients. The conventions and geometry of the one-dimensional model are shown in figure 5.4.

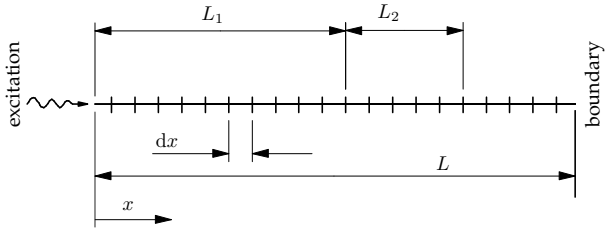

Figure 5.4: Conventions and system layout for simple test case of the state space method.

The grid size $\mathrm{d}x$ in figure 5.4 depends on the length L and the desired number of elements, according to $\mathrm{d}x = L/n$, in which n is the number of elements. By choosing n, the size of the state space system can be varied. This size is equal to $n+1$ (number of nodes). At the left-hand side of the model ($x = 0$), an excitation is applied in an independent variable α. This excitation is convected over a length L_1. Subsequently, over a length L_2 the fluctuating quantity causes a response equal to $h_f\mathrm{d}x$, in which h_f is the local specific transfer function, i.e. the amplitude of the local response due

to a local excitation in α_i. After this length L_2 the fluctuation is convected farther and does not return (i.e. no reflection at the boundary).

On the grid displayed in figure 5.4 an incompressible convection equation for variable α is discretised using the first order upwind scheme:

$$\frac{\partial \alpha}{\partial t} = -u_0 \frac{\partial \alpha}{\partial x} \qquad \Rightarrow \qquad \frac{\Delta \alpha_i}{\Delta t} = \frac{u_0}{\mathrm{d}x}(\alpha_{i-1} - \alpha_i) \tag{5.29}$$

in which u_0 is the convection velocity. The subscript of the convected variable α indicates the node number, starting with node 1 at $x = 0$. With this discretisation, and assuming an excitation of α at $x = 0$, the matrices $\mathbf{A}$, $\mathbf{B}$, $\mathbf{C}$ and D can be constructed as:

$$\mathbf{A} = \begin{bmatrix} 0 & 0 & 0 & 0 & 0 & 0 & 0 \\ 0 & -\frac{u_0}{\mathrm{d}x} & 0 & \ddots & \ddots & \ddots & 0 \\ 0 & \frac{u_0}{\mathrm{d}x} & -\frac{u_0}{\mathrm{d}x} & 0 & \ddots & \ddots & 0 \\ 0 & 0 & \ddots & \ddots & 0 & \ddots & 0 \\ 0 & \ddots & 0 & \ddots & \ddots & 0 & 0 \\ 0 & \ddots & \ddots & 0 & \ddots & \ddots & 0 \\ 0 & 0 & 0 & 0 & 0 & \frac{u_0}{\mathrm{d}x} & -\frac{u_0}{\mathrm{d}x} \end{bmatrix} ; \mathbf{B} = \begin{bmatrix} -\frac{u_0}{\mathrm{d}x} \\ \frac{u_0}{\mathrm{d}x} \\ 0 \\ \vdots \\ \vdots \\ \vdots \\ 0 \end{bmatrix}$$

$$\mathbf{C} = \begin{bmatrix} 0 & 0 & h_f \mathrm{d}x & h_f \mathrm{d}x & 0 & \dots & 0 \end{bmatrix} ; D = 0 \tag{5.30}$$

It can be seen that the $\mathbf{A}$ matrix contains the coefficients that are also seen in the upwind discretisation of the convection equation. Moreover, the $\mathbf{C}$ matrix contains coefficients $h_f \mathrm{d}x$.

Assuming a constant amplitude h_f along L_2, the volume integrated transfer function H_f can be calculated analytically (see equations 4.7 and 4.8). For this specific case, the time delays in these equations can be expressed as $\tau_1 = L_1/u_0$ and $\tau_2 = (L_1 + L_2)/u_0$. In this example, the following values are used: $u_0 = 20$ m s^{-1}, $L_1 = 0.2$ m, $L_2 = 0.1$ m, $h_f = 1$. Since the perturbations are not reflected at the end, the value of L does not influence the solution.

Two grids are considered: $n = 1,000$ and $n = 10,000$. In figure 5.5, the analytical transfer function is compared to the transfer function obtained with the state space method applied to the two different grids. Because the order of the model is still relatively low, the direct method (see section 5.2.1) is used to calculate the transfer function from the state space matrices.

It can be seen that at low frequencies, the transfer function is calculated correctly for both meshes. At higher frequencies, however, the mesh size starts to influence the solution and the deviation from the analytical model becomes larger. Note that this is a problem of the numerical discretisation, and *not* of the state space method. A similar result would be obtained by using transient methods to numerically obtain the transfer function. The required CPU times to obtain the transfer function are 1.2 and 20 seconds for $n = 1,000$ and $n = 10,000$ respectively. Both calculations are performed on a single AMD 1800+ CPU. It must be remarked that because of the band-structure of the coefficient matrix, it is possible to do a direct calculation for a

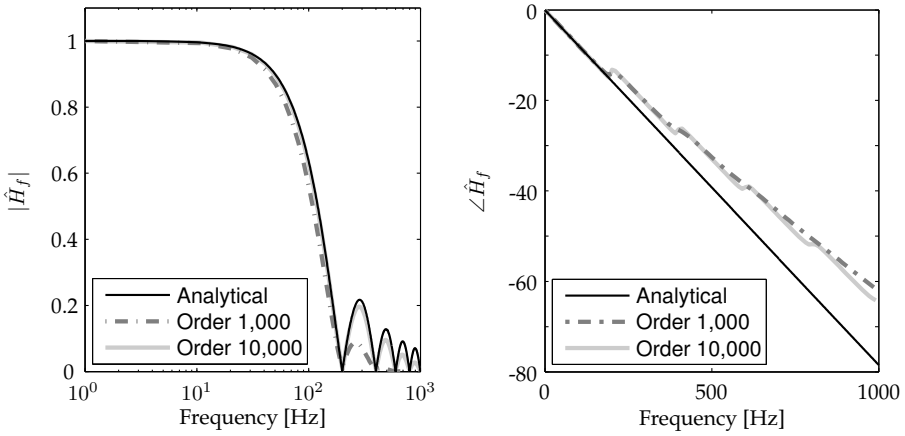

(a) Amplitude (b) Phase

Figure 5.5: FTFs obtained with the linear coefficient method and with the analytical solution of equations 4.7 and 4.8.

relatively high order. With a coefficient matrix where the coefficients are farther from the diagonal, this becomes more difficult (the LU factorisation then fills the matrix).

5.3 Reduction methods

When applying the state space method to CFD problems, the size of the linear model increases dramatically. Typically, the order of the linear representation of a CFD problem is larger than $\mathcal{O}(10^6)$. This large order requires an order reduction step to be applied prior to using the representation for calculating the transfer function. For an overview of reduction methods for large-scale dynamic systems, see [2, 5]. In this thesis, the Implicitly Restarted and Shifted Lanczos method is used to reduce the order of the linear representation. The order reduction step is discussed in this section.

With reduction techniques the full state space system (equations 5.6 and 5.7) is approximated by a dimensionally smaller state space system of the form:

$$\frac{\mathrm{d}\hat{\mathbf{\Psi}}'}{\mathrm{d}t} = \hat{\mathbf{A}}\hat{\mathbf{\Psi}}' + \hat{\mathbf{B}}\phi' \tag{5.31}$$

$$Q' = \hat{\mathbf{C}}\hat{\mathbf{\Psi}}' + D\phi' \tag{5.32}$$

in which the matrices with the hats are low-dimensional projections of the full matrices.

To obtain the reduced order system from the original system, $\mathbf{\Psi}'$ is approximated by $\mathbf{Q_k}\hat{\mathbf{\Psi}}'$, where $\mathbf{Q_k}$ is an orthonormal* projector matrix of size $n \times k$, in which k is

*A matrix $\mathbf{A}$ is orthonormal if $\mathbf{A}^T\mathbf{A} = \mathbf{I}$. This implies that $\mathbf{A}^T = \mathbf{A}^{-1}$.

the order of the reduced model. When this expression for $\mathbf{\Psi}'$ is substituted into the original state space system, the following system is obtained:

$$\mathbf{Q_k}\frac{\mathrm{d}\hat{\mathbf{\Psi}}'}{\mathrm{d}t} = \mathbf{A}\mathbf{Q_k}\hat{\mathbf{\Psi}}' + \mathbf{B}\phi' \tag{5.33}$$

$$Q' = \mathbf{C}\mathbf{Q_k}\hat{\mathbf{\Psi}}' + D\phi' \tag{5.34}$$

Premultiplying the first equation with $\mathbf{Q_k}^T$, for which holds that $\mathbf{Q_k}^T\mathbf{Q_k} = \mathbf{I_k}$ (orthonormal projector matrix), this equation can be written as:

$$\frac{\mathrm{d}\hat{\mathbf{\Psi}}'}{\mathrm{d}t} = \mathbf{Q_k}^T\mathbf{A}\mathbf{Q_k}\hat{\mathbf{\Psi}}' + \mathbf{Q_k}^T\mathbf{B}\phi' \tag{5.35}$$

$$Q' = \mathbf{C}\mathbf{Q_k}\hat{\mathbf{\Psi}}' + D\phi' \tag{5.36}$$

Hence $\hat{\mathbf{A}} = \mathbf{Q_k}^T\mathbf{A}\mathbf{Q_k}$, $\hat{\mathbf{B}} = \mathbf{Q_k}^T\mathbf{B}$ and $\hat{\mathbf{C}} = \mathbf{C}\mathbf{Q_k}$.

The problem is now reduced to finding the orthonormal projector $\mathbf{Q_k}$. This is done with the Lanczos method [61], which, in its origin, is an inexpensive, iterative method to obtain a few largest and/or smallest eigenvalues of a matrix.

The general unsymmetrical version of the Lanczos method is explained in appendix I (see also Golub and van Loan [59]). In the next section, it is shown how the method can serve as a state space model reduction tool. After this, two methods are presented which can be used to overcome the following problems:

1. Due to a poorly chosen starting vector for the Lanczos iteration a stable full system can be transformed into an unstable reduced system. One can implicitly modify the matrix $\mathbf{Q_k}$ and pass immediately to a stable version of the reduced model. This procedure is called the Implicitly Restarted Lanczos method (see Grimme *et al.* [61]).

2. By 'shifting' the coefficient matrix a so-called breakdown of the procedure can be prevented. Moreover, a better approximation around a chosen frequency is obtained.

5.3.1 Lanczos and model reduction

The idea is to use the Lanczos method to match the moments of the transfer function of the linear unreduced system with the reduced system. With the Lanczos method the matching of the moments is done *without* explicitly calculating these moments. The advantage of this becomes clear later in this section.

The moments of the transfer function are the coefficients of a power series expansion of $H(s)$. Expanding the transfer function $H(s) = \mathbf{C}(s\mathbf{I} - \mathbf{A})^{-1}\mathbf{B}$ (for simplicity, D is assumed zero, which is a valid assumption for the systems considered here, where there is a time delay between the location of excitation and the response) in a Taylor series around $s = \sigma$ yields:

$$H(s) = \mathbf{C}(\sigma\mathbf{I} - \mathbf{A})^{-1}\mathbf{B} - \mathbf{C}(\sigma\mathbf{I} - \mathbf{A})^{-2}\mathbf{B}\frac{(s-\sigma)}{1!} + 2\mathbf{C}(\sigma\mathbf{I} - \mathbf{A})^{-3}\mathbf{B}\frac{(s-\sigma)^2}{2!}... \tag{5.37}$$

which can be written more compact as:

$$H(s) = \sum_{j=0}^{\infty} -\mathbf{C}(\mathbf{A} - \sigma\mathbf{I})^{-j}(\mathbf{A} - \sigma\mathbf{I})^{-1}\mathbf{B}(s-\sigma)^j \tag{5.38}$$

$$= \sum_{j=0}^{\infty} \eta_j(\sigma)(s-\sigma)^j \tag{5.39}$$

where $\eta_j(s=\sigma)$ are the moments of the power series:

$$\eta_j(s=\sigma) \equiv \mathbf{C}(\mathbf{A} - \sigma\mathbf{I})^{-j}(\sigma\mathbf{I} - \mathbf{A})^{-1}\mathbf{B} \tag{5.40}$$

To obtain an expansion around $\sigma = \infty$, the Initial Value Theorem known from the Laplace transformation is used:

$$\lim_{s\to\infty} sG(s) = \lim_{t\to 0} g(t) \tag{5.41}$$

where $G(s)$ is the Laplace transform of $g(t)$. The expansion around $\sigma = \infty$ can thus be obtained by letting the time t go to zero in the inverse Laplace transform of $G(s) = H(s)/s$. This inverse Laplace transform can be calculated as:

$$g(t) = \mathcal{L}^{-1}\left\{\frac{H(s)}{s}\right\} = \int_{t=0}^{t} \mathbf{C}\mathrm{e}^{\mathbf{A}t}\mathbf{B}\mathrm{d}t \tag{5.42}$$

Expanding this expression around $t = 0$ yields:

$$g(t) = \mathbf{CB}\frac{t}{1!} + \mathbf{CAB}\frac{t^2}{2!} + \mathbf{CA}^2\mathbf{B}\frac{t^3}{3!}... \tag{5.43}$$

$$= \sum_{j=1}^{\infty} \mathbf{CA}^{j-1}\mathbf{B}\frac{t^j}{j!} \tag{5.44}$$

Using now the Laplace identity $\mathcal{L}\{t^n\} = n!/s^{n+1}$ the power series expansion for $H(s)$ around $\sigma = \infty$ can be obtained by Laplace transforming expression 5.44, yielding:

$$H(s) = sG(s) = \mathbf{CB}s^{-1} + \mathbf{CAB}s^{-2} + \mathbf{CA}^2\mathbf{B}s^{-3}... \tag{5.45}$$

$$= \sum_{j=1}^{\infty} \mathbf{CA}^{j-1}\mathbf{B}s^{-j} \tag{5.46}$$

which results in the following expression for the moments (known as Markov parameters):

$$\eta_j(\sigma = \infty) \equiv \mathbf{CA}^{j-1}\mathbf{B} \tag{5.47}$$

By matching as many moments as possible, the reduced system gives an approximation of the full system.

When comparing the moments obtained when expanding the transfer function around a general σ (equation 5.40) and around $\sigma = \infty$ (equation 5.47) it can be seen

that the former can be obtained by the latter by substituting $\mathbf{A} = (\mathbf{A} - \sigma\mathbf{I})^{-1}$ and $\mathbf{B} = (\sigma\mathbf{I} - \mathbf{A})^{-1}\mathbf{B}$. This is the basis of the Shifted or Rational (since the resulting reduced order model interpolates the transfer function and its derivatives at a single point σ) Lanczos method, which will be discussed in section 5.3.3.

With the general Lanczos method the expansion around $\sigma = \infty$ is matched. This means that the moments of equation 5.47 are matched. In principle, one can simply calculate the moments and obtain a lower order expression for the transfer function. Especially for the expansion of $H(s)$ around $\sigma = \infty$, this would not be very computationally nor memory expensive, since it only requires repeated matrix vector multiplications. However, the computation of these moments has shown to be numerically problematic [55], since the powers of the eigenvalues of $\mathbf{A}$ grow exponentially fast (many eigenvalues have a magnitude larger than 1). This is the reason why the Lanczos method is used: it matches the moments of the transfer function expansion, without explicitly calculating the moments, but by projecting the state space matrices on a reduced space.

In appendix I, it is shown that performing k unsymmetrical Lanczos iterations results in a tridiagonal matrix $\hat{\mathbf{A}}$ such that $\hat{\mathbf{A}} = {\mathbf{P_k}}^{-1}\mathbf{A}\mathbf{Q_k}$, where also $\mathbf{P_k}$ (=${\mathbf{Q_k}}^{-T}$, see appendix I) and $\mathbf{Q_k}$ are results of the unsymmetrical Lanczos iterations. The matrices $\mathbf{P_k}$ and $\mathbf{Q_k}$ satisfy the biorthogonality condition and the Krylov subspace conditions:

$$\text{span}(\mathbf{Q_k}) = \mathcal{K}(\mathbf{A}, \mathbf{B}, k) = \{\mathbf{B}, \mathbf{AB}, \mathbf{A}^2\mathbf{B}, ..., \mathbf{A}^{k-1}\mathbf{B}\} \tag{5.48}$$

$$\text{span}(\mathbf{P_k}) = \mathcal{K}(\mathbf{A}^T, \mathbf{C}^T, k) = \{\mathbf{C}^T, \mathbf{A}^T\mathbf{C}^T, (\mathbf{A}^2)^T\mathbf{C}^T, ..., (\mathbf{A}^{k-1})^T\mathbf{C}^T\} \tag{5.49}$$

It is the construction and use of these two subspaces which connect the Lanczos method to moment matching. From a control point of view, these subspaces span the space in which the *reachability* and the transposed *observability* matrices lie. This means that the matrices span the spaces of the reachable states by controlling with the input ϕ' and the observable initial states when the response and excitation are known, respectively.

The matrices $\mathbf{P_k}$ and $\mathbf{Q_k}$ project the original full order matrix onto those subspaces, resulting in a tridiagonal matrix $\hat{\mathbf{A}}$ which has the *same* first $2k$ moments as the original matrix. This can be shown by noting that for any polynomial function $\mathcal{P}$ there holds:

$$\mathcal{P}(\mathbf{A})\mathbf{Q_k} = \mathbf{Q_k}\mathcal{P}(\hat{\mathbf{A}}) \rightarrow \mathcal{P}(\mathbf{A}) = \mathbf{Q_k}\mathcal{P}(\hat{\mathbf{A}}){\mathbf{Q_k}}^T \tag{5.50}$$

$$\mathcal{P}(\mathbf{A}^T)\mathbf{P_k} = \mathbf{P_k}\mathcal{P}(\hat{\mathbf{A}}^T) \rightarrow \mathcal{P}(\mathbf{A}) = \mathbf{P_k}\mathcal{P}(\hat{\mathbf{A}}){\mathbf{P_k}}^T \tag{5.51}$$

when $\deg(\mathcal{P}) < k$. These properties follow from the Lanczos iteration (see appendix I). To match the first $2k$ moments, the following condition between the reduced and unreduced model must be satisfied:

$$\hat{\mathbf{C}}\hat{\mathbf{A}}^{l+j}\hat{\mathbf{B}} = \mathbf{C}\mathbf{A}^{l+j}\mathbf{B} \tag{5.52}$$

for $0 \leq l \leq k$ and $0 \leq j \leq k$. By using the properties shown in equation 5.50 and 5.51

it can be shown that condition 5.52 is satisfied:

$$\mathbf{C}\mathbf{A}^{l+j}\mathbf{B} = \mathbf{C}\mathbf{A}^{l}\mathbf{A}^{j}\mathbf{B} \tag{5.53}$$
$$= (\mathbf{C}\mathbf{Q_k}\hat{\mathbf{A}}^{l}{\mathbf{Q_k}}^{T})(\mathbf{P_k}\hat{\mathbf{A}}^{j}{\mathbf{P_k}}^{T}\mathbf{B}) \tag{5.54}$$
$$= \mathbf{C}\mathbf{Q_k}\hat{\mathbf{A}}^{l}\hat{\mathbf{A}}^{j}{\mathbf{Q_k}}^{-1}\mathbf{B} \tag{5.55}$$
$$= \hat{\mathbf{C}}\hat{\mathbf{A}}^{l+j}\hat{\mathbf{B}} \tag{5.56}$$

Thus the Lanczos method, by producing the biorthonormal matrices $\mathbf{P_k}$ and $\mathbf{Q_k}$ and therewith the tridiagonal matrix $\hat{\mathbf{A}}$, matches the first $2k$ moments of $H(s)$.

The Lanczos method does not give an 'a priori' global error bound. A measure for the global error of the approximation can be obtained by comparing the transfer function of the full system $H(\omega)$ with the transfer function obtained from the reduced system, $\hat{H}(\omega)$. This measure is defined as the H-Infinity norm (called error norm from now on) according to:

$$|\hat{H} - H|_\infty = \sup_{\omega \in \Re} \left| \hat{H}(\omega) - H(\omega) \right| \tag{5.57}$$

where $\sup$ denotes the supremum, i.e. the least upper bound, or maximum value in case of a vector, of the set at which it operates.

This section will conclude with some interesting properties of the Lanczos generated models. The first property is that the Lanczos model gives exact results at $\sigma = \infty$, while accuracy is lost away from this σ. This property also applies to any other chosen σ, for example when applying the Shifted Lanczos method (see section 5.3.3). The second property is that the Lanczos method tends to converge to well-separated eigenvalues (corresponding to for example eigenfrequencies in the transfer) first. This implies that the Lanczos method typically does a poor job identifying nearly identical eigenvalues.

5.3.2 Implicitly Restarted Lanczos

The Lanczos procedure requires starting vectors to start the iteration. The following starting vectors appear to give good results for model reduction problems [61]:

$$\mathbf{q_1} = \mathbf{B}/\sqrt{|\mathbf{C}\mathbf{B}|} \tag{5.58}$$
$$\mathbf{p_1} = \mathrm{sign}(\mathbf{C}\mathbf{B})\mathbf{C}^{T}/\sqrt{|\mathbf{C}\mathbf{B}|} \tag{5.59}$$

However, these start vectors in combination with the reduction procedure might transform a stable, full system (i.e. the real part of all eigenvalues smaller than zero) into an unstable reduced system. To overcome the consequences of a poor starting vector to construct the reduced model, one could explicitly remove the unstable eigenvalue λ_u from the reduced model by choosing new starting vectors, i.e. $\tilde{\mathbf{q_1}} = (\mathbf{A} - \lambda_u\mathbf{I})\mathbf{q_1}$ and $\tilde{\mathbf{p_1}} = (\mathbf{A} - \lambda_u\mathbf{I})\mathbf{p_1}$, and repeat the whole Lanczos process for k additional steps [61]. However, one could also implicitly modify the matrices $\mathbf{Q_k}$ and $\mathbf{P_k}$ and pass immediately to a stable version of the reduced model $\hat{\mathbf{A}} = {\mathbf{P_k}}^{T}\mathbf{A}\mathbf{Q_k}$. This implicit procedure is subject of the current section.

It is assumed that the Lanczos procedure has resulted in a reduced system matrix $\hat{\mathbf{A}}$. However, some unstable eigenvalues are present in $\hat{\mathbf{A}}$. With the Implicit Restarted Lanczos method, the goal is to remove the unstable eigenvalues from $\hat{\mathbf{A}}$ to arrive at a stable system again. To do so, the unstable eigenvalue λ_u is removed from $\hat{\mathbf{A}}$, resulting in a new, rank-deficient matrix $\hat{\mathbf{A}}' = \hat{\mathbf{A}} - \lambda_u \mathbf{I}$. Subsequently, the orthogonal-triangular decomposition of $\hat{\mathbf{A}}'$ is determined. In this decomposition, the matrix $\hat{\mathbf{A}}'$ is decomposed into an orthogonal matrix $\mathbf{H}$ and an upper triangular matrix $\mathbf{R}$ such that $\hat{\mathbf{A}}' = \mathbf{HR}$. Because $\hat{\mathbf{A}}'$ is non-full rank (an eigenvalue was removed) the last row of the triangular matrix $\mathbf{R}$ is zero. Furthermore, because $\mathbf{H}$ is orthogonal, $\mathbf{H}^T = \mathbf{H}^{-1}$ and $\mathbf{H}^T\mathbf{H} = \mathbf{I}$, so:

$$\hat{\mathbf{A}}' = \mathbf{HR} \tag{5.60}$$

$$\mathbf{H}^{-1}\hat{\mathbf{A}}' = \mathbf{R} \tag{5.61}$$

$$\mathbf{H}^{-1}\hat{\mathbf{A}}'\mathbf{H} = \mathbf{RH} \tag{5.62}$$

Because the last row of $\mathbf{R}$ equals zero, the last row of the matrix $\mathbf{H}^{-1}\hat{\mathbf{A}}'\mathbf{H}$ is equal to zero as well. Moreover, since $\hat{\mathbf{A}}$ is tridiagonal (see appendix I), the last column of $\mathbf{H}^{-1}\hat{\mathbf{A}}'\mathbf{H}$ is also equal to zero. When this last row and column are removed from the matrix, a $k-1 \times k-1$ matrix arises which has no unstable eigenvalue anymore. To arrive at this $k-1 \times k-1$ sub-matrix of $\mathbf{H}^{-1}\hat{\mathbf{A}}'\mathbf{H}$, the new $\mathbf{P_{k-1}}$ and $\mathbf{Q_{k-1}}$ are defined as the appropriate $k-1 \times k-1$ sub-matrices of:

$$\hat{\mathbf{Q_k}} = \mathbf{Q_k}\mathbf{H} \tag{5.63}$$

$$\hat{\mathbf{P_k}} = \mathbf{H}^{-1}{\mathbf{P_k}}^T \tag{5.64}$$

When more unstable eigenvalues have to be removed, the procedure is repeated on the $k-1 \times k-1$ part of the matrix $\mathbf{H}^{-1}\hat{\mathbf{A}}'\mathbf{H}$. The consequence of this procedure is that when a k^{th} order reduced model is obtained with q unstable eigenvalues, the order of the reduced model after the implicit procedure is $k-q$. To account for this decrease of the order of the model due to the unstable modes, additional Lanczos steps are taken, so that the number of extra steps is equal to the number of unstable modes. This finally results in a k^{th} order, stable reduced model. The algorithm is listed in algorithm 1 [61].

5.3.3 Shifted Lanczos

A disadvantages of the Lanczos method is that breakdowns can occur under some circumstances. Also, there may be a large steady-state error, as the Lanczos method approximates the high frequency poles.

A breakdown of the Lanczos method occurs when a division by zero occurs in the process. Looking at the algorithm 2 in appendix I this occurs when β_j or γ_j are zero. The value β_1 is defined as the product of the matrices $\mathbf{B}$ and $\mathbf{C}$. The matrix $\mathbf{B}$ contains only values at the excitation location, while the matrix $\mathbf{C}$ contains only values at the response location. Since in FTF calculations, these locations are usually

Algorithm 1 Implicitly Restarted Lanczos method

Perform k standard Lanczos steps with full reorthogonalisation. This results in $\mathbf{P_k}$ and $\mathbf{Q_k}$. Set q equal to the number of unstable modes in $\hat{\mathbf{A}} = \mathbf{P_k^T A Q_k}$ and set $p = 0$
while $q > p$ **do**
  Increment p
  Perform another standard Lanczos step to obtain $\mathbf{P_{k+p}}$ and $\mathbf{Q_{k+p}}$
  Set q equal to the number of unstable modes in $\mathbf{P_{k+p}^T A Q_{k+p}}$
end while
Obtain $\mathbf{P_{k+p-q}}$ and $\mathbf{Q_{k+p-q}}$ by removing the unstable modes from $\mathbf{P_{k+p-q}^T A Q_{k+p-q}}$ using implicit restarts
Define the stable, reduced-order model to be $\hat{\mathbf{A}} = \mathbf{P_{k+p-q}^T A Q_{k+p-q}}$, $\hat{\mathbf{B}} = \mathbf{P_{k+p-q}^T B}$ and $\hat{\mathbf{C}} = \mathbf{C Q_k}$

separated from each other, a multiplication of the matrices $\mathbf{B}$ and $\mathbf{C}$ yields zero and the Lanczos method breaks down.

With the Shifted Lanczos method the breakdown problem can be overcome. Moreover, it solves the problem of the large error at low frequencies. This is because the standard Lanczos method approximates the expansion of the transfer function around a frequency which is equal to infinity. The expansion of the transfer function $H(s)$ around frequency σ was already given by equation 5.38. When comparing the moments $\eta_j(s = \sigma)$ (equation 5.40) with the moments that are matched with the standard Lanczos method (equation 5.47) it can be seen that a realisation around any frequency σ can be obtained by replacing the matrix $\mathbf{A}$ in the standard Lanczos method with the shifted matrix $(\mathbf{A} - \sigma\mathbf{I})^{-1}$ and the vector $\mathbf{B}$ with $(\sigma\mathbf{I} - \mathbf{A})^{-1}\mathbf{B}$. This is the basis of the Shifted Lanczos method [55].

Another name for the Shifted Lanczos method is the Rational Lanczos method, as it was inspired by the Rational Arnoldi method for computing eigenvalues. In the Shifted Lanczos method, the vector $\mathbf{B}$, which is also the starting vector of the algorithm, is replaced by $(\sigma\mathbf{I} - \mathbf{A})^{-1}\mathbf{B}$. Because the inverse of the square matrix $(\mathbf{A} - \sigma\mathbf{I})$ is a full matrix, the multiplication $(\sigma\mathbf{I} - \mathbf{A})^{-1}\mathbf{B}$ results in a full vector, and therefore the product $\mathbf{CB}$ is cannot be zero anymore. This prevents breakdown of the method. Additionally the approximation becomes better around the shift frequency. As mentioned above, the low frequency approximation of the standard Lanczos method is not very good. Especially at low frequencies, however, a good approximation is needed in case of reconstructing a FTF. This can be realised with the Shifted Lanczos method.

Real and imaginary shift frequencies can be used. Even multiple shift frequencies are possible [55], but require a large amount of extra CPU time and memory. This extra CPU time comes from the fact that in the Shifted Lanczos method, the $\mathbf{A}$ matrix is now replaced by $(\mathbf{A} - \sigma\mathbf{I})^{-1}$, which requires solving systems of linear equations instead of simply multiplying a known sparse matrix with a vector. Obviously, due to memory limitations this inverse matrix cannot be calculated explicitly when the dimension of $\mathbf{A}$ is large. The inverse operation is therefore applied by solving trian-

gular systems obtained from an initial LU decomposition (the linear system can also be solved iteratively, see section 5.3.4). The number of triangular systems that need to be solved is equal to two times the order of the reduced model (see algorithm 2 in appendix I). The number of required LU factorisations is equal the number of shift points used. Since the LU factorisation is the most expensive operation in terms of CPU time and memory, using multiple shift points is less attractive when working with large scale systems. Therefore, only one shift point is used here.

In general, for the approximation of $H(\omega)$ an imaginary shift point gives fast convergence close to the shift point while a real shift point gives a slower convergence in a wider region [60]. Because the transfer functions approximated here are in fact low-pass filters (i.e. much information in the low frequency region), a single real frequency shift of 1 Hz is used in the Shifted Lanczos procedure.

5.3.4 Calculating the inverse of a big sparse matrix

A disadvantage of the Shifted Lanczos method is that an inverse of a big matrix needs to be calculated. Obviously, the inverse of the matrix is never calculated explicitly, one tries to obtain $\mathbf{x}$ in the equation

$$\mathbf{x} = (\mathbf{A} - \sigma\mathbf{I})^{-1}\mathbf{b} \tag{5.65}$$

in an implicit matter. For smaller problems, first a LU factorisation (possibly permuted to increase the numerical accuracy) can be performed and subsequently the result of a multiplication with the inverse matrix can be calculated by forward and backward substitution. Even larger problems can be handled in this way: a MATLAB routine was written which calculates the lower and upper triangular matrices sequentially, and stores parts of these matrices when the used memory of the computer rises above a certain value. The routine is actually a form of a so-called *out-of-core* linear solver. Out-of-core refers to algorithms which process data that is too large to fit into a computer's main memory at one time. Such algorithms must be optimised to efficiently access data stored in slow bulk memory such as the hard drive. Examples of implementations of out-of-core linear solvers can be found in [43, 58, 173].

Still, when the problems become really large, iterative methods have to be used to solve equation 5.65. In those iterative methods it always saves much time when the matrix that needs to be inverted is preconditioned, for example using an incomplete lower-upper factorisation. In this LU factorisation the elements that have a value lower than a drop-tolerance value are omitted. With the lower and upper triangular matrices from the incomplete LU factorisation, an approximate solution vector can be calculated, which is improved with an iterative method. In this thesis, the Bi-Conjugate Gradient (BiCG) method is used when large systems are encountered that need to be solved iteratively. This method has the advantage that it uses relatively little storage. Moreover, it is robust and much is known about problems with this method.

5.3.5 Examples

To show the effectiveness of the Implicitly Restarted Lanczos Method, the method is applied to two example cases. Initially, the order of the first case is taken such that the transfer function of the system can still be exactly determined by the direct method, as given in section 5.2.1. In the second example, an analytical solution is available, giving the opportunity to increase the size of the system that needs to be reduced, and find the limit size of the system that can still be handled by the Lanczos method.

The first state space system is downloaded from `http://www.win.tue.nl/niconet/NIC2/benchmodred.html`. On this website, benchmark state space systems are available. The benchmark system for the Lanczos method is a dynamical system with a single input and a single output. The transfer function of the system contains a few sharp peaks, which makes it more difficult for the Lanczos method to reduce the system.

Figure 5.6 shows the resulting transfer functions of the dynamical system of order 1,006, calculated exactly with the direct method, and first reduced to order 15. The figure shows that a reduced model of order 15 can satisfactory approximate the exact transfer function. A reduction of 97% is therewith achieved.

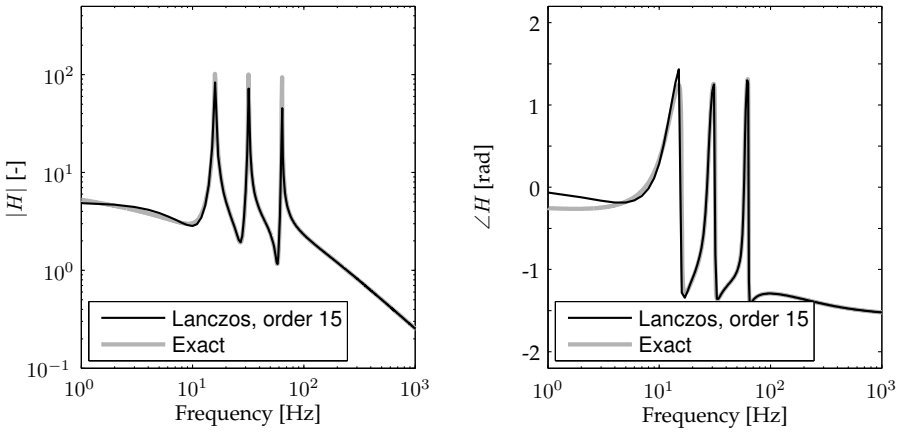

(a) Amplitude (b) Phase

Figure 5.6: Comparison between the exact transfer function of the example problem, obtained via the direct method, and from the Lanczos approximation of order 15.

The next example is the one-dimensional discretised test case discussed in section 5.2.3. The same input values are used again. An analytical expression (see equations 4.7 and 4.8) is available for this example. When the Lanczos method is used to reduce the order of the state space system, it immediately becomes clear that the standard Implicitly Restarted Lanczos method breaks down when $L_1 > 2\mathrm{d}x$, because the multiplication of the $\mathbf{B}$ and $\mathbf{C}$ matrix, needed to obtain the starting vector, yields zero. Therefore, the Implicitly Restarted and Shifted Lanczos method is used here. Sev-

eral parameters can be varied in this method: the shift frequency σ, the order k of reduced system and the way the inverse, needed to obtain the shift matrix, is calculated: via a LU factorisation or using the iterative Biconjugated Gradient method (see section 5.3.4).

By reducing the mesh size, an order of $1 \cdot 10^6$ is chosen for the model. In figure 5.7, this model is reduced to order 5 and 15, using a shift frequency of 1 Hz. Figure 5.8 shows the error norm as a function of the order of the reduced model. Here, the LU factorisation is used to calculate the inverse directly.

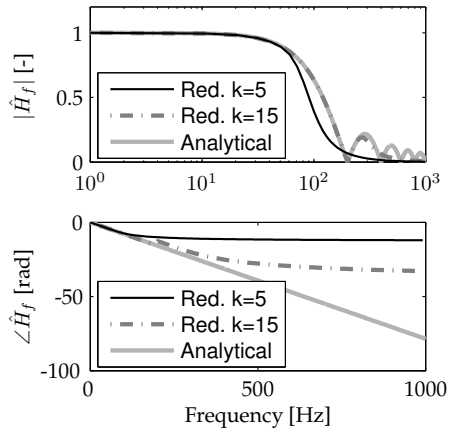

Figure 5.7: Transfer function of model with order $1 \cdot 10^6$ and reduced to order 5 and 15 using a shift frequency of 1 Hz.

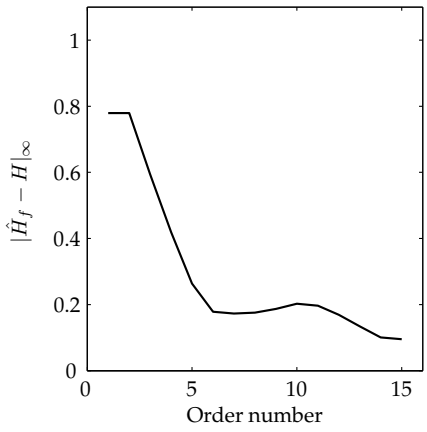

Figure 5.8: Error norm $|\hat{H} - H|_\infty$ as a function of the order of the reduced model.

It can be seen that at low frequencies, the transfer function is predicted correctly, even with a reduced model of order 5 (which is a reduction of $5 \cdot 10^{-6}$ of the original model). At higher frequencies, however, the approximation worsens, but is still acceptable.

Similar cases are ran with a shift frequency of 10 Hz and calculating the inverse with the iterative Biconjugated gradient method. With this iterative method, the system matrix was first preconditioned using an incomplete LU factorisation. Both the iterative Biconjugated gradient method and the incomplete LU factorisation use their standard convergence and drop tolerances, respectively, of $1 \cdot 10^{-6}$. In table 5.1 a summary is given of the different methods, their accuracies and CPU times. It is seen that the iterative method results in the same accuracy, however, higher order reduced models can be constructed with it. This comes at the cost of more CPU time needed to calculate this reduced order model. Moreover, with a shift frequency of 1 Hz the errors are slightly lower than using a higher shift frequency. When using higher frequencies than 10 Hz as shift frequency, many unstable modes arise in the reduced model and the problem had to implicitly restart multiple times. From now on, a shift frequency of 1 Hz is used.

It can be concluded that whenever the LU factorisation can handle the model, it

Inverse	Shift frequency	$\|\hat{H} - H\|_\infty$ (Order nr)	CPU-time [s]
LU	1 Hz	0.264 (5)	45.7
LU	1 Hz	0.096 (15)	215.7
LU	10 Hz	0.342 (5)	45.9
LU	10 Hz	0.109 (15)	216.0
Iterative	1 Hz	0.264 (5)	65.3
Iterative	1 Hz	0.096 (15)	226.1

Table 5.1: Overview of the accuracy and CPU time of the discussed methods.

should be used. When one runs into memory problems, one can shift to an iterative method, which requires less memory, but generally more CPU time.

5.4 Validation linear coefficient method

The performance of the linear coefficient method is now demonstrated in the calculation of the FTF in a *circular* combustion chamber, having the same dimensions as the DESIRE square combustion chamber (the radius of the circular chamber is such that its area is equal to the original DESIRE geometry). The considered combustion chamber is circular to be able to also show the performance of a two-dimensional axisymmetrical implementation of the linear coefficient method.

The axisymmetrical model is reduced by only considering 10 degrees of the circular geometry and imposing periodic boundary conditions at both radial planes to account for the remainder of the combustor. The part of the DESIRE combustor that is modelled here corresponds to Model 3 (see section 3.6), which starts just downstream the fuel injectors. Therefore, the boundary conditions at the inlet of this reduced model come from a simulation with the full geometry. Moreover, to allow to solely fluctuate the equivalence ratio ϕ it is assumed that the fuel is perfectly mixed with air at the inlet of the unsteady model. Operating point 15.2 is considered in this validation case.

The model is meshed with an unstructured mesh of 70,907 elements (21,289 nodes). Most of these elements are concentrated in the flame zone. In this simulation 11 transport equations are solved: 3 momentum equations, 1 mass balance equation, 2 turbulence equations, 1 energy equation and 4 convection-diffusion equations for the transport of the species mass fractions (CH_4, O_2, CO_2 and H_2O).

The flame transfer function between the equivalence ratio and the volume integrated heat release rate is determined in several transient simulations, using impulse excitation in the equivalence ratio. White noise excitation would give more accurate results than impulse excitation, but requires (far) more computational effort [180]. The transient CFD simulations serve as a validation for the results obtained with the linear coefficient method. The simulations are done with two different time steps: 0.5 and 0.25 ms.

For the flow field, it is required to put the outlet at a location where the gradients in the flow are small. However, in the linear coefficient method one is only interested in the heat release rate response. Since acoustic pressure and velocity fluctuations

have very little influence on the heat release rate [111], only convective effects in the flow field can influence the heat release rate. Therefore, it makes sense to omit all coefficients corresponding to axial locations beyond the closing position of the central recirculation zone. Downstream of this closing position, perturbations cannot convect back to the flame anymore, and consequently cannot influence the heat release rate perturbation. This way, the number of nodes in the linear coefficient method could be reduced from 21,289 to 3,923. With 11 independent variables per node, the order of the linear coefficient model becomes 43,153. Using the Lanczos method, the state space model was further reduced to order 25, prior to calculating the transfer function, i.e. a reduction of over 99.9%.

First, only fluctuations in the 4 convection-diffusion equations for the mass fractions are considered. The influence of the other equations and independent variables is removed by keeping them at a constant value in the transient simulation. The transfer functions determined with impulse excitation in a transient simulation and with the linear coefficient method are compared in figure 5.9.

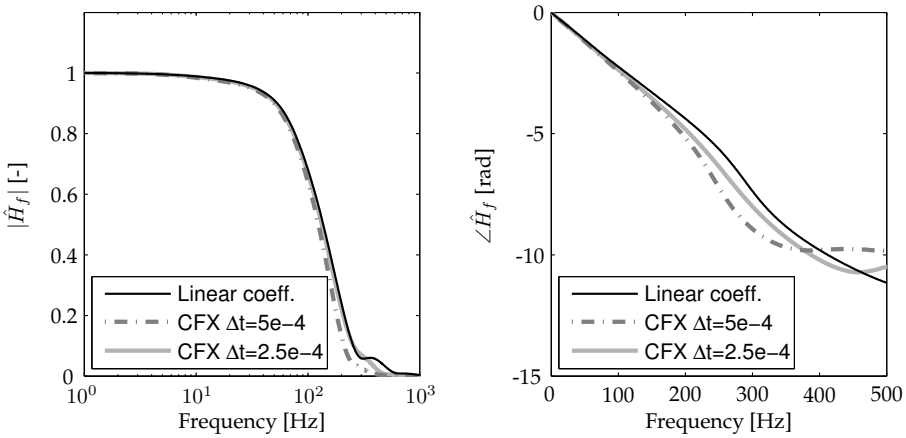

(a) Amplitude (b) Phase

Figure 5.9: Comparison between transfer functions obtained from impulse excitation in CFX and from the linear coefficient method. Only the 4 convection-diffusion equations for the mass fractions are included.

Figure 5.9 shows that when the time step is decreased, the results obtained from impulse excitation in CFX are increasingly approximating the linear coefficient result. This confirms the statement that transfer functions obtained with the linear coefficient method do not suffer from time truncation errors. The transfer functions still look very simple, which is because only the convection and diffusion of the species mass fraction is considered here.

When the enthalpy equation is added to the considered set of equations, the transfer functions shown in figure 5.10 are obtained. The enthalpy equation largely influences the results. This is because it directly influences the temperature, which in turn has a large influence on the reaction rate. While the cut-off frequency remains

more or less the same as with the 4 convection-diffusion equations, additional bumps appear on the spectrum. It is also seen that at some frequencies, the error made with the transient CFD method is large, even with the smallest considered time step.

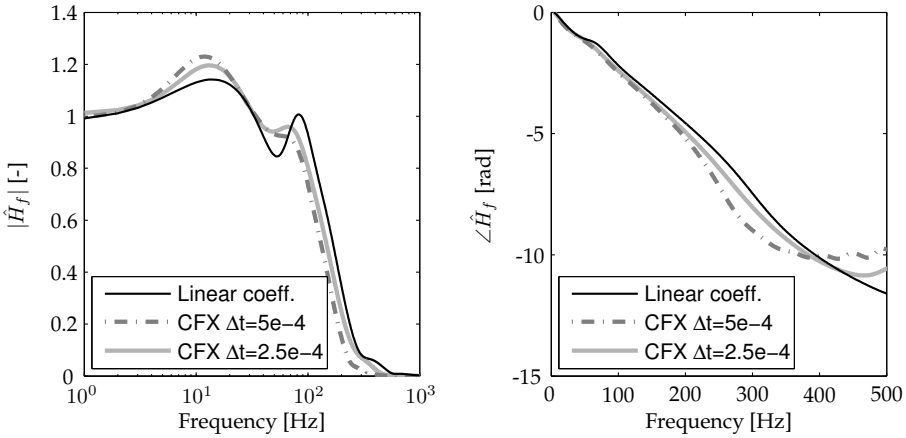

(a) Amplitude (b) Phase

Figure 5.10: Comparison between transfer functions obtained from impulse excitation in CFX and from the linear coefficient method. The 4 convection-diffusion equations for the mass fractions and the enthalpy equation are included.

Since the inclusion of the turbulence equations hardly influences the resulting transfer function, the resulting FTFs are not shown here. Instead, the transfer function of the *complete* model is compared with the transient results in figure 5.11.

Some influence of the hydrodynamical equations can be noticed when comparing figure 5.11 with the previously obtained transfer functions. However, the influence is not large. By considering only the enthalpy and the 4 convection-diffusion equations, already a very good description of the flame transfer function is obtained for this case.

For all considered cases, the linear coefficients are determined using an excitation of 1% for each variable at each node. The effect of perturbing the variables by a higher level would show when the results start to deviate, i.e. when non-linear effects come into play in the simulation. Figure 5.12 compares the transfer functions obtained by extracting linear coefficients with different excitation levels. It is observed that already at an excitation level of 5%, non-linear effects start to influence the results. Since the model is not linear anymore, many implicit restarts of the Lanczos method are needed to remove the unstable, non-linear modes. Note that this does not necessary mean that the whole model behaves non-linear at an excitation level of 5%. The 5% level is the level at which *every* variable is perturbed. In reality, only a variable at the inlet is perturbed, and this perturbation is subjected to damping prior to effecting a perturbation at other variables. Moreover, a perturbation of 5% in, for example, the fuel mass fraction does not mean that the temperature at the same location is also perturbed by 5%.

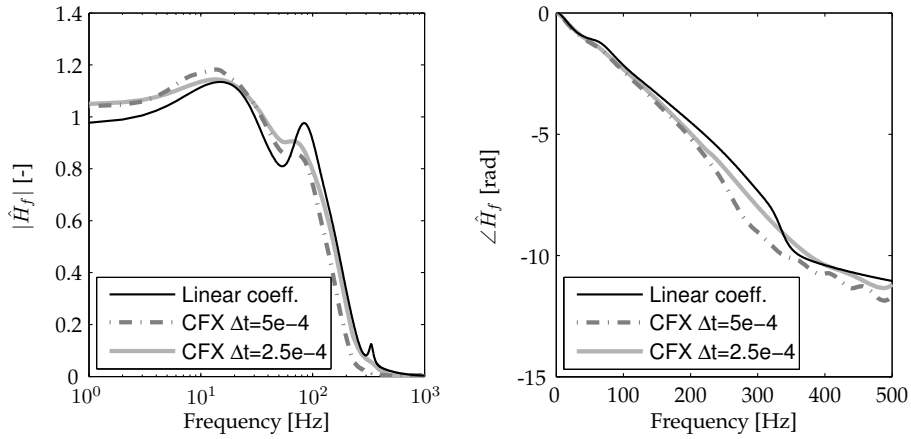

(a) Amplitude (b) Phase

Figure 5.11: Comparison between transfer functions obtained from impulse excitation in CFX and from the linear coefficient method. All equations are included.

Additionally, an axisymmetrical formulation of the linear coefficient method was tested here. The axisymmetrical formulation only requires the inclusion of the nodes at one periodic boundary. Additionally, nodes that are far outside the flame and recirculation zones are omitted. The total order of the state space model for the 11 equations is now further reduced to 15,257 (1,387 nodes considered). Figure 5.13

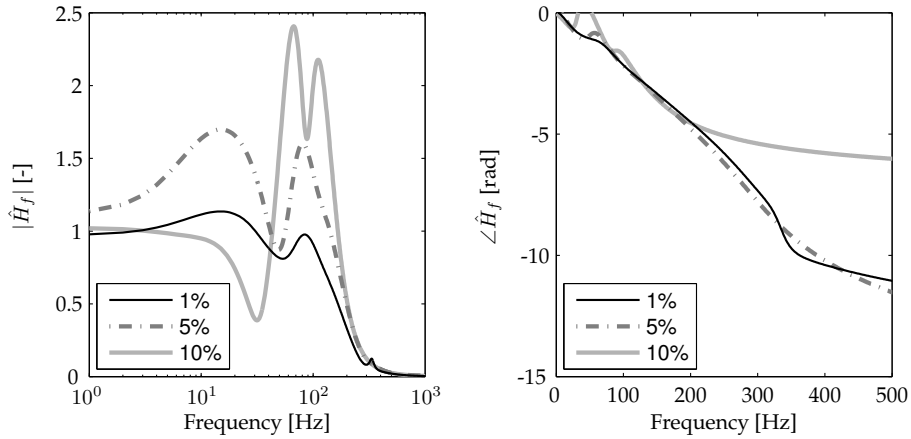

(a) Amplitude (b) Phase

Figure 5.12: Comparison between transfer functions obtained from the linear coefficient method. Different excitation levels are used to obtained the linear coefficients.

shows a comparison between the results obtained with a two-dimensional implementation and the transient CFD results.

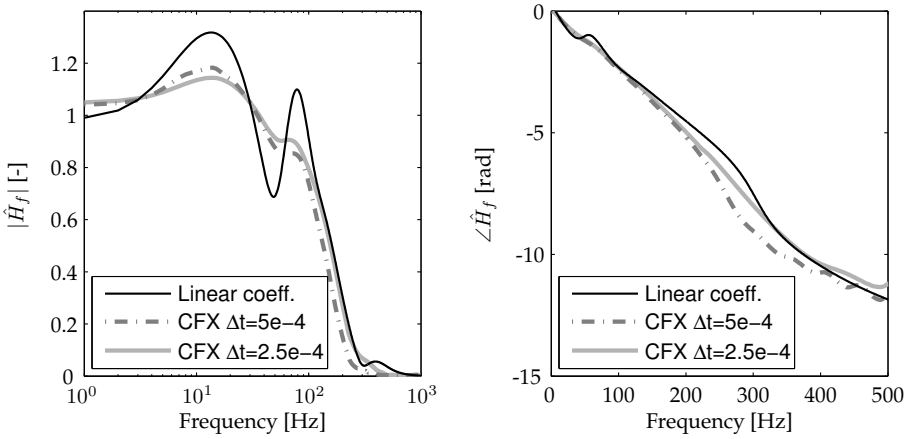

(a) Amplitude (b) Phase

Figure 5.13: Comparison between transfer functions obtained from impulse excitation in CFX and from the axisymmetrical version of the linear coefficient method. All equations are included.

While the peaks occur at the same locations as the CFX results, the level is off. It appears to be very important that the steady-state solution obtained with CFX is mapped onto the same mesh in the linear coefficient method. Mapping the solution on a 2D axisymmetrical mesh results in slightly different residuals which makes the solution not entirely steady-state anymore. Applying the linear coefficient method might then give a wrong solution.

In table 5.2, the CPU times are listed for each method. For relatively small sized problems, the computational effort of the linear coefficient method is shown to be about a factor 10^2 less compared to impulse excitation (for this specific case). The 2D axisymmetrical version of the method is then even a factor of 10^3 times faster than impulse excitation. When the problems become larger, i.e. adding more equations, this relative reduction in computational effort decreases slowly. The reason for this is that the LU factorisation of the coefficient matrix, necessary for shifting the matrix in the Shifted Lanczos method, requires increasingly more calculation time.

More efficient methods for solving linear systems in the Shifted Lanczos method will save computational effort. Also better preconditioners can help here. In summary, much can be gained on the solving algorithm.

When performing a transient simulation in CFX, a similar sized linear problem is solved at each time step. It is known that iterative solvers tend to rapidly decrease in performance as the number of computational mesh elements increases. Performance also tends to decrease if there are large elements aspect ratios present. The performance of the solver is greatly improved by employing multigrid techniques. When employing similar solution techniques in the linear coefficient method, it should be

Element	CPU time [s]			
	4 eqns	5 eqns	7 eqns	11 eqns
Impulse excitation CFX $\Delta t = 0.25$ ms	$9.5 \cdot 10^3$	$1.5 \cdot 10^4$	$2.0 \cdot 10^4$	$3.0 \cdot 10^4$
Reducing to order 25 with Restarted and Shifted Lanczos method	$4.4 \cdot 10^1$	$9.5 \cdot 10^1$	$2.2 \cdot 10^2$	$3.9 \cdot 10^3$
Calculate transfer function from red. model	6	6	6	6
2D Reducing to order 25 with Restarted and Shifted Lanczos method	6.5	$1.1 \cdot 10^1$	$2.0 \cdot 10^1$	$4.8 \cdot 10^1$
2D Calculate transfer function from red. model	6	6	6	6

Table 5.2: CPU times of state space and transient calculations (all preceded by retrieving a steady-state solution.

possible to equal the time needed to reduce the system in size to the equivalence of $2k$ time steps ($2k$ linear systems are solved, see section 5.3.3) in CFX, where k is the size of the reduced system. So when the problem is reduced to order 50, 100 linear systems are solved. When the iterative multigrid solver of CFX is used, this can in principle be done in the same amount of CPU time in which 100 time steps are done.

5.5 Conclusions

With the linear coefficient method, FTFs on the basis of steady-state CFD simulations are shown to be calculated faster and more accurate than when using conventional transient methods and spectral analysis. The method can be used as a design tool in determining the thermo-acoustic behaviour of combustion systems.

The test problems that have been studied with the linear coefficient method range up to size 45,000. Since the coefficient matrices are currently assembled with separate MATLAB routines (see appendix H), the linear coefficient method becomes less efficient for linear models of higher orders. Moreover, the LU factorisation necessary for solving the linear systems in the Shifted Lanczos method become less efficient then.

To remove the limit in size, the assembling of the coefficient matrices should be done directly in the solver code. For implicit solver codes, this should not take significant extra CPU-time, since the implicit approach already requires the assembling of the system matrix for iterating to a solution. Moreover, a multigrid solver should be used to solve the linear systems in the Shifted Lanczos method. When the iterative multigrid solver of CFX would be used, the reduction of the linear description to order k can in principle be done in the same amount of CPU time in which $2k$ time steps are done.

Chapter 6

Experimental validation

6.1 Introduction

The experimental setup designed within the framework of the DESIRE project is able to operate at a maximum absolute pressure of 5 bars. The maximum thermal power of the setup is 500 kW. It is therefore closer to realistic gas turbine conditions than most other experimental setups. At this pressure and power, most thermo-acoustic experimental techniques seen in literature are available in this test rig, such as dynamic pressure measurements, Planar Laser Induced Fluorescence (PLIF) OH, chemiluminescence CH*, active flame perturbation etc. Additionally, the setup distinguishes itself by the fact that it allows the measurement of the dynamic liner vibration as a response to the acoustic field generated by the flame. With these measurements, the complete coupled dynamic system consisting of the thermo-acoustic behaviour of the flame, the acoustic field and the structural vibrations of the liner can be studied.

This chapter starts with an overview of the literature on acoustic measurements performed on experimental combustion setups. Subsequently, a description of the DESIRE setup and its dynamic sensors is given. Next, the conducted steady acoustic measurements are discussed. With 'steady' measurements, the measurements without any active excitation of the flame are indicated. After this, the unsteady measurements are presented. In these unsteady measurements, the fuel mass flow is perturbed. The heat release rate response can assumed to be the result of the by fuel mass flow perturbations induced equivalence ratio perturbations, which is the most likely mechanism for inducing instabilities (see chapter 2). The reason for this is that in lean combustion ($\lambda \approx 2$) of natural gas, approximately 26 times more air than fuel is used (in terms of mass). Referring to equation 2.60, this implies that a perturbation in the fuel mass flow has the largest influence on the equivalence ratio, while the mass flow of the total mixture is hardly perturbed.

Next, it is shown how the flame transfer function (FTF) can be reconstructed from the dynamic data measured during these unsteady measurements. The measured FTFs are compared to the numerically calculated FTFs. This is done at different powers and pressures. Finally, the measured FTFs are used in a stability analysis to

determine the unstable modes of the setup. The results of this stability analysis are validated by measurements taken at an unstable operating point.

6.2 Literature review

Numerous experimental studies have been performed in which the acoustic behaviour of a turbulent, premixed swirl flame is characterised. A categorisation of these experimental studies can be made on the basis of whether the *active* or *passive* flame noise is studied. The active flame noise can only be measured when one of the inlet quantities of the flame is perturbed. Subsequently, the response of the flame in terms of the volume integrated heat release rate is monitored, either by acoustic measurements [130] or by visual (laser, chemiluminescence etc.) techniques [6, 29, 57, 98]. In some papers, phase-locked laser techniques are applied to study the local flame behaviour as a response to the applied oscillations. The experiments discussed in literature are mostly performed at atmospheric pressure and at single burner rigs. Examples of exceptions to this statement are the papers of Cheung *et al.* and Kunze *et al.*. In the former paper, the FTF is determined at 15 bars (in the frequency range below 200 Hz), while the latter paper makes a comparison with transfer functions measured in an annular, multiburner experimental setup.

The passive noise produced by the flame can be measured in the same way as the active noise, only no exciter is required [3, 24, 39]. Consequently, passive noise experiments are more common at elevated pressures than active noise experiments. In some cases, the passive noise can be characterised by just installing dynamic pressure transducers in a combustor, which allows these measurements to be applied in existing combustors.

Yet another category of thermo-acoustic experiments are measurements on the self-excited system. In these measurements, the boundary conditions of the setup are modified until a self-excited oscillation is encountered [39,70,126,145]. Subsequently, explanations are sought for the occurrence of the self-excited oscillation. Moreover, methods to remove the self-excited mode are often given. Sometimes the limit-cycle behaviour of the self-excited instability is discussed [110].

As mentioned earlier, almost all actively perturbed experimental combustion setups seen in literature operate at atmospheric pressure. Nevertheless, the experience of most experimentalists is that the behaviour can significantly change when increasing the mean operating pressure of the rig. It is important to account for this effect, since the final application of most models would be to predict thermo-acoustic behaviour of combustion applications at elevated pressures (i.e. large scale gas turbines operate at a mean pressure between 10 and 30 bars).

The realisation of an experimental combustion setup operating at elevated pressures has large consequences for the design, as well as for the way of operation due to extra safety procedures. Fortunately, the pressure level does not have to increase much to study the effect of the pressure on the thermo-acoustic behaviour of the flame. It is known that the largest influence of the pressure on combustion occurs in the lower pressure range [183] (at high pressures, combustion is to a good approximation independent on the pressure). Therefore, the maximum operating pressure

of the DESIRE setup is limited to 5 bars.

6.3 Description of experimental setup

A cross-section of the DESIRE combustor, showing its main components, is given in figure 6.1. The whole setup is mounted vertically in a specially designed frame. In figure 6.1 the locations of the steady and dynamic sensors are shown in gray boxes. The meaning of the codes used to define the sensors are listed in table 6.1.

Code	Meaning
p	Dynamic pressure sensor
P	Static pressure sensor
T	Thermocouple air
Tv	Thermocouple pressure vessel
Tl	Thermocouple liner
LDV	Laser Doppler Vibrometer optical access
PLIF	Planar Laser Induced Fluorescence optical access

Table 6.1: Meaning of sensor codes used in figure 6.1.

The combustor consists of two square tubes. The inner square tube forms the liner and the outer square tube is the pressure vessel. Between the tubes the cooling air flow is forced. The burner opens into the inner square tube in which the combustion process of the air/natural gas mixture takes place. The combustion process can be observed optically (Laser Induced Fluorescence and natural light emission) through quartz glass windows that are mounted in the liner and pressure vessel on 3 sides of the *combustion* section (indicated with ① in figure 6.1).

Liner vibrations can be observed in the *structural* section (indicated with ② in figure 6.1). Here the liner has a thickness of only 1.5 mm, instead of the 4 mm thickness used for other parts of the liner. Vibrations are measured here with a Laser Doppler Vibrometer (LDV), which looks through a quartz glass window mounted in the pressure vessel [75].

To prevent valve overheating the flue gasses are cooled in the *cooling* section (indicated with ③ in figure 6.1) by injection of a water spray. Additionally, the cooling air from the liner is mixed in the cooling section, which helps to bring down the temperature. Water that does not evaporate is discharged by a condensate drain, mounted at the bottom of the setup.

A more detailed description of the combustor and the design considerations is included in appendix J. This appendix also includes information on the steady sensors that are used in the setup, as well as a description of the applied laser techniques and an overview of the technical specifications of the DESIRE test rig.

6.4 Dynamic sensors

The locations of the dynamic sensors were given in figure 6.1. The sensors comprise acoustic pressure transducers, a Laser Doppler Vibrometer and a pulsator. All

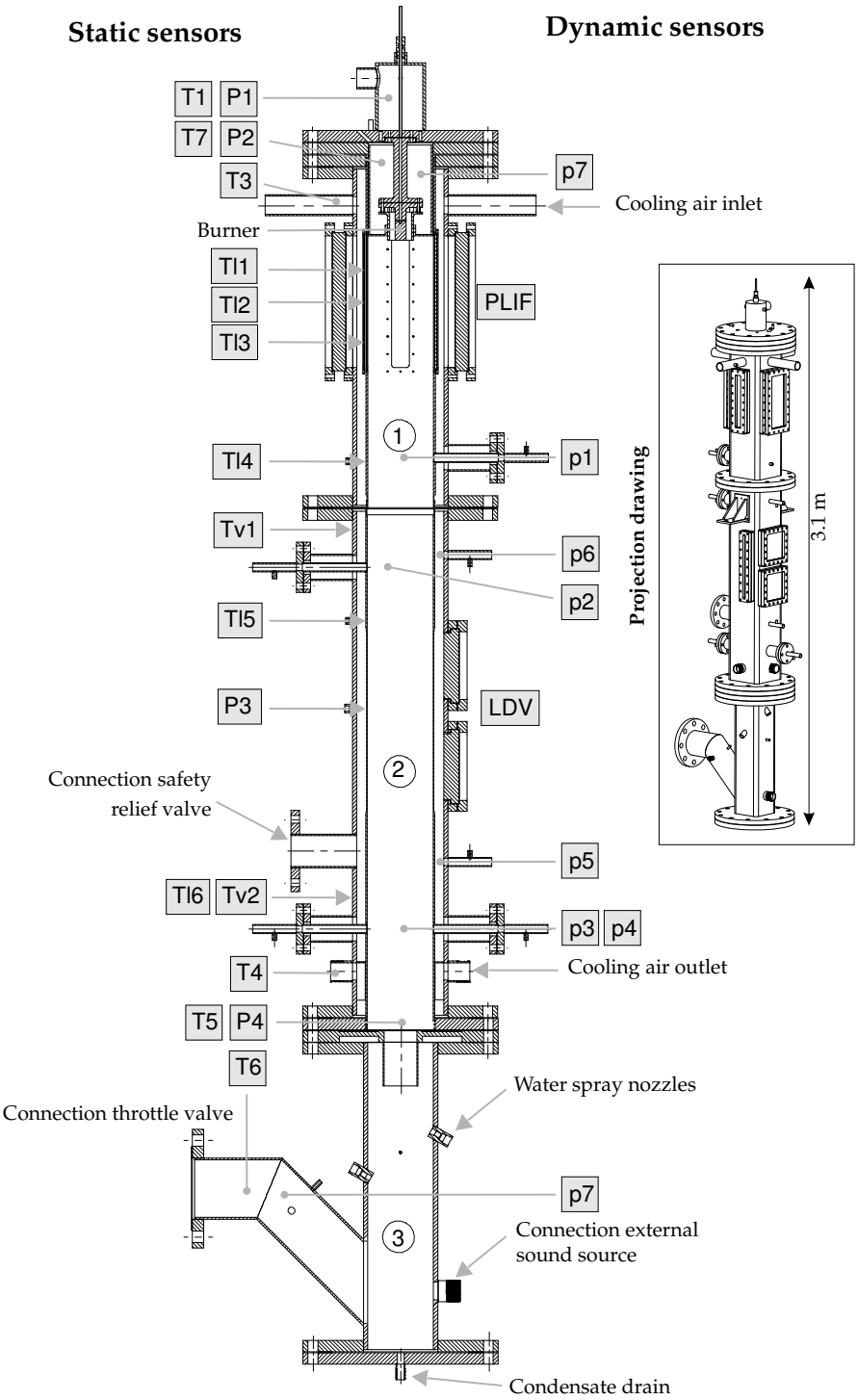

Figure 6.1: Overview of the main components of the DESIRE setup.

signals from the dynamic sensors are sent to the data acquisition box of a SIGLAB analyser system. This data acquisition box is connected to a computer in which the data is further processed.

In this section, the dynamic sensors are discussed in more detail. This includes a discussion on their measurement principle, as well as notes on the accuracy and additional techniques that are used to make the sensor appropriate for the current application (i.e. measurements in a highly turbulent, high temperature and high pressure environment).

6.4.1 Acoustic pressure

Pressure transducers of the type Kulite XCS-190 are used in the setup. When applying these it has to be considered that for combustion purposes, the maximum allowable temperature (175 °C) of the Kulite transducers is low. Moreover, the static pressure has to be compensated in order not to burst the membrane of the transducers at elevated pressures (the burst pressure is 1050 mbar). Both of these aspects will be discussed in this section.

To enable the Kulite to measure acoustic pressure perturbations at elevated mean pressures, the mean pressure is compensated by imposing this pressure to the rear side of the membrane (see figure 6.2).

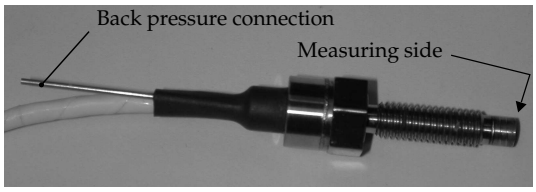

Figure 6.2: A Kulite XCS-190 pressure transducer with the back pressure connection indicated.

The back pressure is supplied by a flexible Teflon hose with an inner diameter of 0.8 mm and an outer diameter of 1.6 mm. The hose is cut to a length of 2 metres and connected to a back pressure supply station, as shown in figure 6.3. The pressure in this station is supplied by a hose which is connected to the combustor. This hose has an inner diameter of 8 mm and a length of 2 metre. A larger diameter hose is used for this last part to make sure that the back pressure supply station can follow the pressure in the combustor fast enough.

The combination of the back pressure supply station (acoustic volume) and the small diameter hose (viscothermal acoustic damping) minimises the acoustic energy transmitted from the combustor to the rear of the membrane of the sensor. Viscothermal acoustic damping can be modelled in the acoustic network model with the so-called 'low-reduced frequency model' [10, 171, 190]). A network model of the back pressure supply system (open-closed system with a volume and two tubes with different radii) shows a quick increase of the transmission loss* with increasing fre-

*The transmission loss (TL) is defined as: $\mathrm{TL} = 20 \log \frac{p_1}{p_2}$ [dB] in which p_1 and p_2 are the pressure amplitudes at both sides of the system. The TL is positive when the pressure amplitude over the system reduces.

quency (see figure 6.4). Apart from a low frequency dip at 17 Hz, the transmission loss is high enough not to disturb the measurements significantly. Additionally, extra acoustic damping can be expected due to the flexible walls of the Teflon hose. Experimental proof for this is given by Huls [75].

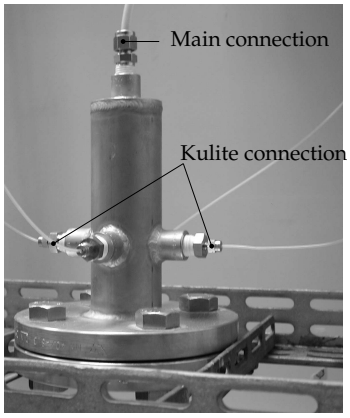

Figure 6.3: Back pressure station connecting the Kulite back pressure hoses with the setup.

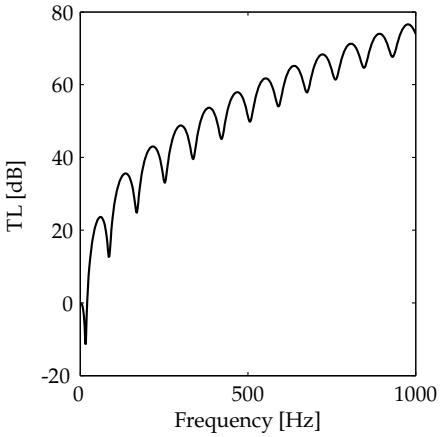

Figure 6.4: Transmission loss of the back pressure supply system.

To remain below their temperature limit, the transducers are mounted flush with a so-called acoustic transmission tube (see figure 6.5). In this transmission tube, the air is stagnant. Hence, the heat from the hot air in the combustor is transported to the sensor by conduction, which is a relatively limited process. To take away the conducted heat, the transmission tube is cooled from the outside by a fan. To remain below the temperature limit of the sensors, it is important that no leakage occurs downstream the mounting of the Kulite sensor. When this happens, heat is *convected* to the Kulite and the temperatures become too high.

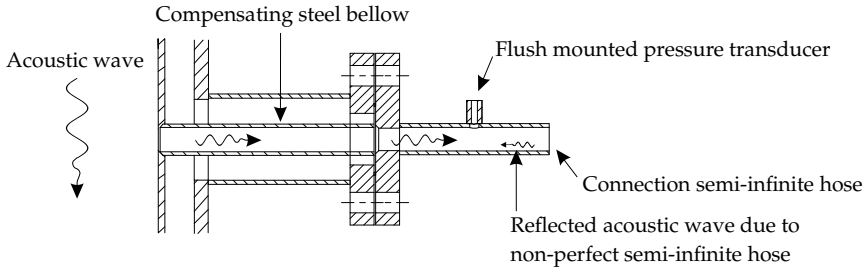

Figure 6.5: Transmission tube system for measuring the acoustic pressure inside the combustor.

When the transmission tube would be closed, standing waves distort the measured pressure signal at the Kulite. In other words, the measured pressure does not correspond to the pressure in the combustor (see figure 6.5). To correct this, the

acoustic transmission tube is elongated by a hose of about 4 metres. The last 1.5 metre of this hose is filled with acoustic damping material. The aim of this elongation and damping is to make sure that no standing waves can occur in the transmission tube. The signal measured by the Kulite is ideally equal in amplitude, and shifted by a phase corresponding to the time delay of an acoustic wave that travels from the inlet of the tube to the location of the Kulite. Under cold conditions, amplitude differences up to 2 dB are measured between the inlet of the transmission tube and the location of the transducer. This indicates that the implemented semi-infinite hose is well, but not perfectly anechoic. The phase shows to be monotonously declining, caused by the distance between the inlet and pressure sensor. The average slope of the phase corresponds to the time delay between the inlet and the sensor. Errors up to 0.5 rad are measured. These errors are acceptable. More information on the semi-infinite hoses and the validation measurements can be found in the PhD thesis of Huls [75]. Applications and solutions for general problems of these semi-infinite hoses can be found in [29, 53, 120, 145, 152].

The pressure transducers are used for two kinds of measurements: the measurement of a transfer function between two locations and the measurement of the auto-spectrum at a certain location. These two measurement techniques, as well as the complications in a combustion application, are discussed now.

The transfer function H_{21} is defined as the ratio between two (complex) pressures p_2 and p_1, which is taken from the ratio between the measured cross- and auto-spectrum:

$$H_{21} = \frac{p_2}{p_1} = \frac{S_{12}}{S_{11}} \tag{6.1}$$

where S_{12} is the cross-spectrum between pressure transducers 1 and 2. The coherence function between these two sensors can be used to check whether uncorrelated noise disturbs the measured transfer. Using the definition of equation 6.1, only uncorrelated noise in p_1 can disturb the transfer function [26, 172]. For a linear system, the transfer function between two locations does not depend on the level of the excitation.

For the auto-spectrum measurements, some extra precautions must be taken to remove the flow noise from the measured signal. When a noise free reference measurement is available, uncorrelated flow noise can be removed by calculating the auto-spectrum at sensor 1 with [103, 169] (also used by Schuermans *et al.* [161] in combustion applications):

$$S_{11} = S_{12}S_{21}/S_{22} = S_{12}S_{12}^*/S_{22} \tag{6.2}$$

where sensor 2 is the noise free reference measurement and the superscript $*$ indicates the complex conjugate. Using this equation, only the part of the auto-spectrum of sensor 1 that is correlated with the signal measured by sensor 2 is selected. In case of the FTF measurements, the excitation of the flame is done with a pulsator. This excitation is noise free and is used for the reconstruction of the auto-spectrum using equation 6.2.

Without active perturbation of the flame, the auto-spectrum measured by a transducer mounted at a different location is used for the reconstruction of the auto-spectrum of sensor 1 in equation 6.2. To minimise the influence of flow noise, the

spacing between the sensors used in the reconstruction is preferably large. Nevertheless, flow noise that is produced at specific locations in the combustor, for instance at the burner exit, can still distort the auto-spectrum measurement. This flow noise is measured by all transducers in the combustor, and is therefore identified as a correlated sound source. However, flow noise is typically a quadrupole type of noise source, while the equivalent source of the flame (heat release rate) is a monopole sound source [35]. For low Mach number flows and combustion applications, the contribution of quadrupole sound sources to the total measured sound is generally much less than the contribution of the monopole sound source resulting from the combustion process (see chapter 2). So when the uncorrelated noise (for example flow noise that is produced at the location where each sensor is mounted to the combustor) is removed with equation 6.2, the remainder of the measured sound consists mainly of the sound produced by the flame. Care must be taken interpreting the auto-spectra in the lower frequency range, where the source strength of flow noise is strongest.

6.4.2 Pulsator

To measure the FTF, the burner inlet conditions need to be actively perturbed. This pulsator can have different forms. Some authors use a siren-like pulsator, i.e. with a rotating part [19, 29, 57, 146]. An advantage of such a pulsator is its high maximum frequency of oscillation. The disadvantage is that the form of the excitation is fixed by the geometry of the siren, i.e. white noise excitation is not possible. Moreover, a sinusoidal excitation would require a complex form of the rotating disc.

Another option is to use a control valve for perturbing the flow. This type of pulsator has a somewhat lower maximum frequency of oscillation. However, it enables the use of any excitation signal. Since the maximum frequency of excitation is still high enough for the experiments performed here, a D633-7320 MOOG control valve is used here (see figure 6.6).

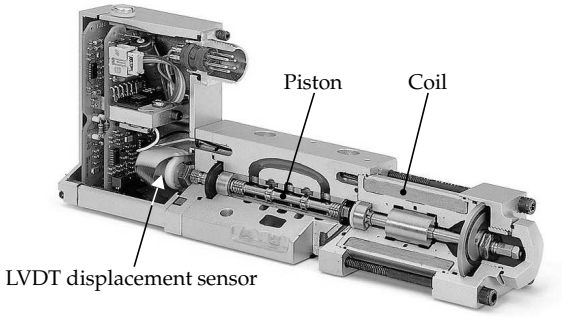

Figure 6.6: MOOG valve.

In the MOOG valve, the flow is perturbed by oscillating a piston. The piston is moved by applying a current through a coil surrounding the piston. This induces an electromagnetic field that interacts with the permanent magnet around the piston.

The actual position of the piston is measured by a Linear Variable Differential Transformer (LVDT). The piston has a maximum stroke of ± 0.35 mm. Without a current, the piston is in its neutral position. Applying a positive current closes the valve, applying a negative current opens the valve farther.

Figure 6.7(a) shows the quasi-steady relationship between the applied excitation voltage and the output voltage given by the LVDT sensor at 1 Hz. Due to internal friction, some hysteresis is seen when moving from the fully opened to the fully closed position, and vice versa. The data is scattered around a mean value.

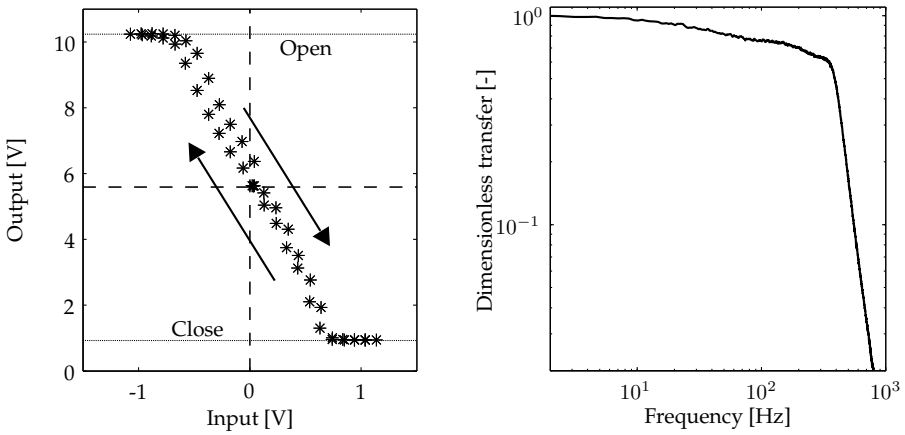

(a) Quasi-steady (b) Dynamic

Figure 6.7: Quasi-steady and dynamic behaviour of the MOOG valve.

When the dynamic transfer between the input and output voltage is considered, it is seen that the valve has a cut-off frequency of 420 Hz (see figure 6.7(b), the displayed transfer has been made dimensionless by scaling with its quasi-static value). Above this frequency, the available level of excitation decreases rapidly.

Due to the frequency dependence and the hysteresis in the valve, the output signal, representing the displacement of the MOOG piston, is used as reference in all measurements.

6.5 Boundary conditions

In the DESIRE test rig contractions are placed at the downstream end of the combustion chamber and upstream of the plenum. These contractions are intended to provide well-defined, acoustically hard end conditions (full reflection of acoustic waves). These end conditions can be easily implemented in the models for flow, acoustics and combustion. Contractions can provide such an acoustically hard end condition due to a pressure drop and an increase in velocity of the gasses. Nevertheless, the pressure drop and velocity are bounded by several aspects.

Firstly, since the downstream acoustic decoupler is effectively mounted between the cooling channel and the combustion chamber, a too high pressure drop can overload the liner. The maximum pressure drop determined by this condition is 50 mbar. Additionally, a too high pressure drop can lead to ignition problems. During ignition, cold gasses with a relatively high density are pushed through the downstream contraction by the expanding hot gasses at the flame front. This leads to an increased pressure drop compared to steady operation. The pressure drop and velocity during ignition must remain low to prevent flash-back.

The optimal size of the contractions follow from a consideration of the maximum allowable pressure drop and velocity, and the realised acoustic reflection coefficient. The upstream contraction is implemented by 12 holes with a diameter of 7 mm. At the downstream side, one circular contraction with a diameter of 75 mm is used. These dimensions are optimal with respect to acoustics and the steady system, as is shown in figure 6.8(a) and (b). In these figures the acoustic reflection coefficient is plotted as a function of the diameter of one hole (upstream boundary) and the diameter of the contraction (downstream boundary). This reflection coefficient has been calculated with the network model including a mean flow and a contraction (see section 2.4.3). The minimum of the absolute value of the reflection coefficient R for the frequency range below 1000 Hz is displayed. This value is determined at nominal conditions (operating point 15.4, see table 3.2 on page 63).

Furthermore, the pressure drop over and velocity through the contraction is plotted for the worst case condition. For the downstream contraction, this condition is ignition (maximum pressure drop) and operation at the nominal condition (maximum velocity). For the upstream contraction, the worst case occurs at maximum power (maximum pressure drop and maximum velocity).

It can be concluded from these figures that the chosen diameters are good com-

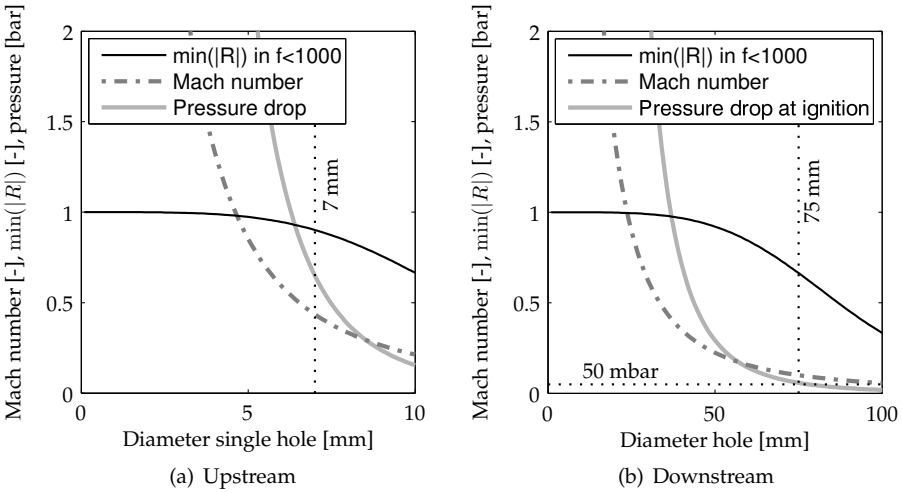

(a) Upstream (b) Downstream

Figure 6.8: Pressure drop, flow velocity and minimum value of reflection coefficient $|R|$ for contractions with an anechoic acoustic element downstream of it.

promises between a high acoustic reflection ($|R| \approx 0.9$ for the upstream decoupler and $|R| \approx 0.7$ for the downstream decoupler) and a low pressure drop. The reflection coefficient of the downstream decoupler is lower than the coefficient of the upstream decoupler because the pressure drop should remain below 50 mbar in order not to overload the liner.

6.6 Validation of the steady-state acoustic system

In this section the measured acoustic field under steady conditions will be compared with the acoustics predicted by the one-dimensional acoustic network model. The foundation of this network model has been discussed in chapter 2. Steady measurements that are not directly related to acoustics, such as species concentrations and heat transfer, are included in appendix J.

The acoustic network representation of the DESIRE test rig is shown in figure 6.9. The numbers in this model indicate the node numbers. The boundaries of the model at nodes 1 and 7 are determined by the upstream and downstream acoustic decouplers. At those locations, the impedances derived in section 6.5 are imposed (indicated as ζ_{up} and ζ_{down}). The pressure sensors, indicated by p1-p3 and p8 in figure 6.9, correspond to the sensors shown in figure 6.1. It can be seen that the locations where the acoustic pressure of the combustor is monitored are also connected to the setup with a transmission tube. In the model, it is assumed that the semi-infinite hose arrangement works perfectly, i.e. an anechoic end condition is imposed at the end of the acoustic transmission tubes. Since the dimensions of the burner details (swirler vanes, radial entry of the flow) are small compared to the acoustic wavelength, the burner is represented by an element with an equivalent length and area (between node 1 and 2). The plenum is also small compared to the acoustic wavelength, and therefore it is represented by an acoustic volume at node 1.

In case of a reacting flow, it is assumed that the temperature at the beginning of the combustion chamber (node 3) is equal to the adiabatic flame temperature. In section 3.7.3 it was shown that an approximately linear temperature gradient exists over the length of the combustion chamber (in figure 6.9 an indication of the temperature is given by the colour of the element). Hence elements accounting for this linear tem-

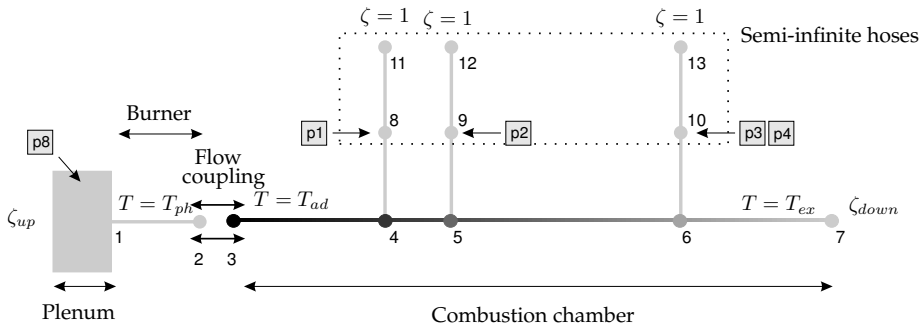

Figure 6.9: Acoustic network representation of the DESIRE setup.

perature gradient are used [167, 178]. The downstream temperature in this element is chosen equal to the measured exit temperature T_{ex} in the combustor. Upstream of the flame, the temperature is equal to the air preheating temperature T_{ph}.

At the area transition from the burner exit (node 2) to the combustion chamber (node 3) the coupling condition derived in section 2.4.2 is used. This coupling condition accounts for the effect of the pressure drop and velocity on the acoustic wave propagation. Furthermore, the mean flow velocity in each tube element is calculated from the local density, cross-sectional area and the (constant) mass flow through the setup. The mean flow velocity influences the upstream and downstream wave numbers in the model.

Without flow, the comparison between the acoustic network model and the measurements is poor, as can be seen by comparing the transfer between transducer p3 and p1 (figure 6.10(a)). The acoustic source in the measurements without flow is realised by connecting a loudspeaker to the water cooler.

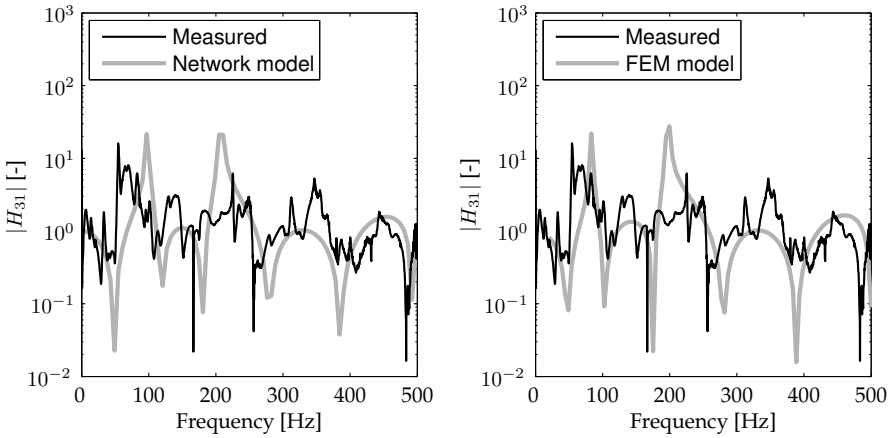

(a) 1D network model (b) FEM model (ANSYS)

Figure 6.10: Amplitude of experimental and modelled transfer function. No flow is present in the setup, and the sound is produced by a loudspeaker connected to the water cooler section.

The discrepancies are due to the acoustic decouplers which do not work without flow. Hence, the whole duct system outside the decouplers contributes to the measured transfer. A FEM model (ANSYS) incorporating the complex geometry of the burner does not show a satisfactory agreement either, as shown in figure 6.10(b). Nevertheless, the results from the FEM model show to be almost similar to the results obtained with the 1D network model, indicating that the complex geometry of the burner can indeed be modelled with a simple 1D tube with a characteristic length and diameter.

In a reacting flow, the flame is modelled by placing an acoustic volume source at node 3 in the acoustic network model (see figure 6.9). Doing so, one assumes that this acoustic source is much stronger than the flow noise in the system. To check this,

the coherence between transducers p1-p2 and p1-p4, measured with and without a flame, is shown in figure 6.11. In both measurements, a flow is present. It is observed that the coherence is much better with the flame on. This indicates that the flame is a strong, coherent source, which is apparently much stronger than the incoherent flow noise. Without a flame, the coherence is bad, especially at higher frequencies. Flow noise that is produced in the combustor (for instance at the burner exit) can still be correlated to a certain extent. Since this flow noise is strongest at lower frequencies, this is noticed by the better coherence at lower frequencies in figure 6.11(b).

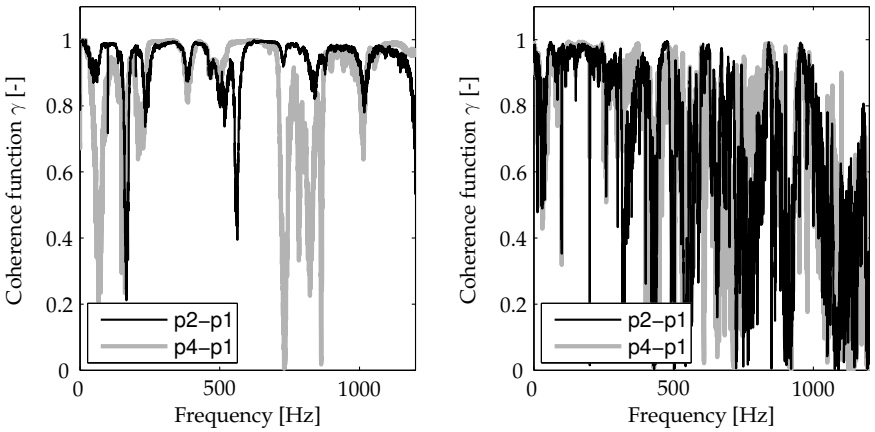

(a) Combustion (b) No combustion

Figure 6.11: Coherence function, with and without combustion.

Figure 6.12 shows a comparison between the measured and modelled amplitude of the transfer functions H_{21} and H_{31} under reacting flow conditions. Operating point 15.7 is considered here (a list of the operating points is given in table 3.2 on page 63). The levels of the peaks are well predicted by the acoustic model, indicating that the reflection coefficients imposed at the boundaries of the model are well predicted. Since they come from the acoustic contraction theory, described in chapter 2, this theory can be considered accurate enough for this application. Moreover a good prediction of the location of the peaks is observed, which is mainly thanks to the element with the linear temperature gradient. Nevertheless, at lower frequencies relatively large deviations between the model and the measurements can be seen. This has several causes. Firstly, since the reflection coefficients that are imposed at the boundaries are not equal to one, the system beyond the decouplers still influences the system between the decouplers. This especially occurs at the lower frequencies. Secondly, the semi-infinite hose arrangement and the back pressure system distort the signal measured by the sensors. Again, this mainly occurs at lower frequencies, where damping is relatively low.

Next, the auto-spectrum is considered. It must be noted that the level of the auto-spectrum depends on the strength of the source. In a reacting flow, the most

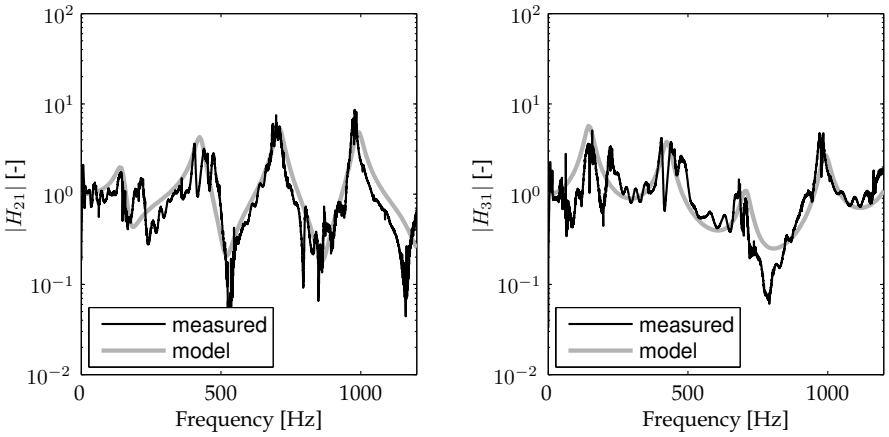

(a) H_{21} (b) H_{31}

Figure 6.12: Amplitude of the transfer function between two different sets of transducers. Comparison with the network model.

significant source is the flame. This source depends on the frequency. So in theory, this source strength can be determined by taking the measured auto-spectrum and modifying the source strength in the model such that the modelled auto-spectrum agrees to the measured auto-spectrum. In figure 6.13 the measured auto-spectrum at operating point 15.7 at transducer p1 is displayed. In the same figure, the auto-spectrum obtained from the network model is shown. In this model, a frequency independent source strength amplitude of $2 \cdot 10^{-5}$ kg/s is used.

By scaling the source strength for each frequency to match the measured auto-spectrum, the flame source strength is determined for operating point 15.4 and 15.7 (see figure 6.14).

In the quasi-steady limit ($f \downarrow 0$), it can be seen that the source strength of the 15.4 flame is somewhat larger than that of the 15.7 flame, which is probably due to the larger power of the 15.4 flame. By dividing the quasi-steady limit by the thermal power of the flame, a measure for the thermo-acoustic efficiency is obtained. The thermo-acoustic efficiency of both case 15.4 and 15.7 is approximately $5 \cdot 10^{-4}$. Due to thermo-acoustic feedback and increased turbulence levels, this is much higher than the typical thermo-acoustic efficiency of open flames [120]. Beyond a frequency of 70 Hz, the source strength spectrum becomes very noisy, due to the absence of certain observed resonances in the model. When a measured resonance peak is missing in the network model, the procedure described above will identify this peak as a peak in the flame source strength. A procedure will be presented later in this chapter to correct for this.

Finally, to check the assumption of one-dimensional sound propagation in the combustor, the transfer function between the pressure transducers p3 and p4 is presented in figure 6.15. These transducers are mounted at opposite locations in a cross-section along the combustor, and should therefore give an equal response. It is seen

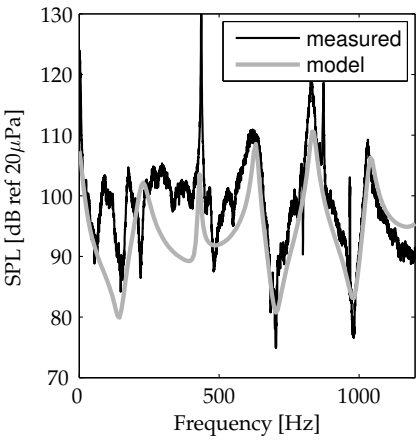

Figure 6.13: Auto-spectrum measured in the setup at operating point 15.7 and from the network model, assuming a frequency independent source strength amplitude of $2 \cdot 10^{-5}$ kg/s.

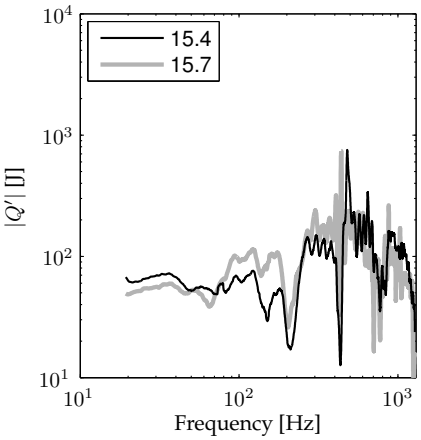

Figure 6.14: Flame source strength.

that this is not entirely true. However, since the lengths of the semi-infinite tubes and the back pressure hoses are not exactly equal for both transducers, this already induces errors. These errors cause the measured transfer to oscillate around the ideal one-dimensional result. No systematic deviation from this ideal one-dimensional re-

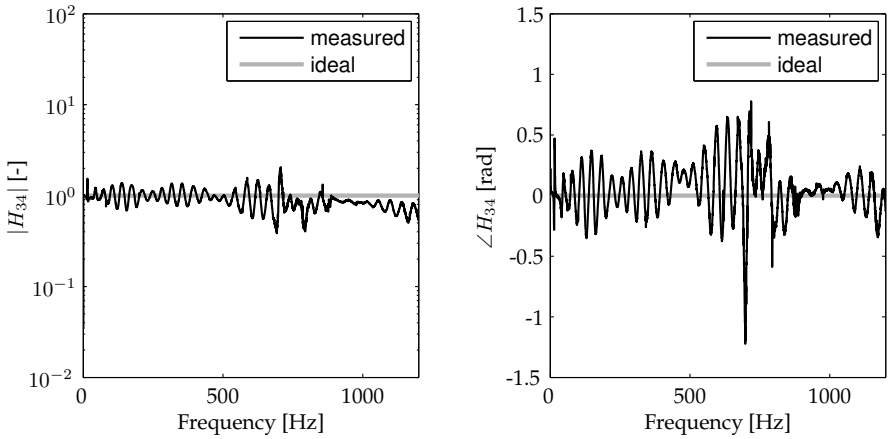

(a) Amplitude (b) Phase

Figure 6.15: Transfer between two pressure transducers, mounted at opposite locations, at the same axial location (transducer p3 and p4).

sult is observed, and therefore it is safe to assume that the acoustics in the combustor are one-dimensional.

6.7 Validation of the unsteady system

In this section the method to measure the FTF is presented. Moreover, the measured transfer functions at several operating points are presented and compared to the numerically obtained transfer functions.

6.7.1 Methodology

An overview of the different elements that play a role in the FTF reconstruction in the DESIRE test rig is shown in figure 6.16. During a FTF measurement, the MOOG valve is driven by an excitation signal V'_{exc}. This moves the MOOG's piston with a displacement δ', resulting in a fuel mass flow perturbation M'_f at the end of the fuel supply line. This eventually causes a heat release rate perturbation Q', which can be detected by the laser measurements via the radical concentration fields. Since this perturbation is proportional to an acoustic sound source M', the perturbation can be measured by the pressure transducers in the combustion chamber.

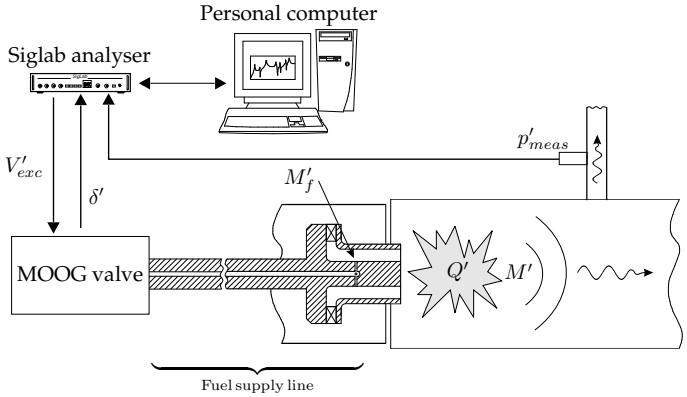

Figure 6.16: Schematic layout of the method which is used to determine the FTF.

The FTF is defined here as Q'/M'_f. Several transfer functions can be combined to finally yield this FTF:

$$H_f = \frac{Q'}{M'_f} \approx \frac{Q'}{M'} \cdot \frac{M'_{model}}{p'_{model}} \cdot \frac{p'_{meas}}{\delta'} \cdot \frac{\delta'}{M'_f} \tag{6.3}$$

The first transfer function in equation 6.3 is obtained from thermodynamics:

$$\frac{Q'}{M'} = \frac{c_0^2}{\gamma - 1} \tag{6.4}$$

In deriving this expression for volume integrated quantities, it is assumed that the factor $\frac{c_0^2}{\gamma-1}$ is constant over the flame. Since both γ and, more importantly, c_0 depend on the temperature, this is not necessarily true. It is generally assumed that this temperature is constant and equal to the adiabatic flame temperature. To verify this, the transfer function between the acoustic response of the flame and the fuel mass flow perturbation, i.e. $M'/M'_f = \int_V \frac{\gamma-1}{c_0^2} q' \mathrm{d}V/M'_f$, has been calculated with CFD (see chapter 4) for a perfectly premixed case at operating point 15.4. This transfer function is compared with $\frac{\gamma-1}{c_0^2} \cdot \int_V q' \mathrm{d}V/M'_f$, in which the factor $\frac{\gamma-1}{c_0^2}$ is determined at the adiabatic flame temperature. Figure 6.17 shows a comparison between these transfers. Both transfers are scaled by the same quasi-steady value.

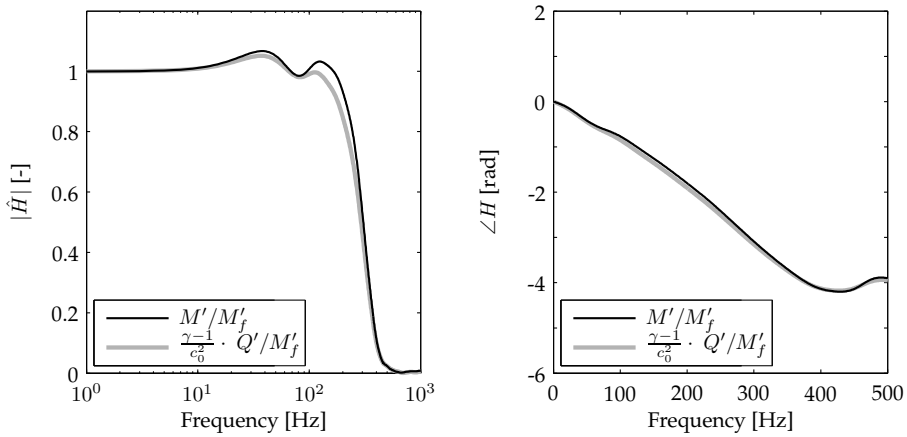

(a) Amplitude (b) Phase

Figure 6.17: Dimensionless FTF according to the definitions M'/M'_f and $\frac{\gamma-1}{c_0^2} \cdot Q'/M'_f$, determined with impulse excitation.

It is observed that the shape of both transfers is nearly equal, while a small error is made in the level of the amplitude at the higher frequencies when taking the factor at the adiabatic flame temperature. With respect to the accuracy of the measurements, these deviations are negligible.

The second transfer in equation 6.3 comes from the acoustic model. It describes the modelled transfer function between an acoustic mass flow source placed at the location of the flame, and the pressure at the locations where physical transducers are present in the test rig. Hence, this transfer completely relies on a good acoustic model, since it is assumed that:

$$\frac{M'_{meas}}{p'_{meas}} = \frac{M'_{model}}{p'_{model}} \tag{6.5}$$

Such an approach has to be taken here, because M'_{meas} is not measured directly in the experiment. For the FTF measurements, using the measured and modelled pressure

at location p3 (farthest away from the flame zone) gave the best results, and is used here.

The next transfer, p'_{meas}/δ', is directly measured in the experiment. Since the ratio of the cross-spectrum and the auto-spectrum is taken to determine the transfer function, uncorrelated noise in the measured pressure signal does not influence the transfer. Because the MOOG displacement signal is noise free, the measured transfer only includes the active noise of the flame.

The final transfer function δ'/M'_f has been obtained from the fuel supply line experiments, which are performed in a separate experiment described in appendix K.

6.7.2 Measurements

The method presented in the previous section is used to determine the FTF. At several operating points, the flame is excited by the MOOG valve. Use is made of Virtual Swept-Sine (VSS) of the SIGLAB spectral analyser. In this method, a sine wave is used as system excitation and this sine wave is stepped through the frequency range of interest. The reference channel measures the excitation signal while the response channels measure the outputs of the system. All input channels are measured using a narrow-band tracking filter whose pass band is centered on the excitation frequency of each step. This helps to reduce the effects of system noise. The transfer function is determined as the ratio between the cross-spectrum and the reference auto-spectrum, which helps to reduce system noise. VSS is suitable when faced with systems with extremely high noise or that are linear within a very narrow range.

Linearity of the measured transfers is checked by comparing measured transfer functions obtained with different levels of excitation at operating point 15.7. This is done for excitation levels of 2.5%, 5%, 7.5% and 10% of the mean fuel mass flow (when the level cannot be reached, i.e. due to the physical limitations of the MOOG valve, the maximum excitation level is used). At these levels, the transfer between the acoustic pressure at microphone p1 and the MOOG displacement δ' is measured. Hence, this transfer contains the fuel supply line transfer, the transfer between the fuel mass flow perturbation at the nozzles and the heat release rate response, and the transfer from this response to the measured acoustic pressure. 84 Frequencies are used, distributed in the range between 5 and 400 Hz. Figure 6.18 shows the amplitude and phase of the transfers. For a linear system, the transfers are identical. For the phase, this is the case. The amplitude, however, shows deviations up to 25% in the high frequency region.

The deviation from linearity at the higher frequencies can be mainly attributed to the non-linear behaviour of the fuel supply line transfer function M'_f/δ'. In appendix K it is shown that this non-linear behaviour can lead to a considerably higher fuel mass flow perturbation than expected from linear assumptions. To confirm that the transfer between the actual fuel mass flow perturbation M'_f and the heat release rate Q' has a wider linear range, integrated CH* chemiluminescence measurements with active excitation of the flame are performed. This is done with a 300 Hz excitation and at four different excitation levels. These levels are the real excitation levels which are corrected for their non-linear increase. Figure 6.19 shows the result for operating

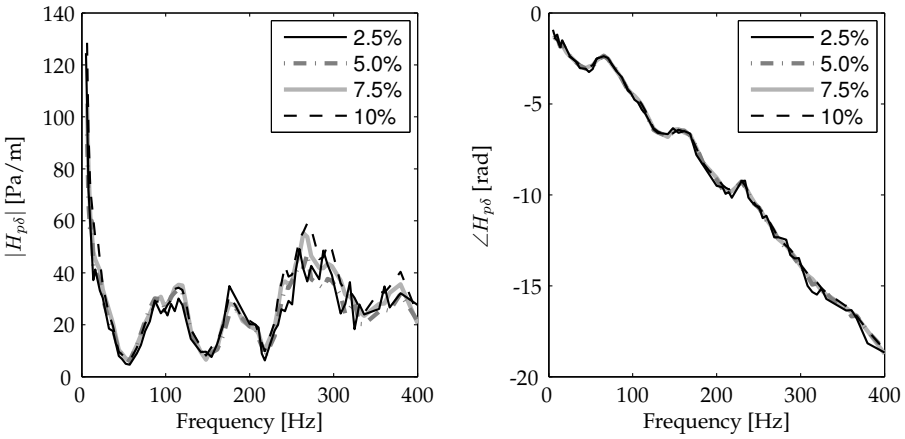

(a) Amplitude (b) Phase

Figure 6.18: Transfer between acoustic pressure at microphone p1 and the MOOG piston displacement δ'. The transfer is determined at different excitation levels.

point 15.7. It can be seen that the heat release rate responses linearly to fuel mass flow perturbations beyond 10% of the mean fuel mass flow.

Nevertheless, the transfer function which is measured in the DESIRE experiment does contain the non-linear behaviour of the fuel supply line. This limits the excitation level. However, when the level is too low, the coherence of the signal drops and it becomes increasingly difficult to distinguish the correlated flame response from the flow noise. When the coherence of a measured transfer at a certain frequency is

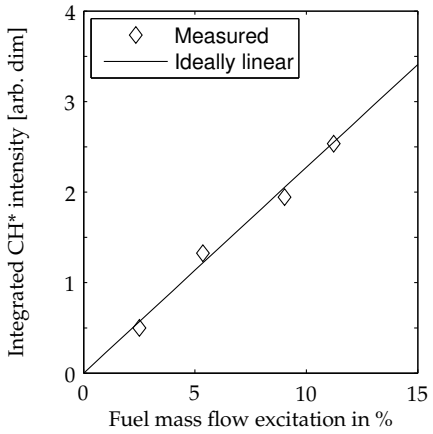

Figure 6.19: Integrated CH* intensity response to excitation at 300 Hz at different excitation levels. Operating point 15.7 is considered here.

below 0.9, it is manually removed from the transfer. Following this rule, 56% of the frequencies had to be removed at 2.5% excitation, indicating that the excitation level is too low. At 5% and higher, less than 10% of the frequencies had to be removed. To remain in the linear regime ánd have enough excitation, 5% excitation is a good choice and is used for the FTF measurements that will be presented in the remainder of this section.

Firstly, the phase of the measured FTF according to equation 6.3 is considered. In this equation, the dominant phases determining the final phase of the FTF are the phases of p'_{meas}/δ' and δ'/M'_f. The reconstructed phase of the FTF is plotted in figure 6.20(a) and (b) for cases 15.4 (150 kW at 1.5 bars) and 15.7 (125 kW at 1.5 bars), respectively. In the figures, the measured phase is compared with the phase obtained from numerical simulations in which the fuel injection nozzles are included (described in section 4.5).

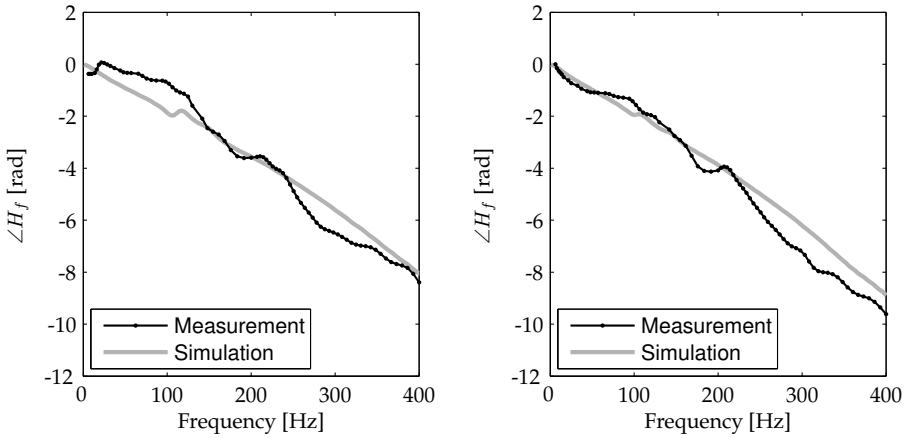

(a) 15.4 (b) 15.7

Figure 6.20: Measured and modelled phase of the FTF.

The agreement between the measurements and the simulations is good, for both the individual cases and the difference between the cases. Both the measurements and the simulations show an approximately linear frequency dependence of the phase. This indicates that a constant (convective) time delay exists between the excitation and the response. The time delays can be extracted from a linear fit of the phase lines. For the measurements, this yields a time delay of 3.8 ms for case 15.7 and 3.3 ms for case 15.4. The difference between these time delays can be explained from the higher velocities at case 15.4. Compared to case 15.7, case 15.4 has 20% higher velocities. Nevertheless, the measurements show only a 8% difference in the time delay between the two cases. The same is true for the simulations: time delays of 3.3 ms (15.7) and 3.0 ms (15.4) can be derived from a linear fit of the phase lines. The difference between these time delays is 10%. The explanation for this lower than expected difference in the time delays is the location of the flame. The simulations show that the 15.7 flame is located closer to the burner exit than the 15.4 flame. This

decreases the time delay from the excitation location to the flame location, which counteracts the increasing time delay due to the decreasing volume flow.

The measured amplitude of the transfer functions is shown in figure 6.21. The transfers look very similar. They have a strong bumpy behaviour, which is actually due to the mismatch of the auto-spectra of the model and the experiments (see figure 6.13), i.e. equation 6.5 does not hold. The reason that the phase reconstruction does not suffer from this is that the phase contribution of equation 6.5 to the reconstructed phase is small.

To correct the mismatch of the auto-spectra of the model and the experiments, it is assumed that the autonomous flame source strength is a known function of the frequency. Measurements of open premixed flames show that the spectrum shape hardly depends on burner size, engine power and flame temperature, although these factors strongly affect the overall level of the spectrum [120,142]. Additionally, parametric studies of acoustic radiation from premixed natural gas-fuelled turbulent flames show that, for a fixed burner diameter, the acoustic spectrum of the flame has a nearly universal shape, whose total power is a function of equivalence ratio and flow velocity [142]. The presumed shape is obtained from the spectrum of the measured CH* intensity at operating point 15.7 (see figure 6.22). The radical CH is linearly related to the heat release rate, and consequently to the flame source strength.

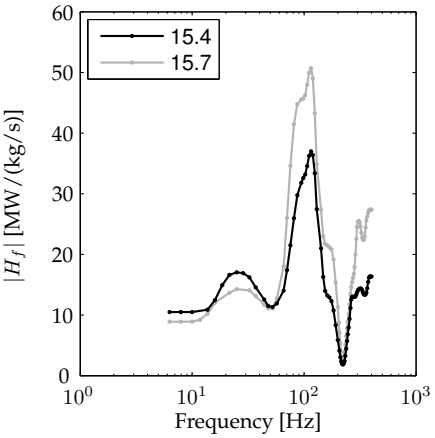

Figure 6.21: Measured amplitude of the FTF.

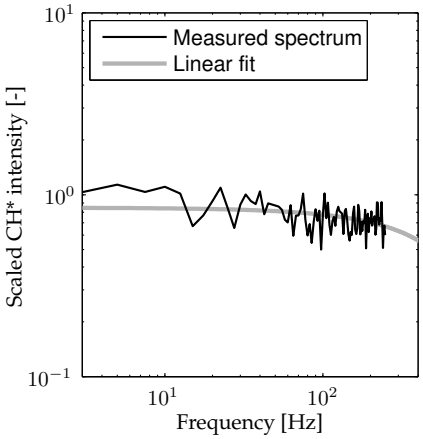

Figure 6.22: Measured spectrum of the CH* intensity.

The sampling frequency of the CH* measurement is 500 Hz, which limits the maximum frequency of the spectrum to 250 Hz. Moreover, some aliasing effects can be expected, since the discrete signal could not be anti-aliased. Nevertheless, a smooth spectrum is observed, of which the shape is approximately flat at low frequencies, and slightly rolls off at higher frequencies.

From the CH* intensity spectrum, a spectrum shape is extracted by fitting the spectrum with a linear function. This linear function has been extrapolated slightly

to obtain spectral information up to 400 Hz. The obtained spectrum shape is also shown in figure 6.22. This spectrum shape is fitted through the flame source data obtained from scaling the auto-spectra (i.e. figure 6.14), yielding M'_{fitted}. Subsequently, the transfer $\frac{M'_{model}}{p'_{model}}$ is determined as:

$$\frac{M'_{model}}{p'_{model}} = \frac{M'_{fitted}}{p'_{measured}} \tag{6.6}$$

This way, the bumps that are not in the model can be accounted for in the FTF reconstruction. The reconstructed transfer function at 15.7 using this approach is shown in figure 6.23(a).

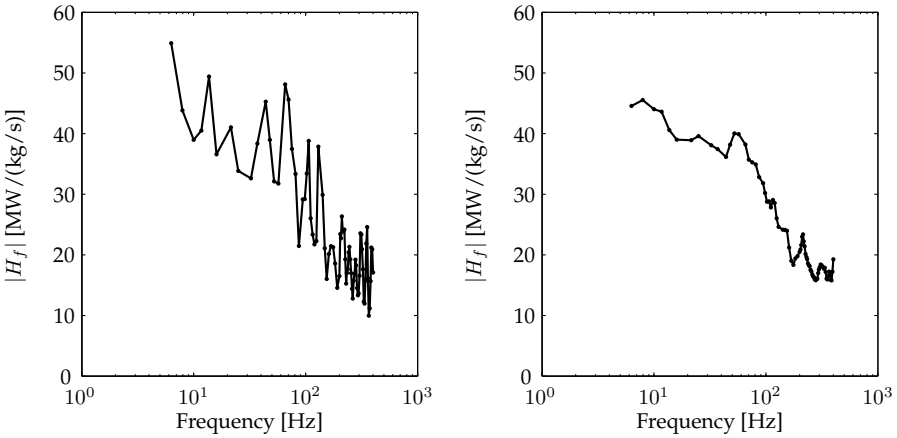

Figure 6.23: Measured amplitude of the FTF at operating point 15.7.

Much of the bumpy behaviour is obviously gone now, and the transfer shows a low-pass filter behaviour. However, the trends are still difficult to observe since there is a lot of noise on the obtained transfer function. To remove this noise, a moving average is applied to the data. The moving average b_i extracted from a data series a_j is defined as:

$$b_i = \frac{1}{n+1} \sum_{j=i-n/2}^{i+n/2} a_j \tag{6.7}$$

in which n determines the width of the moving average. A value of 6 is taken for smoothing the amplitude of the transfer function, corresponding to a frequency width of approximately 20 Hz. At the boundaries of the data, n is decreased so that the moving average can be determined all the way to the boundaries of the data. The amplitude of the transfer function after smoothing is shown in figure 6.23(b). Much more can be observed on the behaviour of the transfer function now.

From figure 6.23(b) it can be seen that the quasi-steady limit of the transfer function lies around 44.5 MW/(kg/s). Dividing the power of the flame by the mean fuel mass flow, this quasi-steady limit is predicted at 40.8 MW/(kg/s), i.e. the net calorific value of the fuel. This agrees well with the value obtained from the reconstructed amplitude of the FTF, which is an indication for the correct application of the different transfer functions in reconstructing the FTF.

It should be noted that at low frequencies, the flow noise could not be effectively removed from the measured auto-spectra using correlation techniques (equation 6.2). Flow noise that is produced at specific locations in the combustor, for instance at the burner exit, can distort the auto-spectrum measurement. This flow noise is measured by all transducers in the combustor, and is therefore identified as a correlated sound source. In the lower frequency range, the strength of this disturbance is strongest, and leads to increased auto-spectrum levels. This was discovered by comparing the FTFs at different operating points; the quasi-steady value of these transfers appeared to depend on the power of the flame. Nevertheless, this quasi-steady value should be constant, since the fuel mass flow is linearly related to the heat released by the flame. The main effect of correlated flow noise on the level of the measured auto-spectra is seen in the frequency range below 40 Hz, as is shown in figure 6.24(a). In this low frequency range, a sudden increase in the sound pressure level (SPL) is seen, which depends on the power of the flame. To remove the flow noise in the low frequency region, the measured SPL is extrapolated by the modelled one, as shown in figure 6.24(b).

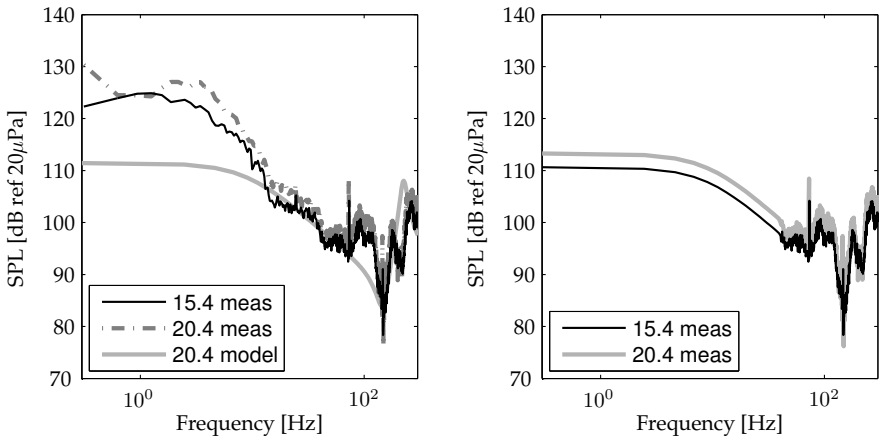

(a) Directly measured (b) Extrapolated with model results

Figure 6.24: Low frequency flow noise in the auto-spectrum measured by microphone p1. The flow noise has been removed by extrapolating the measured spectrum in the low frequency range using the model results.

In figures 6.25(a) and (b) the amplitudes of the measured and modelled FTFs at operating point 15.4 and 15.7, respectively, are displayed. Since the overall level

of the measured FTF depends on the level of the fit of the CH* chemiluminescence spectrum, there is some uncertainty in the quasi-steady value: a variation of 10% has been noticed in the reconstructed quasi-steady values. Therefore, the measured FTFs are normalised by the average value of the amplitudes between 5 and 20 Hz.

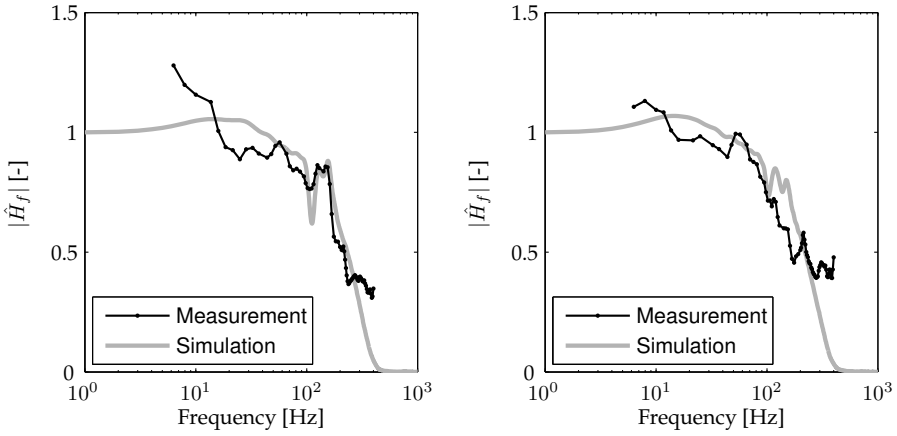

(a) 15.4 (b) 15.7

Figure 6.25: Measured and modelled amplitude of the FTF.

The experimentally obtained transfers show similar behaviour as the transfers obtained from the simulations. A remarkable agreement is seen for case 15.4 (figure 6.25(a)). Just before the spectrum cuts off, the experiments and the simulations agree very well. Also the cut-off frequency is predicted well by the simulations, indicating that the flame length agrees well with the length of the actual flame (see chapter 4). After the cut-off frequency, the modelled transfer function rolls off to a very low value. However, the measured FTF does not drop to a low value as fast as the modelled transfer. This is an important observation with respect to stability behaviour.

6.8 Elevated pressure behaviour

In the previous section two cases at the same operating pressure (1.5 bars) were compared. The difference between these cases was the power and consequently the velocities. In this section, steady and unsteady results at three operating points at higher pressures are considered. The first higher pressure operating point has a thermal power of 190 kW at an operating pressure of 1.9 bars. Since the air factor and preheat temperature are not changed compared to the previously considered cases, the 190 kW case has the same velocities as operating point 15.4 (150 kW at 1.5 bars). By comparing these cases, the influence of the static pressure on the thermo-acoustic behaviour can be studied. The 190 kW case is denoted as operating point 19.4 in the

remainder of this section.

The second higher pressure operating point has a thermal power of 192 kW at an operating pressure of 2.3 bars. The results of this case are compared to the measurements at operating point 15.7. Again, the only difference between these operating points is the mean pressure (two times higher). The 192 kW case is denoted as operating point 23.7. Finally, the third higher pressure point has a thermal power of 250 kW and an operating pressure of 3 bars (operating point 30.7). This operating point again only differs in pressure from operating point 15.7 and 23.7. Hence, the results at operating point 30.7 are compared to those two operating points.

Firstly, the steady-state system is considered, i.e. without fuel mass flow fluctuations applied. To determine the thermo-acoustic efficiencies of the higher pressure cases, the auto-spectrum of the cases is considered. Just as done for operating points 15.4 and 15.7 (see figure 6.14), the flame source strength is extracted from the measured auto-spectrum. This is done by multiplication of this measured auto-spectrum with the *modelled* transfer function between the flame source Q' and the auto-spectrum. From these reconstructions, the quasi-steady values, and therewith the thermo-acoustic efficiencies, can be extracted. The thermo-acoustic efficiencies of all considered cases are plotted in figure 6.26 as a function of the power of the flame. It is observed that when the velocities are kept constant, the thermo-acoustic efficiency hardly depends on the power. When the velocities increase from lower than nominal to the nominal velocity, a slight increase of the thermo-acoustic efficiency is observed. This is the result of the higher degree of turbulence at higher velocities. Correspondingly, more intense heat release rate fluctuations occur, resulting in a slightly higher quasi-steady sound power output of the flame.

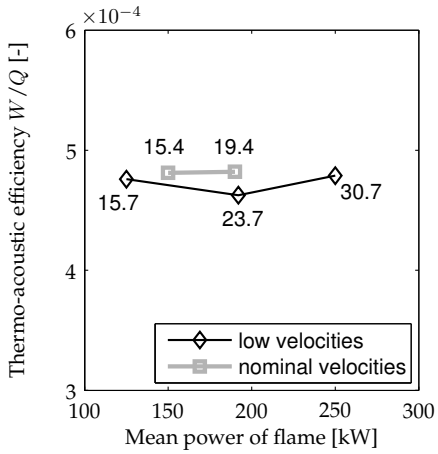

Figure 6.26: Thermo-acoustic efficiency, defined as $\eta = W/Q$, where W is the quasi-steady energy contained in the sound pulse and Q is the mean heat release rate of the flame.

Secondly, the unsteady measurements at elevated pressures are considered. In these unsteady FTF measurements, the unsteady flame source strength is again reconstructed by using a presumed spectrum shape for the steady source strength (for

the exact procedure, see section 6.7.2). The FTF at operating point 19.4, reconstructed from the measured transfer between the MOOG piston displacement and the acoustic pressure in the combustor, is compared to the modelled transfer function in figure 6.27. In this figure, the measured FTF at operating point 15.4 (same velocities) is depicted as well. Since the modelled FTF at 15.4 is almost similar to the one at 19.4, it is not shown in the figures.

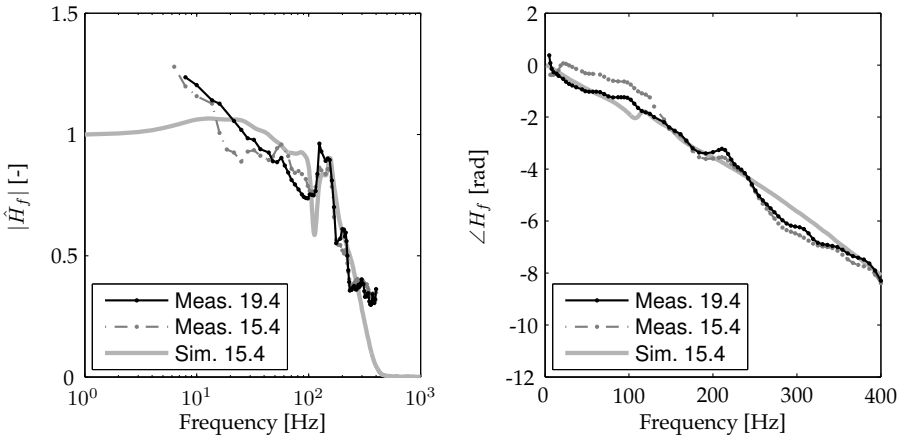

(a) Amplitude (b) Phase

Figure 6.27: Measured and modelled FTF at operating point 19.4 and 15.4.

Just as in the simulations, the measured transfer function at operating point 19.4 shows very little difference with the FTF at operating point 15.4. Again, the two peaks just before the amplitude spectrum cuts off are noticed in both the measured and the modelled FTF. The cut-off frequency is also predicted well by the model, indicating a good prediction of the flame length.

The time delay that can be extracted from the phase plot is similar to the time delay of 15.4, i.e. 3.3 ms. Since the velocities are the same for both cases, this equal time delay indicates that the flame location does not change much when simultaneously increasing the pressure and the power.

Next, the measured FTF at operating points 23.7 and 30.7 is compared to the transfer at operating point 15.7. While the simulations show little difference between the compared cases, the measurements show an effect of the pressure on the FTF, as can be noticed from figure 6.28.

It should be mentioned that the coherence of the measured FTF at operating point 30.7 is much worse than at 15.7 and 23.7. Due to the increased turbulence levels, more noise is present in the system which makes it harder to distinguish the correlated flame response from the uncorrelated flow noise. Consequently, as a result of a too low coherence, about 58% of the measured data has been removed from the data set. These removed data points were mainly located in the higher frequency region, as can be clearly seen in the phase plot in figure 6.28(b). Consequently, the frequency resolution is low in this region. When a smoothing filter is applied in this region, this

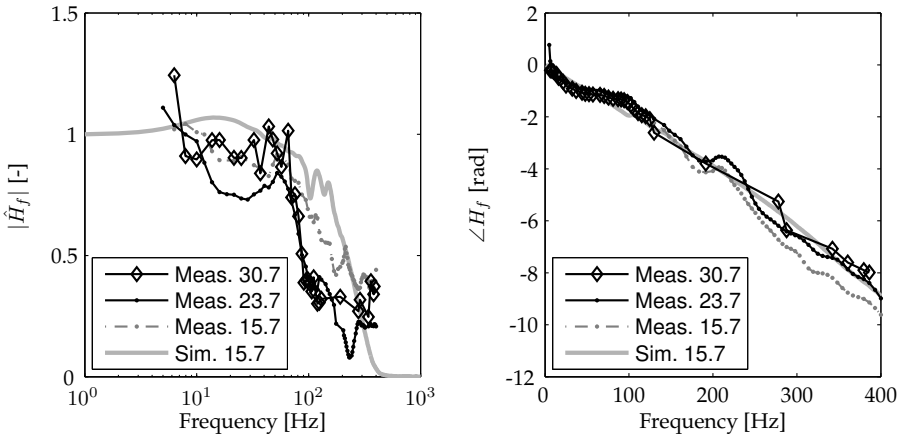

(a) Amplitude (b) Phase

Figure 6.28: Measured and modelled FTF at operating points 30.7 (no smoothing applied), 23.7 and 15.7.

would lead to averaging over a very wide frequency range. Therefore, no smoothing filter has been applied to the FTF of case 30.7.

From the amplitude of the FTFs it is seen that the level of the FTF of cases 30.7 and 23.7 rolls off faster than the lower pressure case 15.7. Nevertheless, the cut-off frequencies of the cases are approximately similar. An explanation for this could be a change in the form of the PDF of the flame response as a function of the time delay (see section 4.2), which can be caused by a change in the reaction rate with the pressure. Since the simulation results did not show this behaviour, this hypothesis could not be checked.

Another difference between the considered operating points is seen in the phase of the FTF (see figure 6.28(b)). While the velocities are equal for the three cases, the time delay at higher pressures is less. A possible explanation for this is that the flame moves somewhat closer to the burner at higher pressures for these specific cases. This could be caused by increased reaction rates at higher pressures [183], which brings the flame closer to the burner exit.

It can be summarised that pressure can have a slight influence on the FTF. As a result of higher rate coefficients, the location of the flame can change at higher pressures. Moreover, an increased roll-off of the amplitude of the FTF is noticed at higher pressures.

6.9 Validation of the unstable operating ranges

To predict instabilities of the system, the FTF of the previous section can be combined with the acoustic model of the combustor. In the current section, an operating point that shows unstable behaviour in the measurements is first selected. Subsequently,

the FTF that is obtained from the simulations at this operating point is coupled to the corresponding acoustic model. The measured FTF is not used here, since it only contains data up to a frequency of 400 Hz, while the measured unstable frequency at the selected operating point lies higher than this frequency. Nevertheless, in the previous section, a good correspondence between the measured FTF and the FTF from the simulations was obtained, which justifies the direct use of the modelled FTF. The section concludes with a discussion on the unstable frequencies found by the coupled model and observed in the measurements. Additionally, the mechanism behind the unstable points is explained and ways to prevent the instabilities are given and tested using the models.

6.9.1 Selection of unstable operating point

The operating point at which unstable behaviour is observed is point 15.7 (125 kW at 1.5 bars). This operating point is usually approached by first increasing the power from 100 to 125 kW. Subsequently, the pressure is increased to 1.5 bars. Just after arriving at operating point 15.7, no unstable behaviour is measured, as can be seen in the auto-spectrum of microphone p1 (see figure 6.29(a) (decibel scale) and (b) (linear scale)). After a short period however, a loud tonal noise starts to build up at 443 Hz. The amplitude of this fluctuation is about 150 times larger than the amplitude without instability. The peak at 443 Hz is very sharp, i.e. has a low bandwidth, in contrast to acoustic eigenfrequencies. In figure 6.29(a) the SPL obtained with the acoustic model is plotted as well (a constant acoustic source value for the flame is assumed here).

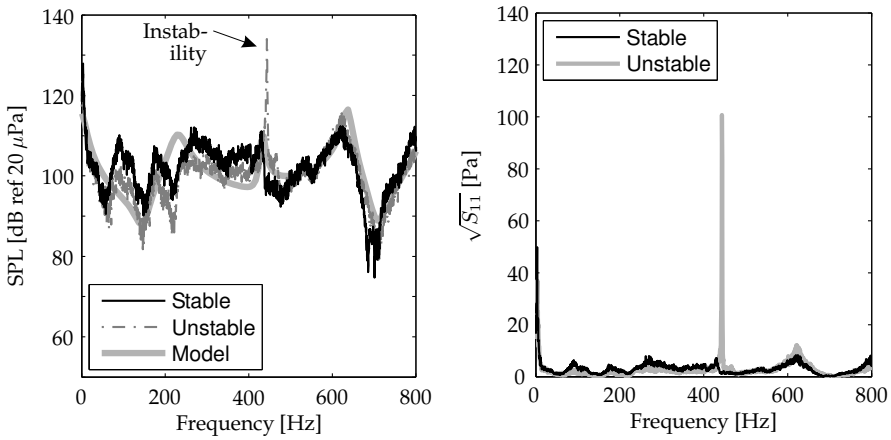

Figure 6.29: Measured and modelled acoustic pressure at operating point 15.7. Two measurements are included: without and with a thermo-acoustic instability.

From the location of the acoustic eigenfrequencies, it can be seen that the unstable

system is somewhat hotter than the stable system (i.e. the eigenfrequencies shift to a higher frequency). During the time the instability built up, the system was still heating up and the eigenfrequencies shifted to a higher value.

The instability at 443 Hz occurs near an acoustic eigenfrequency. The acoustic eigenfrequencies are approximately located at 234, 431, 637 and 850 Hz. Because of the temperature gradient through the combustor and the boundary conditions, the frequencies are not separated by a fixed frequency. However, with the acoustic network model, the frequencies can be identified as $\lambda/2$ modes of the combustor.

6.9.2 Thermo-acoustic model

To see whether the modelled FTF in combination with an acoustic model is able to predict the measured instability, a thermo-acoustic model of the experimental setup is made using the tools presented in chapter 2. This thermo-acoustic model is displayed in figure 6.30. The modifications compared to the acoustic model (see figure 6.9) are the addition of the thermo-acoustic feedback loop and the addition of the fuel supply line. This is done by creating an extra node, labelled 1', between node 1 and 2 at the location of the fuel nozzles. The fuel supply line is now included between node 1' and 8, and is bounded by the impedance of the MOOG valve. A hard acoustic boundary is assumed for this impedance. The FTF is applied between the extra node 1' and the location of the flame (i.e. node 3). The method described in chapter 2 is subsequently used to search for unstable frequencies. Note that no acoustic source has to be imposed now: one is not looking for the harmonic solution anymore (for an unstable system, no harmonic solution exists) but for the frequencies at which the determinant of the system matrix goes to zero.

Just as done in chapter 2, the mechanism inducing the instability is assumed to be the unsteady equivalence ratio at the location where fuel and air are mixed. However, no direct measurement of the flame transfer function between the flame acoustic source Q' and the unsteady equivalence ratio ϕ' is available. Instead, the FTF between Q' and the fuel mass flow perturbation M_f' is measured. Perturbing the fuel mass flow also modifies the air mass flow at the location where fuel and air are mixed. This is due to the thermo-acoustic source of the flame as a response to the fuel mass flow perturbation. This acoustic source couples back to the mixing

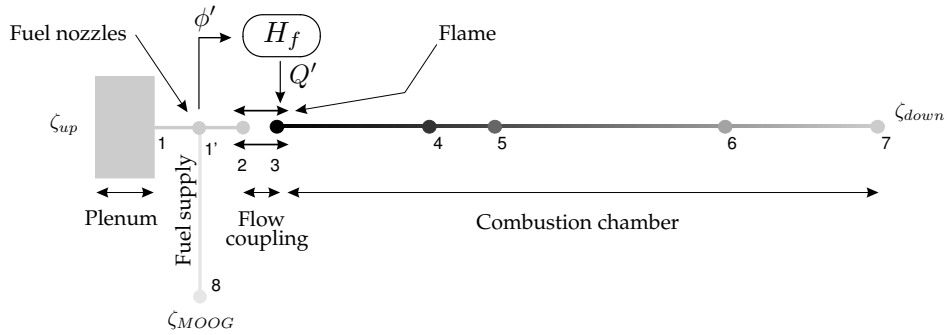

Figure 6.30: Thermo-acoustic network model of the DESIRE setup.

location, where it causes an additional perturbation in the air mass flow. Neglecting this indirect air mass flow fluctuation, the equivalence ratio perturbation resulting from a fuel mass flow fluctuation can be derived from equation 2.60, yielding:

$$\frac{\phi'}{\phi_0} \approx \frac{M_f'}{M_{f,0}} \tag{6.8}$$

Using this relationship and therewith neglecting the indirect air mass flow fluctuation, it has been shown by LES simulations that an error is made up to 20% in ϕ' [164], depending on the considered frequency.

Accepting this error and using equation 6.8, the measured transfer function can be transformed to the following transfer function:

$$\frac{Q'}{\phi'} \approx \frac{Q'}{M_f'} \frac{M_{f,0}}{\phi_0} \tag{6.9}$$

which can be coupled to the acoustic model.

The purpose of transforming the measured transfer function is that the effect of air mass flow fluctuations can be accounted for in the thermo-acoustic network model, since a transfer function involving the equivalence ratio is available. This approach is justified by the fact that in the FTF measurements, the fuel mass flow perturbations are considerably larger than the indirect air mass flow fluctuation, and that the final effect, i.e. perturbing the equivalence ratio, of a fuel or an air mass fluctuation is similar.

6.9.3 Results

The FTF that has been coupled to the acoustic model is obtained from unsteady RaNS simulations, including the fuel injectors. A good agreement between this modelled transfer function and the measured FTF has been observed (see figure 6.25(a) (amplitude) and 6.20(a) (phase)). However, the measured FTF does not contain any data beyond 400 Hz, while the first unstable frequency was found at 443 Hz. Moreover, the quality of the measurements decreases for higher frequencies, therewith taking away the opportunity to extrapolate the data to the desired frequencies. The modelled FTFs do contain information at higher frequencies, and are therefore used. However, to gain insight in the coupled model, a constant value for the amplitude, equal to the quasi-steady value, and a constant time delay, equal to the time delay estimated from the measurements, is assumed first. This implies that $H_f = Q_0/\phi_0 \mathrm{e}^{-\mathrm{i}\omega\tau_{meas}}$.

The eigenfrequencies of the system *without* the feedback loop are shown in figure 6.31(a). These eigenfrequencies all have a positive imaginary part, indicating that they are all stable. The eigenfrequencies are the acoustic eigenfrequencies of the system. Since there is damping present in the system, these eigenfrequencies have a positive imaginary part. Without damping and with perfectly echoic boundaries, all acoustic eigenfrequencies would have an imaginary part equal to zero (neither damped nor unstable). In figure 6.31(a) the groups of eigenfrequencies are indicated that correspond to the Helmholtz mode, resonances in the combustion chamber and resonances in the fuel supply line. It can be seen that the resonances in the fuel

supply line are much more damped than the other resonances, which is due to the high velocities, and consequently the high acoustic damping, in the fuel supply line.

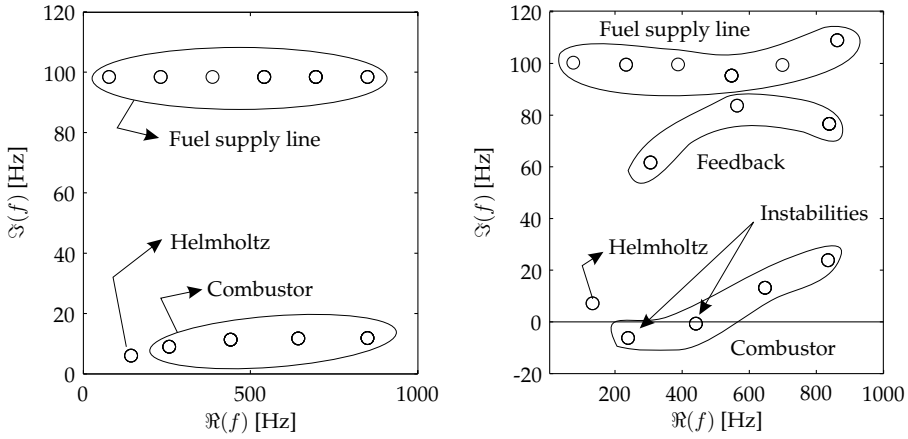

(a) Without feedback.

(b) With feedback, $H_f = Q_0/\phi_0 \mathrm{e}^{-\mathrm{i}\omega\tau_{meas}}$.

Figure 6.31: Complex frequencies for which $|\mathbf{A}| = 0$ for the system depicted in figure 6.30. Operating point 15.7 is considered here.

When the thermo-acoustic feedback loop is included in the analysis (see figure 6.31(b), $H_f = Q_0/\phi_0 \mathrm{e}^{-\mathrm{i}\omega\tau_{meas}}$), the imaginary part of the eigenfrequencies corresponding to the acoustic eigenfrequencies changes and two unstable eigenfrequencies (441 and 239 Hz) are observed. The feedback loop is seen to either promote or discourage the existing eigenfrequencies, i.e. by providing additional damping or by exciting the eigenfrequency ('feeding the resonances'). At the acoustic eigenfrequencies, a large gain is available since the acoustics can be excited easily. When the phase relationship of the feedback loop at the acoustic eigenfrequency is good, an instability can easily develop, as is the case for the two unstable points found in the analysis.

It is also seen in figure 6.31(b) that new eigenfrequencies appear. These eigenfrequencies are the direct result of the feedback loop. Their real frequency depends on the acoustic phase shift and the convective time delay between the mixing location and the 'flame'.

Comparing the measured unstable frequency (443 Hz) with the eigenfrequencies found with the model it can be seen that the frequency is indeed identified as an unstable point (the model yields a frequency of 441 Hz). At lower frequencies, the model also gives an unstable point (239 Hz). The reason why this point is not found in the measurements, might be that the representation of the actual acoustic system with the acoustic model is worse at lower frequencies (see, for example, figure 6.13).

It is noted that the frequency of the instability does not occur at the eigenfrequency that is observed for the system *without* feedback. In this case, the unstable frequencies are located slightly higher than the eigenfrequencies without feedback

(i.e. 441 vs. 431 Hz). This is because the feedback changes the system, and frequencies do not have to lie at the same location anymore. The instability observed in the measurements also occurs slightly higher than the acoustic eigenfrequencies. The original eigenfrequency is still visible though, since excitation of the regular acoustic system remains due to the autonomous flame noise.

With the thermo-acoustic model the cause of the instability can be identified: air or fuel mass flow fluctuations. In this case, it is found that the air mass flow perturbations are responsible for the instability. In figure 6.32, the eigenfrequencies are again displayed, but now calculated with only air fluctuations influencing the equivalence ratio (a) and only fuel fluctuations influencing the equivalence ratio (b). It can be seen that the case with only fuel mass flow perturbations is stable, while the case with air mass flow modulation looks similar to figure 6.31(b), and is unstable.

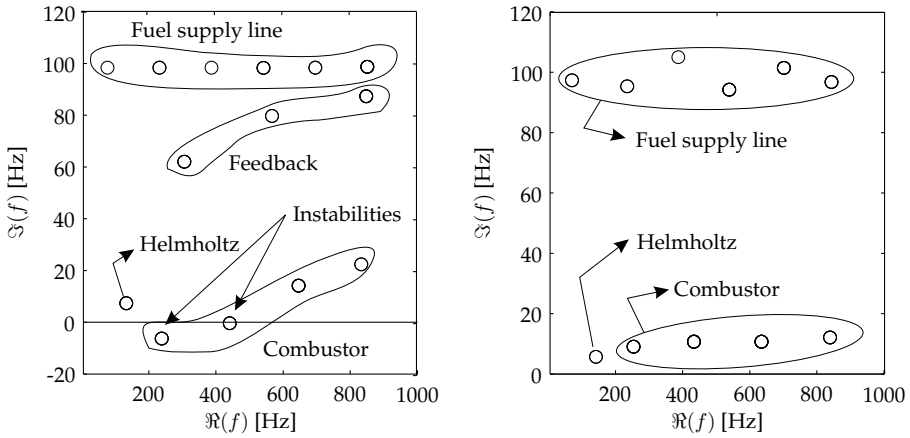

(a) Only air fluctuations.

(b) Only fuel fluctuations.

Figure 6.32: Complex frequencies for which $|\mathbf{A}| = 0$ for the system depicted in figure 6.30. Operating point 15.7 is considered here.

6.9.4 Prevention

When moving from operating point 15.7 to operating point 15.4 (i.e. increasing the thermal power from 125 to 150 kW), the instability disappears. The reason why this happens is threefold. Firstly, the time delay between the mixing location and the flame becomes shorter, which generally moves potential instabilities to a higher frequency, where there is more damping available. Secondly, the velocities, and therewith the acoustic damping, increase. This decreases the gain in the thermo-acoustic feedback loop. Finally, this decrease in gain is also caused by the larger pressure drop over the burner induced by the larger velocities. When the same thermo-acoustic analysis is performed on operating point 15.4 (i.e. using again a transfer function equal to $H_f = Q_0/\phi_0 \mathrm{e}^{-\mathrm{i}\omega\tau_{meas}}$), it can be seen that the analysis indeed shows that the system is more stable (see figure 6.33). Nevertheless, an unstable eigenfrequency

is still found, which can be stable for the same reasons as mentioned in the previous section. However, at the frequency at which unstable behaviour has been measured at operating point 15.7, a stable eigenfrequency is now found. This corresponds to the observation that operating point 15.4 is stable.

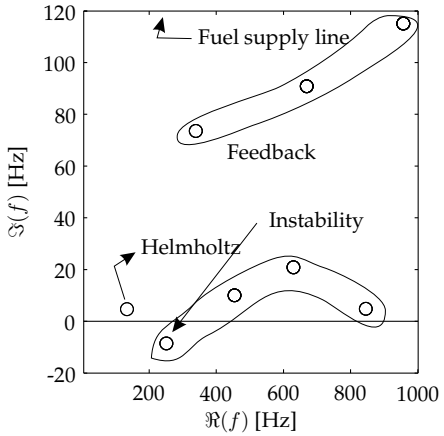

Figure 6.33: Complex frequencies for which $|\mathbf{A}| = 0$ for the system depicted in figure 6.30. Operating point 15.4 is considered here.

The increased acoustic damping and the larger burner pressure drop stabilise the system. This is clearly seen from the location of the eigenfrequencies corresponding to the fuel supply line: the imaginary part of those frequencies is much higher than for case 15.7 and is out of the range of figure 6.33. Moreover, shorter time delays between the mixing location and the flame decrease the risk for a matching feedback loop.

6.9.5 Discussion

For the instability studied in this section, a correct prediction of its frequency and stability has been obtained. However, for these predictions, a constant FTF amplitude equal to the quasi-steady value is assumed. When the *modelled* FTF is used, the 443 Hz frequency is stable. This is the result of the low-pass filter behaviour of the FTF, where the amplitude at 443 Hz is already a factor 100 smaller than the quasi-steady value. Hence, the gain in the thermo-acoustic feedback loop is much smaller, resulting in a more stable system. This might indicate that, as also indicated by the FTF measurement, the FTF amplitude does not decrease as much as predicted by the simulation, but remains at a certain minimum. At 400 Hz, the *measured* FTF amplitude is only about a factor 2 smaller than its quasi-steady value. Assuming that the amplitude at 443 Hz is still only a factor 2 smaller, the instability at 443 Hz is identified as a slightly stable point by the instability search method. Consequently, as a rule of thumb, frequencies located close to the imaginary axis should be considered as candidates for unstable behaviour.

6.10 Conclusions

In the present chapter, steady and unsteady measurements performed on the DESIRE experimental setup were presented. Although a limited number of operating points was considered, a good impression of the thermo-acoustic behaviour of the setup was obtained.

The setup has been designed for validation, i.e. care is taken for well-defined boundaries, a simple geometry etc. The good correspondence of the measurements with the generally simple models confirms that this was effective. Nevertheless, in the low frequency range the used one-dimensional acoustic model fails to correctly describe the acoustic field. This is the result of resonances in system parts beyond the acoustic decouplers. These parts are not included in the acoustic model. The acoustic decouplers do not work perfectly, which is especially manifested in the low frequency range. Moreover, disturbing effects of the semi-infinite hose and the back pressure supply system are more significant at the lower frequencies.

The inaccuracy of the acoustic model in the low frequency range prevents the direct reconstruction of the flame source strength by acoustic measurements. Therefore, another approach to reconstruct the source strength has been undertaken. In this approach, a presumed spectrum shape for the flame source strength is used. This shape is fitted through the source strength reconstructed by the acoustic model. Next, the ratio between the measured acoustic pressure and the fitted spectrum is used to associate the measured acoustic pressure to the flame source strength.

The FTFs that are reconstructed with this approach agree well with the FTFs from the CFD simulations. The good agreement proves that the Unsteady RaNS approach combined with the simple combustion model correctly predicts the flame location and the flame length. Furthermore, effects of the mean pressure on the FTF are noticed. A plausible explanation for these effects is the increasing reaction rate with the pressure, changing the position and shape of the flame. These effects lead to a steeper roll-off in the amplitude and a decrease in the time delay of the FTF.

At operating point 15.7, unstable behaviour has been measured. To check whether the instability search algorithm is able to predict this behaviour, the quasi-steady value of the FTF is coupled to the acoustic network model. When this quasi-steady value of the FTF is used at all frequencies, the instability is found at almost the same frequency as observed in the measurements. Using the same approach, the instability search algorithm predicts that operating point 15.4 is stable, as also observed in the measurements. The increased acoustic damping, the higher burner pressure drop and the smaller time delay in the feedback loop increase the stability at this operating point.

The experimental validation has been done on a well-defined setup, to which relatively simple models apply. More complex combustion systems automatically imply that a more complex modelling approach should be undertaken. Nevertheless, the methods with which the FTF is determined from these models do not change. To also be able to apply the methods to more complex combustion systems, a more advanced combustion model based on a progress variable approach is used for FTF determination. This model will be discussed in the next chapter.

Chapter 7

A progress variable approach

7.1 Introduction

All final flame transfer function (FTF) calculations presented in the previous chapters have been obtained from CFD models. In the validation of these transfers deviations with the experimental results have been observed (see chapter 6), resulting from the various assumptions made in constructing the numerical model. One of the most decisive assumptions that has been made is the use of a single-step, combined Arrhenius/eddy dissipation (ED) model to account for combustion. The principal disadvantage of this model is that it does not account for the influence of turbulent fluctuations on the reaction rate of the reactants, i.e. a δ-PDF distribution is assumed for the variables used to calculate the reaction rate. This implies that the quantity is presumed not to be influenced by turbulent fluctuations. However, when Reynolds numbers are large, the fluctuating quantities can have a large effect on the reaction rate [135]. This phenomenon can be explained by taking the Taylor series of the effective Arrhenius law around $T = \bar{T}$ [119]:

$$\begin{aligned} A \cdot \exp\left(-\frac{T_a}{T}\right) &= ... \\ ... &= A \cdot \exp\left(-\frac{T_a}{\bar{T}}\right)\left[1 + \frac{T_a}{\bar{T}^2}T' + \frac{T_a}{\bar{T}^3}\left(\frac{T_a}{2\bar{T}} - 1\right){T'}^2 + \mathcal{O}({T'}^3)\right] \end{aligned} \tag{7.1}$$

where A is the pre-exponential constant of the reaction and T_a is its activation temperature. Generally, the ratio $T_a/\bar{T}$ is large, which implies that the reaction strongly depends on the temperature fluctuations. Neglecting the term $\frac{T_a}{\bar{T}^3}$ with respect to $\frac{T_a^2}{2\bar{T}^4}$ ($T_a/\bar{T}$ is large), the average of equation 7.1 yields:

$$\overline{A \cdot \exp\left(-\frac{T_a}{T}\right)} \approx A \cdot \exp\left(-\frac{T_a}{\bar{T}}\right)\left[1 + \frac{T_a^2}{2\bar{T}^4}\overline{T'T'} + \overline{\mathcal{O}({T'}^3)}\right] \tag{7.2}$$

since $\bar{T'} = 0$. This expression shows that turbulent fluctuations in the temperature can influence the relative reaction rate via the term $\frac{T_a^2}{2\bar{T}^4}\overline{T'T'}$. Also the higher order

moments of the fluctuations influence the reaction rate. For the global single-step reaction mechanism of methane and an ambient temperature of 1000 K, the factor $\frac{T_a^2}{2\bar{T}^4}$ yields approximately $1.14 \cdot 10^{-4}$. In turbulent flames, temperature fluctuations T' can be as large as 200 K. Substituting this value for T', the factor can be estimated as 4.56, which is higher than the mean contribution (which is unity). This means that the temperature fluctuations can have a significant influence on the relative reaction rate in turbulent flows.

The higher order terms in the Taylor series all contain the term $\frac{T_a^2}{2\bar{T}^4}\overline{T'T'}$ to some power. Since $\frac{T_a^2}{2\bar{T}^4}\overline{T'T'} > 1$, the Taylor series is not always converging [20]. The constants in the Taylor series do provide some convergence though, and about 30 moments have to be considered to accurately account for the influence of fluctuations. This implies that 30 transport equations for the moments of each species in the reaction mechanism would have to be solved, which is computationally not feasible for engineering applications.

Fortunately, the highly non-linear source terms can be removed by constructing so-called reaction progress variables (RPVs), consisting of a linear combination between the species involved in the reaction. This linear combination is chosen such that the source terms with large activation energies balance each other. The final source term of the RPVs contains only the source terms of the reactions with low activation energy [119]. This procedure can be considered as a means to remove the fast chemical reactions from the mechanism by identifying 'steady-state' species and fast reactions which are in partial equilibrium.

The projection of a detailed reaction mechanism onto a limited number of RPVs is done in the CFI-combustion model. This combustion model has been developed and used at the laboratory of Thermal Engineering of the University of Twente [41,90,118, 119, 189]. For small reaction mechanisms (i.e. syngas* combustion) the construction of the RPVs can be done manually [119]. For larger mechanisms (like the oxidation of methane) a more general computational approach must be applied to determine the optimal RPVs. In the CFI model, this is done with the CSP reduction algorithm [41, 122].

In this chapter, the previously used combustion model is replaced by the more advanced CFI-combustion model. After this introduction, the CFI-combustion model will be briefly described. Subsequently, the consequences of applying the CFI-model for the steady solution and the FTF are pointed out for operating point 15.4. Finally, the obtained FTF will be validated with the measured FTF.

7.2 The CFI-combustion model

For methane (or natural gas), the most detailed reaction mechanism that is currently available is the GRI-mech 3.0 mechanism. It consists of 325 elementary reactions involving 53 species and 5 elements. Solving 53 additional transport equations in an already large CFD model is computationally very expensive. Additionally, in RaNS turbulent combustion simulations, transport equations for several moments for each

*Syngas is a mixture of CO and H_2.

species should be solved to account for the effect of turbulent fluctuations on the reaction rate. As a result of the large number of time scales present in the reaction mechanism, the system is very stiff and therefore difficult to solve.

The basic idea of the CFI-combustion model is to map the detailed chemistry mechanism onto a small number of RPVs. In this process, the fast reactions are assumed to be in partial equilibrium and 'steady-state' species are removed from the mechanism. This way, the highly non-linear effects on the reaction rates is removed, and only the second moments of the RPVs need to be considered to account for the effect of turbulent fluctuations.

The CFI-combustion model was first used for the adiabatic combustion of hydrogen-air diffusion flames [82, 83]. It was further developed at the laboratory of Thermal Engineering of the University of Twente. The developments cover the adaption of the model for methane-air combustion [90, 189], inclusion of heat loss through radiation for hydrogen-air flames [118] and methane-air flames [119], and accounting for the second moments of the RPVs and the mixture fraction [118]. The latest developments of the model comprise the use of a computational approach to efficiently determine the RPVs for chemical reaction mechanisms of any size [41]. Moreover, various numerical algorithms used in the CFI model have been optimised.

The numerical algorithm that is currently used in the CFI model to construct the RPVs is the CSP algorithm. The basic idea of CSP was first published by Lam [100] in 1985. The (abstract) theory and strategy of the CSP method is reviewed in [101]. In the next section, a brief overview of the method is given.

7.2.1 The CSP algorithm

The composition of a chemical system can be regarded as a point in composition space, which is a multi-dimensional space in which each dimension represents the concentration of a chemical species. The chemical-kinetic rate equations of the system determine how the composition point moves in the space. The fast reactions move the composition point rapidly in a certain direction. The consequence of this is that the composition point first moves rapidly toward a manifold of reduced dimensionality, then moves along the manifold towards an equilibrium point. In (global) CSP a numerical approach is used to obtain this manifold, i.e. the fast processes are identified and removed from the reaction mechanism. The manifold is parameterised by using relatively few variables which are by definition of the method linearly independent.

A visual interpretation of a manifold can be given when it is assumed that there is only one reaction in the whole reaction mechanism that is determining the complete mechanism. Imagine that this reaction involves a species with mass fraction y_1 reacting with another species with mass fraction y_2. While reacting, the temperature T in the system increases. In figure 7.1, this reaction is 'mapped' onto a two-dimensional manifold, parameterised by the mixture fraction f and the RPV c. At any point on this manifold, all the quantities of the complete reaction mechanism are a function of f and c. The manifold can be extended to more dimensions, allowing more degrees of freedom for the mapping of the reaction.

The so-called CSP S-STEP code [122] results in a $k \times 1$ CSP-vector $\boldsymbol{\eta}$, which is a

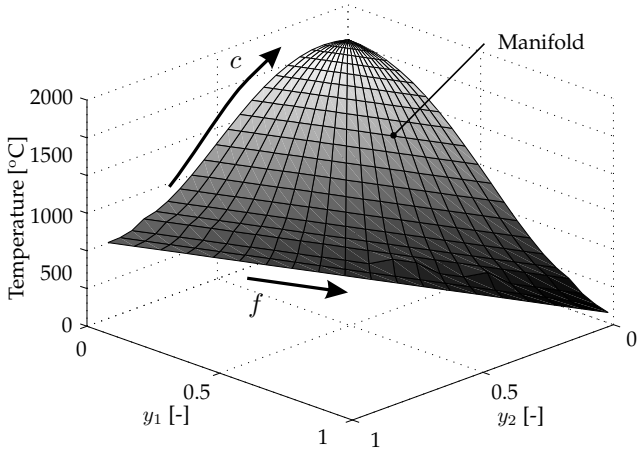

Figure 7.1: Interpretation of a manifold.

linear combination of the total number of species. In the dimensions of $\boldsymbol{\eta}$, k defines the number of RPVs. The matrix $\boldsymbol{\eta}$ can be expressed as:

$$\boldsymbol{\eta} = \mathbf{by} \tag{7.3}$$

where $\mathbf{b}$ is a $k \times N$ matrix containing participation factors, and $\mathbf{y}$ is the $N \times 1$ vector with the species mass fractions. In these dimensions, N equals the total number of species.

Being an order reduction method, the CSP-method shows many similarities with the Lanczos method, presented in chapter 5. The Lanczos method is also suitable for high order systems, it can handle systems with many time scales and it eventually results in a reduced state vector equal to $\mathbf{Q_k}^T\mathbf{y}$, where $\mathbf{y}$ is the original state vector with the mass fractions and $\mathbf{Q_k}^T$ represents the participation of these mass fractions in the RPVs (equivalent to the $\mathbf{b}$ matrix in the CSP-method). In the Lanczos method, the state space matrix $\mathbf{A}$ would indicate how each mass fraction participates in each reaction. No effort has been made to rewrite the problem to the Lanczos method and compare its performance with the CSP method, but it would be an interesting direction for further research.

With the CSP-vectors, the RPVs $\mathbf{c}$ can be constructed. These RPVs are constructed such that their value ranges from 0 (the unburned situation) and 1 (the equilibrium situation). The definition of the j^{th} RPV is therefore:

$$c_j = \frac{\eta_j - \eta_j^u}{\eta_j^{eq} - \eta_j^u} \tag{7.4}$$

where the superscripts u and eq indicate the unburned and equilibrium situations, respectively. The normalisation factor $\eta_j^{eq} - \eta_j^u$ depends on the mixture of fuel and air at the inlet. Moreover, other quantities as the density, the species mass fractions

etc. depend on the mixture of fuel and air. For this purpose, a mixture fraction f is defined as well:

$$f = \frac{\eta - \eta^{in2}}{\eta^{in1} - \eta^{in2}} \tag{7.5}$$

where the superscripts $in1$ and $in2$ are the values of the CSP-vectors at inlet 1 and 2, respectively. Note that any entry of the CSP-vector may be used to construct the mixture fraction, it will always yield the same result. As the mixture fraction does not have a source term, it only depends on the mixing between the species coming from inlet 1 and 2. Obviously, for a perfectly premixed mixture, the mixture fraction is constant.

With equation 7.3 and 7.4, the general species transport equation (equation 3.16) can be converted into a transport equation for the RPVs $\mathbf{c}$. Since $\mathbf{c}$ is a function of the mixture fraction, the product rule of taking derivatives results in derivatives of f as well. Moreover, a source term for $\mathbf{c}$ arises, representing the formation or destruction of the RPVs. For more information, see [41].

7.2.2 Favre averaging

To make the obtained transport equations useful for solving it with a RaNS code, each scalar c_j and f are decomposed into a mean and a fluctuation. Subsequently, the equations are Favre averaged. By multiplying the original transport equation for c_j with c_j'' and applying the Favre averaging procedure, also equations for the transport of the variance of $\mathbf{c}$ are obtained. A similar procedure is performed to obtain an equation for f''. The complete Favre averaged CFI transport equations for $\mathbf{c}$, $\mathbf{c}''$, f and f'' can be found in [41].

After the mapping of the whole reaction mechanism onto the progress variables $\mathbf{c}$ and the mixture fraction f, all species, the density and the temperature have become functions of $\mathbf{c}$, $\mathbf{c}''$, f and f''. This means that for adiabatic flows the following functions can be defined:

$$\bar{\rho} = \bar{\rho}\left(\tilde{\mathbf{c}}, \widetilde{\mathbf{c}''^2}, \tilde{f}, \widetilde{f''^2}\right) \tag{7.6}$$

$$\tilde{\mathbf{y}} = \tilde{\mathbf{y}}\left(\tilde{\mathbf{c}}, \widetilde{\mathbf{c}''^2}, \tilde{f}, \widetilde{f''^2}\right) \tag{7.7}$$

$$\tilde{T} = \tilde{T}\left(\tilde{\mathbf{c}}, \widetilde{\mathbf{c}''^2}, \tilde{f}, \widetilde{f''^2}\right) \tag{7.8}$$

Additionally, the source terms in the turbulent transport equations for the RPVs depend on the values of the mean and variance of the RPVs and the mixture fraction. These relationships are determined before the CFD run and stored in a database. For this purpose the laminar CFI equations are solved for presumed values of $\mathbf{c}$ and f. This creates the so-called laminar database. Subsequently, β-PDFs (probability density function) are assumed for $\mathbf{c}$ and f. Since the RPVs and f are assumed to be statistically independent, the Favre mean value of each scalar $\tilde{\psi}$ in the problem can be calculated with a factorised PDF approach:

$$\tilde{\psi} = \frac{1}{\bar{\rho}} \int_{\mathbf{c}=\mathbf{0}}^{\mathbf{1}} \int_{f=0}^{1} \rho\psi(\mathbf{c}, f) P(\mathbf{c}) P(f) \mathrm{d}\mathbf{c}\mathrm{d}f \tag{7.9}$$

where $P(x)$ is the probability density function of x. Assuming a β-PDF implies that the PDF is fully described by the mean and the variance of the scalar to which is applied.

In the laminar database, each quantity is stored as a function of $\mathbf{c}$ and f. To transform the database to a turbulent one, a grid of combinations of $\left(\tilde{\mathbf{c}}, \widetilde{\mathbf{c}''^2}, \tilde{f}, \widetilde{f''^2}\right)$ is fixed. For each combination of grid points, $P(\mathbf{c})$ and $P(f)$ can be calculated. Using these β-PDFs all mean scalars (mass fractions, temperature, density, source terms etc) are calculated by evaluating expression 7.9. Once all these averages have been determined, the turbulent database is created.

7.2.3 Coupling to RaNS code

During the CFD run, the values for the density and the source terms of the transport equations are needed. These values are extracted from the turbulent database at each time step and for each local combination of the mean and variance of the RPVs and the mixture fraction. In the database, the values for these variables are given only for a grid of values for the mean and variance of the RPVs and the mixture fraction. Interpolation is applied to get the values between the grid points. An efficient search and interpolation algorithm is used to speed up the process [41].

After the CFD run has finished, the values for the mass fractions and the temperature are interpolated from the database. Since these values are not needed for solving the problem, there is no need to do this each time step. The interaction between the database and the CFD flow solver is displayed in figure 7.2.

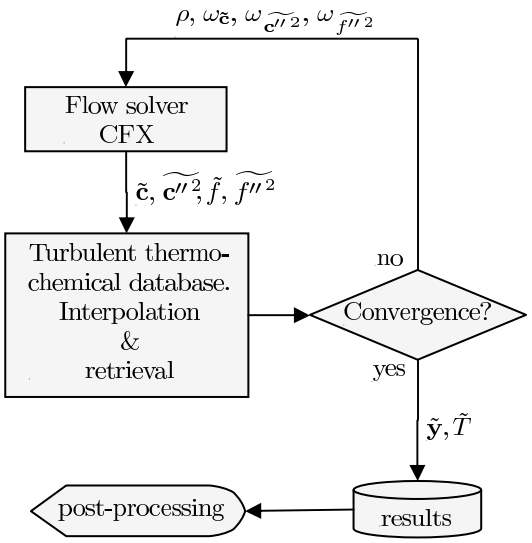

Figure 7.2: Interaction between flow solver and thermo-chemical database.

7.3 Steady solution

A CFI database generated by the CSP-method has been constructed and applied to calculate the steady-state reacting flow solution at operating point 15.4. The imperfectly premixed (IP) case has been considered, since this is the most realistic model available. The used CFI database represents a reduced version of the GRI-3.0 mechanism, which describes the oxidations of methane or natural gas. It allows the solution of very lean to very rich flames. The complete mechanism has been mapped onto a single RPV.

The PDF integration from the laminar database is implemented as a Riemann sum. To increase the accuracy of this Riemann sum, a high resolution in the full range of f is required. To get a good description of the averaged quantities, 200 points for f have been used.

A known problem of reduced chemical systems is that the reduced set sometimes yields unphysical solutions. Because the steady-state relations, on which the reduction is based, are less valid in the lower temperature range, this region is most suspectable to unphysical reduced solutions. Obviously, the lower overall temperatures in lean flames provoke the problem described above. In terms of RPVs, the lower temperature range is represented by the range $c \in [0, c^0]$, where c^0 is the RPV value at which the last valid solution is obtained. A procedure that can be applied to relax the problem is to interpolate the thermochemical data between the last valid solution at c^0 and the values of the cold flow at $c = 0$ [41]. The thermochemical data is subsequently Favre averaged and stored in the turbulent database.

An assessment of the quality of the laminar database can be obtained by comparing the thermochemical quantities with the full laminar solution calculated by PREMIX on a RPV basis (1-step reduced mechanism). This way, the quantities can be compared as a function of the RPV. In the PhD thesis of Derksen, this is done for several CSP-reduced methane reaction mechanisms [41]. As a result of the interpolation between the last valid solution at c^0 and the values of the cold flow at $c = 0$, a good match can be obtained for the temperature as a function of the RPV. The interpolation commences at $c^0 = 0.25$.

Nevertheless, when the laminar source term of c is compared with the detailed PREMIX solution, a large over-prediction of this source term is seen below $c = 0.6$. Likewise, this deviation results from the reduced validity of the steady-state relations at lower temperatures. While the temperature is well-predicted due to the applied interpolation, the source term of the reduced model is over-predicted at values for c below 0.6. This means that the reaction rate is over-predicted as well, which yields an under-predicted flame length. Since the source term of c resulting from the detailed PREMIX solution quickly decays to zero below $c = 0.6$, the source terms of c in the laminar database are clipped to zero below $c = 0.6$. This is a quite crude approach, which needs extra consideration in future research.

No further discussion of the database properties is given here. An extensive discussion on the database construction and its typical properties can be found in Derksen [41].

Figure 7.3 shows the steady-state temperature field obtained with the CFI-model and with the combined Arrhenius/ED model. The flame has a smaller opening angle

than the flame calculated by the combined Arrhenius/ED model. Moreover, the inclusion of the influence of variance on the reaction rate increases the temperature gradients in the reactions zone.

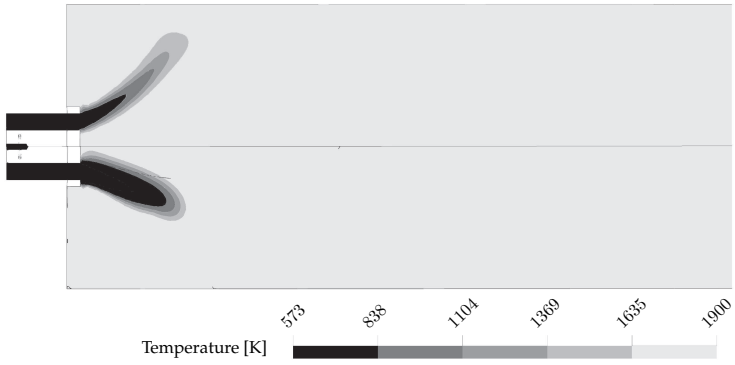

Figure 7.3: Temperature field of case 15.4 (IP), calculated with the combined Arrhenius/ED model (top) and the CFI model (bottom).

As a result of the changed combustion behaviour, a considerably different velocity field is found, as illustrated by the axial velocity field in figure 7.4. The length of the central recirculation zone is somewhat shorter for the CFI-model.

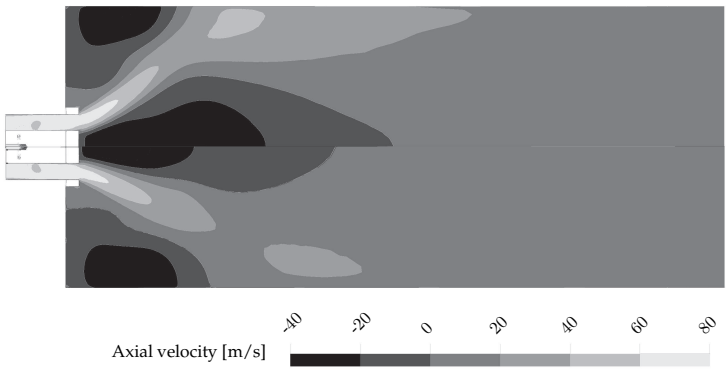

Figure 7.4: Axial velocity field of case 15.4 (IP), calculated with the combined Arrhenius/ED model (top) and the CFI model (bottom).

7.4 Flame transfer function

The thermo-acoustic source term Q' was previously determined directly from the volume integral of the source term $\widetilde{\omega_{CH4}}$ of the CH_4 mass fraction $\widetilde{y_{CH4}}$. In equation 2.16 it has been shown that this source term is related to the thermo-acoustic source via the enthalpy of formation of the species. Since the source terms of all species in

the previously used single-step reaction mechanism are related through stoichiometry, the enthalpies of formation and $\widetilde{\omega_{CH4}}$ are the only data that is needed for the calculation of Q'.

In the CFI model, this thermo-acoustic source term is less straightforward to construct. It is now a function of not only the mean values, but also the variances of the RPV and the mixture fraction. The source term of the RPV does not have to be necessarily proportional to the heat release rate. The RPV is constructed from several species, according to equation 7.3. Not all species involved in the reaction are included in the CSP-vector $\boldsymbol{\eta}$. The species mass fraction of CH_4 is an example of a steady-state species and is therefore not included in the CSP-vector.

To be able to retrieve the source term, equation 2.18 is used. For convenience, this equation is echoed here:

$$q' = \rho c_p \frac{\mathrm{D}T'}{\mathrm{D}t} \tag{7.10}$$

This equation is actually derived from the more exact equation, i.e. including changes in the heat release rate due to changes in the mixture:

$$q' = \rho \frac{\mathrm{D}}{\mathrm{D}t} \int_{T_0}^{T} c_p \mathrm{d}T \tag{7.11}$$

The total derivative in this equation accounts for changes in the local heat release rate due to convection of sensible energy. Since the time period in which the response of the flame is monitored is shorter than the residence time of a particle in the combustor, the extra induced sensible enthalpy does not leave the domain within the monitored time. This means that the system can be considered as a closed system. The consequences of taking the volume integral of equation 7.11 can be shown by using Gauss' theorem and integration by parts:

$$Q' = \int_V \rho \frac{\partial}{\partial t} \left(\int_{T_0}^{T} c_p \mathrm{d}T \right) \mathrm{d}V + \int_V \rho \mathbf{u} \cdot \nabla \left(\int_{T_0}^{T} c_p \mathrm{d}T \right) \mathrm{d}V \tag{7.12}$$

$$= \int_V \rho \frac{\partial}{\partial t} \left(\int_{T_0}^{T} c_p \mathrm{d}T \right) \mathrm{d}V \tag{7.13}$$

since

$$\int_V \rho \mathbf{u} \cdot \nabla \left(\int_{T_0}^{T} c_p \mathrm{d}T \right) \mathrm{d}V = \int_V \nabla \cdot \left(\rho \mathbf{u} \int_{T_0}^{T} c_p \mathrm{d}T \right) \mathrm{d}V - \ldots$$

$$\ldots - \int_V \left(\int_{T_0}^{T} c_p \mathrm{d}T \right) \nabla \cdot (\rho \mathbf{u}) \mathrm{d}V \tag{7.14}$$

and

$$\int_V \nabla \cdot \left(\rho \mathbf{u} \int_{T_0}^{T} c_p \mathrm{d}T \right) \mathrm{d}V = \oint_S \left(\rho \mathbf{u} \int_{T_0}^{T} c_p \mathrm{d}T \right) \cdot \mathbf{n} \mathrm{d}S = 0 \tag{7.15}$$

$$\int_V \left(\int_{T_0}^{T} c_p \mathrm{d}T \right) \nabla \cdot (\rho \mathbf{u}) \mathrm{d}V = \int_{T_0}^{T} c_p \mathrm{d}T \int_V \nabla \cdot (\rho \mathbf{u}) \mathrm{d}V - ...$$

$$... - \int_V \frac{\partial}{\partial V} \left(\int_{T_0}^{T} c_p \mathrm{d}T \right) \int_V \nabla \cdot (\rho \mathbf{u}) \mathrm{d}V \mathrm{d}V = 0 \tag{7.16}$$

The last equation yields zero because the term $\int_V \nabla \cdot (\rho \mathbf{u}) \mathrm{d}V$ in this equation can again be written as a surface integral over the boundaries of the model. Since the system is considered to be a closed system, this surface integral is equal to zero.

The result of equation 7.13 is output after each time step. An impulse fluctuation is imposed at the fuel inlet to excite the flame. For validation purposes, equation 7.13 has been used to reconstruct the FTF with the combined Arrhenius/ED model. As expected, this resulted in the same transfer function as obtained when directly using the volume integral of the source term of the CH_4 mass fraction.

Figure 7.5 shows the calculated FTF at operating point 15.4. In the figure, the calculated FTF is compared to the measured FTF at the same operating point. Furthermore, the FTF obtained with the combined Arrhenius/ED model is displayed.

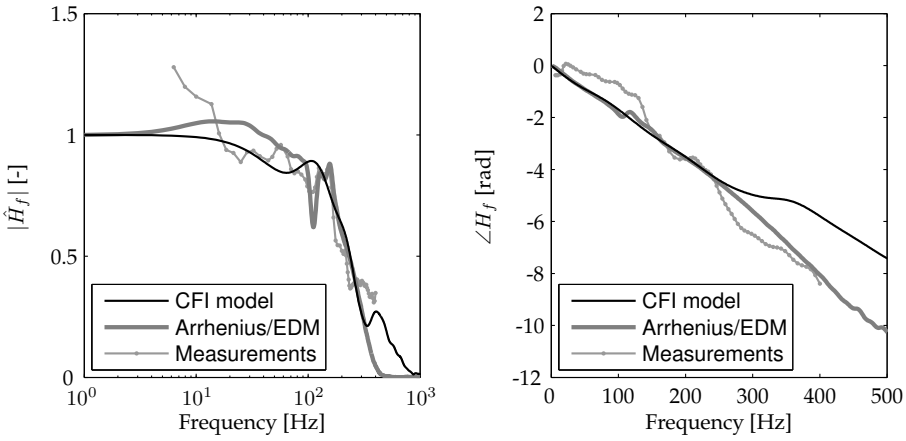

(a) Amplitude (b) Phase

Figure 7.5: Comparison between the measured FTF and the FTF resulting from an IP simulation with the CFI combustion model.

The results calculated with the CFI model show similar trends in the amplitude and phase as the measured FTF. The offset between the measurements and the results obtained with the CFI model might be the result of setting the source terms

in the turbulent database to zero when $c < 0.6$. A more refined modelling of the low temperature behaviour can improve the results obtained with the CFI model, especially since it determines the location of the flame front and its sensitivity to perturbations. Derksen [41] gives directions in which research should proceed to overcome this problem.

Although the amplitude of the FTF calculated with the CFI model misses the distinct peaks at ± 130 and ± 155 Hz (which are in fact present in the FTF calculated with the combined Arrhenius/ED model), the CFI model shows a much larger value for the amplitude at higher frequencies. The small bump just before the amplitude drops to very low values is also recognised in the measurements, although it occurs at a somewhat lower frequency. The FTF amplitude having a significant value at relatively high frequencies can explain the unstable behaviour found at operating point 15.7. Since a higher gain is present now at the observed unstable frequency (443 Hz, see chapter 6), the eigenfrequencies in the stability diagram move to the unstable half of this diagram, increasing the change for an instability to occur.

A phenomenon that can cause an offset of the transient results obtained with the CFI model and with the combined Arrhenius/ED model could be the lack of compressibility when applying the CFI model. As mentioned earlier, the density depends on the CFI quantities and is written to the flow field. In the CFI model a constant pressure is presumed. In the solver code however, the independent variable is the pressure. So this variable is adapted such that mass is conserved after overwriting the density. Consequently, a mismatch arises between the pressure in the CFD model, and the (constant) pressure in the CFI model. However, since the influence of this small mismatch on combustion is little, this does not have serious consequences for the combustion process. Nevertheless, acoustic compressibility effects are suppressed by this procedure.

To show this, the mass conservation equation is considered. In CFX the pressure, temperature and mass fractions are considered as the independent variables. This leads to the following equation for mass conservation:

$$\frac{\partial p}{\partial t} = \frac{p}{T}\frac{\partial T}{\partial t} - p\sum \frac{M_i}{M}\frac{\partial y_i}{\partial t} - RT\nabla \cdot \mathbf{u}\rho \tag{7.17}$$

The first two terms at the RHS of this equation are neglected in the way that the CFI model is coupled to CFX. The change in the density is in CFX completely compensated by changing the pressure. As an example, consider a closed volume: when the density decreases due to combustion, the coupling of the CFI model with CFX will let the pressure decrease in the closed volume. In reality, the pressure increase is less, since the density decrease is partly compensated by the temperature increase:

$$\frac{1}{\rho}\frac{\partial \rho}{\partial t} = \frac{1}{p}\frac{\partial p}{\partial t} - \frac{1}{T}\frac{\partial T}{\partial t} \tag{7.18}$$

in which the influence of changing mass fractions has been neglected.

Incorporating these effects, as done in the combined Arrhenius/ED model, eventually leads to a different coupling between the density, temperature, pressure and species mass fractions. For example, a density increase might not effect the temperature decrease imposed by the CFI database: a local pressure increase may suppress

the temperature decrease. The deviation between the temperature decrease calculated by the CFI database and the smaller decrease due to pressure effects will, at a later time, vanish since the potential energy of the pressure wave will eventually be released in heat. This delayed heat release can affect the FTF.

In this case, however, a simulation in CFX with the combined Arrhenius/ED model and a steady pressure field showed a similar FTF as the transfer obtained with unsteady pressure fluctuations included. Nonetheless, when acoustic wave propagation needs to be simulated with the CFI model coupled to a CFD model, an additional transport equation should be solved for the enthalpy. This way, the correct relationship between pressure and density fluctuations is provided. This is left as a recommendation.

7.5 Conclusions

In this chapter a combustion model, called the CFI model, has been coupled to the CFD model of the DESIRE combustor. In the CFI model, the complete chemical reaction mechanism of methane is mapped onto one reaction progress variable. In the reduction of the chemical mechanism, use is made of the CSP method. It is recommendable to also check the performance of the Implicitly Restarted and Shifted Lanczos method (see chapter 5) in reducing the chemical mechanism.

With the CFI model, a reacting flow solution can be obtained by solving extra transport equations for the mean and variance of this RPV and of the mixture fraction. Comparisons have been made between the steady result obtained with the CFI model and with the combined Arrhenius/ED approach. The flame has a smaller opening angle than the flame calculated by the combined Arrhenius/ED model. Moreover, the inclusion of the influence of variance on the reaction rate increases the temperature gradients in the reaction zone. Obviously, this also affects the velocity field.

The FTF is calculated with the CFI model and compared to the measured FTF. The general shape, i.e. a low-pass filter and a constant time delay, are well predicted by the CFI model. Generally, when the combustion model is able to predict the flame length and the location correctly, the general shape of the flame transfer function is also predicted well. Apparently, both the CFI model and the combined Arrhenius/ED model are able to do this for the current combustion system.

Nevertheless, deviations are observed as well, mainly in the amplitude. The cause of these deviations is probably the fact that the source terms have been clipped to zero for $c < 0.6$. This has been done because the source terms of the reduced model are over-predicted at values for c below 0.6 as a result of the reduced validity of the steady-state relations at lower temperatures. Nonetheless, PREMIX simulations, presented in [41], show that there is still a source term present at low c. A more detailed description of the low temperature behaviour can improve the performance of the CFI model. Additionally, as the coupling between the CFI model and CFX is currently implemented, acoustic compressibility effects are neglected. These compressibility effects should be accounted for when studying acoustic wave propagation. For the current FTF simulations, little effect of acoustics is noticed though.

Chapter 8

Conclusions and recommendations

8.1 Conclusions

The study presented in this thesis is part of the EU project DESIRE. In this EU project, the focus lies on the thermo-acoustic behaviour of gas turbine flames and their interaction with possibly destructive vibrations of the combustor liner. This thesis treats the thermo-acoustic behaviour of turbulent premixed natural gas swirl flames. The interaction with the combustor liner is subject of Huls' PhD thesis [75].

Since the thermo-acoustic problem has a multi-disciplinary character, theory and numerical methods from several different research fields have been employed. The considered subjects range from the theory and implementation of efficient reduction methods for the direct retrieval of a flame transfer function from a steady-state CFD simulation, to the many engineering problems involving the design of an experimental setup for the validation of the developed models.

The objective of the thesis is the development and validation of efficient measurement techniques and numerical algorithms to check combustion systems for their sensitivity to combustion oscillations. In the Introduction (chapter 1), three topics to meet this objective were listed. These topics can be summarised as: the acoustic modelling of combustion systems with thermo-acoustic feedback, efficient methods for the flame transfer function determination and the experimental validation. The conclusions have been organised according to this classification and are discussed below.

Acoustic modelling of combustion systems with thermo-acoustic feedback

The acoustics in combustion systems are shown to be essentially one-dimensional due to the high ratio between the acoustic wavelength and the typical cross-sectional dimensions of the combustion system. An efficient one-dimensional acoustic network model has been used to model this acoustic system. The most important effects

that play a role in the acoustic modelling of combustion systems have been included in this network model. These effects comprise acoustic damping due to turbulence, acoustic reflection at contractions and expansions with a mean flow, modification of the acoustic speed of sound due to a mean flow and the effect of a temperature gradient.

The abstract analogy of the acoustic source of the flame is a monopole sound source. Since the dimensions of the flame are typically much smaller than the acoustic wavelengths, its acoustic effect can be considered as a point source in the acoustic network model. Especially in combustion systems the monopole sound source is dominant, as is also observed in the performed measurements. The location of the source in the acoustic system is very important for the stability of the system. Placing the flame at the location of an acoustic velocity node makes it very easy for the flame to excite the acoustic field, which increases the risk for instabilities.

By coupling the acoustic model with a flame transfer function, the system has no harmonic solution anymore and can become unstable, i.e. the acoustic pressure builds up in time. The coupling of the flame transfer function with the acoustic model is realised by including a source term which depends on one or multiple other acoustic quantities in the system via the flame transfer function.

A stability analysis performed on this coupled model reveals the instabilities of the coupled model. A conservative approach is made with respect to the stability analysis: only the linear stability is assessed in this thesis. Nevertheless, most instabilities are initiated in the linear regime, after which they can develop to the non-linear regime.

Efficient methods for the flame transfer function determination

Several numerical methods for determining the flame transfer function have been presented. In all methods it is assumed that the quantity that is exciting the flame is the unsteady equivalence ratio. Measurements and literature show that this is the principal cause for instabilities in premixed flames.

With an analytical model, it has been shown that the typical low-pass filter behaviour of the flame transfer function can be completely attributed to the fact that a particle spends a finite time in the reaction zone. The finite time delay of the reaction itself also causes a cut-off of the flame transfer function spectrum. However, this cut-off frequency lies at a much higher frequency than the cut-off frequency due to the flame residence time, which was shown by a Well-Stirred Reactor (WSR) model.

While the analytical model and the WSR model can predict the cut-off frequency, local increases or decreases of the flame transfer function due to, for example, movement of the flame front cannot be predicted by this model. This behaviour can only be described when the actual flow field is incorporated in the models. For this purpose, transient CFD simulations in combination with spectral analysis (white noise and impulse excitation have been applied) have been used for the determination of the flame transfer function. Unsteady RaNS simulations have been used for this purpose.

Results obtained with this numerical approach show that a flame that is close to its extinction limit can inhibit low frequency oscillations. Close to extinction, the

flame is less stiff to oscillations resulting in oscillations of the flame front. This leads to low frequency peaks in the flame transfer function. It has been shown that the dimensionless flame transfer function amplitude can only rise above unity when the flame front moves. This phenomenon is the result of variations in the fuel buffered by the flame.

The transient CFD approach was useful for studying the specific thermo-acoustic behaviour of a few selected cases. Due to the required simulation times, a full design study requires too much computational effort. To speed up the calculation of a flame transfer function from CFD, a different approach has been undertaken. In this novel approach, called the linear coefficient method, the discrete equations of the CFD problem are linearised to obtain a linear description of the model. Since the fluctuations are small (as required when using a spectral analysis) this linear description can be used to calculate the flame transfer function *directly* from a steady-state CFD result. Hence no transient simulations are necessary. This implies that there is no time truncation error anymore which makes the linear coefficient method more accurate than transient methods.

Since the order of the obtained linear models is very large, an order reduction step must be applied to the linear system prior to calculating the flame transfer function from it. A modified form of the Lanczos method is used to reduce the linear description. For the test cases presented in this thesis, the linear coefficient method is shown to calculate a flame transfer function faster and more accurate than when using conventional transient methods and spectral analysis. For relatively small-sized problems, the computational effort of the linear coefficient method is about 100 times less than impulse excitation. This speed-up is even larger when comparing the linear coefficient method with white noise excitation.

The numerical simulations in this thesis have been conducted with a relatively simple combined Arrhenius/eddy dissipation combustion model. Nevertheless, a good correspondence of the simulation results with the experimental findings has been obtained. The experimental setup used for validating the numerical results has very well-defined boundary conditions and a relatively simple geometry. The implication of increasing complexity of a combustion system could be that the simple combustion model is not able anymore to accurately describe the flame. Therefore, a more advanced combustion model has been considered as well. This model is called the CFI model and is based on reducing the chemical reaction mechanism by projecting it onto a limited number of reaction progress variables. Simulations with the CFI model show a flame with a smaller opening angle than the flame calculated by the combined Arrhenius/eddy dissipation model. Moreover, the inclusion of the influence of variance on the reaction rate increases the temperature gradients in the reaction zone. Nonetheless, the effect on the flame transfer function is small. Generally, when the combustion model is able to predict the flame length and the location correctly, the flame transfer function is also predicted well.

Experimental validation

The results obtained from the developed models have been validated in cold flow and reacting flow experimental setups. The calculated isothermal flow field from

the specially designed burner has been validated in a water tunnel experiment. A reasonable agreement between the measurements and the RaNS simulations is obtained close to the burner exit. Simulations performed on the same geometry with a LES approach [164] show a much better agreement.

The steady and unsteady reacting flow simulations have been validated in a combustion setup with a maximum thermal power of 500 kW at 5 bars absolute pressure. This setup has been built in the framework of the EU DESIRE project. The setup has been designed for validation, i.e. care is taken for well-defined boundaries, a simple geometry etc. This is confirmed by the good correspondence of the measurements with the generally simple models. One-dimensional heat transfer and acoustic models are sufficient to describe the general behaviour of the system. Moreover, PLIF and Abel transformed chemiluminescence measurements of the OH and CH* fields, respectively, agree well with the opening angle and length of the numerically calculated flame. Most of the reaction occurs at the transition from the flame to the central recirculation zone. This is indicated by the measurements, as well as by the numerical simulations.

Flame transfer functions have been determined experimentally by exciting the fuel mass flow with an amplitude of 5% of the mean flow, and reconstructing the acoustic response of the flame from acoustic pressure measurements in the combustor. The flame response to this perturbation is shown to be linear at this excitation level. A good agreement between the flame transfer function measurements and the simulations is found, which proves that the Unsteady RaNS approach combined with the simple combustion model correctly predicts the flame location and the flame length. Furthermore, effects of the mean pressure on the flame transfer function are noticed. A plausible explanation for these effects is the increasing reaction rate with the pressure, changing the position and shape of the flame. These effects lead to a steeper roll-of in the amplitude and a decrease in the time delay of the FTF.

At a specific operating point of the experimental setup, unstable behaviour has been measured. The frequency of the instability could be matched by the acoustic network model coupled to a flame transfer function. The instability search algorithm also correctly predicts stability behaviour at another operating point, where the increased acoustic damping, the higher burner pressure drop and the smaller time delay in the feedback loop increase the stability.

8.2 Recommendations

The linear coefficient method

For higher order models, the linear coefficient method starts to become inefficient due to two, solvable, reasons:

Firstly, the construction of the linear coefficients is done in a separately written MATLAB routine. This is still very inefficient. To increase the size of the model that can be considered, the retrieval of the coefficient matrices should be implemented directly in the solver code. Ideally, this should completely remove the time spent on

constructing this matrix, since a linear representation is already constructed at each time step in an implicit solver code.

Secondly, two linear systems are solved at each reduction step in the Shifted Lanczos method. Currently, this is done via a LU factorisation. However, for large sized problems, this approach becomes inefficient. To overcome this, an iterative multigrid solver (for example of the CFD solver code itself) should be used for solving these linear systems.

With the two measures listed above, a flame transfer function calculation with the linear coefficient method reduces to one steady RaNS calculation with a few additional time steps for the Shifted Lanczos reduction.

Lanczos versus CSP

In the CSP method a so-called low-dimensional manifold is constructed along which the reaction occurs, i.e. the fast processes are identified and removed from the reaction mechanism. What the method actually does is reducing the chemical mechanism in order, while keeping the slow processes in the reduced description. This could also be done using the Implicitly and Shifted Lanczos method described in this thesis. The performance of the Lanczos method should be compared with that of CSP in reducing chemical reaction schemes.

Compressibility and the CFI model

With the CFI model, the local density is retrieved from the database and written to the flow field. Subsequently, the solver modifies the pressure, which is the independent variable, such that the mass conservation equation is satisfied. The consequence is that only density changes affect the pressure. In reality, changes in the temperature and species mass fractions also influence the pressure. Incorporating these effects leads to a different coupling between the density, temperature, pressure and species mass fractions. For example, a density increase might not result in the temperature decrease incorporated in the CFI database: a local pressure increase can reduce the temperature decrease. When acoustic wave propagation needs to be simulated with the CFI model coupled to a CFD model, an additional transport equation should be solved for the enthalpy. This way, the correct relationship between pressure and density fluctuations is provided.

Prevention of instabilities

There are many directions in which research in preventing instabilities can proceed. A promising direction is to study combustion systems in which the flame is not necessarily placed at the beginning of the combustor. The acoustic energy input of the flame to the acoustic system can significantly be reduced by stabilising the flame at a carefully chosen location in the combustor. An acoustic volume source placed in a pressure node cannot excite the acoustic field.

With the thermo-acoustic model described in this thesis, the possibility for applying side branch resonators in the burner can be studied. With side branch resonators,

sound of a specific frequency can be reflected, therewith breaking the thermo-acoustic feedback loop. In literature, Helmholtz resonators have been applied to combustors to damp a specific frequency [9,63]. However, no research has been found on placing such dampers in the thermo-acoustic feedback loop itself, for instance in the burner.

Finally, it seems beneficial to mix the reactants as close to the flame as possible. This reduces the convective time delay to the flame and shifts possible feedback mechanisms to higher frequencies, where more damping is present. Moving the mixing location closer to the flame implies that the mixing of the reactants should occur faster to reach the same level of premixing.

Measurements

The steady and unsteady measurements which are described in this thesis should be performed at more operating points. It is interesting to study the effect of heat loss on the flame transfer function by varying the amount of cooling air used. Additionally, extra measurements should be performed on the correlation between the flame transfer function determined from CH* chemiluminescence measurements and reconstructed from the acoustic pressure measurements. CH levels might not be a correct marker for the heat release rate in case of unsteady flows [64]. The described measurement can conclude about this.

Finally, to study local flame behaviour phase-average OH (and more favourably CH) PLIF measurements should be done while driving the flame at a fixed frequency.

Nomenclature

General

The symbols that are used throughout this thesis are categorised into Roman, Greek and Mathematical symbols. A list of these symbols is given here. This list contains the symbols, their descriptions and their dimensions (if applicable). Occasionally the same symbol is applied for different quantities, in such cases the context of the symbol explains its meaning.

The symbol list is followed by a list of abbreviations used in the text. Finally a table listing the so-called 'standard air conditions' is given. These conditions fix the temperature, pressure and composition of the air, and are used in some models in the thesis.

The following typographic conventions are applied for the symbols. Fluctuating quantities are always expressed in characters *with* an apostrophe. A mean quantity is indicated with a subscript 0 or an over-bar. Total quantities do not have an addition. When a symbol represents a scalar it is written in a normal mathematic font like a or ρ. For a vector, a bold character in lowercase, e.g. $\mathbf{p}$ is used, whereas a matrix or a tensor is written in bold uppercase, like $\mathbf{A}$ or $\mathbf{\Psi}$.

Roman

Δf	Frequency resolution of Fourier transform	[Hz]
ΔH	Net calorific heat of combustion	[J/kg]
Δt	Discrete time step in simulation	[s]
Δt_{pulse}	Time length of a pulse applied to the system	[s]
Δx	Characteristic grid spacing of discrete mesh	[m]
a	Ratio between area and perimeter of a cross-section	[m]
A	Pre-exponential constant in Arrhenius law	[1/s]
A_{EBU}	Eddy Break-Up coefficient	[-]
A^p	Periodic fluctuating scalar A	
$\mathbf{A}$	Matrix for general purpose	
$\mathbf{A}$	Matrix of state space system	
$\mathbf{b}$	Matrix containing participation factors in CSP-vector	
$\mathbf{B}$	Matrix of state space system	

c	Acoustic speed of sound	[m/s]
c	Connectivity number of mesh	[-]
c_a	Mass fraction of O_2 present in the air	[-]
c_{eff}	Acoustic speed of sound corrected by mean flow ($= c_0 \pm u_0$)	[m/s]
c_f	Mass fraction of CH_4 present in the fuel	[-]
c_j	j^{th} reaction progress variable	[-]
c_p	Specific heat capacity at constant pressure of mixture	[J/kgK]
c_p^i	Specific heat capacity at constant pressure of species i	[J/kgK]
c_s	Acoustic speed of sound at source location	[m/s]
c_v	Specific heat capacity at constant volume	[J/kgK]
C	Constant for general purpose	
$\mathbf{C}$	Matrix of state space system	
d_j	Diameter of perpendicularly penetrating jet	[m]
D	Diameter	[m]
D	Molecular diffusivity of mixture	[m^2/s]
D	Scalar of state space system	
D_e	Diameter annular passage	[m]
D_h	Diameter burner hub	[m]
D_i	Molecular diffusion coefficient of species i	[m^2]
$\dot{\mathbf{D}}$	Rate of strain tensor	[1/s]
$\mathbf{D_i}$	Laminar diffusion of species i ($= \rho D_i \nabla y_i$)	[kg/m^2s]
$\mathbf{D_q}$	Laminar heat conduction ($= \kappa \nabla T$)	[W/m^3]
f	Frequency	[Hz]
f	Mixture fraction	[-]
f'	Acoustic perturbation for general purpose	
f_n	Nyquist frequency	[Hz]
f_s	Sampling frequency	[Hz]
f_{turb}	Characteristic turbulence frequency	[Hz]
$\mathbf{f}$	Momentum generation due to a force exerted on the fluid	[N/m^3]
h	Heat transfer coefficient	[W/m^2K]
h_f	Local specific transfer function	[W/m]
h_i	Total enthalpy of species i	[J/kg]
h_p, h_q	Orthogonalisation coefficients in Gram-Schmidt process	
h_{tot}	Total enthalpy	[J/kg]
h_0^i	Enthalpy of formation of species i	[J/kg]
H_{21}	Transfer function between location 2 and 1	
H_f	Flame transfer function	
$\hat{H}_f$	Dimensionless flame transfer function	[-]
H_{local}	Local flame transfer function	
H_{um}	Fuel supply line transfer function	[Hz]
J	Index of acoustic elements in network formulation	
J	Ratio of momentum of penetrating jet and main flow	[-]
k	Turbulence kinetic energy	[m^2/s^2]
k	Wave number ($= \omega/c_0$)	[rad/m]
k_{xy}	Reynolds stress component in x,y direction	[m^2/s^2]
$k^{\pm}$	Wave number corrected by mean flow ($= \omega/(c_0 \pm u_0)$)	[rad/m]

K	Loss coefficient at area transition	[-]
l_t	Characteristic turbulence length scale	[m]
L	Distance for general purpose	[m]
$\mathbf{L}$	Lower triangular matrix from LU factorisation	
L_{flame}	Flame length	[m]
m	Volumetric mass flow	[kg/m^{3}s]
m	Total number of time steps	[-]
m	Number of inputs in state space system	[-]
M	Mass flow	[kg/s]
M_f	Fuel mass flow	[kg/s]
$\mathcal{M}_s$	Mass flow source	[kg/s]
M_w	Axial thrust	[kgm^2/s^2]
M_θ	Axial flux of angular momentum	[kgm^2/s^2]
n	Interaction index in $n-\tau$ model	[-]
n	Mode number of instability	[-]
n	Total number of independent variables	[-]
n_{node}	Number of nodes	[-]
n_{var}	Number of independent variables at a node	[-]
$\mathbf{n}$	Outward pointing normal of a plane	[m^2]
$\hat{\mathbf{n}}$	Discrete outward pointing unit normal of integration plane	[m^2]
N	Number of discrete time steps per period	[-]
$\mathbf{N}$	Shape function vector	[-]
p	Pressure	[Pa]
p	Number of outputs in state space system	[-]
$\hat{p}^+$, $\hat{p}^-$	Complex pressure amplitudes of 1D sound wave	[Pa]
$\mathbf{p_i}$	i^{th} column of matrix $\mathbf{P_k}$	
$\mathbf{P}$	Permutation matrix	
$\mathbf{P_k}$	Inverse transpose of orthonormal projector matrix $\mathbf{Q_k}$ ($= \mathbf{Q_k}^{-T}$)	
q	Volumetric heat release rate release by flame	[W/m^3]
q_f	Volumetric heat release rate absorbed by flame	[W/m^3]
$\mathbf{q_i}$	i^{th} column of matrix $\mathbf{Q_k}$	
Q	Heat release rate	[W]
$\mathbf{Q_k}$	Orthonormal projector matrix of size $n \times k$	
R	Specific gas constant of mixture	[J/kgK]
R	Radius for general purpose	[m]
R	Acoustic reflection coefficient	[-]
R	Correction factor for coupling 1D elements with a mean flow	[ms]
R_u	Universal gas constant	8.3144 [J/molK]
s	Specific entropy	[J/kgK]
s	Shear wave number	[-]
s_{21}	Distance between location 1 and 2	[m]
s_L	Laminar flame speed	[m/s]
S	Area	[m^2]
S	Sparsity of matrix	[-]
S_f	Area of flame front	[m^2]
S_n	Swirl number	[-]

S_{pulse}	Fourier transform of a unit pulse with length Δt_{pulse}	
S_{FF}	Auto-spectrum of excitation signal F	
S_{FX}	Cross-spectrum of excitation signal F and response signal X	
S_{XX}	Auto-spectrum of response signal X	
t	Time	[s]
t_{chem}	Chemical time scale	[s]
t_{Kol}	Kolmogorov time scale	[s]
t_L	Laminar flame time scale	[s]
t_{turb}	Turbulence time scale	[s]
T	Temperature of fluid	[K]
T	Time period in which one harmonic cycle takes place	[s]
T_1	Time scale of turbulent fluctuation	[s]
T_2	Time scale of periodic fluctuation	[s]
T_a	Activation temperature	K
T_{ex}	Combustion exit temperature	[K]
T_{ph}	Preheating temperature	[K]
u	Velocity	[m/s]
u'_s	Structural velocity fluctuation	[m/s]
u'_t	Characteristic turbulence velocity fluctuation	[m/s]
$\mathbf{U}$	Upper triangular matrix from LU factorisation	
v_θ	Tangential velocity	[m/s]
V	Volume	[m^3]
V_{exc}	MOOG excitation signal	[V]
w	Axial velocity	[m/s]
W	Acoustic energy	[W]
W_i	Molar weight of species i	[kg/mol]
x, y, z	Cartesian coordinates	[m]
x_n, y_n, z_n	Natural coordinates of element	[-]
$\mathbf{x}$	Coordinate vector of field point	[m]
y	Mass fraction for general purpose	[-]
y_a	Air mass fraction	[-]
y_f	Fuel mass fraction	[-]
Y_{max}	Maximum penetration of perpendicularly penetrating jet	[m]
Z_c	Characteristic acoustic impedance	[kg/m^2s]
Z_s	Specific acoustic impedance	[kg/m^2s]

Greek

α	Convected variable in incompressible convection equation	[-]
β	Relationship between heat release rate from heated gauze in Rijke tube and the velocity	[kgm/s^2]
β_t	Turbulent damping coefficient	[1/m]
γ	Ratio between specific heat capacities ($= c_p/c_v$)	[-]

γ^2	Coherence function	[-]
Γ_0	Vena contracta factor	[-]
δ	Displacement of MOOG piston	[m]
δ_L	Laminar flame thickness	[m]
ε	Time truncation error	
ϵ	Turbulence eddy dissipation	[m^2/s^3]
ζ	Scaled (dimensionless) acoustic impedance	[-]
η	Thermo-acoustic efficiency	[-]
$\boldsymbol{\eta}$	CSP-vector	[-]
η	Attenuation constant of sound waves	[-]
η_j	Moments in power series around frequency σ	[-]
η_{Kol}	Kolmogorov length scale	[m]
κ	Thermal diffusivity	[kg/ms]
κ_t	Turbulence diffusivity	[kg/ms]
λ	Thermal conductivity	[W/mK]
λ	Acoustic wavelength ($= c_0/f$)	[m]
λ	Air factor ($= 1/\phi$)	[-]
λ_i	i^{th} eigenvalue of matrix	[-]
μ	Dynamic viscosity of fluid	[kg/ms]
μ_t	Turbulence viscosity	[kg/ms]
ν	Kinematic viscosity, or momentum diffusivity of fluid	[m^2/s]
ρ	Density of fluid	[kg/m^3]
ρ_e	Excess density of fluid	[kg/m^3]
σ	Viscous stress tensor	[Pa]
σ_{max}	Maximum stress	[Pa]
σ	Frequency around which the Lanczos method is shifted	[rad/s]
τ	Time delay for general purpose	[s]
τ_1, τ_2	Time delays between which a constant non-zero transfer is assumed	[s]
τ_{conv}	Convective time delay	[s]
τ_{sound}	Time delay of an acoustic wave	[s]
τ_{turb}	Characteristic turbulence time scale	[s]
τ_u	Time delay of velocity perturbation	[s]
τ_{WSR}	Residence time in WSR	[s]
τ_ϕ	Time delay of equivalence ratio perturbation	[s]
$\tau_{\mathbf{x}}$	Time delay between excitation and location $\mathbf{x}$	[s]
ϕ	Equivalence ratio ($= 1/\lambda$)	[-]
ψ	Friction factor	[-]
ψ	Independent variable in CFD problem	
$\boldsymbol{\Psi}$	Vector with variable values at nodes of element	
ω	Angular frequency ($= 2\pi f$)	[rad/s]
ω	Chemical source term	[kg/m^3s]
ω_i	Imaginary part of angular frequency	[rad/s]
ω_r	Real part of angular frequency	[rad/s]

Mathematical

$\|x\|$	Absolute value of x	
$\angle x$	Angle of (complex) x	[rad]
x^*	Complex conjugate of x	
$\times$	Cross product	
$\deg(\mathcal{P})$	Degree of a polynomial $\mathcal{P}$	
$\det(\mathbf{A})$	Determinant of matrix $\mathbf{A}$	
$\otimes$	Direct product between two vectors	
:	Double inner product of two tensors	
$x\|_s$	Expression x is evaluated at condition s	
$\tilde{x}$	Favre average of a quantity x	
x''	Fluctuation corresponding to Favre average of x	
∇	Gradient operator	
$\|\mathbf{x}\|_\infty$	H-Infinity norm of vector $\mathbf{x}$	
$\mathbf{I}$	Identity matrix	
$\Im(x)$	Imaginary part of x	
$\mathrm{i} = \sqrt{-1}$	Imaginary unit	
$\cdot$	Inner product	
$\mathbf{A}^{-1}$	Inverse of matrix $\mathbf{A}$	
$[J\mathbf{A}]$	Jacobian of matrix $\mathbf{A}$	
$\mathcal{K}(\mathbf{A}, \mathbf{x}, k)$	Krylov matrix	
∇^2	Laplace operator ($= \nabla \cdot \nabla$)	
$\mathcal{L}(g(t))$	Laplace transform of $g(t)$ ($= G(s)$)	
$\hat{\mathbf{A}}$	Low order approximation of vector or matrix $\mathbf{A}$	
$\frac{\mathrm{D}}{\mathrm{D}t}$	Material derivative	
$\sup \|\mathbf{x}\|$	Maximum value of vector $\mathbf{x}$	
$\mathcal{O}$	Order	
$\frac{\partial}{\partial t}$	Partial derivative	
$\mathcal{P}(\mathbf{A})$	Polynomial function of matrix $\mathbf{A}$	
$P(x)$	Probability density function of x	
$r(\mathbf{x})$	Rayleigh quotient of vector $\mathbf{x}$	
$\Re(x)$	Real part of x	
$\bar{x}$	Reynolds average of a quantity x	
$\mathrm{sign}(x)$	Signum function, is -1 for $x < 0$, 0 for $x = 0$, or 1 for $x > 0$	
$s(x)$	Standard deviation of x	
$\mathrm{span}(\mathbf{A})$	Subspace generated by the vectors in the columns of matrix $\mathbf{A}$	
Σ	Summation	
$\mathbf{A}^T$	Transpose of vector or matrix $\mathbf{A}$	

Abbreviations

ADC	A/D converter
BiCG	BiConjugate Gradient
CFD	Computational Fluid Dynamics
CFL	Courant-Freidricks-Levy number
CPU	Central Processing Unit
CTA	Constant Temperature Anemometry
CV	Control Volume
DNS	Direct Numerical Simulation
DOF	Degree(s) Of Freedom
DSP	Digital Signal Processing
EBU	Eddy-Break-Up
FEM	Finite Element Method
FVM	Finite Volume Method
FFT	Fast Fourier Transform
FTF	Flame Transfer Function
GR	Growth Rate of unstable fluctuations
LDV	Laser Doppler Vibrometer
LES	Large Eddy Simulations
LVDT	Linear Variable Differential Transformer
NS	Navier-Stokes
PDF	Probability Density Function
RaNS	Reynolds averaged Navier-Stokes
RPV	Reaction Progress Variable
SCMH	Standard Cubic Metres per Hour
SISO	Single Input Single Output
SPL	Sound Pressure Level
TBC	Thermal Barrier Coating
TL	Transmission Loss
VLES	Very Large Eddy Simulations
WSR	Well-Stirred Reactor

Standard air conditions

Parameter	Value	Parameter	Value
T	293.15 [K]	ν	$15.1 \cdot 10^{-6}$ [m^2/s]
ρ	1.2 [kg/m^3]	y_{O2}	0.2315 [-]
p	$1 \cdot 10^5$ [Pa]	y_{N2}	0.7685 [-]
μ	$18.2 \cdot 10^{-6}$ [kg/ms]	W	28.85 [g/mol]

Appendix A

The flame source term

To obtain the flame source term, the thermodynamic relationship among the pressure, density and entropy is written as:

$$\frac{\mathrm{D}p}{\mathrm{D}t} = \left.\frac{\partial p}{\partial \rho}\right|_s \frac{\mathrm{D}\rho}{\mathrm{D}t} + \left.\frac{\partial p}{\partial s}\right|_\rho \frac{\mathrm{D}s}{\mathrm{D}t} \tag{A.1}$$

The linearised form of this equation states:

$$\frac{\mathrm{D}p'}{\mathrm{D}t} = c_s^2 \frac{\mathrm{D}\rho'}{\mathrm{D}t} + \left.\frac{\partial p}{\partial s}\right|_\rho \frac{\mathrm{D}s'}{\mathrm{D}t} \tag{A.2}$$

in which c_s is the speed of sound at the source location. The coefficient $\left.\frac{\partial p}{\partial s}\right|_\rho$ can be rewritten using thermo-dynamic relationships for an ideal gas:

$$\left.\frac{\partial p}{\partial s}\right|_\rho = \frac{\left.\frac{\partial p}{\partial T}\right|_\rho}{\left.\frac{\partial s}{\partial T}\right|_\rho} = \frac{\rho T R}{c_v} \tag{A.3}$$

since $\mathrm{d}s(T,\rho) = \frac{c_v}{T}\mathrm{d}T + \frac{p}{T}\mathrm{d}(\frac{1}{\rho})$ and $p = \rho R T$. Using equation A.2 and A.3 the following relationship can be derived:

$$\frac{\mathrm{D}}{\mathrm{D}t}\left(\frac{p'}{c_0^2} - \rho'\right) = \left(\frac{c_s^2}{c_0^2} - 1\right)\frac{\mathrm{D}\rho'}{\mathrm{D}t} + \frac{\rho T R}{c_0^2 c_v}\frac{\mathrm{D}s'}{\mathrm{D}t} \tag{A.4}$$

The negative of the argument of the time-derivative in equation A.4, i.e. $\rho' - \frac{p'}{c_0^2}$ is called the 'excess density' ρ'_e [35]. This excess density satisfies the mass conservation equation. Using the mass conservation equation in the form $\rho'_e \nabla \cdot \mathbf{u} = -\frac{\rho'_e}{\rho}\frac{\mathrm{D}\rho}{\mathrm{D}t}$, equation A.4 can be written as:

$$-\frac{\partial^2 \rho'_e}{\partial t^2} = \frac{\partial}{\partial t}\left[\left(\frac{c_s^2}{c_0^2} - 1 + \frac{\rho'_e}{\rho}\right)\frac{\mathrm{D}\rho'}{\mathrm{D}t} + \frac{\rho T R}{c_0^2 c_v}\frac{\mathrm{D}s'}{\mathrm{D}t} + \nabla \cdot (\mathbf{u}\rho'_e)\right] \tag{A.5}$$

The LHS of this equation is equal to the monopole source term in Lighhill's analogy (equation 2.6), i.e.:

$$-\frac{\partial^2 \rho'_e}{\partial t^2} = \frac{\partial^2}{\partial t^2}\left(\frac{p'}{c_0^2} - \rho'\right) \tag{A.6}$$

Therefore, the RHS of equation A.5 can replace this source term in Lighthill's analogy. For an ideal gas with constant heat capacity, $\frac{c_s^2}{c_0^2} - 1 + \frac{\rho'_e}{\rho} = 0$ and the first RHS term in equation A.5 vanishes. The remaining source terms are coming from sound produced by spatial density variations $\nabla \cdot (\mathbf{u}\rho'_e)$ (dipole source term) and as a result of non-isentropic processes $\frac{\rho T R}{c_0^2 c_v}\frac{\mathrm{D}s'}{\mathrm{D}t}$, like combustion (or vapour condensation) in the bulk flow or as a result of heat loss at the wall. A dimensional analysis to estimate the relative magnitude of the source terms shows that sound generation by combustion processes is $\mathcal{O}(\mathrm{Ma}^{-2})$ stronger than sound generation due to spatial density variations [35]. So for low Mach-numbers, this term can be neglected.

It is now convenient to express the remainder of the source term in terms of convected heat release rate perturbations q'_f [W m^{-3}]:

$$q'_f = \rho T \frac{\mathrm{D}s'}{\mathrm{D}t} \tag{A.7}$$

This relationship is subsequently substituted into the combustion source term, yielding:

$$\frac{\partial}{\partial t}\left[\frac{\rho T R}{c_0^2 c_v}\frac{\mathrm{D}s'}{\mathrm{D}t}\right] = \frac{\partial}{\partial t}\left[\frac{R}{c_0^2 c_v} q'_f\right] \tag{A.8}$$

For an ideal gas, the specific gas constant can be written in terms of the specific heat at constant pressure and at constant volume, according to $R = c_p - c_v$. This relationship is used to rewrite the factor $\frac{R}{c_0^2 c_v}$ in equation A.8:

$$\frac{R}{c_0^2 c_v} = \frac{\left(\frac{c_p}{c_v} - \frac{c_v}{c_v}\right) c_v}{c_0^2 c_v} = \frac{\gamma - 1}{c_0^2} \tag{A.9}$$

The final inhomogeneous convective wave equation in terms of pressure perturbations, having a thermo-acoustic source as source term, reads:

$$\frac{1}{c_0^2}\frac{\mathrm{D}^2 p'}{\mathrm{D}t^2} - \nabla^2 p' = \frac{\partial}{\partial t}\left[\frac{\gamma - 1}{c_0^2} q'\right] \tag{A.10}$$

To gain more insight in the mechanisms that *generate* heat release rate perturbations, the thermo-dynamic definition of enthalpy is used to obtain an expression for the heat release rate in terms of independent quantities. A change in total enthalpy h_{tot} is related to a change in entropy, pressure and species mass fractions as in the following equation:

$$\mathrm{d}h_{tot} = T\mathrm{d}s + \frac{1}{\rho}\mathrm{d}p - \sum_{i=1}^{n} h_0^i \mathrm{d}y_i \tag{A.11}$$

in which h_0^i is the enthalpy of formation of species i.

The conservation of enthalpy for a closed system is given by the following transport equation [13]:

$$\rho \frac{\mathrm{D}h_{tot}}{\mathrm{D}t} = \frac{\mathrm{D}p}{\mathrm{D}t} - \nabla \cdot \mathbf{D_q} - \sigma : \nabla \mathbf{u} \tag{A.12}$$

in which $\nabla \cdot \mathbf{D_q}$ represents the heat flow by conduction. The operator : represents the double inner product of two tensors, which are second-rank in case of a three-dimensional problem.

The material derivative of the enthalpy can be written as a function of the material derivatives of the entropy, pressure and species mass fraction using equation A.11:

$$\rho \frac{\mathrm{D}h_{tot}}{\mathrm{D}t} = \rho T \frac{\mathrm{D}s}{\mathrm{D}t} + \frac{\mathrm{D}p}{\mathrm{D}t} - \rho \sum_{i=1}^{n} h_0^i \frac{\mathrm{D}y_i}{\mathrm{D}t} \tag{A.13}$$

Combining equations A.12 and A.13 leads to:

$$\rho T \frac{\mathrm{D}s}{\mathrm{D}t} = -\nabla \cdot \mathbf{D_q} - \sigma : \nabla \mathbf{u} + \rho \sum_{i=1}^{n} h_0^i \frac{\mathrm{D}y_i}{\mathrm{D}t} \tag{A.14}$$

Rewriting the variables in terms of the sum of a space and time-independent part and a fluctuating part yields:

$$\rho T \frac{\mathrm{D}s'}{\mathrm{D}t} = -\nabla \cdot \mathbf{D_q}' - \sigma : \nabla \mathbf{u}' + \rho \sum_{i=1}^{n} h_0^i \frac{\mathrm{D}y_i'}{\mathrm{D}t} \tag{A.15}$$

Subsequently, the relationship between entropy and heat release rate perturbations (equation A.7) is used to obtain an expression for the fluctuating heat release rate:

$$q_f' = -\nabla \cdot \mathbf{D_q}' - \sigma : \nabla \mathbf{u}' + \rho \sum_{i=1}^{n} h_0^i \frac{\mathrm{D}y_i'}{\mathrm{D}t} \tag{A.16}$$

Appendix B

The Rijke tube

As a test case for the network model with its heat release rate source depending on acoustic properties in the system, a Rijke tube is considered (see figure B.1). The equations of this Rijke tube are based on a paper by Heckl [66], who performed a study on active noise control applied to a Rijke tube. This test case was also used by Klein [88] to test a modal analysis method for its ability to find instabilities. Finally, Deuker [42] used the same case to test the use of the Nyquist criterion*.

The fluctuating heat release rate from the gauze in the Rijke tube as a function of the velocity perturbation at the time $t - \tau$ can be written as:

$$q'(t) = \beta u'(t - \tau) \tag{B.1}$$

in which β depends on the geometry of the gauze and the properties of the air and is determined by King's law [87]. This β equals $\frac{Q'}{f'}\Big|_{flame}$ given in equation 2.48. In that equation the mass flow perturbation at node 2 of an element depends on the velocity perturbation at node 1. In this case, however, both perturbations should be at the same node of the element, which slightly changes the boundary condition of equation 2.50.

The parameters that Heckl used in her calculations are given in table B.1.

Parameter	Value	Parameter	Value
β	187 [kg m s^{-2}]	c_0	358 [m s^{-1}]
τ	$15 \cdot 10^{-5}$ [s]	R	0.0223 [m]
γ	1.4 [-]	L_1	0.3 [m]
ρ_0	1.2 [kg m^{-3}]	L_2	0.7 [m]
R	-0.986-i0.12 [-]	η	$1.6 \cdot 10^{-2}$ [-]

Table B.1: Parameters used for the calculations on the Rijke tube.

*Finding instabilities with the Nyquist criterion requires the determination of the transfer functions in the thermo-acoustic feedback loop. With these transfer functions a closed loop transfer function H_{closed} can be constructed. Finally, the unstable frequencies are the frequencies at which the argument of H_{closed} crosses the zero axis while its absolute value is larger than 1.

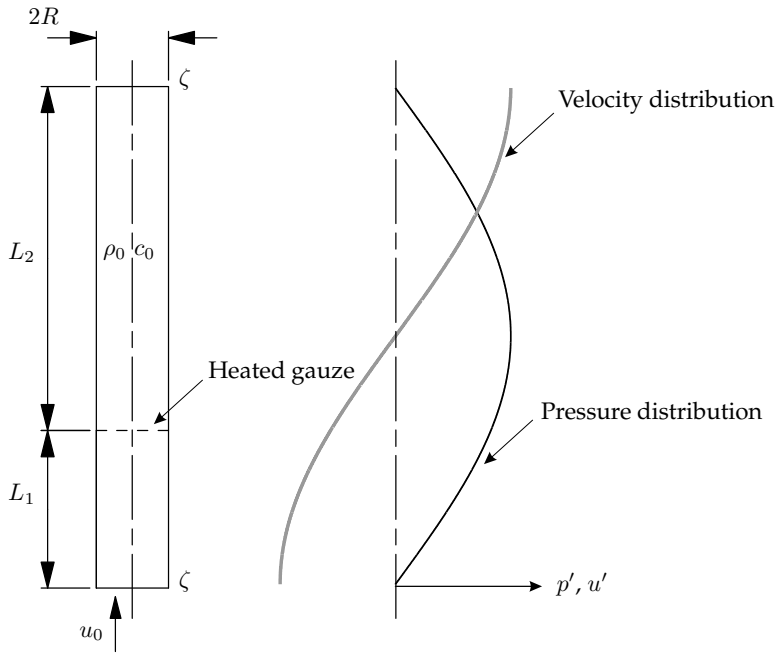

Figure B.1: Symbolic conventions for the Rijke tube [66].

In table B.1, η is an attenuation constant of the sound waves travelling along the tube.

In her paper, Heckl shows that an instability lies at $\Re(f) = 178.3$ Hz and $\Im(f) = -0.49$ Hz. However, when implementing the matrix from which she calculates this instability and determining its determinant, it appears that the eigenfrequency lies at $\Re(f) = 179.36$ Hz and $\Im(f) = +0.21$ Hz, which is a stable point. Heckl also gives a symbolic expression of the determinant of her matrix, which also yields this different value.

When the system is implemented in the network model, the eigenfrequency lies at $\Re(f) = 179.36$ Hz and $\Im(f) = +0.21$ Hz, which is exactly the same as found by Heckl's model. This indicates that both models are correct, but that the input values given in Heckl's paper are not the ones she used for her calculations.

Appendix C

Time and spatial discretisation

CFX uses an unstructured mesh on which the fluid equations are solved. Numerical diffusion ('gradient smearing') is minimised when the flow enters the elements normal to their faces. A structured mesh is therefore more favourable when the flow direction does not change much (see figure C.1). However, generally the flow direction changes throughout the flow field. For these kind of flows, the 'randomness' of the mesh provides a certain kind of independence with respect to the direction of the flow. Consequently, the unstructured mesh is more accurate than the structured one.

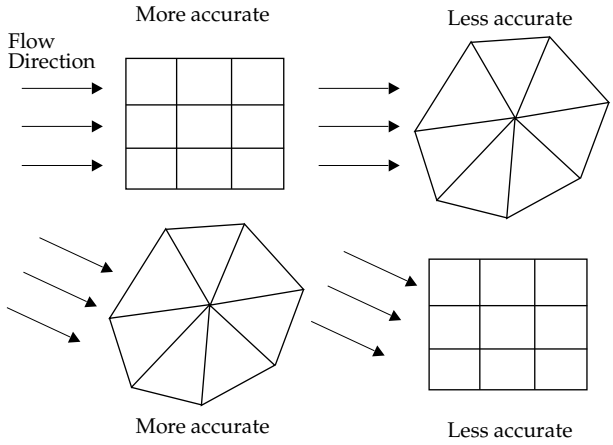

Figure C.1: Influence of the flow direction on the accuracy of an unstructured and a structured mesh.

Spatial discretisation

When possible, all results in this thesis are calculated using a second order spatial discretisation, thereby minimising the numerical diffusion effect of the first order

upwind scheme. Generally, the first order advection scheme is chosen to get preliminary results before getting more accurate results with the second order scheme. This procedure is chosen to prevent overshoots and undershoots and to maintain robustness.

In this section the general finite-volume numerical discretisation of the fluid dynamic equations is discussed. The general species transport equation (equation 3.16) is discretised on the two-dimensional grid displayed in figure C.2. The extension to the three-dimensional case is straightforward.

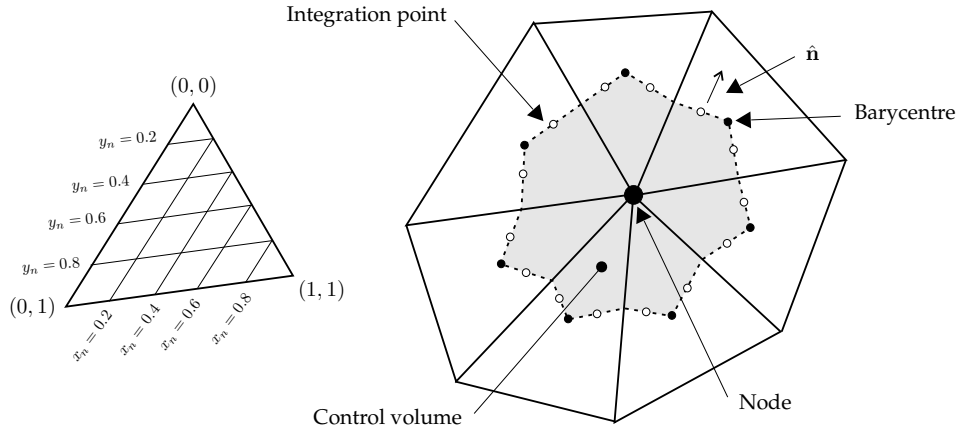

Figure C.2: Control volume in two-dimensional triangular mesh.

The variable values are only stored at the nodes of the mesh (co-located variables). Nevertheless, using linear shape functions of the element under consideration, the variable value at any location within the element can be calculated. For a triangular element, as depicted in figure C.2, the shape function vector $\mathbf{N}$ would be:

$$\mathbf{N} = \begin{bmatrix} x_n \\ y_n \\ 1 - x_n - y_n \end{bmatrix} \tag{C.1}$$

where x_n and y_n are the natural coordinates of the element, ranging from 0 to 1 as depicted in figure C.2. The value of a variable at location $\mathbf{x}_n = (x_n, y_n)$ can be calculated with:

$$\psi = \mathbf{N}^T \mathbf{\Psi} \tag{C.2}$$

in which $\mathbf{\Psi}$ is the vector with the variable values at the nodes of the element.

The spatial derivatives at any position in the element can be calculated with the Jacobian J of the shape functions:

$$\nabla\psi = [J\mathbf{N}(\mathbf{x})]^T \mathbf{\Psi} \tag{C.3}$$

The Jacobian $[J\mathbf{N}(\mathbf{x})]$ can be rewritten in terms of derivatives to the natural coordinates of the shape functions: $[J\mathbf{N}(\mathbf{x})] = \left([J\mathbf{N}(\mathbf{x}_n)]^T \mathbf{X}\right)^{-T} [J\mathbf{N}(\mathbf{x}_n)]$, where the matrix $\mathbf{X}$ contains the coordinates of the nodes of the element.

The general species transport equation is subsequently integrated over the control volume in figure C.2. This control volume is obtained by connecting the midpoints of the element edges and the geometric centroid of the element. The new volume mesh that arises from the control volumes is called the dual mesh. More specifically, the way the dual mesh is created here makes it a barycentric dual. Variants are the Voronoi dual, where the edges of the dual mesh must always be perpendicular to the edges of the original (primal) mesh. The barycentric dual puts less restrictions on the form of the primal mesh (with a Voronoi dual, the vertices of the dual mesh do not necessarily have to lie inside the elements of the primal mesh). Additionally, more extensive calculations are required for the Voronoi mesh in the simulation [121]. The barycentric dual is therefore preferred.

The volume integrated species transport equation reads:

$$\int_V \frac{\partial \bar{\rho}\tilde{y}_i}{\partial t}\mathrm{d}V + \int_V \nabla\cdot(\bar{\rho}\tilde{\mathbf{u}}\tilde{y}_i)\mathrm{d}V - \int_V \nabla\cdot(\bar{\rho}D_i + \frac{\mu_t}{\mathrm{Sc}_t})\nabla\tilde{y}_i\mathrm{d}V = \int_V \bar{\omega}_i\mathrm{d}V \tag{C.4}$$

Applying Gauss' theorem on the convective and diffusive term to replace the volume integral by an integral over the element surface S yields:

$$\int_V \frac{\partial \bar{\rho}\tilde{y}_i}{\partial t}\mathrm{d}V + \oint_S (\bar{\rho}\tilde{\mathbf{u}}\tilde{y}_i)\cdot\mathbf{n}\mathrm{d}S - \oint_S (\bar{\rho}D_i + \frac{\mu_t}{\mathrm{Sc}_t})\nabla\tilde{y}_i\cdot\mathbf{n}\mathrm{d}S = \int_V \bar{\omega}_i\mathrm{d}V \tag{C.5}$$

in which $\mathbf{n}$ the outward pointing unit surface normal.

Equation C.5 is now discretised. The time derivative and the source term are written as the product of the nodal value and the volume V of the control volume. The surface integrals are evaluated at each flat area ΔS of the surface. The surface normal is located at the midpoint ip (integration point, see figure C.2) of this area. Also the variable values are evaluated at ip. The discretised version of equation C.5 (the other transport equations are discretised in a similar way) reads:

$$\left(\frac{\partial \bar{\rho}\tilde{y}_i}{\partial t}\right)_{node} V + \sum_{ip}\left((\bar{\rho}\tilde{\mathbf{u}}\tilde{y}_i)\cdot\hat{\mathbf{n}}\Delta S\right)_{ip} - \sum_{ip}\left((\bar{\rho}D_i + \frac{\mu_t}{\mathrm{Sc}_t})\nabla\tilde{y}_i\cdot\hat{\mathbf{n}}\Delta S\right)_{ip} = (\bar{\omega}_i)_{node} V \tag{C.6}$$

in which $\hat{\mathbf{n}}$ is the discrete outward pointing unit normal of the current integration plane. For a triangle described by three vertices $\mathbf{x_1}$-$\mathbf{x_3}$, $\hat{\mathbf{n}}\Delta S$ can be calculated with:

$$\hat{\mathbf{n}}\Delta S = \frac{(\mathbf{x_3}-\mathbf{x_1})\times(\mathbf{x_2}-\mathbf{x_1})}{|(\mathbf{x_3}-\mathbf{x_1})\times(\mathbf{x_2}-\mathbf{x_1})|}\Delta S \tag{C.7}$$

$$= \frac{1}{2}(\mathbf{x_3}-\mathbf{x_1})\times(\mathbf{x_2}-\mathbf{x_1}) \tag{C.8}$$

When the first order accurate upwind scheme is used, the transported variables in the advection* term in equation C.6 (i.e. $\bar{\rho}$ and $\tilde{y}_i$) are taken from the node at

*In meteorology, the difference between convection and advection lies in the direction of the transport of heat through the flow of matter from one location to the other. Advection occurs in the horizontal plane and convection in the vertical. In general fluid dynamics, the distinction between both terms is that convection is usually used in case of transport of heat from one part of the fluid to another by movement of the fluid itself, while advection refers to the process of transport of a substance solely by mass motion. So advection is a more general term, for it can refer to transport of any quantity, like energy, entropy and chemical species.

the centre of the control volume which is directly upwind of the integration point. A second order discretisation can be obtained when the upwind value is corrected according to:

$$\tilde{y}_i^{ip} = \tilde{y}_i^{up} + \nabla \tilde{y}_i^{ip} \cdot \mathbf{r} \tag{C.9}$$

where $\mathbf{r}$ is the vector from the upwind node to the integration point.

Time discretisation

CFX uses a fully implicit time discretisation scheme. Here, the second order central difference time discretisation scheme is used. This scheme discretises the first order time derivative at the new time step n as:

$$\frac{\partial \psi^n}{\partial t} = \frac{\frac{3}{2}\psi^n - 2\psi^{n-1} + \frac{1}{2}\psi^{n-2}}{\Delta t} \tag{C.10}$$

Appendix D

Swirl number definition

In combustion applications, swirl influences the flame size, shape, stability and combustion intensity [168]. The degree of swirl is usually characterised by the swirl number S_n, which is a non-dimensional measure of the angular momentum added to the flow, and is represented by the axial flux of swirl momentum divided by the axial flux of axial momentum, times the equivalent nozzle radius.

One of the most common definitions of the swirl number S_n is taken from Gupta [62] and reads:

$$S_n = \frac{M_\theta}{RM_w} = \frac{\int_S \rho v_\theta w r \mathrm{d}S}{R \int_S \rho w^2 \mathrm{d}S} \tag{D.1}$$

in which M_θ and M_w are the axial flux of angular momentum and the axial thrust, respectively. Moreover, v_θ and w are the tangential and axial velocities.

In this definition, the pressure term and turbulent stress terms are omitted, as is common in literature. The effect of omitting these terms is a certain lack of downstream conservation of M_θ and M_w. For a free jet in stagnant surroundings, these momentum terms should remain constant. However, in a confined combustor, viscous dissipation can decrease the momentum terms.

When the swirl number is larger than 0.6, the flow is categorised as a strongly swirling flow. These flows posses sufficient radial and axial pressure gradients to cause a central recirculation zone, which is not observed for weaker degrees of swirl.

As an integral formulation the swirl number does not give information on the actual shape of the underlying velocity profiles, which may have a significant influence on the flow evolution. For low degrees of swirl ($S \simeq 0.2$) a solid body rotation plug flow can be assumed for the axial and tangential velocity profiles (i.e. $w = w_0$ and $v_\theta = v_\theta^0 r/R$). For higher degrees of swirl, however, the plug flow resemblance breaks down, since the major part of the flow leaves the burner near the outer edge of the exit [30].

The swirl number is evaluated at various axial locations in the isothermal simulation of operating point cold 10.1. The swirl number development of a perfectly premixed reacting flow performed at operating point 15.1 is determined as well. Fig-

ure D.1 depicts both swirl numbers as a function of the axial distance from the burner exit.

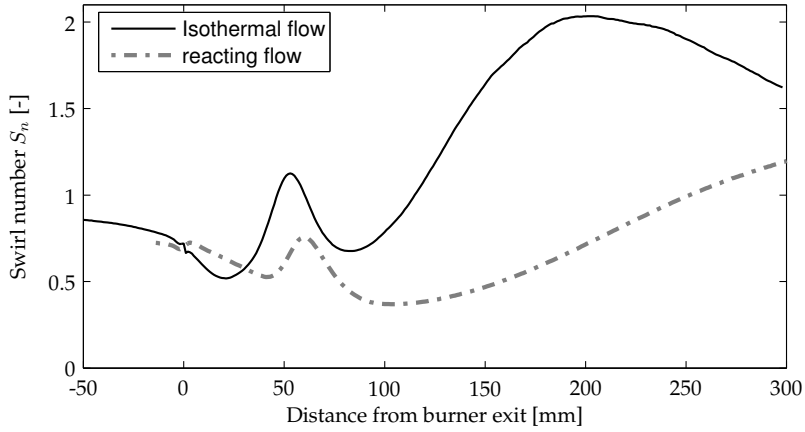

Figure D.1: Swirl number of isothermal and reacting flow as a function of the distance from the burner exit.

It is observed that the net effect of combustion is to reduce the swirl number compared to the non-reacting conditions. Combustion (thermal expansion) reduces the importance of the centrifugal forces with respect to flow inertia by increasing the latter substantially [184].

When the flow enters the annular passage ($-50 < x < 0$) the swirl number is 0.86. This number decreases to 0.72 at the burner exit. From there on, the recirculating flow field causes some variation in the swirl number, but the net effect of the area expansion at the burner exit is to increase the swirl number. Gupta [62] also showed this phenomenon with a simplified flow field of an incompressible flow passing through a sudden expansion in cross-sectional area. The increase of the swirl number at an area expansion is caused by a relatively larger decrease in M_w compared to M_θ. Mass conservation requires the axial velocity to decrease at an area expansion. However, it does not require the tangential velocity to decrease. At the axial location ($x \approx 50$ mm) where the jet impinges on the walls a peak in the swirl number is seen. The axial momentum of the jet decreases considerably here due to the impact on the wall. The momentum is partly recovered farther downstream, but M_w keeps decreasing faster than M_θ.

Appendix E

Grid-size dependence study

The computational domain of the DESIRE combustor geometry, bounded by the boundaries as depicted in figure E.1, is discretised by mainly tetrahedron elements. The mesh is preferably dense in regions with large gradients, and coarse in regions with small gradients. In figure E.1 three regions are showed. These regions are meshed with different sized elements. The used unstructured mesh allows a fast and smooth transition from one region to another.

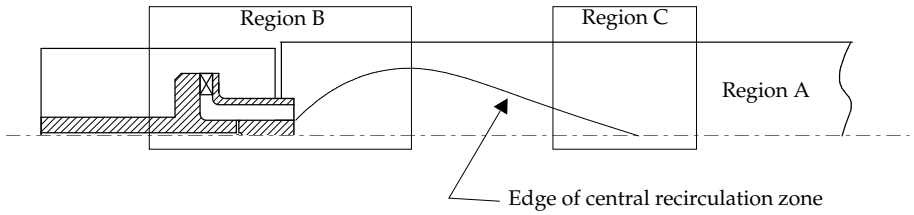

Figure E.1: Regions with different sized mesh.

For axisymmetrical flows, it is important to limit the size of the elements on the symmetry-line, since the axisymmetrical contributions are predominant near the centreline. Slight errors in the radial velocity approximations can produce large errors in the solution [139].

In the burner and at the burner outlet, the mesh should be dense enough to capture the large gradients. This especially applies to the shear zone between the jet coming out of the burner and the relatively stagnant flow in the combustion chamber. Away from the burner, the mesh size can increase, until the point where the recirculation zone closes at the centreline. Here a high mesh density is required to let the recirculation zone 'choose' its closing point. The length of the central recirculation zone appears to be very sensitive to the chosen mesh, and therefore this length was monitored when searching for a grid-independent solution of the three models discussed in section 3.6.

A second order spatial discretisation scheme is used whenever possible, and

therefore the truncation error of the discrete approximation decreases with Δx^2, while for first order discretisations the error decreases with Δx (Δx is the typical mesh edge length). So less elements are needed to obtain a grid-independent solution with the second-order scheme than with a first-order scheme. Since the number of control volumes is directly related to the computational effort required to compute a solution, second-order methods are generally preferred over first-order methods. However, for Model 1 and 2 (see section 3.6), it was not possible to obtain a stable second-order solution. Therefore, the first-order scheme has been used in these cases.

Model 1 is considered first (refer to figure 3.13). Besides giving a satisfactory grid-independent solution monitored by the stagnation point of the recirculation zone, Model 1 should also give grid-independent profiles for the velocity and the turbulence quantities at the planes where these quantities are transferred to Model 2 and 3. Four sets of meshes are generated for Model 1. The typical mesh sizes and total number of elements and nodes of these meshes are listed in table E.1.

	Δx [mm]				
Mesh	Region A	Region B	Region C	Nodes	Elements
Coarse	10	8	4	105,493	357,378
Intermediate	7.5	6	3	192,084	675,499
Fine	6.25	5	2.5	384,231	1,513,886
Very fine	5	4	2	583,135	2,291,423

Table E.1: Mesh edge lengths and total number of nodes and elements used in the grid-independency check of Model 1.

On the four meshes, the isothermal flow field corresponding to operating point 10.1 (see table 3.2) is calculated. The iteration process is continued until the RMS residuals have converged until machine accuracy. In figure E.2(a), the stagnation location of the central recirculation zone is plotted as a function of the mesh edge length in region A.

Because the truncation error is a first-order function of the mesh edge length Δx, a linear fit is plotted through the found stagnation points in figure E.2(a). As can be seen from this figure, the line can be extrapolated to $\Delta x = 0$, giving the stagnation point which would be obtained on a mesh with an infinitely small mesh size. This extrapolation procedure gives a value of 393.8 mm. The relative errors in the location of the stagnation point are depicted in figure E.2(b) for the different meshes. Clearly the required computational effort, as given by the number of elements, increases tremendously when the error is decreased.

As a compromise between the computational effort and relative error, the fine mesh will be used for Model 1. To show that this fine mesh yields grid-independent solutions at the planes where boundary conditions are transferred to Model 2 and 3, the velocity profiles at these planes (15 and 55 mm upstream of the burner exit) are compared for the very fine and the fine mesh. The profiles are considered to be axisymmetrical and plotted against the radius of the burner in figure E.3. A very good correspondence between the compared profiles at each plane is noticed, showing that the boundary conditions extracted from Model 1 can be considered grid-

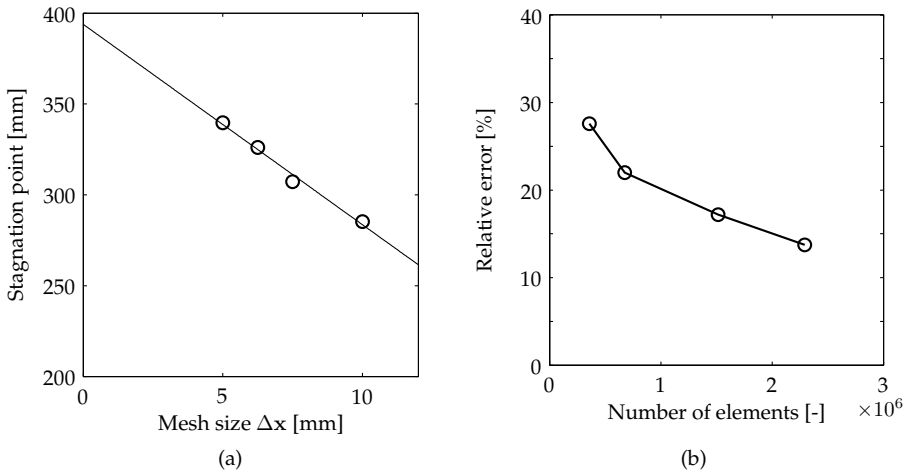

(a) (b)

Figure E.2: Stagnation point as a function of the mesh size (a) and relative error as a function of the number of elements (b). Model 1 is considered here.

independent.

A similar analysis is subsequently performed on Model 2. In this model, the fuel injection nozzles are included. Moreover, combustion is accounted for by a combined single-step Arrhenius model and an eddy dissipation model. Both these phe-

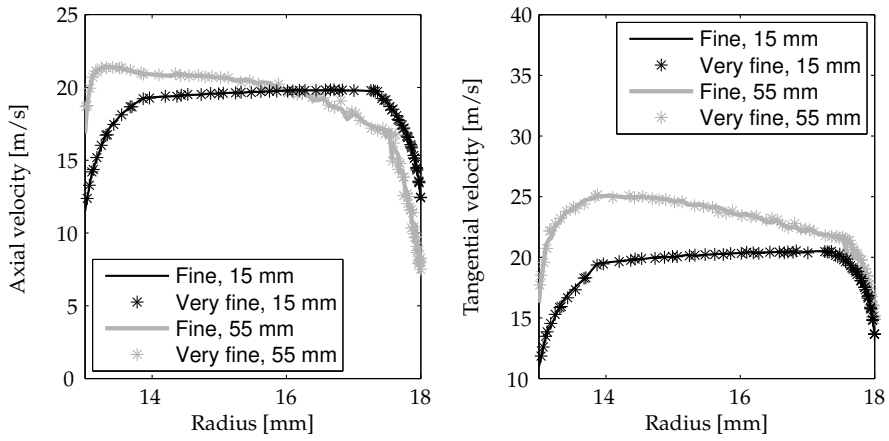

(a) Axial velocity (b) Tangential velocity

Figure E.3: Comparison between inlet profiles extracted from the fine and very fine Model 1. Two different inlet planes are compared: the plane located at 15 mm upstream of the burner exit (used for Model 3) and the plane 55 mm upstream of the burner exit (used for Model 2).

nomena require an increased mesh resolution. For Model 2, the profiles are compared for two different meshes. The fine mesh has a 3,046,958 elements, while the coarse mesh has 'only' 1,080,249 elements. In both models, most of the elements are concentrated around the fuel injection nozzles, since mixing is considered to be very important in this model.

The axial velocity profiles along the centreline are illustrated in figure E.4 for the coarse and the fine model. Although the number of elements differs almost a factor of 3, the profiles look very similar. Apparently, the grid at the location where fuel and air are mixed is grid-independent already at the coarse grid. Additionally, the imperfectly premixed combustion makes the flame more stable, which makes the stagnation point of the central recirculation zone less sensitive to the mesh.

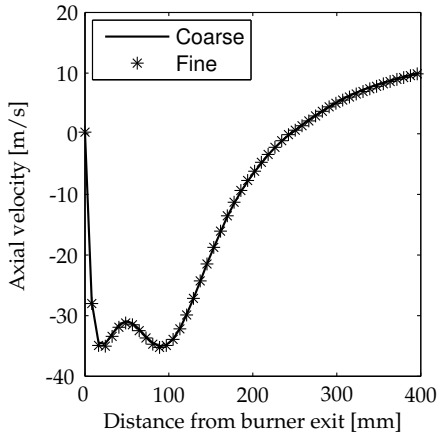

Figure E.4: Axial velocity profile along the centreline of the combustion chamber of Model 2.

Finally, the stagnation point of the central recirculation zone of Model 3 is considered for different meshes. The inlet profiles of the considered case come from a simulation with Model 1. Again, combustion is included in the analysis. Three different meshes are considered. The number of nodes and elements for each mesh is listed in table E.2. In the table, a characteristic mesh edge length is shown as well, corresponding to the mesh edge length in the flame zone.

Mesh	Δx [mm]	Nodes	Elements
Coarse	4.2	41,149	178,026
Intermediate	3.5	61,850	280,154
Fine	2.8	111,559	527,018

Table E.2: Mesh edge lengths and total number of nodes and elements used in the grid-independency check of Model 3.

The location of the stagnation point is displayed in figure E.5(a) as a function of the mesh edge length of each considered mesh. Again, a linear fit has been made of the resulting points, yielding the value at an infinite mesh density. With this value,

the relative error can be calculated. This error is plotted in figure E.5(b) as a function of the number of elements.

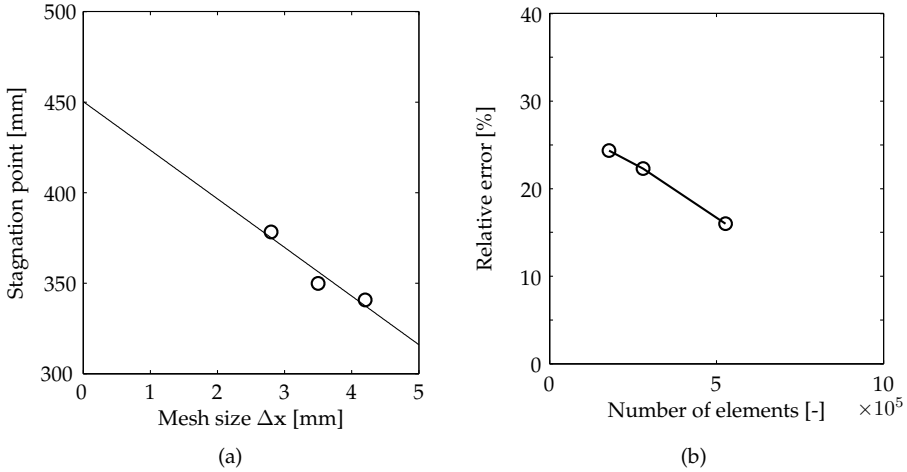

Figure E.5: Stagnation point as a function of the mesh size (a) and relative error as a function of the number of elements (b). Model 3 is considered here.

Apparently the fine mesh still yields a relative error of 16% in the stagnation point. Again, it is reminded that the location of the stagnation point is very sensitive, especially for perfectly premixed combustion. To support this statement that the relative error in the stagnation point is a worst case estimation of the error introduced by the grid, the axial and tangential velocity profiles of the intermediate and the fine mesh is plotted for two different planes within the flame zone (see figure E.6).

Since Model 3 will mainly be used for transient simulations meant to obtain the FTF, a finer mesh than the currently considered finest mesh is not desired. Therefore, to have the smallest possible error, the fine mesh is used for Model 3.

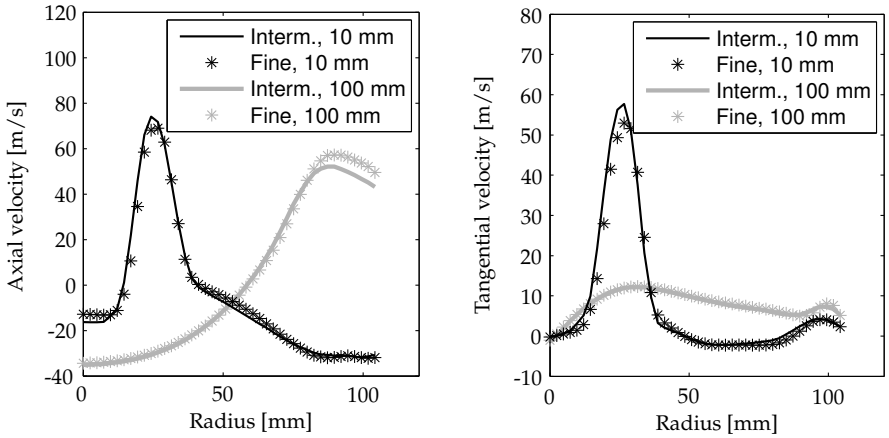

(a) Axial velocity (b) Tangential velocity

Figure E.6: Velocity profiles for two different meshes at the planes 10 and 100 mm from the burner exit. Model 3 is considered.

Appendix F

Water tunnel measurements

Introduction

The water tunnel is a geometrically exact copy of the DESIRE test rig. Two aspects are different in the construction though: no contraction is included at the end of the water tunnel, and the water tunnel is constructed from perspex to be able to study the flow profiles with laser techniques. The fluid medium that is used is water instead of air. Just as the DESIRE test rig, the water tunnel consists of a 'combustion' chamber, a swirl burner, a plenum room, an acoustic decoupler and an 'air' supply room (see figure F.1).

When modelling the combustion process using CFD, the first step is to predict the isothermal flow properties accurately, before adding the complexities of combustion. The water tunnel is designed to validate the isothermal CFD simulations for the DESIRE test rig. In the water tunnel experiment the velocity profiles are measured. By equating the Reynolds numbers in the water tunnel and the cold flow simulations, both flows behave similarly (the dimensionless equations describing the flow are the same for equal Reynolds numbers, see for example [137]) and are comparable. Since the water tunnel is designed to be actual size, the diameters do not affect the Reynolds number. The kinematic viscosity of water is about $1/13^{\text{th}}$ that of air at room temperature, therefore the ratio of the velocity of water to air also has to be about $1/13^{\text{th}}$.

Water flows out of the stainless steel vessel downward through a circular tube (see figure F.1). A 1.5 kW frequency driven water pump subsequently pumps the water into the 'air' supply room, through the acoustic decoupler, into the plenum room and finally through the burner into the 'combustion' chamber. Here, Laser Doppler Velocimetry (LDV) measurements are done to obtain the burner velocity profiles. The LDV system is positioned with a x, y, z traverse system. The measurement data from the LDV system is further processed with a DIFA spectral analyser installed on a PC.

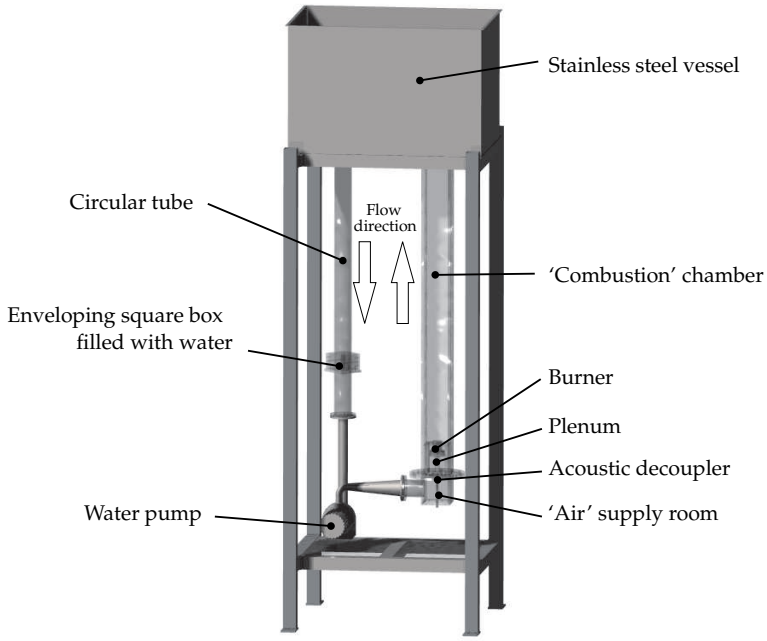

Figure F.1: Overview of the DESIRE water tunnel.

Laser Doppler Velocimetry

Forward scattering Laser Doppler Velocimetry (LDV) is the technique used to determine the velocity profiles in the water tunnel. The Doppler effect forms the basis of LDV. Incident light from a laser is scattered by small moving particles, causing a shift in frequency. This frequency shift is called the Doppler effect and is the same phenomenon as the frequency shift heard when a vehicle with a siren passes by. The light scattering particles are an essential part of the LDV measurement system. Liquid flows normally contain enough particles of the correct size – comparable to one micron – to scatter the laser light with sufficient intensity for the photodetector to generate high-quality Doppler signals. The two most frequently used LDV methods are the reference beam method and the dual beam method. The reference beam method is historically the basic mode of LDV, and it is more commonly used in water applications. It is also the method used in this water tunnel experiment. With the reference beam method, a bright main beam and two less intense reference beams, split from the original laser output, are used. At the point where the beams cross, a measurement volume arises in which the velocity of the particles can be measured (see figure F.2).

When particles in the fluid move with velocity u across the measurement volume, the light from the intense main beam is scattered. This scattered light is mixed with the light from the directly passing reference beam on the surface of a photodetector. The photodetector produces an electrical output oscillating with the frequency dif-

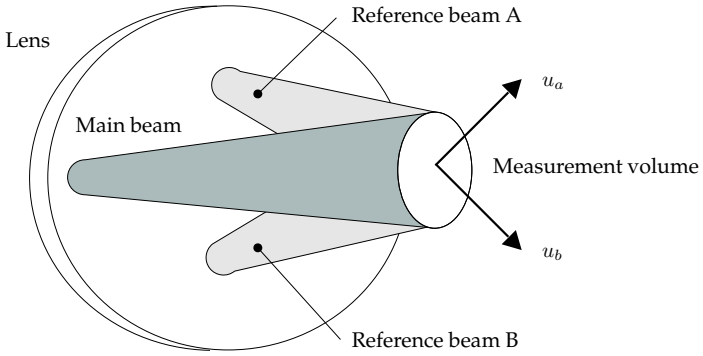

Figure F.2: Measurement volume at the intersection of the reference and main beams.

ference equal to the Doppler shift. The Doppler frequency value is proportional to the velocity of the particle. With two reference beams, two instantaneous velocity components in the plane perpendicular to the optical axis can be measured. With these two components, any component in that plane can be obtained by a coordinate transformation.

The coordinate frame for the measurements is defined as shown in figure F.3 (top view). Using the coordinate conventions shown in figure F.3, the velocity components in the z and x directions are obtained from the LDV measurements.

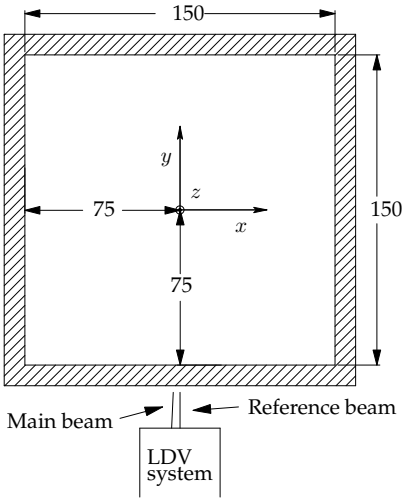

Figure F.3: Coordinate frame for water tunnel measurements (top view).

Calibration of the water pump

The volume flow is not explicitly measured. Therefore, before measurements downstream of the burner can be taken, the pump has to be 'calibrated', i.e. the relationship between the water volume flow and the pump driving frequency needs to be determined. For this purpose, the velocity profile in the circular supply tube is determined as a function of the pump driving frequency using the LDV system. A square box filled with water is placed around the circular tube (see figure F.1) to minimise diffraction effects of the laser beams (the diffraction indices of water and perspex are very similar). However, still some non-linear diffraction occurs when traversing perpendicular to the optical axis (figure F.4(a)). This makes it impossible to determine the correct position of the measurement volume (determined by the crossing point of the laser beams). When traversing the laser along the y-axis, the two reference beams are not diffracted. However, the main beam, which enters the box under a small angle (3.6 degrees), is diffracted in a non-linear way (figure F.4(b)). Therefore, the position of the measurement volume varies non-linearly with the laser y-position.

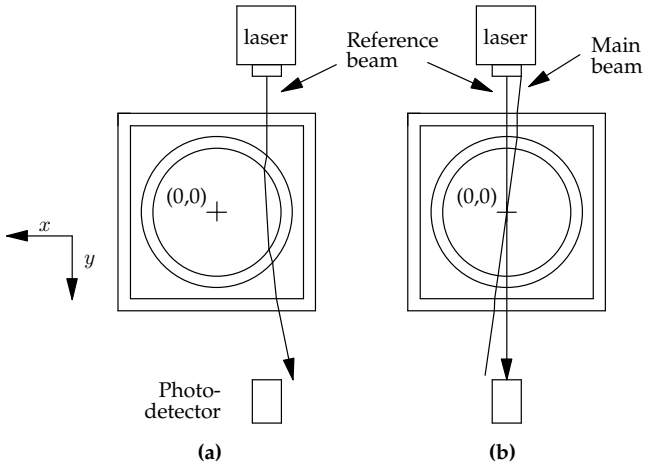

Figure F.4: Effects of diffraction during the calibration of the pump. Figure (a) shows the diffraction of the reference beams when traversing in the x-direction. Figure (b) shows the diffraction of the main beam, causing the crossing point of the main beam with the reference beams to vary non-linearly when traversing in the y-direction.

Nevertheless, a general impression of the flow profile can be obtained. Figure F.5(a) shows the flow profile at 5 Hz, i.e. the lowest considered pump driving frequency (remember that this profile is non-linearly shrunk in the y-direction, therefore the diameter appears to be only about 67 mm instead of the actual diameter of 100 mm). The flow is seen to behave in a turbulent fashion (generating a plug flow profile), and therefore the higher levels of the pump driving frequency are expected to be fully turbulent as well.

A complete profile is also measured for a driving frequency of 20 Hz (figure F.5(b)). It can be seen that the velocity profile is slightly lower in the centre. This

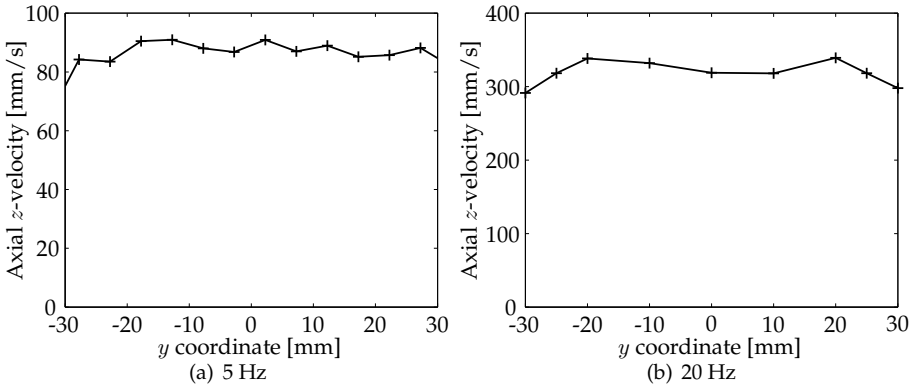

Figure F.5: Velocity profile in circular tube at different pump driving frequencies.

can be explained by the swirling nature of the water flowing down the tube and into the rotating pump. However, the ratio between the maximum velocity peaks and the centre velocity is minimal.

Next, the average velocity taken at each driving frequency is multiplied by the tube cross-sectional area to obtain the mean volume flow. This volume flow in m^3/h is plotted against the pump driving frequency in figure F.6. This plot shows that the pump behaves linearly according to the equation $y = 0.45x + 0.3$. At operating point 10.1 (see table 3.2) the volumetric flow rate of air is 200 m^3/h. The ratio of the kinematic viscosity of air to water at 293 K is 13.2. Hence, to have the same Reynolds numbers, the volumetric flow rate for the water should be 15.15 m^3/h, which yields an operating frequency of 33.2 Hz for the water pump.

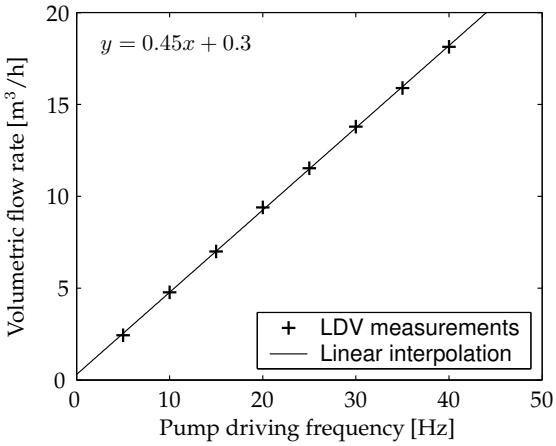

Figure F.6: Water tunnel volumetric flow rate as a function of the pump driving frequency.

Reynolds independency

The first measurements in the section downstream of the burner are done at a pump driving frequency of 33.2 Hz, corresponding to a volume flow of 15.15 m^3/h. With this volume flow, the Reynolds number is equal to the Reynolds number when using air with a volume flow of 200 m^3/h. However, during these measurements it is noticed that in some points the results are 'clipped' at maximum value of 2 m/s. This results in faulty measurements. The clipped-off velocity results are due to the use of a lens with an insufficient focal length. The focal length determines the size of the measurement volume, and this is directly related to the maximum velocity that can be measured. A 400 mm focal-length lens with a measurement volume of 6.5x0.22x0.22 mm (y x x x z) is used. A 600 mm focal-length lens is available, but measurements with this lens also shows clipped results in some points. Moreover, the measurement volume of this lens is 15x0.32x0.32 mm, which decreases the accuracy of the measurements (the measured velocity at a discrete point is actually the average velocity in the measurement volume). Therefore, it has been decided to lower the volume flow to let the velocities fall into the range that can be measured by the 400 mm lens.

To be able to compare the high flow calculations with the low flow measurements the flow has to be Reynolds-independent, i.e. the *shape* of the flow profiles should be independent of the volume flow. When the flow is Reynolds-independent, the measured velocities can be normalised by the mean area velocity u_z^0 (i.e. Q/S_{cc}, the volume flow divided by the cross-sectional area of the combustion chamber), and a comparison between CFD results and the measurements can be made with these normalised, dimensionless velocities.

Generally, a flow can be considered Reynolds-independent when $\mathrm{Re} > 10^4$ [137]. This is confirmed by a RaNS CFD simulation of the flow in the water tunnel. The simulation is done at two volume flows: the nominal volumetric flow rate and $1/3^{\mathrm{th}}$ of the nominal volumetric flow rate. In figure F.7 the dimensionless axial velocities obtained from both simulations are compared at different distances from the burner exit. It is observed that the profiles are indeed self-similar, which implies that the flow is Reynolds-independent.

When the volume flow is lowered to $1/3^{\mathrm{th}}$ of the nominal volume flow, the velocities all fall within the measurement range of the 400 mm lens. $1/3^{\mathrm{th}}$ of the nominal volume flow equals a volumetric water flow of 5.22 SCMH, which corresponds to a pump driving frequency of 11 Hz.

Mechanical strength

During the measurements described above, the pressure in the air supply room and in the plenum is monitored. Due to the 1000-fold higher density and the only 10-fold lower flow velocities, the pressure drop over the acoustic decoupler is approximately 10 times higher in water than in air. This pressure drop is combined with a static pressure load of about 0.3 bar in the air supply room due to the water column. To calculate the maximum allowable pressure in the air supply room a simple model of

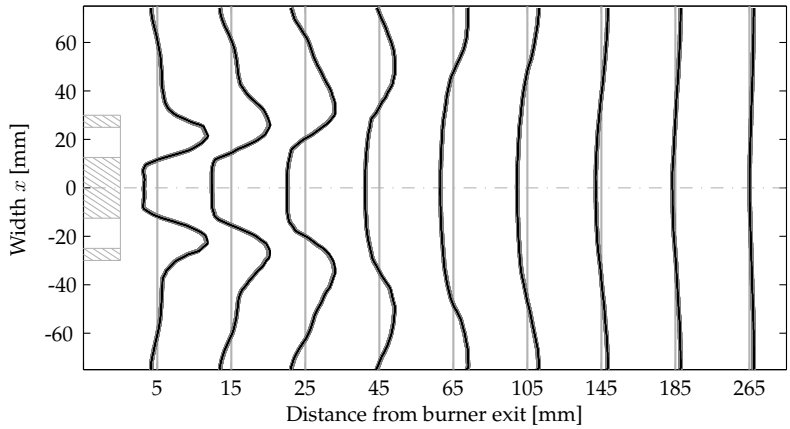

Figure F.7: Mean dimensionless axial velocity profiles for at the nominal volume flow (——) and at $1/3^{\text{th}}$ of the nominal volume flow (▬).

the square room is made. It is assumed that the geometry and loading do not vary significantly in the axial direction of the air supply room (plain strain). The room can now be modelled as a two-dimensional square consisting of beams and with a uniform inside pressure (see figure F.8).

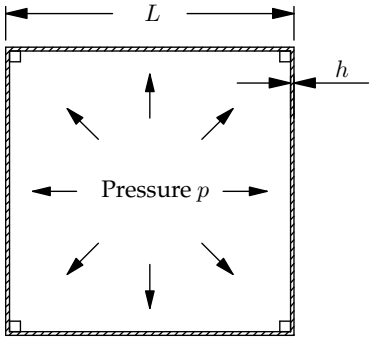

Figure F.8: Model used for determining the maximum pressure for the system.

A simple beam strength analysis shows that the maximum stresses σ_{max} occur in the corners of the model and can be expressed as:

$$\sigma_{max} = \frac{pL^2}{2h^2} + \frac{pL}{2h} \tag{F.1}$$

with $h = 1$ cm and $L = 15$ cm. So the maximum yield strength of perspex ($\sigma = 75$ MPa) is reached when a pressure of 13.6 bars is imposed on the structure. To account for possible weaknesses in the joints at the corners of the model, where the stresses are highest, a pressure of 7.5 bar is the maximum allowable pressure for the

air supply room. This is high enough, considering that an over-pressure of 0.35 bars is measured at a pump frequency of 11 Hz.

Data acquisition

Data acquisition is done using a DIFA spectral analyser installed on a PC. The two transient signals (the two instantaneous velocity components) from the photomultipliers are sampled at 800 Hz for 40.96 seconds. Subsequently, the mean value and the variances of the 32,768 samples are determined. The mean value is defined as:

$$\bar{u} = \frac{1}{n}\sum_{i=1}^{n} u^i \tag{F.2}$$

in which n is the number of samples, and u^i is the value of the velocity u of the i^{th} sample. The variances in the x and z directions are equal to the Reynolds stresses k_{xx} and k_{zz} respectively and are defined as:

$$k_{xx} = \frac{1}{n}\sum_{i=1}^{n}(u_x^i - \bar{u_x})^2 \tag{F.3}$$

$$k_{zz} = \frac{1}{n}\sum_{i=1}^{n}(u_z^i - \bar{u_z})^2 \tag{F.4}$$

The Reynolds stress k_{xz} $(= k_{zx})$ is defined as:

$$k_{xz} = \frac{1}{n}\sum_{i=1}^{n}\left[(u_x^i - \bar{u_x})(u_z^i - \bar{u_z})\right] \tag{F.5}$$

To check whether a sampling frequency of 800 Hz is high enough to catch most of the phenomena in the flow, the time signal is transformed to the frequency domain. Figure F.9 shows the power spectral density (PSD), referenced to its value at 1 Hz, of the axial velocity at a point just above the burner exit. The pump frequency of 11 Hz appears clearly in this plot (due to its presence in the flow, or due to interference of the electronics). No other explicit harmonic behaviour of the flow is noticed. Furthermore, the PSD at 400 Hz is more than two orders of magnitude lower than the low frequency velocity amplitudes.

Also, the measuring time of 40.96 s is long enough, as the mean value and the variance does not change significantly when increasing the measuring time.

Measurement points

Using the conventions of figure F.3, the z and x velocities are measured in 9 different x-y planes downstream of the burner exit. The first plane is located at the lowest possible cross-section that enabled clearance of the laser beam above the swirl burner

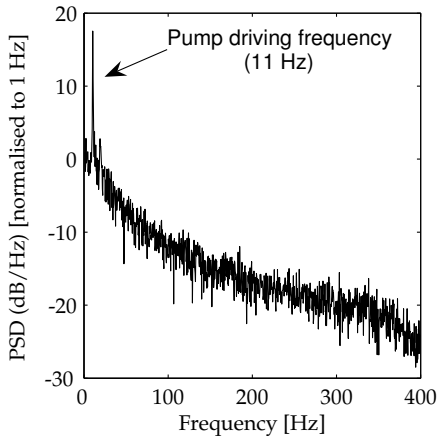

Figure F.9: Power spectral density of the axial velocity.

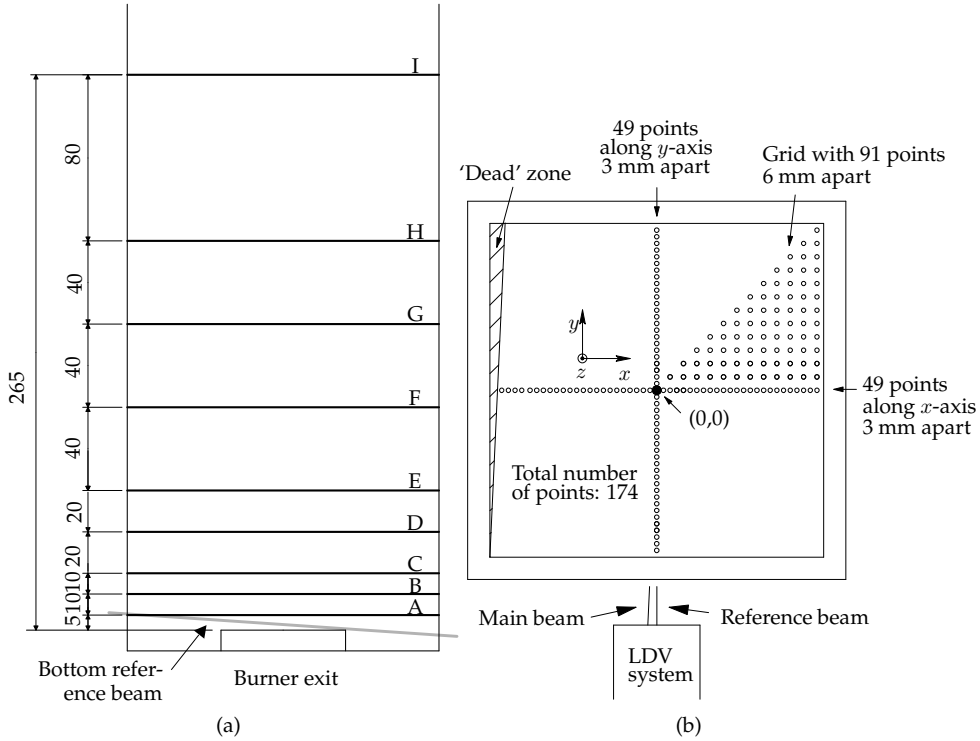

Figure F.10: Cross-sectional view of measuring planes (a) and grid layout of data points in a plane (b).

(see figure F.10(a)). This is determined experimentally to be 5 mm above the burner exit. A layout of the data points measured in each plane is shown in figure F.10(b).

There are a total of 174 data points. Because of symmetry considerations, only one half-quadrant is fully measured. Furthermore, the velocity profiles along the x and y axis are determined. Because the main beam enters the water tunnel under an angle, there is a small 'dead' zone in which no measurements can be taken due to diffraction of the main beam.

The first measurement plane is called 'A'. All subsequent planes are at varying heights above A. For a complete cross-sectional view of the horizontal layers, see figure F.10(a). The next planes are named alphabetically, from 'A' till 'I'. It is not possible to measure higher than plane 'I' because the traverse equipment has an upper limit of 275 mm in the z-direction.

Because of the difference in refractive indices of both perspex and water to air, the displacement of the laser is amplified in the water tunnel. To derive the position of the crossing point of the laser beams in the water tunnel, it is necessary to determine the exact correction factor. With this portion of the experiment, it is feasible to obtain a single correction factor because the wall of the tunnel is flat, i.e. the main beam always enters and exits the tunnel at the same angle. To determine the correction factor experimentally, a series of velocity measurements are taken approaching the inner walls of the tunnel. When a measurement turned out to be near 0 m/s, accompanied with a low photodetector signal, it is concluded that the inside wall has been reached. By performing this test at both inside walls, it is determined that a displacement of the laser of 109 mm resulted in a displacement in the water of 150 mm. This yields a correction factor of 0.7267 (i.e. 1 mm in water is 0.7267 mm in air). So, for each traverse along the y-axis, it is necessary to multiply the desired (actual) distance by the correction factor to obtain the traverse readout (apparent) position. Along the x-axis, no correction factor is needed because the laser only projects in the y-direction, leaving no room for error in the perpendicular x-direction.

Appendix G

Selected LES results

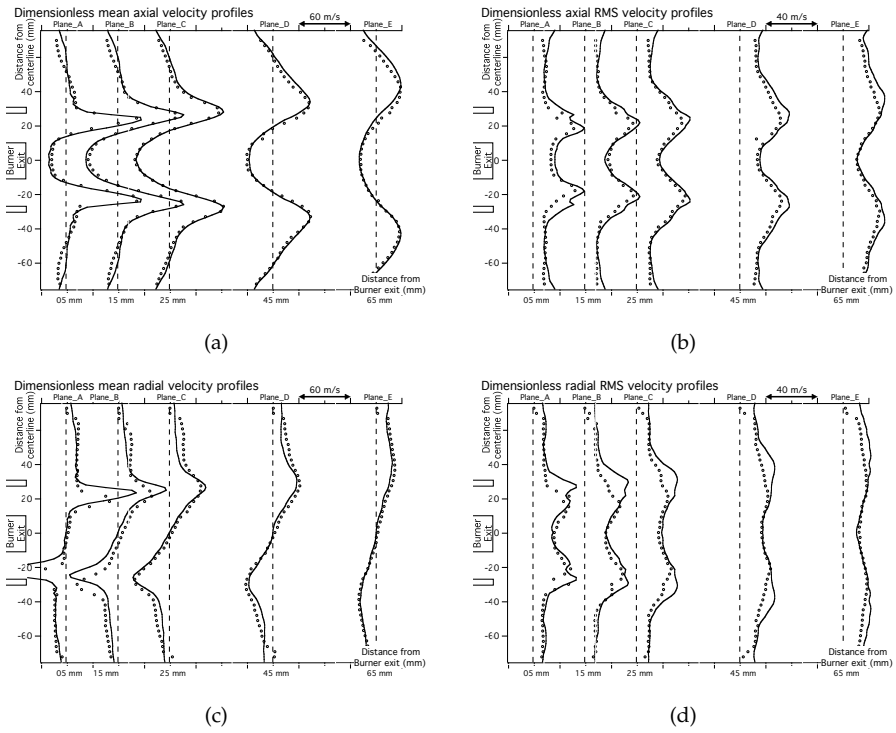

Figure G.1: Comparison of statistical profiles, obtained from water tunnel measurements and isothermal LES simulations [164]. The symbols represent the experimental data, the solid lines are the LES data. The dashed line is the zero line. Continued on next page.

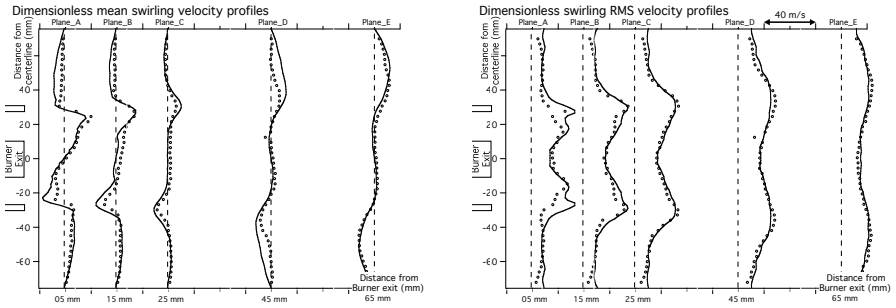

(e) (f)

Figure G.1 (continued)

Appendix H

Flowchart CFX2FTF

The program implemented in MATLAB to obtain the coefficients is called CFX2FTF. The flowchart of CFX2FTF is given in figure H.1. The different routines shown in the flowchart are discussed in the order of the flowchart.

read CFX data : In this routine, the data from a converged steady-state CFX simulation is read. The variable values at each node are read. Also constants like the molar mass and some combustion model constants are input here. Moreover, the element numbers and the corresponding node numbers are read. Finally, for each node the node numbers to which this node is coupled are read.

manual input : The manual input includes information about the variable that is excited, the frequency range in which the transfer function needs to be calculated, the order of the reduced model etc.

calculate time derivatives & get reaction rate @ node : This is the main routine of the program. Later in this appendix, this routine will be further discussed. The routine calculates the time derivatives and heat release rate at a certain node, given the variable values at surrounding nodes and the mesh data from CFX.

node evaluated for first time? : When the node is evaluated for the first time, no variable is perturbed. For each node, the variable values obtained from the steady-state CFX simulation are used to calculate the steady time derivatives $\frac{\partial \psi_i}{\partial t}^s$ of each equation at each node (ideally, these steady time derivatives are zero). Moreover, the steady heat release rate Q^s is calculated.

un-perturb previous variable @ node : In the subsequent loops, each variable at each node will be perturbed sequentially. Before perturbing the next variable, the previous one is un-perturbed.

assemble A & C matrices : When the considered variable at the node is perturbed, the coefficients of the **A** and **C** matrices at this node can be calculated from the difference with the steady-state values (*assemble* **A** *&* **C** *matrices*), i.e.:

$$a_{ij} = \frac{\frac{\partial \psi_i}{\partial t}^{new} - \frac{\partial \psi_i}{\partial t}^{s}}{\Delta \psi_j} \tag{H.1}$$

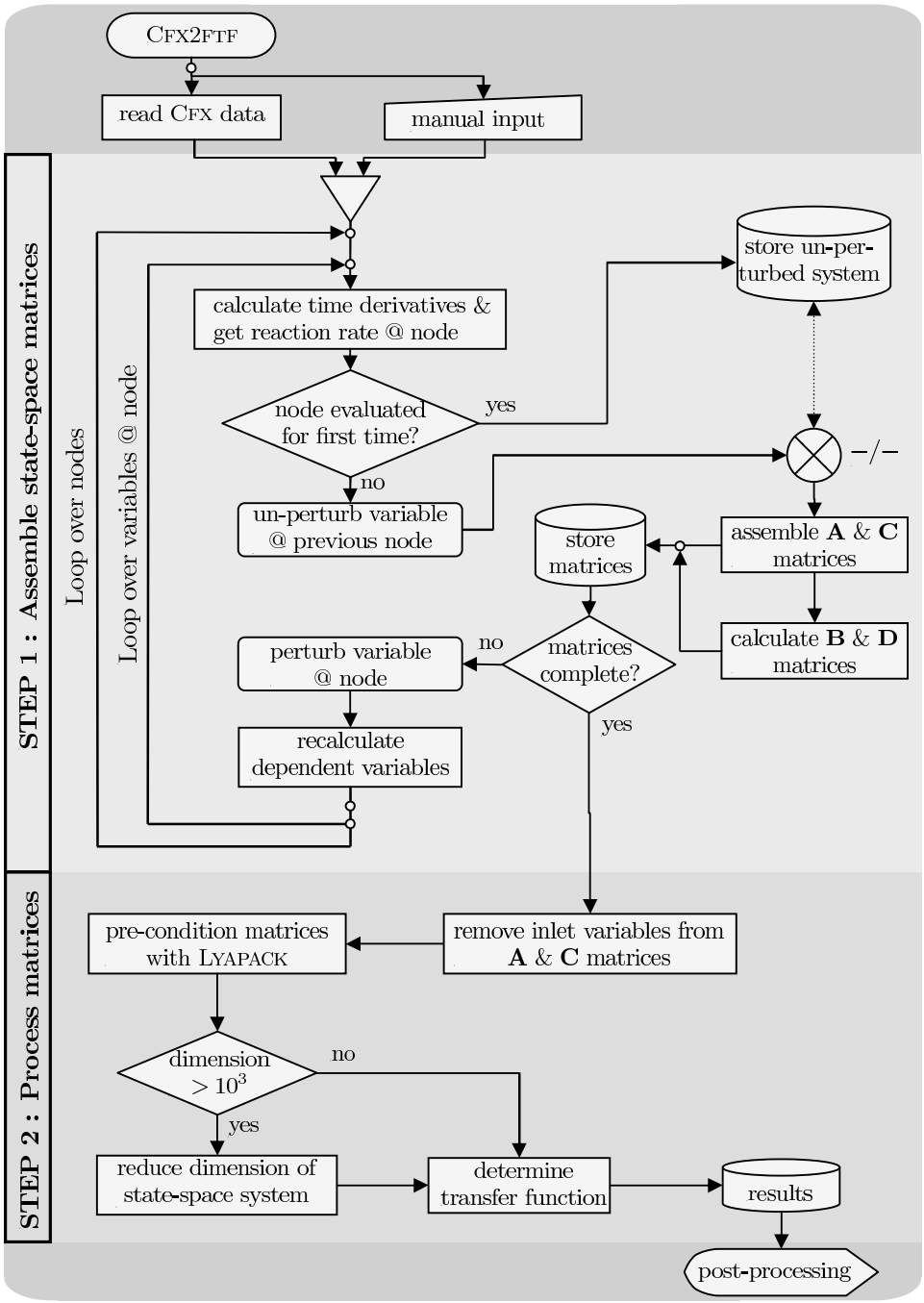

Figure H.1: Flowchart of CFX2FTF.

in which $\Delta\psi_j$ is the variable that is perturbed and $\frac{\partial\psi_i}{\partial t}$ is the time derivative of equation i. The superscripts s and new indicate the time derivative of the steady, unperturbed situation or of the perturbed situation, respectively.

The coefficients of the $\mathbf{C}$ matrix give the relationship between a fluctuation in the *volume integrated* heat release rate and the perturbed variable, i.e.:

$$c_j = \frac{Q^{new} - Q^s}{\Delta\psi_j} \tag{H.2}$$

The integrated heat release rate is a global variable, so the $\mathbf{C}$ matrix is one-dimensional.

calculate B & D matrices : After the $\mathbf{A}$ and $\mathbf{C}$ matrices are calculated, the $\mathbf{B}$ and D matrices can be constructed from them. The procedure for this is explained in section 5.2.3.

matrices complete : When the complete $\mathbf{A}$, $\mathbf{B}$, $\mathbf{C}$ and D matrices are calculated the program proceeds to the processing of the matrices. Otherwise the next independent variable will be perturbed.

perturb variable @ node : The current (independent) variable at the current node is increased with 1%. For a reacting flow simulation, the independent variables are: the 3 velocities, the pressure, the temperature (not the enthalpy, because this variable depends on multiple other variables, like the mass fractions and the temperature), the turbulence kinetic energy, the turbulence eddy dissipation and the mass fractions of 4 species (CH_4, O_2, CO_2 and H_2O). In total, 11 independent variables are considered.

recalculate dependent variables : After changing an independent variable, all dependent variables need to be recalculated. For example, when the temperature is changed, the density, which is a dependent variable, must be recalculated.

remove inlet variables from A & C matrices : The coefficients of the $\mathbf{B}$ and D matrices are obtained from the $\mathbf{A}$ and $\mathbf{C}$ matrices, respectively. Because the variables that are located at the inlet, i.e. y^{in}_{CH4} and y^{in}_{O2}, are the boundary conditions, they should not be included in the $\mathbf{A}$ and $\mathbf{C}$ matrices. The rows and columns corresponding to the inlet are therefore removed from the $\mathbf{A}$ and $\mathbf{C}$ matrices.

precondition matrices with LYAPACK : The state space matrices are preconditioned using the pre-conditioner '`au_pre`' of the LYAPACK software [131, 132]. This preconditioner consists of a transformation of the input data (matrices $\mathbf{A}$, $\mathbf{B}$ and $\mathbf{C}$) such that the transformed data has an improved structure from the numerical point of view.

dimension $> 10^3$: When the dimension of the obtained state space system is larger than 10^3, an order reduction step is performed. The Implicitly Restarted and Shifted Lanczos method is used for this purpose, see section 5.3.

The most important subroutine in the CFX2FTF program is the routine in which the time derivatives and the heat release rate at the current node is calculated. This routine includes the discretisation and assembling of the equations, in the same way as done in CFX. The flowchart of the routine, named GETRHS, is shown in figure H.2. In the same way as done for the CFX2FTF program, the GETRHS routine is discussed in the order of the flowchart.

get reaction rate @ node : Given the values of the variables at the current node, the reaction rate at the node is calculated. From the reaction rate, the heat released in the current control volume can be calculated. This information is necessary for constructing the **C** matrix.

determine elements connected to node : In this step, the elements containing the current node are determined. These elements are considered in the next loop, because they each contain a part of the control volume (see figure C.2) of the current node.

determine element type : In CFX2FTF two types of elements are currently available: the prism element, containing 6 nodes, and the tetrahedron element, containing 4 nodes. In this step, the type of the currently considered element is determined.

get tetrahedron/prism info : Depending on the element type, the integration points (see figure C.2) in terms of the natural coordinates of the element are obtained. Moreover, the outward directed surface normal at the integration points is determined.

get variable values at integration points : Given the natural coordinates of the integration points and the element type, the variable values at the integration point can be calculated. Moreover, the gradient of the variables can be calculated using the Jacobian of the shape functions. This routine makes use of the functions *convert nat. coordinates of prism/tetrahedron to real coordinates and derivatives*, which, given the natural coordinates and the coordinates of the element nodes, calculates the gradient and the value at the natural coordinates.

sum contributions to equations : Using the variable values, gradients and surface normals, all at the current integration point, the contribution of the integration point to each equation can be calculated (using the theory as described in section C).

all coupled elements considered? : When all the elements that contain the current node are considered, the equations are complete. The time derivatives of the equations and the heat release rate are the output of the routine GETRHS.

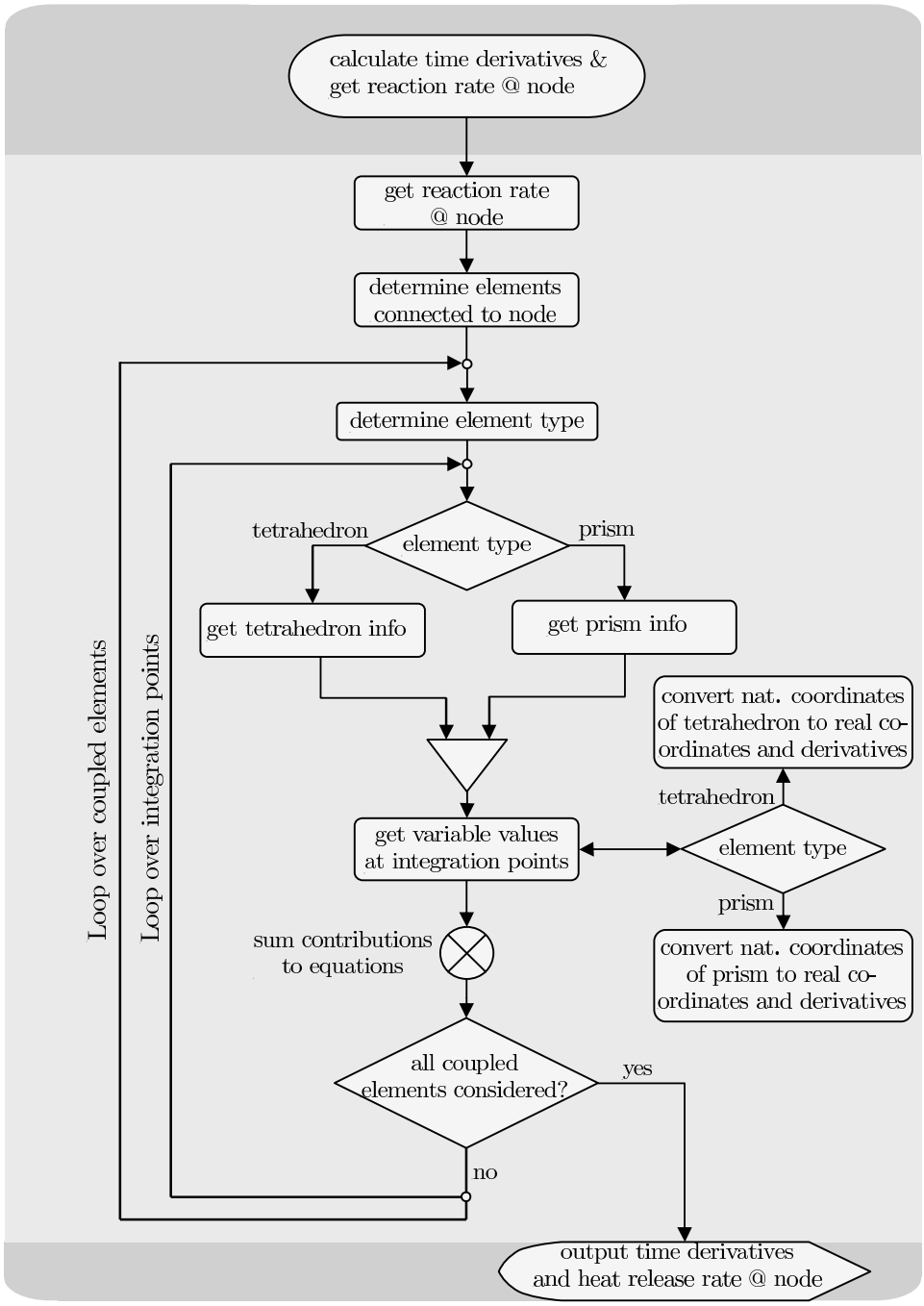

Figure H.2: Flowchart of subroutine getRHS.

Appendix I

The general unsymmetrical Lanczos method

The explanation of the general unsymmetrical Lanczos method starts with the concept of Krylov spaces [59]. A Krylov matrix $\mathcal{K}$ is a matrix of the form:

$$\mathcal{K}(\mathbf{A}, \mathbf{x}, n) = [\mathbf{x}, \mathbf{A}\mathbf{x}, \mathbf{A}^2\mathbf{x}, ..., \mathbf{A}^{n-1}\mathbf{x}] \tag{I.1}$$

while the Krylov *space* is the space spanned by the columns of the Krylov matrix. Moreover, the Rayleigh quotient $r(\mathbf{x})$ is defined as:

$$r(\mathbf{x}) = \frac{\mathbf{x}^T\mathbf{A}\mathbf{x}}{\mathbf{x}^T\mathbf{x}} \qquad \mathbf{x} \neq \mathbf{0} \tag{I.2}$$

A property of the Rayleigh quotient is that its maximum and minimum values represent the maximum and minimum eigenvalue of $\mathbf{A}$, respectively [59]. These eigenvalues are indicated as $\lambda_1(\mathbf{A})$ and $\lambda_n(\mathbf{A})$, in which n is the dimension of the square matrix $\mathbf{A}$.

Now assume that $\mathbf{q_i} \subseteq \Re^n$ is a sequence of orthonormal column vectors, and let $\mathbf{Q_k} = [\mathbf{q_1}, .., \mathbf{q_k}]$. Using expression I.2 the largest eigenvalue M_k of the matrix $\mathbf{Q_k}^T\mathbf{A}\mathbf{Q_k}$ can be written as

$$M_k = \lambda_1(\mathbf{Q_k}^T\mathbf{A}\mathbf{Q_k}) = \max_{\mathbf{y}\neq 0} \frac{\mathbf{y}^T(\mathbf{Q_k}^T\mathbf{A}\mathbf{Q_k})\mathbf{y}}{\mathbf{y}^T\mathbf{y}} = \max_{||\mathbf{y}||_2=1} r(\mathbf{Q_k}\mathbf{y}) \leq \lambda_1(\mathbf{A}) \tag{I.3}$$

In the Lanczos algorithm the key issue is to choose $\mathbf{Q_k}$ such that M_k is an increasingly better estimate of $\lambda_1(\mathbf{A})$. When $k < n$, this results in a $k \times k$ matrix $\hat{\mathbf{A}} = \mathbf{Q_k}^T\mathbf{A}\mathbf{Q_k}$, approximating the largest eigenvalues of the $n \times n$ matrix $\mathbf{A}$.

When $\mathbf{q_{k+1}}$ is chosen such that

$$\text{span}\{\mathbf{q_1}, ..., \mathbf{q_{k+1}}\} = \text{span}\{\mathbf{q_1}, \mathbf{A}\mathbf{q_1}, ..., \mathbf{A}^{k-1}\mathbf{q_1}, \mathbf{A}^k\mathbf{q_1}\} \tag{I.4}$$

it is ensured that the new approximation of the largest eigenvalue is better than the previous one [59]. This is because the added vector $\mathbf{q_{k+1}}$ is then chosen such that

the vector space span of $\mathbf{Q_{k+1}}$ contains the direction in which the gradient of the Rayleigh quotient increases most rapidly, since

$$\nabla r(\mathbf{x}) = \frac{2}{\mathbf{x}^T\mathbf{x}}(\mathbf{Ax} - r(\mathbf{x})\mathbf{x}) \in \text{span}\{\mathbf{x}, \mathbf{Ax}\} \tag{I.5}$$

This means that when the space spanned by projector matrix $\mathbf{Q_k}$ is taken equal to the Krylov space of $\mathcal{K}(\mathbf{A}, \mathbf{q_1}, k)$, the eigenvalues of the reduced $k \times k$ matrix $\mathbf{Q_k}^T\mathbf{AQ_k}$ are progressively better approximation of the original matrix' eigenvalues. The Lanczos method is used to efficiently compute the orthonormal basis for this Krylov subspace.

The projected matrix $\mathbf{\hat{A}} = \mathbf{Q_k}^T\mathbf{AQ_k}$ is assumed to be tridiagonal, i.e. a square matrix with nonzero coefficients only on the diagonal and horizontally or vertically adjacent the diagonal. This allows an inexpensive calculation of the eigenvalues of $\mathbf{\hat{A}}$ once the orthonormal matrix $\mathbf{Q_k}$ is found. The elements of the tridiagonal matrix $\mathbf{\hat{A}}$ can be computed in a direct way by setting $\mathbf{Q_k} = [\mathbf{q_1}, ..., \mathbf{q_k}] = [\mathbf{q_1}, \mathbf{Aq_1}, ..., \mathbf{A}^k\mathbf{q_1}]$ and:

$$\mathbf{\hat{A}} = \mathbf{Q_k}^T\mathbf{AQ_k} = \mathbf{Q_k}^{-1}\mathbf{AQ_k} = \begin{bmatrix} \alpha_1 & \gamma_1 & 0 & 0 & 0 \\ \beta_1 & \alpha_2 & . & 0 & 0 \\ 0 & . & . & . & 0 \\ 0 & 0 & . & . & \gamma_{k-1} \\ 0 & 0 & 0 & \beta_{k-1} & \alpha_k \end{bmatrix} \tag{I.6}$$

For clarity, the inverse transpose of the $\mathbf{Q_k}$ matrix is denoted as $\mathbf{P_k}$, i.e. $\mathbf{Q_k}^{-T} \equiv \mathbf{P_k}$. The $\mathbf{Q_k}$ and $\mathbf{P_k}$ matrices consist of k vectors:

$$\mathbf{Q_k} = [\mathbf{q_1}, ..., \mathbf{q_k}] \tag{I.7}$$

$$\mathbf{P_k} = [\mathbf{p_1}, ..., \mathbf{p_k}] \tag{I.8}$$

When comparing columns in $\mathbf{AQ_k} = \mathbf{Q_k}\mathbf{\hat{A}}$ and $\mathbf{A}^T\mathbf{P_k} = \mathbf{P_k}\mathbf{\hat{A}}^T$ it is found that

$$\mathbf{Aq_i} = \gamma_{i-1}\mathbf{q_{i-1}} + \alpha_i\mathbf{q_i} + \beta_i\mathbf{q_{i+1}} \qquad \gamma_0\mathbf{q_0} \equiv 0 \tag{I.9}$$

$$\mathbf{A}^T\mathbf{p_i} = \beta_{i-1}\mathbf{p_{i-1}} + \alpha_i\mathbf{p_i} + \gamma_i\mathbf{p_{i+1}} \qquad \beta_0\mathbf{p_0} \equiv 0 \tag{I.10}$$

for $i = 1, ..., k-1$. The biorthonormality condition $\mathbf{P_k}^T\mathbf{Q_k} = \mathbf{Q_k}^{-1}\mathbf{Q_k} = \mathbf{I_k}$ implies $\alpha_i = \mathbf{p_i}^T\mathbf{Aq_i}$ and

$$\beta_i\mathbf{q_{i+1}} \equiv \mathbf{r_i} = (\mathbf{A} - \alpha_i\mathbf{I})\mathbf{q_i} - \gamma_{i-1}\mathbf{q_{i-1}}) \tag{I.11}$$

$$\gamma_i\mathbf{p_{i+1}} \equiv \mathbf{s_i} = (\mathbf{A} - \alpha_i\mathbf{I})^T\mathbf{p_i} - \beta_{i-1}\mathbf{p_{i-1}}) \tag{I.12}$$

Note that $1 = \mathbf{p_{i+1}^T q_{i+1}} = (\mathbf{s_i}/\gamma_i)^T(\mathbf{r_i}/\beta_i)$ so that $\gamma_i = \mathbf{s_i}^T\mathbf{r_i}/\beta_i$. In the variant of the Lanczos method that is used here, β_i is set to $\sqrt{|\mathbf{s_i}^T\mathbf{r_i}|}$, so that $\gamma_i = \text{sign}(\mathbf{s_i}^T\mathbf{r_i})\beta_i$.

The algorithm for obtaining the biorthogonormal matrices $\mathbf{Q_k}$ and $\mathbf{P_k}$ is listed in algorithm 2.

Using this algorithm, the matrices $\mathbf{Q_k}$, $\mathbf{P_k}$ $(= \mathbf{Q_k}^{-T})$ and $\mathbf{\hat{A}}$ can be calculated iteratively. The extremal eigenvalues of $\mathbf{\hat{A}}$ turn out to be very good approximations

Algorithm 2 General unsymmetrical Lanczos method

$\beta_1 = \sqrt{|\mathbf{CB}|}$
$\gamma_1 = \text{sign}(\mathbf{CB})\beta_1$
$\mathbf{q_1} = \mathbf{B}/\beta_1$
$\mathbf{p_1} = \mathbf{C}^T/\gamma_1$
$\mathbf{q_0} = \mathbf{0}$
$\mathbf{p_0} = \mathbf{0}$
for $i = 1$ to k **do**
  $\alpha_i = \mathbf{p_i}^T \mathbf{A} \mathbf{q_i}$
  $\mathbf{r_i} = (\mathbf{A} - \alpha_i \mathbf{I})\mathbf{q_i} - \gamma_i \mathbf{q_{i-1}}$
  $\mathbf{s_i} = (\mathbf{A} - \alpha_i \mathbf{I})^T \mathbf{p_i} - \beta_i \mathbf{p_{i-1}}$
  $\beta_{i+1} = \sqrt{|\mathbf{s_i}^T \mathbf{r_i}|}$
  $\gamma_{i+1} = \text{sign}(\mathbf{s_i}^T \mathbf{r_i})\beta_{i+1}$
  $\mathbf{q_{i+1}} = \mathbf{r_i}/\beta_{i+1}$
  $\mathbf{p_{i+1}} = \mathbf{s_i}/\gamma_{i+1}$
end for

of the extremal eigenvalues of $\mathbf{A}$. It can be seen that the starting vectors $\mathbf{q_1}$ and $\mathbf{p_1}$ of the Lanczos procedure are given by:

$$\mathbf{q_1} = \mathbf{B}/\sqrt{|\mathbf{CB}|} \tag{I.13}$$

$$\mathbf{p_1} = \text{sign}(\mathbf{CB})\mathbf{C}^T/\sqrt{|\mathbf{CB}|} \tag{I.14}$$

This appears to give good results for model reduction problems [61].

During the Lanczos iteration, there is a good chance that the orthogonality between $\mathbf{q_i}$ and $\mathbf{p_i}$ is lost (see [59], page 481). This loss of orthogonality causes a fill of the tridiagonal matrix $\hat{\mathbf{A}}$. To prevent this, each newly computed vector $\mathbf{p_{i+1}}$ and $\mathbf{q_{i+1}}$ is explicitly orthogonalised against the columns of the already calculated matrices $\mathbf{P_i}$ and $\mathbf{Q_i}$, respectively. This is done here by one iteration of a classical Gram-Schmidt process. In this process, the orthogonalisation coefficients h_p and h_q are first calculated:

$$h_p = \mathbf{P_i}^T \mathbf{q_{i+1}} \tag{I.15}$$

$$h_q = \mathbf{Q_i}^T \mathbf{p_{i+1}} \tag{I.16}$$

Subsequently these coefficients, indicating the deviation from orthogonality, are subtracted from the new vectors, resulting in improved orthogonal vectors:

$$\widetilde{\mathbf{q_{i+1}}} = \mathbf{q_{i+1}} - \mathbf{Q_i} h_p \tag{I.17}$$

$$\widetilde{\mathbf{p_{i+1}}} = \mathbf{p_{i+1}} - \mathbf{P_i} h_q \tag{I.18}$$

Generally, one iteration is enough to get the vectors orthogonal again.

Appendix J

Description DESIRE setup

Layout and control

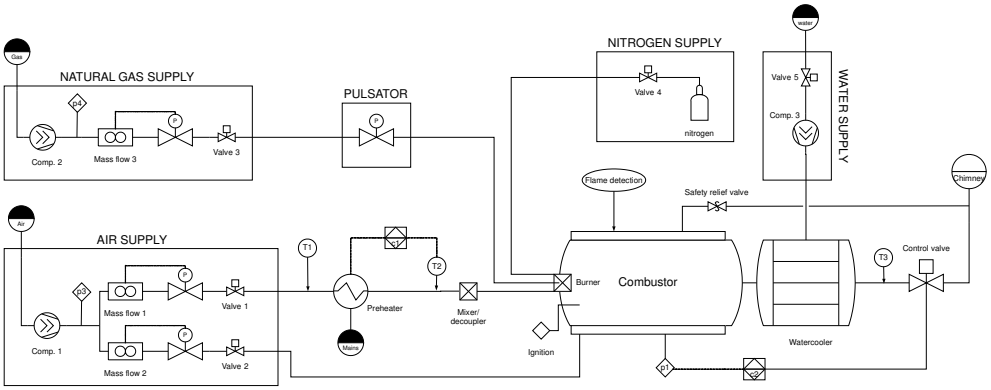

Figure J.1: Schematic layout of the DESIRE setup.

Figure J.1 shows the simplified layout of the DESIRE test rig. All connecting ducts of the setup are chosen such that the Mach number remains below 0.3. Keeping the velocity below this value prevents the generation of intense flow noise [144].

Compressed air is provided from a Diesel engine driven dual scroll compressor (Comp. 1) at a pressure of 10 bar gauge. The air mass flow is split into a combustion air flow (Mass flow 1) and a cooling air flow (Mass flow 2). Each flow is controlled by a Bronckhorst mass flow controller with a maximum mass flow of 500 SCMH (Standard Cubic Metre per Hour). Natural gas is supplied also at 10 bar gauge from a small natural gas compressor station (Comp. 2). This gas mass flow is controlled by a third Bronckhorst mass flow controller (Mass flow 3), having a maximum mass flow of 60 SCMH. All mass flow controllers have an accuracy of 1% of their full scale.

The flows from both compressors pass through several filters to clean the gas flow before it arrives at the sensitive mass flow controllers. The flow from the air

compressor is first cooled by a heat exchanger and subsequently dried by a dryer. This way, the conditions of the air can be kept constant for the experiments.

The air that is used for combustion is subsequently preheated by a 120 kW electrical preheater. This preheater is able to heat an air flow of 360 grams per second from room temperature to 300°C. The heaters are installed to simulate gas turbine conditions at the inlet of the combustor. In a gas turbine, combustion air comes directly from the compressor, where its temperature is increased by compression. In the DESIRE rig, the air is pre-conditioned to have a well-controlled air flow. The consequence is that the supplied air is cold. By heating the air with a preheater, the lean conditions at which a gas turbine operates can be reached.

The natural gas flow is led through a pulsator, which is able to pulsate this flow with a maximum frequency of 400 Hz and a pulsation level of several percentages of the mean mass flow, dependent on the operating condition and the frequency of oscillation. The pulsator is discussed in more detail in section 6.4.2.

The combustion air and natural gas are supplied to the burner, which has been presented in chapter 3. The burner exits in the combustor, around which cooling air flows to keep the liner temperature below is maximum value. This cooling air is mixing again with the flue gasses downstream the combustor. This mixture is further cooled by a water spray. Subsequently, the mixture passes through a throttle valve which controls the pressure in the combustor. Downstream the throttle valve the mixture of water vapour and flue gasses is discharged by the chimney.

The entire test rig is remotely controlled and diagnosed by a control system implemented in LabView. With a view to safety and noise production the test rig is placed in an isolated concrete walled laboratory with a safety expansion roof. Separated by a corridor there is a room for the operator and the investigators.

Combustor

In figure J.2, a photograph of the DESIRE combustor is displayed. In the same figure a picture of the flame, taken through the quartz glass windows, is inserted. A cross-sectional view of the combustor has been presented in figure 6.1. The combustor consists of two square tubes. The inner square tube forms the liner and the outer square tube is the pressure vessel. Between the tubes the cooling air flow is forced. A one-dimensional heat transfer model is used to determine the cooling channel height and to predict the amount of cooling air necessary to keep the liner below its maximum temperature [107]. A channel height of 20 mm seems to be optimal to keep both the liner and the cooling air outlet temperature below their maximum values. In the corners of the square annulus, filler strips are used to prevent the air from collecting in the corner of the channel.

The burner opens into the inner square tube in which the combustion process of the air/natural gas mixture takes place. The combustion process can be observed optically (Laser Induced Fluorescence and natural light emission) through quartz glass windows that are mounted in the liner and pressure vessel on 3 sides of the *combustion* section (indicated with ① in figure 6.1). Suprasil quartz glass is used to prevent absorption of the ultraviolet light range (short wavelength). In this range,

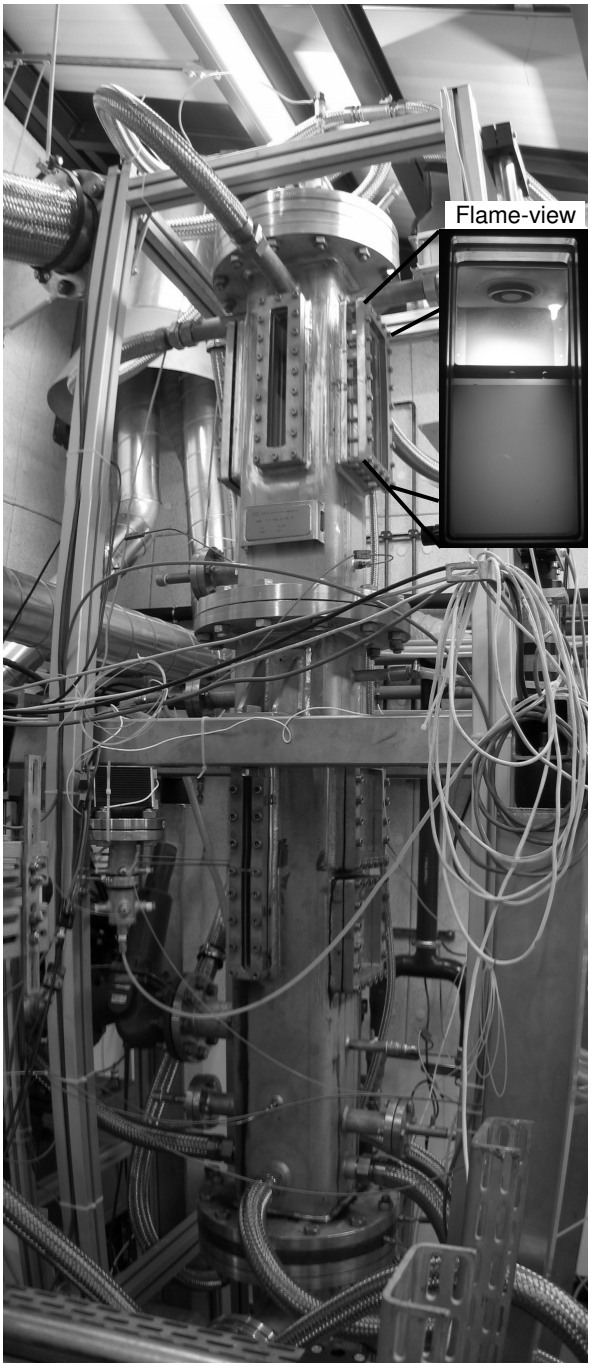

Figure J.2: Photograph of the DESIRE setup. Inserted in the picture is a view on the flame, through the Suprasil quartz glass windows.

the PLIF measurements take place. The view port size is 120×300 mm. However, the liner windows have been shortened (see flame-view in figure J.2) due to breaking of these windows as a result of the thermal expansion and the accompanied axial curvature of the liner. The real view port is therewith diminished to 120×150 mm, which is still large enough to see the whole flame.

Due to the quartz glass windows the combustion section does not have structural vibrations of interest. These vibrations are observed in the *structural* section (indicated with ② in figure 6.1). Here the liner is all metal and the casing has a glass window to allow vibration measurement with a Polytec Laser Doppler Vibrometer (LDV). The glass window is made from a lower quality quartz glass than the other windows, since it only has to transmit the visible light range (the LDV operates at a light wavelength of 633 nm).

The exit of the cooling air channel is directly connected to the water cooler, located downstream of the combustion chamber. Therefore, both the pressure in the cooling air channel and in the combustion chamber is controlled by the throttle valve downstream of the water cooler. Due to contractions between the combustion chamber and the water cooler, and between the cooling air channel and the water cooler, there exists a pressure difference between the combustion chamber and the cooling channel. The maximum pressure difference that can occur under steady conditions and during ignition is determined with a simple model that calculates the pressure drops over the contractions using the Bernoulli equation. The maximum pressure drop over the liner is 36.5 mbar (over-pressure in combustion chamber), which occurs at maximum power (500 kW) and maximum pressure (5 bar), *without* cooling air flowing. Looking at more realistic situation (i.e. with cooling air flow, of which the cooling air has an outlet temperature of about 700 K), the pressure drops all lie below 31 mbar. This pressure drop is acceptable from a structural point of view.

To prevent valve overheating the flue gasses are cooled down in the *cooling* section (indicated with ③ in figure 6.1) by injection of a water spray. The water is supplied by a 2.4 kW Kranzle K160TST high pressure water cleaner, which can supply water with a pressure up to 130 bars, and a maximum water flow of 11 l/min. Four spray nozzles atomise the water in the cooling section. At low powers, i.e. up to 200 kW, only one spray nozzle is needed to cool the hot flue gasses. The spray nozzles (Spraybest PJ40) have a spray angle of 90 degrees and are located such that they do not interfere. The nozzles supply a maximum water flow of 5.34 l/min at 70 bars pre-pressure. Additionally, the cooling air from the liner is mixed in the cooling section, which helps to bring down the temperature. Water that does not evaporate is discharged by a condensate drain, mounted at the bottom of the setup.

The maximum allowable pressure of the whole setup is 5 bars gauge. At this pressure, a safety relief valve opens, discharging all gas in the combustor to the chimney.

Thermal barrier coating

In gas turbine combustors, a thermal barrier coating (TBC) is commonly used to decrease the temperatures of the liner and pressure vessel and to protect the liner wall from oxidation. With respect to heat transfer, the TBC reduces the temperature

by two effects:

1. relatively low conductivity

2. increase in the emissivity coefficient, which reduces the effect of radiative heat loading

In gas turbines, TBCs can reduce the liner temperature with about 50 degrees [106]. Peak temperatures can be reduce by up to 200 degrees [38]. With a typical thickness of 0.5 mm and a typical conductivity of $\lambda = 2$ W/mK [92], the conductive heat transfer coefficient of a TBC is about $h \approx 4000$ W/m^{2}K. Typical convective heat transfer coefficients in the DESIRE setup lie around 500 W/m^{2}K, so the TBC would conduct heat relatively well compared to the convective heat transfer to the walls. Moreover, the emissivity coefficient does not differ very much from that of the metal surface (i.e. 0.75 for the coating [92] versus about 0.8 for the metal surface). In gas turbines, typical convective heat transfer coefficients are of the same order as the coefficient of the TBC, and then the TBC has considerable influence on the transferred heat. In this application, however, a TBC would not influence the liner temperature much, and is therefore not used in the DESIRE setup.

Frame

The DESIRE experimental setup is mounted vertically in a specially designed frame (see figure J.3).

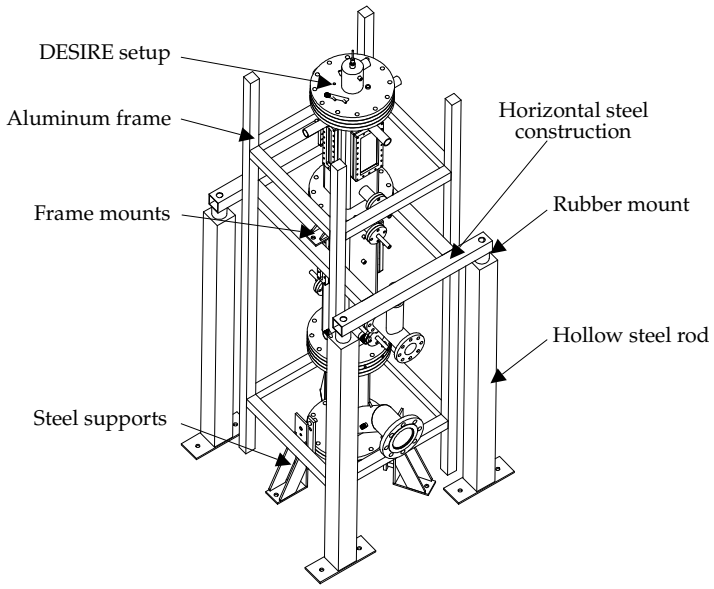

Figure J.3: DESIRE setup mounted in its supporting frame.

The supporting frame is designed such that vibrations of the setup itself are minimised. This is achieved by mounting the setup on a horizontal steel construction, which is mounted onto 4 vertical square, hollow steel beams via rubber mounts. These rubber mounts have several advantages [116]:

1. Since the horizontal steel construction can move freely relative to the vertical beams, the effective length between the center of mass and the ground level is reduced
2. Due to the rubber mounts, the system has 1 damped eigenfrequency at a low frequency, while the remaining eigenfrequencies (above 3 times the first eigenfrequency) are overdamped due to the hysteresis in the rubber

Three steel supports at the bottom of the setup clamp that setup. The intention of these clamps is to prevent the setup to oscillate as a pendulum.

The frame is made of stainless steel 316, which is relatively stiff and has a good temperature resistance. Around the setup, a separate aluminum frame is placed that is not connected to the setup in any way. On this frame, measurement equipment can be mounted vibration free.

Steady sensors

In figure 6.1 the locations of the steady sensors are displayed. The temperature is measured at different locations by Thermoelectric K-type thermocouples with a diameter of 3 mm (MTS-15303-K-250). These thermocouples can measure temperatures between -40 and 1200°C with an accuracy of ± 2.5°C. At positions where the temperature of a material is measured, the tip of the thermocouple is pressed against the material. In case of the liner thermocouples, the thermocouple is shielded to reduce the influence of the cooling air on the measured temperature.

The static pressure is measured by Special Instrument 'Clic' pressure transducers, which are able to measure both the absolute pressure, and the pressure relative to another pressure. The pressure is measured via a hose connected to the setup to prevent overheating of the pressure sensor. The sensor has an accuracy of 0.25% of its full range. The liner pressure difference is measured by a sensor with a full range of 2 bars, yielding an accuracy of ± 5 mbar. The remaining pressure sensors have a full range of 7 bars with an accuracy of ± 17.5 mbar.

Laser techniques

The combustion section contains several windows that are used for laser techniques which can detect certain radicals in the flame. It is often assumed that CH* (electronically excited molecules are indicated with a '*') is linearly related to the heat release rate. CH is only present in the reaction zone, in contrast to OH, which is formed due to splitting of water and therefore extends its zone with high concentration to the exhaust gas side of the flame zone. As a consequence, not its concentration but its gradient is related to the heat release rate.

The radical CH* is measured by chemiluminescence. During the chemical reactions in the combustion process some species become electronically excited. In this state, the molecule is highly reactive so its lifetime is short (1-100 ns). At the end of its life, the molecule can fall back to its ground state, releasing energy in the form of heat and light (natural emission). Each molecule emits a characteristic spectrum, which makes it possible to identify individual species in a flame. With chemiluminescence, this natural light emission of the CH* radical is detected by a camera and a filter in front of the camera.

A disadvantage of chemiluminescence is that it is a line of sight technique, which means that the measured CH concentration is the integral of all CH in the line of sight of the camera. Imagine a cylindrical, uniformly distributed flame shape. With chemiluminescence the measured signal is not uniform, as can be seen in figure J.4. When the shape of the flame is known, special techniques can be applied to obtain a planar picture from the line of sight measurements, e.g. Abel transformation ('onion peeling') in case of an axisymmetrical shape [1]. An advantage of the line of sight character of the technique is that it directly gives information on the volume integrated heat release rate.

Since the shape of the flame in the DESIRE setup is not clearly defined, another laser technique is used as well. With this technique, the radical field in the cross-section of the flame can be measured directly. This technique is called Planar Laser Induced Fluorescence (PLIF). PLIF measurements have been started with OH because of its high concentration and therefore expected good signal strength. In future measurements, the use of H_2CO and CH are recommended as a flame front marker.

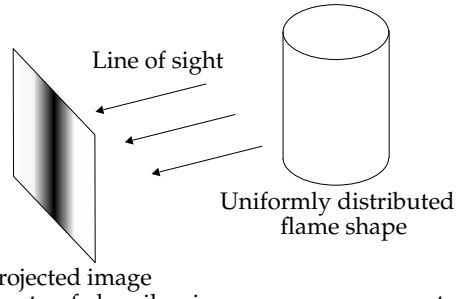

Figure J.4: Integrating property of chemiluminescence measurement of a uniformly distributed cylindrical flame shape.

Some results from the PLIF technique have already been used in chapter 3. More information on the background of the technique and the application to the DESIRE setup can be found in [65]. The basic PLIF measurement technique is depicted in figure J.5.

A 400 Hz XeCl excimer laser (Lambda Physic 240i) pumps a tunable dye laser (Lambda Physic Scanmate 2). The laser beam is converted into a laser sheet (height 75 mm and thickness 1 mm) using a series of mirrors. This laser sheet is sent through the flame in the combustion chamber of the experimental setup.

The fluorescence signal from the excited molecules is filtered by a band pass filter 'UG11' followed by a high pass filter 'WG305' to block the laser light. The OH

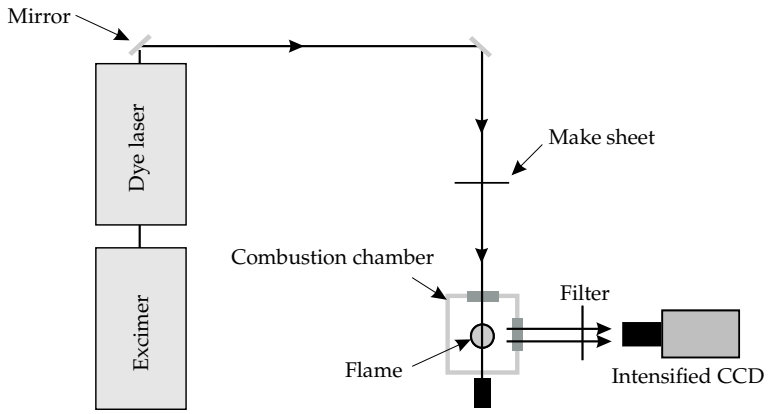

Figure J.5: Schematic layout of the PLIF system to measure fields of radicals.

signal is recorded with a 1000 Hz CCD camera (Roper Scientific Motionscope). The fluorescence signal is amplified by a high speed image intensifier (LaVision).

In the average pictures shown in this thesis, the laser is pulsed with 10 Hz. At this frequency each pulse has an energy of 0.5 mJ. Subsequently, the OH field is recorded with the intensified CCD camera at 10 Hz. Under these conditions, the intensifier has a shutter time of 50 ns. From the pictures taken by the camera, an average and RMS OH field is determined. 200 pictures are taken to calculate these quantities.

Species concentrations

For the steady system, reliable species concentration measurements are conducted at operating points 15.4, 15.7 and 30.7. At both operating points 15.4 and 15.7 the absolute pressure is 1.5 bars. At operating point 30.7 the absolute pressure is twice as large. The powers at the three operating points are 125 kW (15.7), 150 kW (15.4) and 250 kW (30.7). Since both the pressure and the power of operating points 15.7 and 30.7 differ by a factor 2, the velocities are equal for these two operating points. A summary of the measured data is given in table J.1. To remove ambiguity when comparing different sets of data, the NO levels are referenced to 15 percent oxygen on a dry basis [106]. For all operating points the temperature of the inlet air could be kept at 300°C, with a maximum error of 3%.

Operating point	Comb. outlet temp. [°C]	O_2 [vol%]	NO [ppm ref 15% O_2]
15.7	949	14.3	4.1
15.4	1036	13.7	3.6
30.7	1060	14.4	3.8

Table J.1: Steady-state measurements at three operating points.

The measured oxygen content in the ambient air is 20.3 vol% for the measurements at the three operating points. Burning at an air factor of 1.8, and using an equal amount of cooling air, (0.8+1.8)/(1.8+1.8)=72.2% of the total air flow is not used for combustion. So assuming complete combustion and accounting for the part of the inlet volume flow that consists of fuel, 14.4 vol% O_2 should be present in the exhaust gasses. This value compares well with the measured concentrations at all operating points, although at operating point 15.4 the measured value is somewhat lower than the calculated value. This might be due to leaking of cooling air.

The measured NO levels listed in table J.1 have an accuracy of ± 0.1 ppm. In practical situations, the most important mechanism for NO production is the so-called Zeldovich mechanism. Since the NO production via this mechanism strongly depends on the temperature, it is called thermal NO. As a result of the well-premixed reactants, the low adiabatic flame temperature, and probably most importantly, the strong heat loss through the combustor, the measured NO levels are low. In the next section it is shown that the higher the thermal power, the lower the relative heat loss. This implies that the temperature gradient through the combustor decreases with the thermal power, resulting in higher NO levels for higher powers, as can be deducted from the NO level at 250 kW (operating point 30.7). Moreover, compared to operating point 15.4, operating point 15.7 has 20% lower velocities, which increases the combustor residence time by the same amount. Consequently, NO has more time to form at operating point 15.7 compared to 15.4, which results in a higher NO level.

The NO production can be numerically estimated in a CFD simulation by solving an extra transport equation for the NO mass fraction. This transport equation calculates the thermal NO emission based on the simplified Zeldovich mechanism. In the transport equation, it is assumed that the NO production is not influenced by turbulence, i.e. a δ-PDF is employed. An adiabatic simulation at operating point 15.4, using the CFI combustion model (see chapter 7), shows a NO level of 42.8 ppm (ref 15% O_2) at the combustor exit. This level can be considered as an upper bound for the produced NO, which agrees with the lower measured values. Obviously, heat loss should be included in the CFD model to get a better approximation of the actual measured NO levels.

Heat transfer

The heat loss *to the cooling air* can be calculated by measuring the inlet and outlet temperatures of the cooling air. With the mass flow, known from the mass flow controllers, and the c_p value of air, the heat taken by the cooling air is calculated. Note that this is the heat taken by the cooling air only. The total heat loss from the combustion chamber is the sum of the heat loss to the cooling air and to the surroundings (via the pressure vessel). Based on the adiabatic flame temperature and the measured temperature at the outlet of the combustor, the total heat loss from the combustion gasses can be determined. An overview of the measured heat losses and the heat loss determined by the 1D heat transfer model [107], using the same mass flows, adiabatic temperature and inlet temperatures as in the measurements, is shown in table J.2. The heat losses are taken relative to the total heat input at the

specific operating point. The heat transferred to the surroundings is in both cases determined from the difference between the total heat loss and the heat taken by the cooling air.

Operating point	Taken by cooling air		Lost from combustor		To surroundings	
	Meas.	1D model	Meas.	1D model	Meas.	1D model
15.7	22%	19%	27%	30%	5%	11%
15.4	21%	18%	23%	27%	2%	9%
20.4	20%	18%	23%	26%	3%	8%

Table J.2: Heat balance in DESIRE setup, measured and determined with 1D heat transfer model [107].

A reasonable agreement is seen between the model and the measurements, especially considering the fact that the Nusselt correlation is used for predicting the convective heat transfer to the liner, while CFD simulations showed that especially near the flame this assumption is erroneous [107]. The relative heat loss is seen to decrease when the power is increased, a trend that is also predicted by the model. The difference between operating point 20.4 and 15.4 is not very large. Nevertheless, at operating point 15.7 significantly more heat is lost. This can be explained by the lower velocities at this operating point, which increases the residence time and therefore the heat loss.

The heat transfer model also yields temperatures at various locations. These temperatures are compared with the temperatures measured in the test rig (see table J.3). The comparison is done for operating point 10.5.

	Liner temp. [°C]	Pressure vessel temp. [°C]	Comb. outlet temp. [°C]	Cooling air outlet temp. [°C]
Meas.	516 (mean)	266 (mean)	938	269
Model	589 (max)	261 (max)	1200	294

Table J.3: Comparison between temperatures obtained with 1D heat transfer model and measured temperatures.

The largest deviation is seen in the combustor outlet temperature. Apparently the combustion air loses more heat than in the model. An explanation for this is that the convective heat transfer coefficient in reality is larger near the flame than assumed in the model. Also the flame radiates much heat directly to the surroundings via the large windows. Still, the good agreement between the liner and pressure vessel temperatures makes the model a good tool for obtaining an indication of the expected temperatures in the setup. Based on the model it is decided to use a one-to-one ratio between cooling air and combustion air for all operating points.

Technical specifications

Mass and Energy flow characteristics	
Optically accessible section followed by structurally observed section	
Air flow for combustion separated from air flow for cooling	
Minimum-maximum natural gas flow	3-15 g/s
Minimum-maximum test rig power level	35-500 kW
Safety valve release	5 bar gauge
Maximum combustion air flow	180 g/s
Maximum cooling air flow	180 g/s
Maximum air supply by compressor	360 g/s at 10 bar gauge
Air preheater nominal power	120 kW
Air inlet temperature	290-673 K
Acoustic fundamental frequency at 1600 K	$\pm$100 Hz
Burner Design	
Burner with engineering grade mixture fraction uniformity	
Radial slot air swirler followed by axial annular nozzle	
Natural gas injection at the upstream end of the nozzle through 4 holes ($D = 2$ mm)	
Nominal swirl number	0.7
Nominal power	100 kW/bar
Material	SS 310
Liner design	
Inner cross-sectional area	150x150 mm^2
Length	1.8 m
Thickness	4 mm (1.5 mm at structural section)
Natural frequency	$\pm$200 Hz
Material	SS 310
Maximum temperature	800°C
Maximum pressure	50 mbar gauge
Pressure vessel design	
Inner cross-sectional area	198x198 mm^2
Material	SS 316
Maximum temperature	400°C
Maximum pressure	5 bar gauge

Appendix K

Fuel supply line experiments

For the reconstruction of the FTF from the measurements, the fluctuating fuel mass flow at the fuel nozzle must be known. The fuel mass flow is excited by a MOOG valve, which is located at approximately 1 metre upstream of the fuel supply nozzles. Due to acoustic effects in the fuel supply line, the mass flow perturbation at the MOOG valve does not have to be equal to the mass flow perturbation at the fuel nozzles. Due to lack of space and possible disturbance of the flow, it is not possible to measure the fluctuating fuel mass flow directly at the nozzles of the DESIRE setup during a FTF measurement. For this reason a real-scale experimental model of the fuel supply is made [89] (see figure K.1).

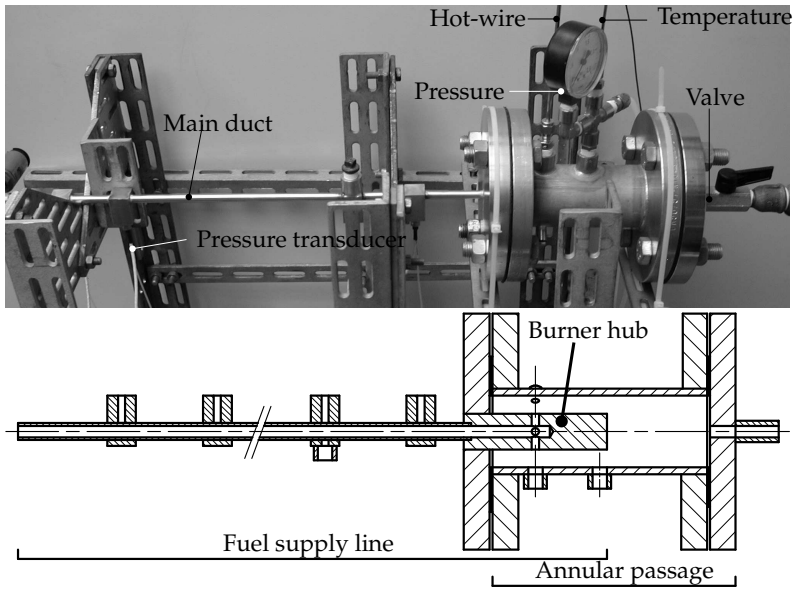

Figure K.1: Photo and cross-sectional view of the real-scale experimental model of the fuel supply line.

It can be seen that only the annular passage of the burner is included in the experimental model. Simulated experiments with the acoustic network model showed that the combustion chamber, downstream the annular burner passage, hardly influences the acoustic fluctuations at the fuel nozzles [89]. The high velocities and pressure drop prevent acoustic waves to significantly propagate in the fuel supply line.

In the real-scale model, the mass flow perturbation at the fuel nozzles has been reconstructed from the pressure fluctuation measured by a pressure transducer in the annular passage. The relationship between pressure fluctuations and mass flow fluctuations at the fuel nozzles is explained with the help of a schematic view of the annular passage in which the fuel nozzles exit (see figure K.2). A fluctuating mass flow M'_f enters the annular passage. The pressure perturbation p' in the annular passage is measured with a Kulite pressure transducer. The annular passage has a volume V and the flow exits the annular passage via a nozzle. The flow in the nozzle is (near) choking, so an acoustic reflection coefficient of 1 is assumed at this exit.

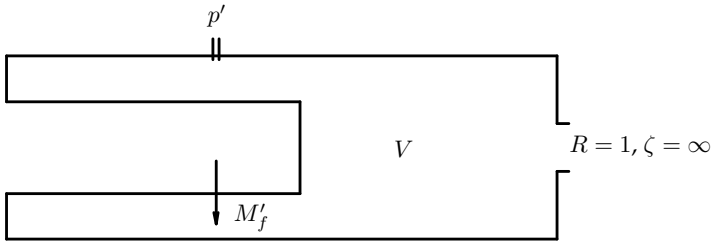

Figure K.2: Schematic view of the annular passage

The dimensions of the annular passage are small compared to the acoustic wavelengths in the considered frequency range. This means that a quasi-steady acoustic approach can be used to transform the measured pressure to the velocity perturbation at the fuel nozzles.

Integrating the mass conservation equation over the volume of the annular passage gives:

$$\int_V \left[\frac{\partial \rho}{\partial t} + \bigtriangledown \cdot (\rho \mathbf{u})\right] \mathrm{d}V \approx V\frac{\mathrm{d}\rho}{\mathrm{d}t} + \int_V \bigtriangledown \cdot \rho \mathbf{u} \mathrm{d}V = 0 \tag{K.1}$$

where the quasi-steady assumption is used that the density does not depend on the location (i.e. no standing waves). Applying the Gauss theorem yields:

$$V\frac{\mathrm{d}\rho}{\mathrm{d}t} + \oint_S \rho \mathbf{u} \cdot \mathbf{n} \mathrm{d}S = 0 \tag{K.2}$$

The cross sectional areas S_{in} and S_{out} are defined as the total area of the four fuel nozzles and the area of the exit of the passage, respectively. Similarly, u_{in} and u_{out} are the velocity perpendicular to the exit of the fuel nozzles and to the exit of the passage, respectively. Equation K.2 can now be written as:

$$V\frac{\mathrm{d}\rho}{\mathrm{d}t} + \rho(u_{out}S_{out} - u_{in}S_{in}) = 0 \tag{K.3}$$

Linearising this equation and assuming a harmonic time dependence gives:

$$V\mathrm{i}\omega\rho' - \rho u'_{in} S_{in} = 0 \tag{K.4}$$

The velocity perturbation at the outlet completely disappears since an acoustic reflection coefficient of 1 was assumed.

Using the isentropic relationship between the acoustic pressure and density ($p'/\rho' = c_0^2$), this can be rewritten as:

$$\frac{V\mathrm{i}\omega}{c_0^2} p' - \rho u'_{in} S_{in} = 0 \tag{K.5}$$

Hence, the velocity fluctuation can be written as:

$$u'_{in} = \frac{V\mathrm{i}\omega}{\rho S_{in} c_0^2} p' \tag{K.6}$$

With this equation, the measured pressure can be converted to the velocity perturbation at the fuel nozzle exit.

Using a pressure transducer appears to yield more reliable data than measuring the velocity fluctuation downstream the nozzles with a hot-wire sensor. When a hot-wire would be used, a few assumptions are made: constant velocity profile in radial direction at any moment within a period of oscillation, rotational symmetry and an incompressible flow. These assumptions can break down. Firstly, the Nusselt number at the hot-wire is different for pulsated flows, as the boundary layer is modified. Secondly, the velocity profile can change as a function of the frequency. Both effects can influence the velocity measured by the hot-wire. Therefore the mass flow perturbation reconstructed from the measured unsteady pressure is more reliable.

An example of the transfer function between the displacement of the MOOG valve piston and the reconstructed velocity perturbation at the fuel nozzles, indicated here as H_{um}, obtained at operating point 15.7 is shown in figure K.3. The transfer is determined at discrete frequencies by using sinus excitation. Although the resolution with this type of excitation is less than with, for example, a sinus sweep excitation, the coherence is perfect, even for lower frequencies.

The phase shift that is noticed between the MOOG piston displacement and the velocity fluctuation at the fuel nozzle is almost perfectly linear. This shows that there is constant time delay between the two locations. Using the length of the fuel supply line and the sum of the speed of sound and the convection speed, the time delay should be 4.2 ms. The time delay derived from the phase is 4.4 ms. This corresponds well with the calculated delay.

In the FTF measurements, it is attempted to have an equal perturbation amplitude of the fuel mass flow at all considered frequencies. Since the displacement of the MOOG piston decreases at higher frequencies (see figure 6.7(b)), the excitation of the MOOG valve has to increase with the frequency to achieve the same displacement of the MOOG piston. Additionally, the fuel supply line transfers show a frequency dependent response of the velocity perturbation at the fuel nozzles. This implies that the MOOG excitation should be frequency dependent as well to have the same velocity perturbation at the fuel nozzles. The level of excitation that can be reached

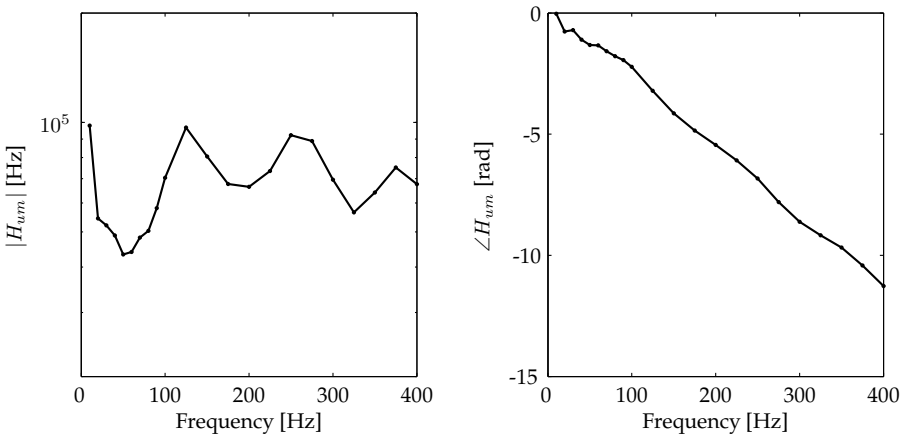

(a) Amplitude (b) Phase

Figure K.3: Fuel supply line transfer function. The displayed transfer is measured under the conditions of operating point 15.7 (125 kW at 1.5 bars).

is limited though: it is bounded by the maximum displacement of the MOOG piston. When a constant amplitude of 5% of the mean fuel mass flow is desired, the required excitation amplitude of the MOOG valve is shown in figure K.4 for a power of 125 and 150 kW, both at 1.5 bars. In this figure, an additional line is displayed, showing the excitation at which the maximum piston displacement is reached. This is a bound for the maximum excitation that can be achieved. Figure K.5 shows the

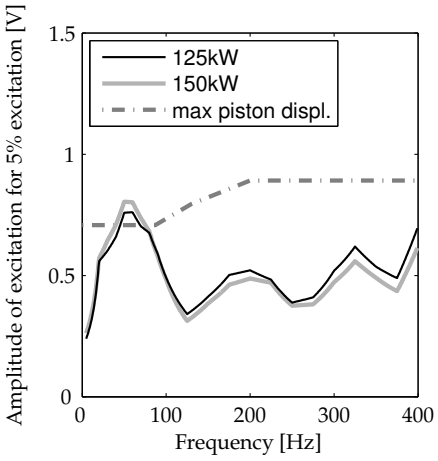

Figure K.4: Excitation amplitude at velocity perturbation of 5%.

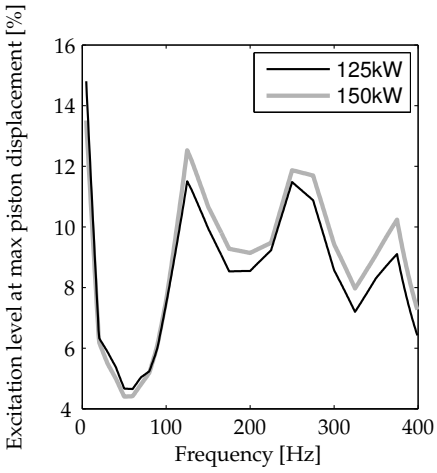

Figure K.5: Maximum velocity perturbation that can be physically reached with the MOOG valve.

maximum level of excitation for both powers.

To show that an excitation of 5% is still in the (approximate) linear regime of the fuel supply line, the amplitudes of the reconstructed relative velocity fluctuation and the piston displacement are plotted as a function of the excitation level in Volts (see figure K.6(a), the MOOG valve is driven with a frequency of 200 Hz). The situation of operating point 15.7 is considered here. In the figure, the piston displacement is normalised such that it coincides with the velocity amplitude at the lowest excitation.

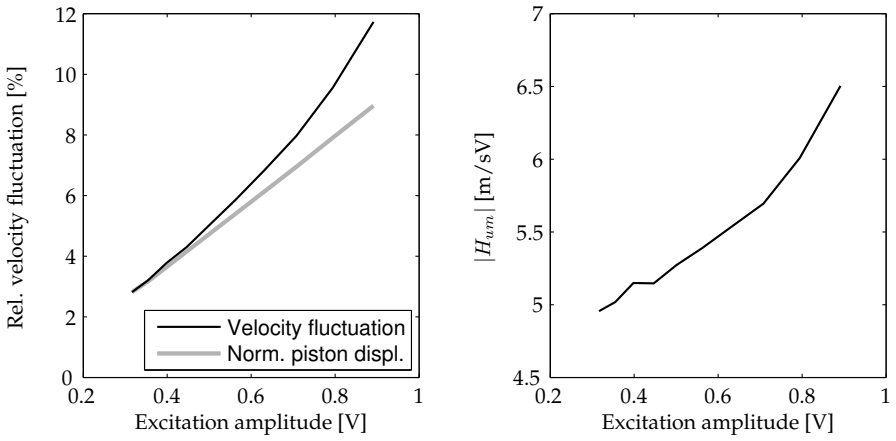

(a) Amplitude (b) Transfer

Figure K.6: Amplitudes and transfers as a function of the MOOG excitation level.

It can be seen that non-linear behaviour commences quite soon. A velocity fluctuation of 5% is considered as the maximum level at which the fuel supply line behaviour can be considered linear. The non-linear behaviour is also seen when considering the transfer function between the MOOG displacement in Volts and the reconstructed velocity fluctuation, again measured as a function of the excitation amplitude in Volts (see figure K.6(b)). The figure shows that the transfer function increases with almost 18% when doubling the excitation level, while it should remain constant for linear systems.

Using the procedure described in this appendix, the transfer function H_{um} is measured at the operating points at which the FTF is determined. The measured transfers are used during the unsteady measurement to calculate the fuel mass flow perturbation from the known displacement of the MOOG valve.

Bibliography

[1] N.H. Abel. Auflösung einer mechanischen Aufgabe. *Journal für die reine und angewandte Mathematik*, 1(2), 1826.

[2] A.C. Antoulas and D.C. Sorensen. Approximation of large-scale dynamical systems: an overview. *Int. Journal Appl. Math. Comput. Sci.*, 11(5):1093–1121, 2001.

[3] C.A. Arana, B. Sekar, M.A. Mawid, and C.B. Graves. Determination of thermoacoustic response in a demonstrator gas turbine engine. *Journal of Engineering for Gas Turbines and Power*, 124:46–57, 2002.

[4] G.B. Ashcroft, K. Takeda, and X. Zhang. A numerical investigation of the noise radiated by a turbulent flow over a cavity. *Journal of Sound and Vibration*, 265:43–60, 2003.

[5] Z. Baj. Krylov subspace techniques for reduced-order modeling of large-scale dynamical systems. *Applied Numerical Mathematics*, 43:9–44, 2002.

[6] R. Balachandran, A.P. Dowling, and E. Mastorakos. Response of turbulent premixed flames subjected to inlet velocity and equivalence ratio perturbations. In *Proceedings of the European Combustion Meeting 2005*, 2005.

[7] D.W. Bechert. Sound absorption caused by vorticity shedding, demonstrated with a jet flow. *Journal of the Acoustical Society of America*, 70(3):389–405, 1980.

[8] J.M. Beér and N.A. Chigier. *Combustion aerodynamics*. Applied Science Publishers Ltd, London, 1972.

[9] V. Bellucci, B. Schuermans, D. Nowak, P. Flohr, and C.O. Paschereit. Thermoacoustic modeling of a gas turbine combustor equipped with acoustic dampers. In *Proceedings of ASME Turbo Expo 2004. 2004 Power for Land, Sea, and Air. Vienna, Austria, June 14-17, 2004*, volume GT2004-53977, 2004.

[10] W.M. Beltman. *Viscothermal wave propagation including acousto-elastic interaction*. PhD thesis, University of Twente, 1998.

[11] D. Bernier, S. Ducruix, F. Lacas, S. Candel, N. Robart, and T. Poinsot. Transfer function measurements in a model combustor: Application to adaptive instability control. *Combustion Science and Technology*, 175:993–1013, 2003.

[12] D.A. Bies and C.H. Hansen. *Engineering Noise Control, theory and practice*. E&FN SPON, London, 1996.

[13] R.B. Bird, W.E. Stewart, and E.N. Lightfoot. *Transport phenomena*. John Wiley and Sons, New York, 1960.

[14] R.D. Blevins. *Applied Fluid Dynamics Handbook*. Van Nostrand Reinhold Company Inc., New York, 1984.

[15] D. Bohn, G. Deutsch, and U. Kruger. Numerical prediction of the dynamical behavior of turbulent diffusion flames. *Journal of Engineering for Gas Turbines and Power*, 120:713–720, 1998.

[16] S. Boij and B. Nilsson. Reflection of sound at area expansions in a flow duct. *Journal of Sound and Vibration*, 260:477–498, 2003.

[17] S. Boij and B. Nilsson. Scattering and absorption of sound at duct expansions. *Journal of Sound and Vibration*, 289:577–594, 2006.

[18] P. Boineau and Y. Gervais. Turbulent flame acoustic power spectrum determination. *Acoustics, waves, vibrations*, 326(IIb):747–754, 1998.

[19] R.J.J. Boot. Het aeroakoestisch gedrag van diafragma's. Master's thesis, Technische Universiteit Eindhoven, 1995.

[20] R. Borghi. Turbulent combustion modelling. *Progress in Energy and Combustion Science*, 14:245–292, 1988.

[21] G. Bosch and W. Rodi. Simulation of vortex shedding past a square cylinder with different turbulence models. *International Journal for Numerical Methods in Fluids*, 28:601–616, 1998.

[22] L. Boyer and J. Quinard. On the dynamics of anchored flames. *Combustion and Flame*, 82(1):51–65, 1990.

[23] K.N.C. Bray. Turbulent transport in flames. *Proceedings: Mathematical and Physical Sciences*, 451:231–256, 1941.

[24] G. Cabot, D. Vauchelles, B. Taupin, and A. Boukhalfa. Experimental study of lean premixed turbulent combustion in a scale gas turbine chamber. *Experimental Thermal and Fluid Science*, 28, 2004.

[25] S.M. Candel and T.J. Poinsot. Interactions between acoustics and combustion. *Proceedings of The Institute of Acoustics*, 10(2):103–153, 1988.

[26] T. J. Cavicchi. *Digital signal processing*. John Wiley & Sons, Inc. New York, 2000.

[27] CERFACS. CERFACS - CFD Team, `http://www.cerfacs.fr/cfd/`, (Accessed 9/29/2005).

[28] P. Chatterjee, U. Vandsburger, W.R. Saunders, V.K. Khanna, and W.T. Baumann. On the spectral characteristics of a self-excited Rijke tube combustor – numerical simulation and experimental measurements. *Journal of Sound and Vibration*, 283:573–588, 2005.

[29] W.S. Cheung, G.J.M. Sims, R.W. Copplestone, J.R. Tilston, C.W. Wilson, S.R. Stow, and A.P. Dowling. Measurement and analysis of flame transfer function in a sector combustor under high pressure conditions. *Proceedings of ASME TURBO EXPO 2003, 2003-GT-38219*, pages 1–8, 2003.

[30] N.A. Chigier and J.M. Beér. Velocity and static-pressure distributions in swirling jets issuing from annular and divergent nozzles. *Transactions of the ASME–Journal of Basic Engineering*, 86:788796, 1964.

[31] J.H. Cho and T.C. Lieuwen. Modeling the response of premixed flames to mixture ratio perturbations. *Proceedings of ASME TURBO EXPO 2003*, 2003.

[32] J.H. Cho and T.C. Lieuwen. Laminar premixed flame response to equivalence ratio oscillations. *Combustion and Flame*, 140:116–129, 2005.

[33] E.W. Christiansen, S.D. Tse, and C.K. Law. A computational study of the oscillatory extinction of spherical diffusion flames. *Combustion and Flame*, 134:327–337, 2003.

[34] J.M. Cohen, B.E. Wake, and D. Choi. Investigation of instabilities in a lean premixed step combustor. *Journal of Propulsion and Power*, 19(1):81–88, 2003.

[35] D.G. Crighton, A.P. Dowling, J.E. Ffowcs Williams, M. Heckl, and F.G. Leppington. *Modern methods in analytical acoustics*. Springer-Verlag, London, 1992.

[36] L. Crocco. Aspects of combustion instability in liquid propellant rockets motors. Part i. *Journal of the American Rocket Society*, 21:163–178, 1951.

[37] L. Crocco. Aspects of combustion instability in liquid propellant rockets motors. Part ii. *Journal of the American Rocket Society*, 22:11–26, 1952.

[38] S. Crocker, D. Nickoluas, D. Smith, and E. Clifford. CFD modeling of a gas turbine combustor from compressor exit to turbine inlet. *ASME paper 98-GT-184*, 1998.

[39] S. Dawson and J.A. Fitzpatrick. Measurement and analysis of thermoacoustic oscillations in a simple dump combustor. *Journal of Sound and Vibration*, 230(3):649–660, 2000.

[40] J.E. Dec and J.O. Keller. Pulse combustor tail-pipe heat-transfer dependence on frequency, amplitude, and mean flow rate. *Combustion and Flame*, 77(3-4):359–374, 1989.

[41] M.A.F. Derksen. *On the influence of steam on combustion*. PhD thesis, University of Twente, 2005.

[42] E. Deuker. *Ein Beitrag zur Vorausberechnung des akustischen Stabilitätsverhalten von Gasturbine-Brennkammern mittels theoretischer und experimenteller Analyse von Brennkammerschwingungen*. PhD thesis, RWTH Aachen, 1995.

[43] J.J. Dongarra, S. Hammarling, and D.W. Walker. Key concepts for parallel Out-Of-Core LU factorization. *Parallel Computing*, 23:49–70, 1997.

[44] A.P. Dowling. The calculation of thermoacoustic oscillations. *Journal of Sound and Vibration*, 180(4):557–581, 1995.

[45] A.P. Dowling. A kinematic model of a ducted flame. *Journal of Fluid Mechanics*, 394:51–72, 1999.

[46] A.P. Dowling. Singing flames - the coupling of acoustics and combustion. In *Tenth International Congress on Sound and Vibration*, 2003.

[47] A.P. Dowling and A.S. Morgans. Feedback control of combustion oscillations. *Annu. Rev. Fluid Mech.*, 37:151–82, 2005.

[48] I.D.J. Dupère and A.P. Dowling. The absorption of sound near abrupt axisymmetrix area expansions. *Journal of Sound and Vibration*, 239(4):709–730, 2001.

[49] P. Durrieu, G. Hofmans, G. Ajello, R. Boot, Y. Euregan, A. Hirschberg, and M.C.A.M. Peters. Quasisteady aero-acoustic response of orifices. *Journal of the Acoustical Society of America*, 110(4):1859–1872, 2001.

[50] B. Eck. *Ventilatoren. Entwurf und Betrieb der Radial-,Axial- und Querstromventilatoren*. Springer-Verlag, Berlin-Heidelberg-New York, 1972.

[51] M. Elsari and A. Cummings. Combustion oscillations in gas fired appliances: Eigenfrequencies and stability regimes. *Applied Acoustics*, 64:565–580, 2003.

[52] C.A. Fannin. *Linear modeling and analysis of thermoacoustic instabilities in a gas turbine combustor*. PhD thesis, Virginia Polytechnic Institute and State University, 2000.

[53] E.C. Fernandes. *The onset of combustion-driven acoustic oscillations*. PhD thesis, Universidade Technica de Lisboa, 1998.

[54] G.F. Franklin, J.D. Powell, and A. Emami-Naeini. *Feedback control of dynamic systems*. Addison-Wesley Publishing Company, third edition, 1994.

[55] K. Gallivan, E. Grimme, and P. van Dooren. A rational Lanczos algorithm for model reduction. *Numerical Algorithms*, 12(1-2):33–63, 1996.

[56] Th.M. Geerssen. *Physical properties of natural gases*. N.V. Nederlandse Gasunie, third edition, 1988.

[57] A. Gentemann, C. Hirsch, K. Kunze, T. Sattelmayer, and W. Polifke. Validation of flame transfer function reconstruction for perfectly premixed swirl flames. In *Proceedings of ASME Turbo Expo 2004. 2004 Power for Land, Sea, and Air. Vienna, Austria, June 14-17, 2004*, volume GT2004-53776, 2004.

[58] J.R. Gilbert and S. Toledo. High-performance out-of-core sparse LU factorization. In *Proceedings of the 9th SIAM Conference on Parallel Processing for Scientific Computing*, 1999.

[59] G.H. Golub and C.F. van Loan. *Matrix computations*. The Johns Hopkins University Press, third edition, 1996.

[60] E. Grimme. *Krylov projection methods for model reduction*. PhD thesis, University of Illinois at Urbana-Champaign, 1997.

[61] E.J. Grimme, D.C. Sorensen, and P. van Dooren. Model reduction of state space systems via an Implicitly Restarted Lanczos method. *Numerical Algorithms*, 12:1–31, 1995.

[62] A.K. Gupta, D.G. Lilley, and N. Syred. *Swirl Flows*. Abacus Press, 1984.

[63] D.L. Gysling, G.S. Copeland, D.C. McCormick, and W.M. Proscia. Combustion system damping augmentation with helmholtz resonators. *Journal of Engineering for Gas Turbines and Power*, 122(2):269–274, 2000.

[64] Y. Hardalupas and M. Orain. Local measurements of the time-dependent heat release rate and equivalence ratio using chemiluminescent emission from a flame. *Combustion and Flame*, 139:188–207, 2004.

[65] M. Harleman. Characterizing flame behavior in a lean premixed turbulent methane burner with optical techniques. Master's thesis, University of Twente, 2005.

[66] M.A. Heckl. Active control of the noise from a Rijke tube. *Journal of Sound and Vibration*, 124(1):117–133, 1988.

[67] H. Herlufsen. *Dual Channel FFT Analysis (Part 1)*. Number 1 in Technical Review. Bruel & Kjaer, 1984.

[68] M. Hettel, H. Buchner, P. Habisreuther, H. Bockhorn, and N. Zarzalis. Modelling of flame frequency response of turbulent premixed flames. In *Proceeding of the European Combustion Meeting 2003*, 2003.

[69] N. Hettel, P. Habisreuther, and H. Bockhorn. Unsteady Reynolds-averaged Navier-Stokes (URANS) modeling of flame transfer functions of turbulent premixed jet flames. In *Twelfth International Congress on Sound and Vibration*, 2005.

[70] D.A. Hobson, J.E. Fackrell, and G. Hewitt. Combustion instabilities in industrial gas turbines – Measurements on operating plant and thermoacoustic modeling. *ASME*, 122, 2000.

[71] G.C.J. Hofmans. *Vortex Sound in Confined Flows*. PhD thesis, TU Eindhoven, 1998.

[72] G.C.J. Hofmans, R.J.J. Boot, P.P.J.M. Durrieu, and Y. Auregan A. Hirschberg. Aeroacoustic response of a slit-shaped diaphragm in a pipe at low Helmholtz number, 1:Quasi-steady results. *Journal of Sound and Vibration*, 244(1):35–56, 2001.

[73] S.M.R. Hosseini and C.J. Lawn. Non-linearities in the thermo-acoustic response of a premixed swirl burner. In *Twelfth International Congress on Sound and Vibration*, 2005.

[74] S. Hubbard and A.P. Dowling. Acoustic resonances of an industrial gas turbine combustion system. *Journal of Engineering for Gas Turbines and Power*, 123(4):766–773, 2001.

[75] R.A. Huls. *To be published*. PhD thesis, University of Twente, 2006.

[76] R.A. Huls, A. de Boer, and J.B.W. Kok. A transfer function approach to structural vibrations induced by thermoacoustic sources. In *Eleventh International Congress on Sound and Vibration*, 2004.

[77] R.A. Huls, A. de Boer, and J.B.W. Kok. Experimental validation of the interaction between combustion and structural vibration. In *Twelfth International Congress on Sound and Vibration*, 2005.

[78] R.A. Huls, J.B.W. Kok, and A. de Boer. Vibration of the liner in an industrial combustion system due to an acoustic field. In *International Forum on Structural Dynamics and Aeroelasticity*, 2003.

[79] R.A. Huls, J.F. van Kampen, J.B.W. Kok, and A. de Boer. Fluid structure interaction to predict liner vibrations in an industrial combustion system. In *Tenth International Congress on Sound and Vibration*, 2003.

[80] J.-G. Ih, C.-M. Park, and H.-J. Kim. A model for sound propagation on capillary ducts with mean flow. *Journal of Sound and Vibration*, 190(2):163–175, 1996.

[81] U. Ingard and V.K. Singhal. Sound attenuation in turbulent pipe flow. *Journal of the Acoustical Society of America*, 55(3):535–538, 1974.

[82] J. Janicka and W. Kollmann. A two-variable formalism for the treatment of chemical reactions in turbulent H_2-air diffusion flames. In *17^{th} symposium (International) on Combustion, The Combustion Institute, Pittsburg, USA*, pages 421–430, 1979.

[83] J. Janicka and W. Kollmann. The calculation of mean radical concentractions in turbulent diffusion flames. *Combustion and Flame*, 44:319–336, 1982.

[84] W.M. Kays. Turbulent Prandtl number - where are we? *Journal of Heat Transfer*, 116(2):284–295, 1994.

[85] L. Khezzar. Velocity measurements in the near field of a radial swirler. *Experimental Thermal and Fluid Science*, 16:230–236, 1998.

[86] J. Kim, P. Moin, and R. Moser. Turbulence statistics in fully developed channel flow at low Reynolds number. *Journal of Fluid Mechanics*, 177:133–166, 1987.

[87] L.V. King. On the convection of heat from small cylinders in a stream of fluid. *Philosphical Transactions of the Royal Society*, A214:373–432, 1914.

[88] S.A. Klein. *On the acoustics of turbulent non-premixed flames*. PhD thesis, University of Twente, 2000.

[89] J.H. Kleinlugtenbelt. Acoustic flow oscillations in fuel supply lines. Technical report, University of Twente, 2005.

[90] J.B.W. Kok, J.J.J. Louis, and J.H. Yu. The IRST model for turbulent premixed nonadiabatic flames. *Combustion Science and Technology*, 149:225–247, 1999.

[91] J.B.W. Kok and S. van der Wal. Mixing in T-junctions. *Applied Mathematical Modelling*, 20:232–243, 1996.

[92] M.F.J. Koolloos. *Behaviour of low porosity microcracked thermal barrier coatings under thermal loading*. PhD thesis, Technische Universiteit Eindhoven, 2001.

[93] V.N. Kornilov, K.R.A.M. Schreel, and L.P.H. de Goey. Experimental transfer function of acoustically perturbed Bunsen-type flame. In *Proceedings of the European Combustion Meeting 2005*, 2005.

[94] W. Krebs. EU Project DESIRE: Status presentation. In *CAME-GT Combustion Workshop, Stuttgart*, 2003.

[95] W. Krebs, R. Walterskotter, P. Flohr, G. Walz, and S. Hoffman. Effect of burner design parameters on thermoacoustic stability of annular gas turbine combustors. In G.G. Hirs, editor, *ECOS 2000, Biomass, coal and oil gasification and acoustic of combustion*, volume 4. University of Twente, 2000.

[96] U. Krüger, J. Hüren, S. Hoffmann, W. Krebs, P. Flohr, and D. Bohn. Prediction and measurement of thermoacoustic improvements in gas turbines with annular combustion systems. *Journal of Engineering for Gas Turbines and Power*, 123(3):557–566, 2001.

[97] C. Külsheimer and H. Büchner. Combustion dynamics of turbulent swirling flames. *Combustion and Flame*, 131:70–84, 2002.

[98] K. Kunze, C. Hirsch, and T. Sattelmayer. Transfer function measurements on a swirl stabilized premix burner in an annular combustion chamber. In *Proceedings of ASME Turbo Expo 2004. 2004 Power for Land, Sea, and Air. Vienna, Austria, June 14-17, 2004*, volume GT2004-53106, 2004.

[99] J.C. Lagarias, J.A. Reeds, M.H. Wright, and P.E. Wright. Convergence properties of the Nelder-Mead Simplex method in low dimensions. *SIAM Journal of Optimization*, 9(1):112–147, 1998.

[100] S.H. Lam. *Recent advances in the aerospace sciences*, chapter Singular perturbation for stiff equations using numerical methods, pages 3–20. Plenum Press, New York and London, 1985.

[101] S.H. Lam and D.A. Goussis. The CSP method for simplifying kinetics. *International Journal of Chemical Kinetics*, 26:461–486, 1994.

[102] B.E. Launder and B.I. Sharma. Application of the energy-dissipation model of turbulence to the calculation of flow near a spinning disc. *Letters in Heat and Mass Transfer*, 1:131–138, 1974.

[103] J. Lavrentjev, M. Åbom, and H. Bodén. A measurement method for determining the source data of acoustic two-port sources. *Journal of Sound and Vibration*, 183(3):517–531, 1995.

[104] C.J. Lawn. Interaction of the acoustic properties of a combustion chamber with those of premixture supply. *Journal of Sound and Vibration*, 224(5):785–808, 1999.

[105] J. LeConte. On the Influence of Musical Sounds on the Flame of a Jet of Coal Gas. *American Journal of Science and Arts*, 23(2):62–67, 1858.

[106] A.H. Lefebvre. *Gas turbine combustion*. Taylor and Francis, second edition, 1998.

[107] U. Lekic and J.F. van Kampen. Heat transfer in the DESIRE-test rig. Technical report, University of Twente, 2002. Internal report, can be obtained at the section Thermal Engineering.

[108] T. Lieuwen and B.T. Zin. The role of equivalence ratio oscillations in driving combustion instabilities in low NOx gas turbines. In *Proceedings of the Twenty Seventh Symposium on Combustion*, pages 1809–1816. The Combustion Institute, 1998.

[109] T.C. Lieuwen. *Investigation of Combustion Instability Mechanisms in Premixed Gas Turbines*. PhD thesis, Georgia Institute of Technology, 1999.

[110] T.C. Lieuwen. Experimental investigation of limit-cycle oscillations. *Journal of Propulsion and Power*, 18:61–67, 2002.

[111] T.C. Lieuwen, Y. Neumeier, and B.T. Zinn. The role of unmixedness and chemical kinetics in driving combustion instabilities in lean premixed combustors. *Combustion Science and Technology*, 135:193–211, 1998.

[112] M.J. Lighthill. On sound generated aerodynamically. I. General theory. *Proceedings of the Royal Society of London. Series A, Mathematical and Physical Sciences*, 211(1107):564–587, 1952.

[113] M.J. Lighthill. On sound generated aerodynamically. II. Turbulence as a source of sound. *Proceedings of the Royal Society of London. Series A, Mathematical and Physical Sciences*, 222(1148):1–32, 1954.

[114] M.J. Lighthill. The Bakerian lecture, 1961. Sound generated aerodynamically. *Proceedings of the Royal Society of London. Series A, Mathematical and Physical Sciences*, 267(1329):147–182, 1962.

[115] G.M. Lilley. The source of aerodynamic noise. *International Journal of Aeroacoustics*, 2(3-4):241–253, 2003.

[116] P.B. Lindley. *Engineering design with natural rubber*. The Malaysian Rubber Producers' Research Association, fourth edition, 1974.

[117] A.N. Lipatnikov and P. Sathiah. Effects of turbulent flame development on thermoacoustic oscillations. *Combustion and Flame*, 142:130–139, 2005.

[118] J.J.J. Louis. *On turbulent combustion of coal gas*. PhD thesis, University of Twente, 1997.

[119] J.J.J. Louis, J.B.W. Kok, and S.A. Klein. Modeling and measurements of a 16-kW turbulent nonadiabatic syngas diffusion flame in a cooled cylindrical combustion chamber. *Combustion and Flame*, 125(1-2):1012–1031, 2001.

[120] J.R. Mahan, A. Karchmer, and H.H. Hubbard (editor). *Aeroacoustics of Flight Vehicles, Theory and Practice–Volume 1: Noise Sources*, chapter Combustion and core noise, pages 483–517. NASA Reference Publication 1258, 1991.

[121] M. Marrone. Computational aspects of the cell method in electrodynamics. *Progress in Electromagnetics Research*, 32:317–356, 2001.

[122] A. Massias, D. Diamantis, E. Mastorakos, and D.A. Goussis. An algorithm for the construction of global reduced mechanisms with csp data. *Combustion and Flame*, 117:685–708, 1999.

[123] K.R. McManus, T. Poinsot, and S.M. Candel. A review of active control of combustion instabilities. *Prog. Energy Combust. Sci.*, 19:1–29, 1993.

[124] C.L. Morfey. Acoustic energy in non-uniform flows. *Journal of Sound and Vibration*, 14:159–170, 1971.

[125] H.N. Najm, P.H. Paul, C.J. Mueller, and P.S. Wyckoff. On the adequacy of certain experimental observables as measurements of flame burning rate. *Combustion and Flame*, 113(3):312–332, 1998.

[126] W.B. Ng, K.J. Syed, and Y. Zhang. The study of flame dynamics and structures in an industrial-scale gas turbine combustor using digital data processing and computer vision techniques. *Experimental Thermal and Fluid Science*, 29:715–723, 2005.

[127] F. Nicoud and T. Poinsot. Thermoacoustic instabilities: Should the Rayleigh criterion be extend to include entropy changes? *Combustion and Flame*, 142:153–159, 2005.

[128] C. Pankiewitz and T. Sattelmayer. Hybrid methods for modelling combustion instabilities. In *Tenth International Congress on Sound and Vibration*, 2003.

[129] S. Park, A. Annaswamy, and A. Ghoniem. Heat release dynamics modeling of kinetically controlled burning. *Combustion and Flame*, 128:217–231, 2002.

[130] C.O. Paschereit, B. Schuermans, W. Polifke, and O. Mattson. Measurement of transfer matrices and source terms of premixed flames. *Journal of Engineering for Gas Turbines and Power*, 124:239–247, 2002.

[131] T. Penzl. *LYAPACK Users' Guide*, 2000.

[132] T. Penzl. LYAPACK, `http://www.tu-chemnitz.de/sfb393/lyapack/`, (Accessed 12/27/2005).

[133] N. Peters. *Turbulent combustion*. Cambridge University Press, 2000.

[134] A.D. Pierce. *Acoustics, An introduction to its physical principles and applications*. Acoustic Society of America, New York, 1994.

[135] T. Poinsot and D. Veynante. *Theoretical and Numerical Combustion*. Edwards, Philadelphia, second edition, 2005.

[136] W. Polifke, A. Poncet, C.O. Paschereit, and K.Döbbeling. Reconstruction of acoustic transfer matrices by instationary computational fluid dynamics. *Journal of Sound and Vibration*, 245(3):483–510, 2001.

[137] S.B. Pope. *Turbulent Flows*. Cambridge University Press, 2000.

[138] S. Prakash, S. Nair, T.M. Muruganandam, Y. Neumeier, T. Lieuwen, J. Seitzman, and B.T. Zinn. Acoustic sensing and mitigation of lean blow out in premixed flames. *AIAA 2005-1420, 43rd Aerospace sciences meeting, Reno, NV*, 2005.

[139] F. Put. *Numerical simulation of condensation in transonic flows*. PhD thesis, University of Twente, 2003.

[140] A.A. Putnam. *Combustion-driven oscillation in industry*. American Elsevier, New York, 1971.

[141] A.A. Putnam, F.E. Belles, and J.A.C. Kentfield. Pulse combustion. *Progress in Energy and Combustion Science*, 12(1):43–79, 1986.

[142] R. Rajaram and T. Lieuwen. Parametric studies of acoustic radiation from premixed flames. *Combustion Science and Technology*, 175(12):2269–2298, 2003.

[143] J.W.S. Rayleigh. The Explanation of certain Acoustical Phenomena. *Nature*, XVIII:319–321, 1878.

[144] J.W.S. Rayleigh. *The theory of sound*, volume II. Dover publications, New York, 2^{th} edition, 1896.

[145] G.A. Richards and M.C. Janus. Characterization of oscillations during premix gas turbine combustion. *Transactions of the ASME*, 120:294–302, 1998.

[146] G.A. Richards, M.J. Yip, E. Robey, L. Cowell, and D. Rawlins. Combustion oscillation control by cyclic fuel injection. *Journal of Engineering for Gas Turbines and Power*, 119:340–343, 1997.

[147] S.W. Rienstra. Sound transmission in slowly varying circular and annular lines ducts with flow. *Journal of Fluid Mechanics*, 380:279–296, 1999.

[148] S.W. Rienstra and A. Hirschberg. *An introduction to acoustics*. Available from `http://www.win.tue.nl/~sjoerdr/papers/`, 2002.

[149] P.L. Rijke. Notiz uber eine neue art, die luft in einer an beiden enden offenen Rohre in schwingungen zu versetzen. *Annalen der Physik*, 107:339343, 1859.

[150] F.J.J. Rosendal. *Swirling flows in expanding tubes*. PhD thesis, University of Twente, 1993.

[151] S. Roux, G. Lartigue, T. Poinsot, U. Meier, and C. Bérat. Studies of mean and unsteady flow in a swirled combustor using experiments, acoustic analysis and large eddy simulations. *Combustion and Flame*, 141:40–54, 2005.

[152] M. Salikuddin, R. Burrin, and W. Brown. Design and characterisation of a high temperature and high frequency infinite line pressure probe. In *AIAA 12 Aeroacoustics Conference, San Antonio, Texas*, 1989.

[153] P. Sathiah, A. Lipatnikov, and J. Chomiak. A numerical study of effects of turbulent flame structures on ducted flame oscillations. In *Tenth International Congress on Sound and Vibration*, 2003.

[154] P. Sathiah, A. Lipatnikov, and J. Chomiak. A numerical study of effects of turbulent flame speed development on ducted flame oscillations. In *Eleventh International Congress on Sound and Vibration*, 2004.

[155] T. Sattelmayer. Influence of the combustor aerodynamics on combustion instabilities from equivalence ratio fluctuations. *ASME Paper*, GT2000-0082, 2000.

[156] T. Sattelmayer and W. Polifke. Assesment of methods for the computation of the linear stability of combustors. *Combustion Science and Technology*, 175:453–476, 2003.

[157] T. Sattelmayer and W. Polifke. A novel method for the computation of the linear stability of combustors. *Combustion Science and Technology*, 175:477–497, 2003.

[158] H. Schimmer and D. Vortmeijer. Acoustical oscillation in a combustion system with a flat flame. *Combustion and Flame*, 28:17–24, 1977.

[159] J.U. Schlüter. Large-eddy simulations of combustion instability suppression by static turbulence control. *Center for Turbulence research, annual research briefs*, pages 119–130, 2001.

[160] G.E. Schneider and M.J. Raw. Control volume finite-element method for heat transfer and fluid flow using colocated variables. *Numerical Heat Transfer*, 11:363–390, 1987.

[161] B. Schuermans, V. Bellucci, F. Guethe, F. Meili, P. Flohr, and C.O. Paschereit. A detailed analysis of thermoacoustic interaction mechanisms in a turbulent premixed flame. In *Proceedings of ASME Turbo Expo 2004. 2004 Power for Land, Sea, and Air. Vienna, Austria, June 14-17, 2004*, volume GT2004-53831, 2004.

[162] B. Schuermans, H. Luebcke, and P. Flohr. Analysis of combustion instabilities using unsteady CFD with frequency dependent impedances. In *Twelfth International Congress on Sound and Vibration*, 2005.

[163] T. Schuller, D. Durox, and S. Candel. Self-induced combustion oscillations of laminar premixed flames stabilized on annular burners. *Combustion and Flame*, 135:525–537, 2003.

[164] A.X. Sengissen, T.J. Poinsot, J.F. van Kampen, and J.B.W. Kok. Response of a swirled non-premixed burner to fuel flow rate modulation. In *Complex effects in Large Eddy Simulation*, 2005.

[165] W.C. Strahle. On combustion generated noise. *Journal of Fluid Mechanics*, 49(2):399–414, 1971.

[166] W.C. Strahle. Some results in combustion generated noise. *Journal of Sound and Vibration*, 23(1):113–125, 1972.

[167] R.I. Sujith, G.A. Waldherr, and B.T. Zinn. An exact solution for one-dimensional acoustic fields in ducts with an axial temperature gradient. *Journal of Sound and Vibration*, 184(3):389–402, 1995.

[168] N. Syred and J.M. Beér. Combustion in a swirling flow : A review. *Combustion and Flame*, 23(2):143–201, 1974.

[169] M. Terao and H. Sekine. In-duct pressure measurements to determine sound generation, characteristic reflection and transmission factors of an air moving device in air-flow. *InterNoise 89*, pages 143–146, 1989.

[170] A. Thomas and G.T. Williams. Flame noise: sound emission from spark-ignited bubbles of combustible gas. *Proceedings of the Royal Society of London. Series A, Mathematical and Physical Sciences*, 294(1439):449–466, 1966.

[171] H. Tijdeman. On the propagation of sound waves in cylindrical tubes. *Journal of Sound and Vibration*, 39:1–33, 1975.

[172] H. Tijdeman. *College notes "Inleiding modaal analyse en experimenteel trillingsonderzoek (in Dutch)*. Universiteit Twente, Technische Mechanica, 1990.

[173] S. Toledo. A survey of out-of-core algorithms in numerical linear algebra. *DIMACS Series in Discrete Mathematics and Theoretical Computer Science, External Memory Algorithms*, 50:161–179, 1999.

[174] P.G. Tucker and Z. Pan. URANS computations for a complex internal isothermal flow. *Computational Methods Applied Mechanical Engineering*, 190:3893–2907, 2001.

[175] S.R. Turns. *An introduction to combustion, concepts and applications*. McGraw-Hill, Inc., 1996.

[176] L.-C. Valdès and D. Santens. Influence of permanent turbulent air flow on acoustic streaming. *Journal of Sound and Vibration*, 230(1):1–29, 2000.

[177] F.J.M. van der Eerden. *Noise reduction with coupled prismatic tubes*. PhD thesis, University of Twente, 2000.

[178] J.F. van Kampen. Silent Reflections, on the characterisation and reduction of fan noise by means of acoustic resonators. Master's thesis, University of Twente, 2001.

[179] J.F. van Kampen, J.B.W. Kok, and Th.H. van der Meer. One-dimensional acoustic modelling of thermoacoustic instabilities. In *Tenth International Congress on Sound and Vibration*, 2003.

[180] J.F. van Kampen, J.B.W. Kok, and Th.H. van der Meer. Prediction of thermo-acoustic spectra in gas turbine combustors using unsteady RaNS CFD simulations. In *Eleventh International Congress on Sound and Vibration*, pages 3477–3484, 2004.

[181] J.F. van Kampen, J.B.W. Kok, and Th.H. van der Meer. Efficient retrieval of a flame transfer function from a steady-state CFD simulation. In *Twelfth International Congress on Sound and Vibration*, 2005.

[182] D. Veynante and L. Vervisch. Turbulent combustion modeling. *Progress in Energy and Combustion Science*, 28:193–266, 2002.

[183] J. Warnatz, U. Maas, and R.W. Dibble. *Combustion*. Springer-Verlag, Berlin, 1996.

[184] R. Weber and J. Dugué. Combustion accelerated swirling flows in high confinements. *Progress in Energy and Combustion Science*, 18(4):349–367, 1992.

[185] P. Weigand, X.R. Duan, W. Meier, U. Meier, M. Aigner, and C. Bérat. Experimental investigations of an oscillating lean premixed CH4/air swirl flame in a gas turbine model combustor. In *Proceedings of the European Combustion Meeting 2005*, 2005.

[186] P. Wesseling. *Principles of computational fluid dynamics*. Springer-Verlag, 2001.

[187] F.A. Williams. *Combustion theory*. The Benjamin/Cummings Publishing Company Inc., second edition, 1985.

[188] J.E. Ffowcs Williams. The noise from turbulence convected at high speed. *Proceedings of the Royal Society of London, Series A*, 255:469–503, 1963.

[189] J.H. Yu. *On formation of NO_x and CO in turbulent premixed combustion*. PhD thesis, University of Twente, 1996.

[190] C. Zwikker and C. Kosten. *Sound absorbing materials*. Elsevier, Amsterdam, 1949.

Nawoord

Nu u het hele proefschrift grondig hebt gelezen, wil ik u erop wijzen dat de totstandkoming ervan onmogelijk was geweest zonder de hulp en het vertrouwen van een groot aantal mensen.

Allereerst wil ik mijn directe begeleider Jim Kok bedanken. Hij heeft mij 4 jaar geleden het vertrouwen gegeven om in de thermo-akoestiek te promoveren. De enthousiaste begeleiding en de vrijheid die hij mij gegeven heeft om tot de afronding van dit werk te komen, heb ik als bijzonder prettig ervaren. Ook mijn promotor Theo van der Meer heeft een groot aandeel gehad in mijn onderzoek. De vele discussies die we hebben gevoerd gedurende de promotie en tijdens het bespreken van het proefschrift waren altijd zeer verhelderend. Verder deed Theo ook mee met veel sociale activiteiten van de vakgroep, zoals hardlopen of een biertje na het werk (al dan niet in 'De Kikker').

De samenwerking binnen het DESIRE project was bijzonder prettig en de halfjaarlijkse bijeenkomsten heb ik als zeer interessant en leuk ervaren. Binnen de UT wil ik hiervoor bedanken: André de Boer, Bert Wolbert, Peter van der Hoogt, Jim Kok, Theo van der Meer, Genie Stoffels en Rob Huls. Buiten de UT heb ik een zeer prettige samenwerking gehad met Alois Sengissen, Robert Dannecker, Berthold Noll en Werner Krebs.

Binnen het onderzoek is er een bijzondere testopstelling gerealiseerd. Chris Bakker, Nutte Dijkstra en Mark Landman zijn hierbij onmisbaar geweest. Bedankt daarvoor! Voor alle computer zaken kon ik altijd aankloppen bij Eise Veenstra. Ook de hulp die we van Eise hebben gehad bij het realiseren van een Linux cluster heb ik zeer gewaardeerd.

Dan een apart paragraafje voor Sally en Debbie! Ik kon bij jullie altijd terecht voor snoepjes, taarten en lekkere broodjes. Ook hebben jullie ervoor gezorgd dat ik mij nooit zorgen hoefde te maken over allerlei zaken die niet direct met mijn onderzoek te maken hadden. Sally en Debbie, bedankt voor alles!

Ik heb tijdens mijn promotie een aantal kamergenoten versleten. Allemaal prima kamergenoten, niets mis mee! Het eerste jaar deelde ik de kamer met Rob Huls. Samen met hem heb ik ook het DESIRE project aangepakt. Rob, bedankt voor de interessante discussies en de samenwerking. Het overgrote deel van mijn promotie zat ik samen met Sjoerd Pater op de kamer. Qua kennis vulden wij elkaar prima aan. Verder hielden we beiden van chocoladevlokken als broodbeleg. De lege pakken vlokken die we in de loop der tijd verorberd hebben werden opgestapeld voor het raam, wat de kamer erg herkenbaar maakte. Sjoerd, bedankt voor de gezellige

tijd. Tenslotte verhuisde ik naar een kamer met Nutte Dijkstra, later kwam Michiel Willemse er ook bij. Door de goed gevulde koelkast transformeerde deze kamer aan het einde van de middag menigmaal tot borrelruimte, wat zorgde voor de nodige ontspanning tijdens het schrijven van dit proefschrift.

Binnen de vakgroep Thermische Werktuigbouwkunde heerste er altijd een prima sfeer. Zo goed zelfs, dat er ook vaak buiten het werk om werd afgesproken voor sociale activiteiten. Samen met de vakgroep Technische Mechanica deden (en doen we!) mee aan de jaarlijkse Batavierenrace. Voor een wat kleinere groep mensen was ook het rugby toernooi van de ERC een jaarlijks terugkerende happening. Deze evenementen gaven altijd aanleiding tot veel sterke verhalen gedurende de koffiepauzes die erop volgden. Andere activiteiten die mij op dit moment te binnen schieten en die ik zeker erg zal gaan missen zijn: het voetballen in de koffiepauzes, diagonaaltjes trekken bij de Muur, avondjes stappen, borrels, barbecues etc. Mensen die ik hiervoor wil bedanken zijn: Sjoerd, Nutte, Joost van der Handdoek, Michiel, Hans, Eddy, Marco, Bogdan, Marcel, Genie, Bram, Runga Kutta, Marc, Artur, Ziad en Roy.

Terug weer naar het serieuzere vlak. Ik wil Bram de Jager en Marco Derksen bedanken voor hun waardevolle commentaar op het proefschrift en de bijdragen die zij eraan hebben geleverd door de discussies die we gevoerd hebben. Ook de afstudeerders die ik gedurende mijn promotie heb mogen begeleiden, hebben allemaal een flinke bijdrage geleverd aan het eindresultaat. In dit verband dank ik Rob Kleinlugtenbelt, Uros Lekic, Michiel Willemse en Julien Jachmich.

Aangezien mijn 'roots' bij de vakgroep Technische Mechanica liggen, had ik ook veel contact met de mensen aldaar. Dit contact beperkte zich wederom niet tot binnen het werk. Ik wil de volgende mensen hiervoor bedanken: Clemens B., Raf, Richard L., Rob, Marcoon, Marieke, Ekke O., Bert K., Marten en René.

Natuurlijk zijn er ook veel mensen die buiten de UT om veel invloed hebben gehad op het eindresultaat. Pa, Ma, Marleen en Paulien, bedankt voor alle gezelligheid en het vertrouwen dat jullie in mij hebben gehad toen ik naar het 'verre oosten' vertrok.

Tenslotte wil ik natuurlijk Jacqueline bedanken. We hebben een lange tijd ver weg van elkaar gewoond. Ondanks de afstand wist je mij altijd op te beuren als ik er even doorheen zat. Ook heb je mij de tijd gegund om de promotie gedurende veel weekenden en avonden af te ronden. Thanxxx!

Met dit proefschrift sluit ik niet alleen een periode als promovendus af. Ook verlaat ik na bijna 10 jaar de UT en Enschede. Ik kijk met veel nostalgie terug op deze periode (betekent dat dat ik oud word?!?). Ik heb het altijd prima naar mijn zin gehad en wil iedereen daar nogmaals voor bedanken!

Jaap

Enschede, januari 2006